

LEG 179 SYNTHESIS: GEOCHEMISTRY, STRATIGRAPHY, AND STRUCTURE OF GABBROIC ROCKS DRILLED IN ODP HOLE 1105A, SOUTHWEST INDIAN RIDGE¹

John F. Casey,² Debleena Banerji,² and Pedram Zarian²

ABSTRACT

Oxide-free olivine gabbro and gabbro and oxide olivine gabbro and gabbro make up the bulk of the gabbroic suite recovered from Ocean Drilling Program (ODP) Leg 179 Hole 1105A, which lies 1.2 km away from Hole 735B on the eastern transverse ridge of the Atlantis II Fracture Zone, Southwest Indian Ridge. The rocks recovered during Leg 179 show striking similarities to rocks recovered from the uppermost 500 m of Hole 735B during ODP Leg 118. The rocks of the Atlantis platform were likely unroofed as part of the footwall block of a large detachment fault on the inside corner of the intersection of the Southwest Indian Ridge and the Atlantis II Transform at ~11.5 Ma. We analyzed the lithologic, geochemical, and structural stratigraphy of the section. Downhole lithologic variation allowed division of the core into 141 lithologic intervals and 4 main units subdivided on the basis of predominance of oxide gabbroic vs. oxide-free gabbroic rocks. Detailed analyses of whole-rock chemistry, mineral chemistry, microstructure, and modes of 147 samples are presented and clearly show that the gabbroic rocks are of cumulate origin. These studies also indicate that geochemistry results correlate well with downhole magnetic susceptibility and Formation MicroScanner (FMS) resistivity measurements and images. FMS images show rocks with a well-layered structure and significant numbers of mappable layer contacts or compositional contrasts. Downhole cryptic

¹Casey, J.F., Banerji, D., and Zarian, P., 2007. Leg 179 synthesis: geochemistry, stratigraphy, and structure of gabbroic rocks drilled in ODP Hole 1105A, Southwest Indian Ridge. *In* Casey, J.F., and Miller, D.J. (Eds.), *Proc. ODP, Sci. Results*, 179: College Station, TX (Ocean Drilling Program), 1–125. doi:10.2973/odp.proc.sr.179.001.2007

²Department of Geosciences, University of Houston, Science and Research 1 Building, 4800 Calhoun Road, Houston TX 77204, USA. Correspondence author: jfcasey@uh.edu

mineral and whole-rock chemical variations depict both “normal” and inverse fine-scale variations on a scale of 10 m to <2 m with significant compositional variation over a short distance within the 143-m section sampled. A Mg# shift in whole-rock or Fo contents of olivine of as much as 20–30 units over a few meters of section is not atypical of the extreme variation in downhole plots. The products of the earliest stages of basaltic differentiation are not represented by any cumulates, as the maximum Fo content was Fo₇₈. Similarly, the extent of fractionation represented by the gabbroic rocks and scarce granophyres in the section is much greater than that represented in the Atlantis II basalts. The abundance of oxide gabbros is similar to that in Hole 735B, Unit IV, which is tentatively correlated as a similar unit or facies with the oxide gabbroic units of Hole 1105A. Oxide phases are generally present in the most fractionated gabbroic rocks and lacking in more primitive gabbroic rocks, and there is a definite progression of oxide abundance as, for example, the Mg# of clinopyroxene falls below 73–75. Coprecipitation of oxide at such early Mg#s cannot be modeled by perfect fractional crystallization. In situ boundary layer fractionation may offer a more plausible explanation for the complex juxtaposition of oxide- and nonoxide-bearing more primitive gabbroic rocks. The geochemical signal may, in part, be disrupted by the presence of mylonitic shear zones, which strike east-west and dip both to the south and north, but predominantly to the south away from the northern rift valley where they formed. Downhole deformation textures indicate increasing average strain and crystal-plastic deformation in units that contain oxides. Oxide-rich zones may represent zones of rheologic weakness in the cumulate section along which mylonitic and foliated gabbroic shear zones nucleate in the solid state at high temperature, or the oxide may be a symptom of former melt-rich zones and hypersolidus flow, as predicted during study of Hole 735B.

INTRODUCTION

Considerable research efforts have been directed toward revealing the structure and constitution of the lower oceanic crust as well as understanding magma chamber processes and geometries responsible for formation of the plutonic portions of the crust at spreading centers. Studies of seafloor plutonic samples have provided remarkably little direct knowledge of the structure and constitution of the plutonic foundations of the oceanic crust despite its obvious volumetric importance. Studies have likewise not clearly enabled definition of magma chamber processes that relate to production of mid-ocean-ridge basalt (MORB). The paucity of samples, the difficulties maintaining pseudostratigraphic control on dredge or dive samples in tectonically complex regions, and the altered and deformed nature of many abyssal plutonics have all in some way hampered investigations aimed at sampling a complete section of the lower plutonic crust with seafloor collections.

Drilling efforts of the Ocean Drilling Program (ODP) to investigate lower oceanic crust have been more successful than more conventional sampling techniques in obtaining in situ samples and started to yield significant results when Site 735 near the Atlantis II Fracture Zone of the Indian Ocean was drilled during Leg 118. The first significant penetration (~500 m) into a gabbroic massif was unexpectedly achieved with high recovery (~90%) toward the end of the leg (Robinson, Von Herzen, et al., 1989). In the late 1980s the Offset Drilling Working Group pro-

posed a plan for capitalizing on sites, like Site 735, where tectonic dismemberment had created windows of opportunity to drill the lower oceanic crust and mantle. The goal of the program was to drill offset holes within dismembered sections to build a composite picture of the entire oceanic crustal section. Two legs followed during which gabbroic and ultramafic rock were drilled in the Hess Deep in the Pacific Ocean during Leg 147 (Gillis, Mevel, Allan, et al., 1993) and, subsequently, near the Kane Fracture Zone along the Mid-Atlantic Ridge (MARK area) during Leg 153 (Cannat, Karson, Miller, et al., 1995). The *JOIDES Resolution* revisited the Southwest Indian Ridge (SWIR) during Leg 176 to deepen the previously drilled Hole 735B and achieved penetration to 1500 m with excellent recovery. This greatly enhanced and completely transformed the way we view the nature of the plutonic section of the oceanic crust (Dick, Natland, Miller, et al., 1999; Dick et al., 2000). Finally, to partly address bare rock spudding problems during prior offset drilling legs, Leg 179 was conceived as an engineering leg to test the hammer drill-in casing system near Hole 735B and to drill a hole along the Ninetyeast Ridge for emplacement of a downhole seismometer (Pettigrew, Casey, Miller, et al., 1999). Leg 179 was unexpectedly able to add to plutonic recovery on the Atlantis Bank because of delays in a resupply ship visit that inhibited resumption of hammer tests at Site 1104. A bare rock spud using a tricone bit was drilled to 15 meters below seafloor (mbsf), followed by several days of rotary coring in Hole 1105A to a depth of 158 mbsf within the gabbroic massif of the Atlantis platform. The hole is ~1.2 km east-northeast of Hole 735B and was logged with the Formation MicroScanner (FMS) and other downhole tools (Pettigrew, Casey, Miller, et al., 1999).

Ocean Drilling Program Leg 179 set out with two primary objectives:

1. To test the recently developed hammer drill-in casing system on the Atlantis Bank, Southwest Indian Ridge, and
2. To drill a cased reentry hole into basaltic basement on the Ninetyeast Ridge to allow future installation of an ocean floor geophysical observatory, the Ninetyeast Ridge Observatory (NERO).

The second primary objective specifically included drilling a single hole as deep as possible into basement and installing a reentry cone and casing beyond basement to prepare the Ninetyeast Ridge site for installation of an ocean-bottom observatory. The observatory will be installed at a later date and will be part of the future network of seafloor observatories proposed in the International Ocean Network program. Drilling reached 493.8 mbsf, sufficient depth to create an acceptable borehole below casing for the downhole seismometer installation. Total penetration into basement was 122 m, and total penetration below casing reached 79.4 m. This significant penetration below the casing, as well as the firm attachment to basement, should isolate the geophysical instrument from noise reported from other ocean floor seismometer installations. Both these objectives were accomplished during Leg 179.

Hammer drill testing was completed at Sites 1104 and 1106 (virtually coincident locations but positioned from different beacons after a hiatus in testing while waiting for resupply). These tests provide a wealth of information regarding the viability of the hammer drill-in casing system as a new tool for investigating the solid Earth. Although the testing was not completed as planned, design changes resulting from tests that were completed were made to accommodate future legs where the hammer drill was deployed successfully. Based on the results of the first sea

trial of the hammer drill-in casing system and follow-up legs, we are confident that continued development will soon allow us to sample the deep ocean crust in environments where, with rare exceptions, we have historically been unable to operate (Pettigrew, Casey, Miller, et al., 1999).

Drill string acceleration data were acquired at two sites occupied during Leg 179 (Pettigrew, Casey, Miller, et al., 1999). Myers et al. (Chap. 1, this volume) determined that drill string acceleration signals vary inversely with porosity measured from logging and core data. The signal amplitude varies with lithology, with sediment amplitude roughly one-half that of either basalt or gabbro. Significant energy radiates through the seafloor but behaves differently when passing through various formations. The authors proposed that drill string acceleration may provide a useful tool to evaluate drilling conditions and formation properties encountered at the bit.

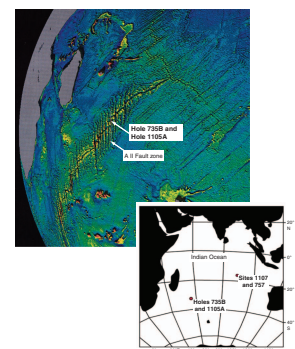
Because of contingencies developed during Leg 179, certain ancillary objectives were not accomplished during hammer drilling, but one contingency drilling site was cored on the Atlantis Bank, Southwest Indian Ridge (Pettigrew, Casey, Miller, et al., 1999). This chapter is a synthesis of results from structural, geochemical, and downhole information now available for ODP Hole 1105A, the contingency drilling site. Drilling penetrated into a gabbroic massif on the Atlantis Bank, along the eastern transverse ridge of the Atlantis II Fracture Zone offsetting the Southwest Indian Ridge. The hole is proximal to Hole 735B, drilled into the same gabbroic massif during Legs 118 and 176. The gabbroic massif appears to have been exposed as a consequence of core complex formation at ~11.5 Ma at the northern Southwest Indian Ridge intersection with the Atlantis II Transform (Dick et al., 1991; Natland and Dick, 2002).

Located only 1.2 km from Hole 735B, Hole 1105A represents the first hole with good recovery to have been drilled in such close proximity to another high-recovery hole. The value of this lies in the attempt to correlate various aspects of each hole and the attempt to construct a two-dimensional (2-D) model of the geometry of the plutonic complex beneath the Atlantis Bank and the magmatic and structural features in both holes. This synthesis paper reports largely on the results of Leg 179 that pertain to Hole 1105A and studies of the core and logging data collected. Further details of the hammer drill sites and the NERO site where no core recovery was possible can be obtained from the Leg 179 *Initial Reports* volume (Pettigrew, Casey, Miller, et al., 1999). Because the leg was an engineering leg, significant results are reported in the *Initial Reports* volume. For developments of the of the hammer drill system since Leg 179, readers are referred to further results of tests conducted during Leg 191 (Holloway and Shipboard Scientific Party, 2001).

TECTONIC AND GEOLOGIC SETTING OF ATLANTIS II FRACTURE ZONE

Southwest Indian Ridge (Fig. F1) extends 7200 km from the Bouvet Triple Junction to the Rodriguez Triple Junction and has been in existence since the breakup of Africa and Antarctica (Norton and Sclater, 1979). Half-spreading rates over the last 34 m.y. calculated for the Southwest Indian Ridge at the Bouvet Triple Junction (Lawver and Dick, 1983) and near the Indian Ocean Triple Junction (Tapscott et al., 1980)

F1. Free-air gravity map, p. 57.

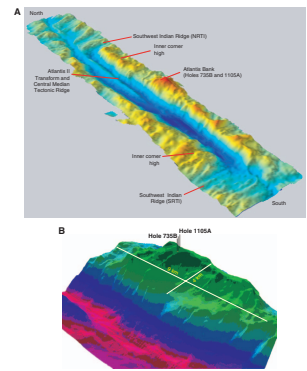


are 0.78 and 0.8 cm/yr, respectively. Thus, the SWIR is at the very slow end of the spreading rate spectrum (Fisher and Sclater, 1983). Various features of slow-spreading ridges including deep rift valleys, rough topography, and abundant exposures of plutonic and mantle rocks are all typical characteristics of Southwest Indian Ridge (Fig. F1).

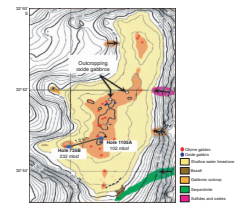
The Atlantis II Fracture Zone is one of many large-offset and high-relief fracture zones offsetting the Southwest Indian Ridge axis (Dick et al., 1991; Meyer et al., 1989). It has a left lateral offset of 199 km, which represents a ~20 m.y. offset of the SWIR (Engel and Fisher, 1975). The transform extends approximately north-south along longitude ~57°E (Fig. F1). It has a very deep (>6 km) transform valley (Dick et al., 1991) and contains a median tectonic ridge and high flanking transverse ridges on both sides of the transform (Fig. F2). The valley walls are extremely steep for large distances and are covered with extensive debris and talus. The ridge transform intersections (RTIs) are marked by deep nodal basins, lying on the transform side of the neovolcanic zones that define the present-day spreading axes, and intersect clearly defined rift valleys with a relief of >2200 m and widths of 22–38 km (Dick, Natland, Miller, et al., 1999).

Hole 1105A is located on the east side of the Atlantis II Transform Fault, which offsets the Southwest Indian Ridge. It is situated at a unique outcrop of lower oceanic crust exposed on a 15-km-long wave-cut terrace (Fig. F3) at 730 m water depth (Dick et al., 1991). The platform exposures of plutonic rock are thought to have formed at ~11.5 Ma as a core complex at the northern RTI as part of the Antarctic plate (Dick et al., 1991). Schwartz et al. (2005), utilizing Pb/U ages, determined that the Atlantis Bank likely formed between 11.2 and 12.5 Ma, very similar to the proposed magnetic ages determined. Hosford et al. (2003) showed through analysis of magnetic data from ridge segment AN-1 (north of the Atlantis Bank) out to 25-Ma lithosphere (south of Atlantis Bank) that spreading rates during formation of the Atlantis Bank were highly asymmetric. Half-rates of ~0.85 cm/yr were documented to the south and 0.55 cm/yr to the north of ridge segment AW-1. At the time of formation the gabbroic and ultramafic rocks outcropping on the Atlantis Bank are thought to have been unroofed and exposed on a low-angle detachment fault on the southern flank of the rift valley near the RTI that was subsequently partially uplifted above sea level and then transported to its present position approximately half-way along the transform. Analysis of the seafloor fabric around the Atlantis Bank shows that the platform margins display a north-south seafloor fabric truncated north and south of the bank by an east-west spreading tectonic fabric (Fig. F4). We interpret the Atlantis Bank fabric to possibly represent remnants of a corrugation fabric typical of core complexes or megamullions observed in the Atlantic Ocean (e.g., Tucholke et al., 1997), although this is less clear because part of the mass was above sea level and eroded (Dick et al., 1991). Figure F4 is a three-dimensional (3-D) view of the transform domain with a false-color illustration of the north-south transform-parallel seafloor fabric. The fabric is defined by first creating a slope map from an unfiltered bathymetric grid on the Atlantis Transform and then defining the aspect of slope. The aspect map is draped on bathymetry, and the image depicts color changes at positions of maximum slope or changes in slope direction. The trends of the color changes are parallel to the steepest slopes and axes of slope direction change. Linear morphology of large- or small-scale structures such as corrugations or faults and their continuity become readily apparent, as highlighted by color changes. The transform-

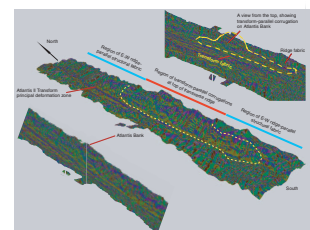
F2. Area bathymetry maps, p. 58.



F3. Bathymetric map of drill sites, p. 59.



F4. Bathymetric map draped with aspect of slope grid, p. 60.



parallel fabric appears to be very distinct from elsewhere along the Atlantis Bank transverse ridge where the fabric typically parallels the spreading center. The transform-parallel corrugations manifested by the aspect map appear to persist on the lower part of the eastern wall of transform valley.

Baines et al. (2003) inferred that the same north-south fabric may be caused by more recent transform-parallel normal faulting of unknown origin, in part to explain the excess elevation of the transverse ridge and in particular the Atlantis Bank. We are, however, struck by the fact that these transform-parallel seafloor fabric elements over the eastern transverse ridge are truncated by east-west spreading center-parallel faults and seafloor fabrics just north and south of the platform, as is typical over many of the core complex counterparts that have been studied in the Atlantic (Tucholke et al., 1998). If large ridge-parallel faults originate nearer the ridge axis, as seems likely, and the transform-parallel corrugations are cut by the ridge-parallel faults, it is likely the corrugations originated near the ridge axis and not off axis, as inferred by the model of Baines et al. (2003). That the steep parts of the mullion corrugations could nucleate high-angle transform-parallel normal faults subsequent to unroofing is certainly possible. Gravitational collapse along a normal-slip surface parallel to the transform wall is also possible, as are normal slip surfaces related to differential subsidence rates on seafloor adjacent to the transform, as predicted by Fox and Gallo (1984). The stress field necessary to create nearly transform-parallel pure normal slip faults as suggested by Baines et al. (2003), other than collapse caused by high relief, is indeed somewhat uncertain. The excess elevation of the transverse ridge and local normal slip faulting, in part, could be aided by bending strains and extensive subsurface volume expansion of 20%–40% caused by serpentinization of mantle material. Materials collected during submersible dives and dredges and drill core taken along the transform valley walls adjacent to Atlantis Bank have recovered suites of highly serpentinized ultramafic rocks (MacLeod et al., 1998). Sustained tectonic activity along the transform could lead to fracture-assisted fluid penetration in the regions adjacent to the transform and enhanced hydration and transformation of mantle material to crustal material and densities. This may, in part, explain some of the excess elevation along the transverse ridge.

It is important to note that our FMS analyses of fractures and shear zones in Hole 1105A and those of Hole 735B (Iturrino et al., 2002) show that these fractures and shear zones typically strike parallel to the northern ridge axis approximately east-west and have normal senses of slip. These shear zones and faults appear to have a conjugate relationship with moderate dips either toward the ridge axis (north) or away from the ridge axis (south), which may be due to normal inward-dipping ridge axis faults as well as conjugate faults resulting from bending stresses during footwall rollover (e.g., Tucholke et al., 1998). Transform-parallel normal fault trends inferred by Baines et al. (2003) are represented in the core. Likewise, Iturrino et al. (2002) show that fault plane solutions from recorded earthquakes in the region are either north-south-striking strike-slip faults or east-west-striking normal faults, with an absence of north-south-striking normal fault solutions. The 3-D image shown by Baines et al. (2003) could alternatively be inferred to show a typical transform-parallel mullion corrugation structure on the uneroded flanks of Atlantis Bank.

Formation of low-angle detachment faults and core complexes such as the Atlantic Bank are generally thought to be the consequence of

amagmatic or magma-poor extension at the ridge and development of a master fault, which lead to exposure of a plutonic or serpentinized mantle section of the oceanic lithosphere (Fig. F4). The core complex effectively forms a tectonic window (Karson et al., 1987; Karson and Winters, 1992; Cannat and Casey, 1995; Tucholke et al., 1998) into the lower oceanic crust or upper mantle exposed on the footwall of a now low-angle detachment. Holes 1105A and 735B appear to be drilled on such a tectonic window on the Atlantis Bank (Dick, Natland, Miller, et al., 1999). Hole 1105A was located to help constrain the overall structure of the massif exposed on the platform and to compare with the upper regions of Hole 735B. Drilling in Hole 1105A provides an opportunity to understand the dimensions of subaxial magmatic systems and continuity of structure, lithology, and magmatic facies. It also provides the opportunity to constrain magmatic and structural processes along strike of the ridge axis at a very slow spreading center. These opportunities are based on possible similarities and correlations between Hole 1105A and the upper part of Hole 735B, holes with ~1.2 km of lateral offset (Fig. F3).

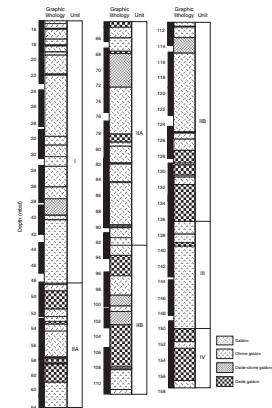
HOLE 1105A LITHOSTRATIGRAPHY AND MAGNETIC SUSCEPTIBILITY

During 5 days of drilling, Hole 1105A penetrated 158 m into the Atlantis Bank gabbroic massif. The measured cored interval was 143 m, starting 15 m below the seafloor. Core recovery was 118.43 m of gabbroic rocks (total recovery = 82.8%), in line with the high recovery rates in Hole 735B. Together with logging results (Miller et al., [Chap. 3](#), this volume; Zarian et al., 2002), this high core recovery provides nearly complete coverage of the rock types drilled and a comprehensive view of pseudostratigraphy and structure in the gabbroic section cored (see the Leg 179 *Initial Reports* volume; Pettigrew, Casey, Miller, et al., 1999).

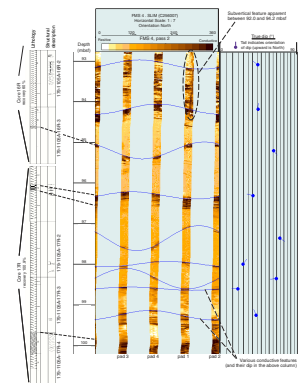
The recovered cores record a wide variety of rock types ranging from gabbro, oxide gabbro, olivine gabbro, and oxide olivine gabbro to fewer troctolitic gabbro, gabbroonorite, and felsic rocks such as trondhjemite. A total of 141 lithologic intervals (Fig. F5) were defined within the core on the basis of distinct changes in mode, modal proportions, grain size, and/or texture. Four rock types were delineated by the shipboard scientists in constructing Figure F5: gabbro, olivine gabbro, oxide gabbro, and oxide olivine gabbro. Well-defined igneous layer contacts or structural boundaries of these intervals are preserved in many sections of the core. The highly layered nature of the gabbroic rocks documented within the core is supported by visual and thin section examination of the core, high-quality continuous FMS logs of the borehole (e.g., Fig. F6), other logs, and whole-core magnetic susceptibility measurements (Pettigrew, Casey, Miller, et al., 1999).

Gabbroic rocks constitute the majority of the recovered igneous lithologies (>99% by volume) with only a very minor component of felsic veins (<1%) (Pettigrew, Casey, Miller, et al., 1999). The gabbroic rocks are characterized by mostly medium- to coarse-grained granular textures and display modal, textural, and grain size variations. Regularly to irregularly developed igneous layering and rare igneous lamination are present within intervals, and many of the contacts between defined intervals are marked by mesoscopic layer boundaries (Pettigrew, Casey, Miller, et al., 1999). Grain size variations are extreme within the

F5. Lithologic unit summary, p. 61.



F6. FMS image from Hole 1105A, p. 62.



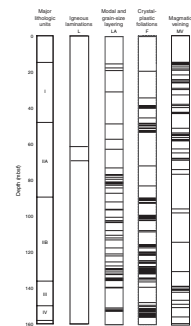
core: 2% pegmatitic gabbro, 67% coarse-grained gabbro, 28% medium-grained gabbro, and 3% fine-grained gabbro (Pettigrew, Casey, Miller, et al., 1999). Modally, the gabbroic rocks range from gabbro (36%) to olivine gabbro (43%), oxide gabbro (17%), oxide olivine gabbro (4%), and minor gabbro-norite (Pettigrew, Casey, Miller, et al., 1999; Thy, **Chap. 2**, this volume). The principal gabbroic rock types are defined based on the presence or absence of olivine, orthopyroxene, and/or Fe-Ti oxide minerals. The contacts of the intervals were visually characterized to be mainly caused by modal, modal proportion, grain size, and textural changes or combinations of these. As detailed modal analysis was conducted on the samples included in this synthesis, we are able to further refine rock types as they are presented in downhole plots.

Late magmatic veins of leuco-gabbro to granophyre are present throughout most of the core. They represent a large compositional range extending to diorite and trondhjemite, constituting the more silicic end-members. These veins are often thin, several centimeters or less in width, so they are not defined as separate intervals. Despite their volumetrically minor importance, they are of considerable interest because they may represent the final products of magmatic differentiation and strongly influence mass balance calculations (see the Leg 179 *Initial Reports* volume; Pettigrew, Casey, Miller, et al., 1999). Most of the recovered core is characterized by random orientations of coarse-grained, elongated, or tabular minerals such as plagioclase and clinopyroxene with no sign of compaction or preferred dimensional orientation. However, weak magmatic lamination can be observed locally, and evidence of ductile shear zones and crystal-plastic deformation is observed in localized intervals throughout the cored section. The distribution of magmatic lamination, layering, deformation, and magmatic veining is shown in Figure F7 (Pettigrew, Casey, Miller, et al., 1999).

Minerals identified as secondary or metamorphic under the microscope include talc, serpentine, smectite, magnetite, calcite, epidote, chlorite, brown hornblende, green hornblende, actinolite, and plagioclase. In addition, orange-brown to pale greenish brown phlogopitic mica is present in trace amounts in some olivine gabbro samples. It is not certain, however, whether this mica is primary or secondary (Pettigrew, Casey, Miller, et al., 1999). The secondary and metamorphic mineralogy of the core is limited to fewer than the 12 mentioned mineral species. This apparent simplicity in mineral assemblages microscopically examined is partly because most gabbroic samples from which thin sections were made were not taken from the late magmatic veins or their vicinities, and only optical determination of the minerals was conducted. Samples analyzed during this study were generally little altered.

The 141 lithologic intervals were grouped into summary Units I–IV in order to facilitate description and comparison with the core recovered during Leg 118 (Robinson, Von Herzen, et al., 1989; Dick et al., 1991). Units I and III are characterized by more abundant oxide-free olivine gabbro and gabbro, and Units II and IV are characterized by more abundant oxide-rich oxide gabbro, oxide olivine gabbro, and oxide gabbro-norite. The summary units and intervals illustrated in Figure F5 are mainly based on modal oxide abundances and grain-size characteristics. Magnetic susceptibility is strongly correlated with oxide abundance in Holes 1105A and 735B (e.g., Natland, 2002). In particular, Unit II in Hole 1105A and Unit IV in Hole 735B are strongly similar in abundances of oxide-rich gabbroic rock types and high magnetic susceptibilities. They, in fact, may be correlative units within the Atlantis Bank gabbroic massif. Although Unit II in Hole 1105A is significantly thicker

F7. Distribution structures in Hole 1105A, p. 63.



than Unit IV in Hole 735B, the magnetic susceptibility values and lithologies are strikingly similar in each hole. Both contain vertically persistent zones of gabbroic rocks with high average oxide content and significant thickness.

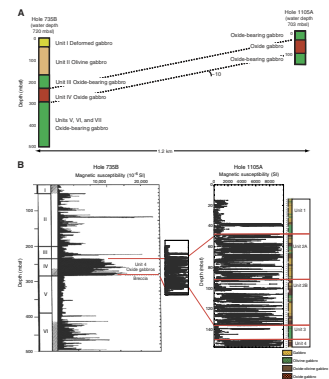
These oxide-rich units may be part of the same facies, with the thickness of the unit increasing toward the center of the Atlantis Bank platform (i.e., toward Hole 1105A). Alternatively, the differences in thickness from one hole to the other may result from structural complexities in one or both holes, caused by shear zones noted in each hole (e.g., three mylonites in Hole 1105A) (see “[Hole 1105A Deformation Extent and Core Microstructure](#),” p. 34, and discussions of Hole 735B in Niu et al., 2002, and Dick, Natland, Miller, et al., 1999). Figure F8 depicts magnetic susceptibility values for Hole 1105A and the upper part of Hole 735B. The unit boundaries in Hole 1105A strongly correlate with sharp decreases or increases in average magnetic susceptibility, similar to the definition of Unit IV in Hole 735B (Natland, 2002). Further refinements and core-logging correlations between magnetic susceptibility, oxide-bearing lithologies, and FMS data for Hole 1105A are presented in Miller et al. ([Chap. 3](#), this volume).

The nature of the contacts and the petrographic variability between and within individual intervals provide important constraints on the magmatic and tectonic history of Hole 1105A gabbros. Natland and Dick (2002) argued, based on the bulk rock data from the Leg 179 *Initial Reports*, against correlation between Unit II of Hole 1105A and Unit IV of Hole 735B because they suggested (1) that the range of TiO_2 , SiO_2 , Zr, and Y bulk rock values in Unit II of Hole 1105A did not correlate or reach the extreme levels (lows or highs) typical of Unit IV in Hole 735B and (2) that Unit II of Hole 1105A contained more primitive olivine gabbro than Unit IV in Hole 735B. Based on the more comprehensive data set for Leg 179 reported below, we are not able to confirm significant differences in the range of compositions between Hole 1105A (Unit II) and Hole 735B (Unit IV), with TiO_2 contents in Hole 1105A ranging as high as 7.56 wt% and SiO_2 contents as low as 33.37 wt% where oxides are abundant. The abundances of Zr and Y in Hole 1105A Unit II samples are comparable and in some intervals exceed the ranges documented in Unit IV samples from Hole 735B. We also note that the downhole variation across Unit IV of Hole 735B may not be as well documented as the oxide gabbro interval in Hole 1105A. Because the average sampling interval in Hole 1105A is significantly less than 1 m, there are nearly three times as many bulk and mineral analyses over the same interval of Hole 1105A when compared with Hole 735B. Therefore, the three cryptic units defined by Natland and Dick (2002) in Hole 735B in this interval may underestimate the number of more primitive intervals present. In particular, the three cryptic chemical trend lines defined for Unit IV in Hole 735B often cross trend lines that could be defined by adjacent samples, perhaps indicating underestimation of the scale of variation. Therefore, we cannot as readily dismiss the possibility that the units are related in some fashion and could, in general, be correlated laterally as part of the same magmatic facies or units.

Modal Mineralogy

Modal mineral abundances of primary phase olivine, clinopyroxene, plagioclase, opaque oxides, orthopyroxene, and inverted pigeonite are presented in Table T1 and facilitate comparisons with whole-rock and

F8. Potential stratigraphic correlation between Holes 735B and 1105A, p. 64.



T1. Modal analysis of gabbros, p. 105.

mineral chemistry presented below. Scans of each thin section are presented in the volume “**Supplementary Material**” for comparison, and Figure F9 shows six examples of igneous cumulate textures largely devoid of deformation features. Although most modes of moderate to fine grain-sized thin sections are considered reliable, there were several very coarse gabbroic rocks analyzed for which we consider the modes to be unreliable based on analysis of standard thin sections (e.g., Samples 179-1105A-9R-2, 17–20 cm, and 27R-4, 29–31 cm). These poorly defined modes are indicated in Table T1 by asterisks. Limited sample sizes and the necessity to analyze the bulk chemistry of each sample prohibited more detailed analyses of these coarse samples with oversized thin sections; however, as in shipboard studies, the data provide information on the nature and relative proportion of the phases crystallizing downhole and in most cases appear to directly correlate with whole-rock chemistry. In addition, the data are useful in establishing when oxides, pigeonite, and orthopyroxene begin to fractionate in the crystallization sequence. Except for samples that may have had mixed lithologies (silicic veins and compositional layer boundaries), rocks were classified based on modes of magmatic minerals as (1) oxide-free olivine gabbro and gabbro, (2) oxide-bearing (0.1%–5% opaque oxides) olivine gabbro and gabbro, and (3) oxide (>5% opaque oxides) olivine gabbro and gabbro. This classification conforms with the International Union of Geological Sciences (IUGS) classification in utilizing the term “oxide” as a modifier if the accessory mineral is >5%. In order to allow comparison with usage in Hole 735B (Dick, Natland, Miller, et al., 1999) and prior usage (Thy, **Chap. 2**, this volume) in Hole 1105A, in which rocks are labeled oxide if they are >1% opaque oxides (Dick et al., 2002), we simply indicate samples with any “magmatic” oxides in the range of 0.1–5 mod% as “oxide bearing.” Exsolved oxide in clinopyroxene and oxide associated with alteration products of olivine and clinopyroxene were not included in the oxide mode. Gabbronorites were also described by Thy (**Chap. 2**, this volume), but although orthopyroxene or inverted pigeonite is present in thin sections, the samples described are not *sensu stricto* gabbronorites as noted by Thy. We agree with Thy (**Chap. 2**, this volume) that the presence of orthopyroxene or inverted pigeonite (or its inversion products) are important petrogenetic markers and worth noting, but they were sampled in a limited number of shipboard sections and they can be depicted in downhole modal plots by their presence in certain oxide-rich intervals without presenting a rock name that does not necessarily fit the mode. Orthopyroxene-bearing samples were more extensively described in Hole 1105A by Thy (**Chap. 2**, this volume) and in Hole 735B (Robinson, Von Herzen, et al., 1989; Dick, Natland, Miller, et al., 1999), but after review of modal and bulk data we refrain from using rock names that overlap because these phases are present within either oxide-bearing or oxide gabbros. They are also associated with dioritic rocks, resulting in multiple overlap in rock names and modifiers. Thy (**Chap. 2**, this volume) notes the overlap in terminology; he states gabbronorites are also oxide gabbros in his chosen terminology. We also have not used the term “apatite” gabbro as in Thy (**Chap. 2**, this volume) because we find that the more appropriate term for these gabbros is actually oxide gabbro because of the high abundance of oxide minerals associated with apatite. The association of high abundance of accessory apatite (<5%) with high modal abundance of magmatic oxide (>5%) renders the two names overlapping, and the modifier conflicts with IUGS nomenclature. Thus, we chose the IUGS nomenclature for clarity. This is also consistent with

F9. Igneous cumulate texture, p. 65.



Leg 179 Shipboard Scientific Party (1999b). The terms “melanocratic” and “leucocratic” preface rock names if modal abundances of mafic or felsic phases warranted. However, these terms were seldom used, and mainly in shipboard visual core descriptions (VCDs). No troctolitic rocks were observed in the section. Granophyric veined gabbro, quartz diorite, and trondhjemites were also analyzed for bulk chemistry, but heterogeneities (intimate mixtures of gabbro and granophyre), alteration, or deformation in many of these samples prohibited accurate modal analysis and in some cases resulted in difficult separations and analysis. The irregular nature of the veins and the common inclusion of small xenoliths of gabbroic rocks complicated their analysis. In addition, thin sections were not returned on these mixed silicic samples and a few gabbroic sections because such heterogeneities caused plucking of slide fragments during the trim and grinding process (total of 11 sections lost). Thus, modal and mineral chemistry data are not available for these 11 samples because of limited sample availability, as most of the sample was used for bulk analysis. They are available for 137 of our samples. We were, however, able to collect whole-rock data on all 148 samples included in this study.

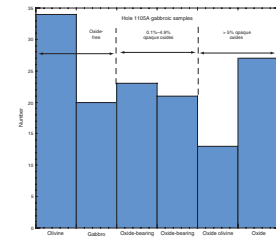
The relative abundances of various gabbroic rock types sampled in Hole 1105A are displayed in a histogram in Figure F10. Downhole variations in modal abundance are illustrated in Figure F11 and include both our modal analysis (137 sections) and shipboard modal analysis (42 sections). The data from this study are included in Table T1, which shows the considerable amount of fine structure within the hole where rock types and modal abundances vary significantly on a small scale (1 m or less). Plagioclase and clinopyroxene dominate modes in the gabbroic section. Modal layer boundaries are defined by the appearance or disappearance of modal oxide, olivine, orthopyroxene, or inverted pigeonite. Small-scale variation is also clear from magnetic susceptibility measurements and the large number of lithologic intervals established during visual core description. Although sampling in Hole 735B was much coarser, the intimate juxtaposition and interlayering of relatively primitive olivine gabbro and oxide gabbro in Hole 735B led Dick et al. (2002) to propose multiple small melt flow channels and oxide gabbro intrusions to explain such fine-scale variation. We will examine this hypothesis in more detail with the finer scale of sampling available to us from Hole 1105A. Figure F11 also displays good correlation with shipboard definition of major lithologic units in that there is a general lack of oxide minerals in Units I and III and abundant oxides in Units II and IV. The average gabbroic modal composition of the cored interval, based on available modes from Hole 1105A, consists of 56.98% plagioclase, 32.37% clinopyroxene, 6.79% olivine, and 3.84% Fe-Ti oxides.

WHOLE-ROCK GEOCHEMISTRY

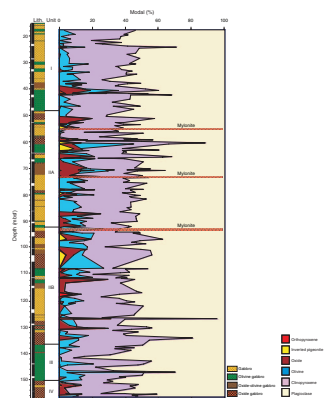
Analytical Methods

A total of 148 samples were analyzed by inductively coupled plasma–atomic emission spectroscopy (ICP-AES) at the University of Houston as part of our study for whole-rock major and minor elements (Table T2), trace elements including Zr, V, Ba, Sr, Ni, Cr, Co, Zn, Cu, Sc, and Y (Table T3), and rare earth elements (REEs) including La, Ce, Nd, Sm, Eu, Gd, Dy, Er, and Yb (Table T4). Methods are described in Casey (1997) and Smith (1994). Adding these analyses to shipboard X-ray fluores-

F10. Rock types in Hole 1105A, p. 66.



F11. Modal distribution of primary minerals in Hole 1105A, p. 67.



T2. Major element analysis of gabbros, p. 108.

T3. Trace element analysis of gabbros, p. 111.

T4. REE analysis of gabbros, p. 114.

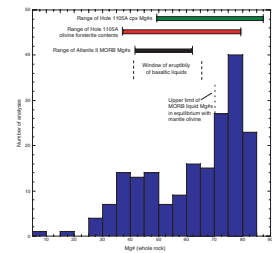
cence (XRF) analyses of 42 samples brings the total number of samples analyzed for major, minor, and certain trace elements to 190. REEs, Sc, and Y were analyzed by preconcentration utilizing chromatographic separation techniques followed by ICP-AES analysis (see method references above). Over the 143-m cored interval, the 190 samples analyzed provide an average sampling interval of 0.77 m. In the plots of whole-rock analysis, our data were supplemented with the shipboard data when overlap in element sets occurred. Unfortunately, REEs were not analyzed on board the ship because of limitations of onboard analytical techniques, and plots are therefore restricted to 148 samples. The whole-rock data, presented here, represent the entire data set now available for Hole 1105A. Whole-rock major and trace element geochemistry generally shows that the analyzed gabbroic rocks are cumulate in origin, whereas the more silicic rocks may have meltlike compositions.

Major Elements

Whole-rock Mg#s ($\text{Mg}/[\text{Mg}+\text{Fe}]\times 100$) of all plutonic rocks ranging from olivine gabbros to trondhjemites cover an exceptionally wide range from 85.4 to 6.3 (Fig. F12). This Mg# range represents a much wider range of dominantly cumulate magmatic differentiates than exhibited by Atlantis II MORB Mg#s (61.9–42.2) (Johnson and Dick, 1992). In nonoxide-bearing plutonic rocks, Mg# can be used in a general way as an index of fractionation because it largely reflects the changes in composition of the Mg# of cumulus clinopyroxene and olivine, which are very close in value. In oxide-bearing and especially oxide-rich gabbro, however, Mg# varies more rapidly downhole with increasing modal percent of opaque oxides. Whole-rock Mg# is less directly correlatable with mineral Mg# value and is not reliable as an index of fractionation in these rocks; thus, the Mg# of mafic minerals is more reliable as an indicator. Oxide-poor trondhjemites and quartz diorites appear to reflect near-liquid compositions based on their whole-rock chemistry (also see Thy, Chap. 2, this volume).

The Atlantis II basalts are characterized by Fe# ($\text{Fe}/[\text{Fe}+\text{Mg}]\times 100$) values of 38.6–58.2 (average = ~44). The Atlantis II Transform basaltic compositional range (Johnson and Dick, 1992) corresponds to a magma density range centered on the density minimum of the tholeiitic basalt magma fractionation trend. The range is within the “window of eruptibility” along the tholeiitic trend (Fig. F12) that was defined by Stolper and Walker (1980). More primitive parental melts or more fractionated iron-rich basalts in equilibrium with many of the Hole 1105A plutonic minerals would be denser and less likely to erupt. It is not surprising, therefore, that the range of compositions and the fractionation extents are greater in the plutonic foundations of the crust than in basalts. The olivine gabbros in Hole 1105A have Mg#s commonly in excess of the maximum for basaltic liquid (69–71), which defines the most primitive possible basaltic liquids likely to be in equilibrium with oceanic residual mantle olivine. Mg#s of Hole 1105A gabbroic rocks range as high as ~85.4. Samples with Mg#s between 71 and 85, which includes 45% of those analyzed, are too primitive to represent the composition of congealed melts. These samples must represent the more magnesium cumulate products derived from crystallization of melts that were somewhat more fractionated than mantle-equilibrium melts (also see discussions in Dick et al., 2002; Niu et al., 2002), and the plutonic whole-rock values reflect the higher Mg#s of cumulus phases in equilibrium with MORB (Fig. F12). Samples with lower Mg#s in the range of

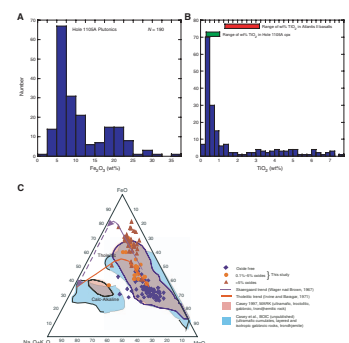
F12. Whole-rock Mg#s, p. 68.



basaltic liquid samples with whole-rock Mg#s <70–71, based on trace element abundances (see below), also do not appear to represent basaltic liquid compositions. The average Mg# of all samples for Hole 1105A is 62.7 because of the significant amounts of ferrogabbroic to granophyric rocks averaged within the section. As in the case of the deeper Hole 735B, the cumulate rocks analyzed are far too evolved over this limited section to mass balance back to a primitive melt composition (also see Dick et al., 2002; Niu et al., 2002). Thus, parental magmas that fractionated cumulate phases were more evolved than any primary magmas from the mantle and indicate that the most primitive cumulates are not represented in the cored interval, as might be expected from the limited section cored. A similar conclusion was reached by Dick et al. (2002) for the broader cored interval in Hole 735B. Like Hole 735B, the cored section in Hole 1105A does not include the most primitive cumulates. Cannat and Casey (1995) and Cannat (1996) observed a range of gabbroic, dunitic, troctolitic, and pyroxenite bodies within residual mantle material in the 14°–16°N region of the Mid-Atlantic Ridge that suggested the existence of discrete magma bodies crystallizing in the lithospheric residual mantle. Similar rocks were recovered during Leg 153 (e.g., Cannat et al., 1997; Casey, 1997). High-Mg# cumulates found in the Bay of Islands ophiolite and other ophiolites generally occur sandwiched between the base of the layered gabbro section and the underlying residual mantle. This may indicate that deeper penetrations would be required to sample the “missing,” more primitive cumulates. A comparison with the Mg#s in Hole 735B shows that even after drilling 1.5 km into the lower crust, primitive cumulates were not been sampled. It seems likely that the missing cumulates could be found by either deeper penetration at the base of the gabbroic cumulates, as plutons within the residual mantle section below (e.g., Cannat and Casey, 1995), or in dismembered lozenges of a mafic–ultramafic transition zone along a flow line within the lower crust. Predicting a drilling strategy for sampling these primitive cumulates would be, at best, difficult within a single hole.

Most gabbroic rocks with whole-rock Mg# > 71 have <0.1 mod% opaque oxide content. If oxides are present, they are typically alteration related. At Mg# < 65, most samples have >1.0 mod% opaque oxides. The appearance of oxides at high Mg# does not fit perfect fractional crystallization (PFX) modeling of Atlantis II basalts because the model predicts their appearance at much lower Mg#s. The systematic trend toward increasing modal abundances of opaque oxides with decreasing whole-rock Mg# would be expected if opaque oxides have accumulated. Opaque oxide abundances therefore, in part, control the Mg#s of more fractionated cumulate rocks. Samples with oxide abundances >1% typically have whole-rock Fe₂O₃ (total iron as Fe₂O₃) >10 wt% in Hole 1105A gabbroic rocks. Oxide abundances in oxide gabbros range as high as ~25%, and whole-rock Fe₂O₃ abundances reach as high as ~35 wt% (Fig. F13A). In high-Mg# samples, whole-rock abundances of TiO₂ (Fig. F13B) are generally low and not well correlated with Fe₂O₃ abundances. When Fe₂O₃ < 10 wt%, TiO₂ abundances tend to be <1 wt% and often significantly lower. When Fe₂O₃ > 10 wt%, however, TiO₂ and Fe₂O₃ abundances are highly correlated, with both Fe₂O₃ and TiO₂ reflecting increasing modal percentages of opaque oxides ranging from magnetite to titanomagnetite in composition. SiO₂ is negatively correlated with both Fe₂O₃ and TiO₂ in this range. TiO₂ contents reach as high as 7.56 wt% in oxide gabbros, similar to the range observed in

F13. Whole-rock Fe₂O₃ and TiO₂ and AFM plot, p. 69.

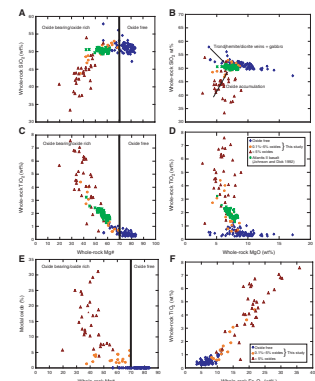


Hole 735B (Dick et al., 2002). Figure F10B shows the total range of whole-rock TiO_2 contents in plutonic rocks (0.09–7.56 wt%) as well as the abundance of TiO_2 within clinopyroxene in Hole 1105A gabbroic rocks and within Atlantis II basalts. In general, the Hole 1105A plutonic rocks are depleted in TiO_2 , with 64% of the samples having <1 wt% and 42% having <0.5 wt%. In contrast to Atlantis II basalts, which show a range of TiO_2 values from 1.29 to 3.24 wt% (average = 1.96 wt%), the majority of Hole 1105A gabbroic rocks are far too depleted in TiO_2 to represent any similar congealed MORB liquid compositions. This depletion generally indicates a cumulus origin for these rocks. Titanium behaves incompatibly with respect to clinopyroxene, olivine, and plagioclase, and therefore the low TiO_2 in oxide-poor to oxide-free cumulate gabbroic rocks can be interpreted to indicate cumulates with somewhat low percentages of intercumulus trapped melt. Upon crystallization of Fe-Ti oxides and their obvious accumulation in the oxide gabbros, TiO_2 can far exceed the abundances expected in equilibrium ferrobasaltic liquids, which reach a maximum of ~3.00–3.50 wt% when Atlantis II basalts are modeled by PFX. Thus, it is also important to note that iron- and titanium-rich gabbroic rock compositions are far removed from congealed ferrobasaltic melt compositions, and therefore the rock and oxides themselves must be, in part, cumulus in origin.

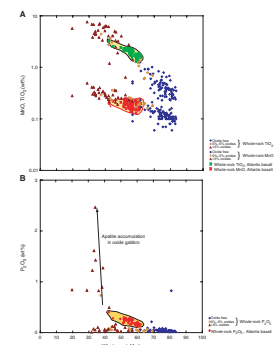
The large relative diversity of the samples analyzed from Hole 1105A, in terms of overall geochemistry, lithologic variation, and iron enrichment, can be illustrated on an alkali-iron-magnesium (AFM) diagram comparing the Hole 1105A data to other large oceanic data sets such as the plutonic suites from the MARK area along the Mid-Atlantic Ridge and the Bay of Islands ophiolite (Fig. F13C). Comparison shows that the Hole 1105A gabbroic samples follow a strong iron enrichment trend, like the other suites, but that the extent of oxide enrichment surpasses those of the Bay of Islands ophiolite and the MARK plutonic rocks and more closely resembles the Skaergaard enrichment extent (also see Thy, Chap. 2, this volume). In this respect, Hole 1105A samples are quite similar to Hole 735B samples (Dick, Natland, Miller, et al., 1999), as might be expected if the oxide units can be correlated.

Bulk rock SiO_2 vs. Mg# or MgO plots show that SiO_2 is restricted to a narrow range when olivine, clinopyroxene, and plagioclase are the dominant cumulus phases and are the main controls on bulk composition. Oxide accumulation leads to significant depletion in SiO_2 (Fig. F14A, F14D) with values descending from ~51 to 33 wt% as oxide modal abundances increase, similar to samples from Hole 735B. Trondhjemitic and dioritic veins within gabbroic rocks analyzed lead to SiO_2 enrichment trends, and these appear to be represented in granophyric liquid addition trends in Figure F14A, F14D, and F14E. Similar mineralogic and melt or oxide controls are exhibited when bulk rock TiO_2 is plotted vs. Mg#, MgO, and Fe_2O_3 (Fig. F14B, F14E, F14F). Fe_2O_3 and TiO_2 are highly correlated because of oxide content, and, likewise, the Mg#s of oxide gabbros are highly correlated with modal oxide abundances (Fig. F14C, F14F). Minor elements P_2O_5 and MnO show typical increasing incompatible element trends with decreasing bulk Mg#. In the more iron rich oxide gabbros, however, apatite accumulation trends are observed that drive P_2O_5 values to >4 wt% (Fig. F15). These apatite-bearing gabbros are also described by Thy (Chap. 2, this volume). Like TiO_2 , abundances of MnO and P_2O_5 in oxide-free gabbros and olivine gabbros are lower than in Atlantis II basalts, with which they could be in equilibrium, again reflecting their cumulate nature.

F14. Whole-rock gabbroic variation, p. 70.



F15. Whole-rock incompatible minor elements, p. 71.



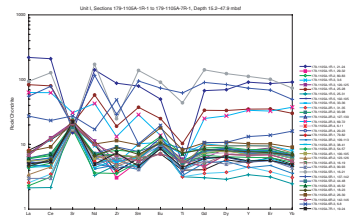
Whole-rock MnO abundances are largely controlled by fractionation and the consequent increasing MnO abundances within clinopyroxene and olivine with increasing extents of fractional crystallization, but will also be affected by increasing trapped intercumulus melt contents.

Trace Elements

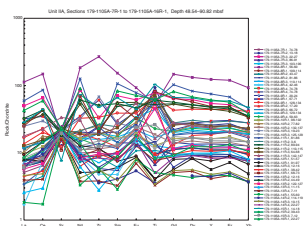
Whole-rock trace element abundances (Tables T3, T4) in the gabbroic rocks depend on the composition of the parent melt from which the cumulus crystals solidified, the partitioning behavior between melt and crystalline phases, the modal mineralogy of the sample, the percentage and composition of residual intercumulus melt trapped within the crystal framework, or reactive crystallization products of slow migratory melts infiltrated through or trapped in the cumulate network or crystal mush (e.g., Irvine, 1980; Casey, 1997; Agar et al., 1997; Coogan et al., 2000; Coogan et al., 2001; Dick et al., 2002). The trapped melt abundance is best manifested generally by comparing the whole-rock abundances of incompatible trace elements to those of known MORB melts in the region and expected in equilibrium cumulus phases. The trace element patterns on extended REE diagrams generally help to distinguish plutonic rocks formed by congealing of melts (e.g., Hart et al., 1999) vs. those of dominantly cumulate origin (e.g., Casey, 1997; Hertoegen et al., 2002; Niu et al., 2002).

Trace elements reported here range from compatible (e.g., Ni and Cr) to highly incompatible (e.g., light REEs [LREEs]) during crystal fractionation. Extended REE spidergrams are presented for each of the samples analyzed in Hole 1105A. Elements are listed in order of incompatibility during mantle melting (Sun and McDonough, 1989) and normalized to chondrite using values of Anders and Grevesse (1989). Spidergrams are plotted for Unit I (Fig. F16), Subunit IIA (Fig. F17), Subunit IIB (Fig. F18), Unit III (Fig. F19), and Unit IV (Fig. F20). Figure F21A–F21C shows extended REE diagrams plotted on the basis of oxide-free, oxide-bearing, and oxide-rich lithologies, respectively. Most samples plotted show large positive Sr anomalies and smaller positive Eu anomalies, indicating that the sample suites are largely cumulate in origin, with significant plagioclase accumulation. Because Sr has a sufficiently high partition coefficient (K_d) in plagioclase, the bulk distribution coefficient approaches 1 during crystallization of the basalt, creating negative Sr anomalies in the liquid and positive anomalies in cogenetic primitive cumulates and leading to nearly constant Sr abundances in each (Casey, 1997). Eventually, in fractionated oxide gabbros the adjacent REEs and other trace elements increase due to fractionation of the melt and exceed the nearly constant Sr abundance, creating negative Sr anomalies in some evolved gabbroic rocks. Eu anomalies are typically positive in gabbroic rocks, increasing with increasing modal plagioclase abundances. Frozen liquids typically have negative Sr and Eu anomalies because of plagioclase fractionation. Several granophyric rocks from Hole 1105A have major and trace element characteristics similar to those expected of highly fractionated congealed melts with negative Sr, Eu, and Ti anomalies. In addition, many of the gabbroic rocks highly enriched in oxides are characterized by low to negative Eu anomalies and negative Sr anomalies, as well as highly enriched REE abundances. These highly fractionated oxide gabbros and oxide olivine gabbros typically have positive or negative Ti anomalies, reflecting either oxide accumulation if positive or crystallization from melts that have already experienced extensive prior oxide precipitation if significantly negative.

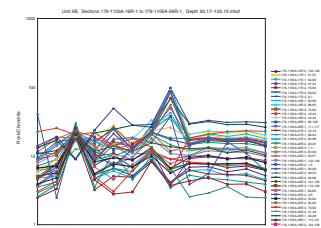
F16. Chondrite-normalized REE of gabbroic rocks, Unit I, p. 72.



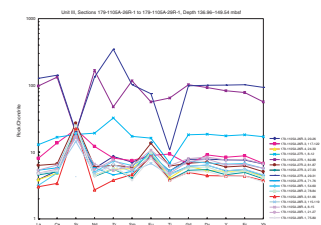
F17. Chondrite-normalized REE of gabbroic rocks, Subunit IIA, p. 73.



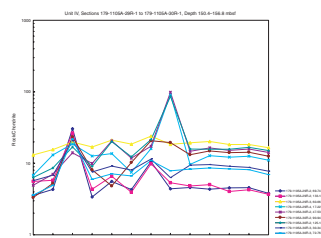
F18. Chondrite-normalized REE of gabbroic rocks, Subunit IIB, p. 74.



F19. Chondrite-normalized REE of gabbroic rocks, Unit III, p. 75.



F20. Chondrite-normalized REE of gabbroic rocks, Unit IV, p. 76.

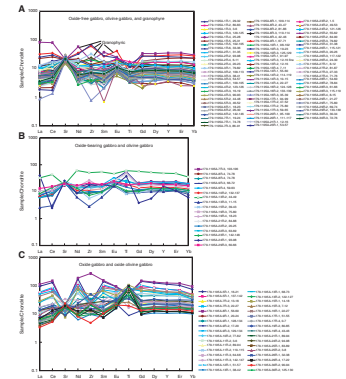


Saturation of oxides is evident from the positive Ti anomalies (oxide accumulation effects) and negative Ti anomalies (oxide depletion effects) in samples with elevated REE abundances. Whereas the analyzed samples with these positive or large negative anomalies typically show the most elevated REE and incompatible element abundances, gabbroic rocks in which REE abundances are $<10\times$ chondrite usually lack such large Ti anomalies. Small negative Ti anomalies in more primitive samples may also be a symptom of dominantly spinel facies mantle melting (Casey, 1997) or may also result from primitive magmas mixing with more evolved magmas that have undergone oxide precipitation, perhaps in a magma chamber boundary layer. Likewise, oxide gabbroic rocks typically have highly variable Zr anomalies that are dominantly positive, reflecting zircon accumulation, except in highly fractionated oxide gabbros or felsic granophyric rocks such as diorite and trondhjemite, which can have negative or positive Zr anomalies because of significant prior zircon fractionation or accumulation. The most highly evolved felsic rocks and certain evolved oxide gabbros are also typically characterized by negative Sr, Eu, and Ti anomalies and highly enriched REE signatures. The more silicic plutonic rocks based on these and other major element compositional characteristics may be close to liquid compositions.

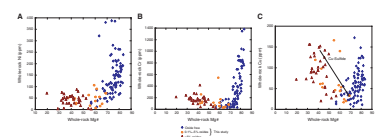
Overall REE abundances (Table T4) show a wide range of compositions in the samples analyzed. LREEs such as La and Ce range from $<1\times$ to $>110\times$ chondrite. Similar ranges are observed in heavy REEs (HREEs) as well, reflecting the overall dominantly flat patterns to slightly LREE depleted observed in REE data, although the most enriched samples, which are typically oxide-rich gabbros and more silicic samples, tend to show slightly elevated chondrite-normalized (cn) LREE/HREE ratios (e.g., $[La/Yb]_{cn}$) that range from >1 to 3. The more depleted samples, typically oxide-free to oxide-poor gabbroic samples, tend to show lower ratios ($<1-0.2$). One anomalous oxide gabbro pegmatite was characterized by a very large ratio of >6.0 . Oxide-depleted granophyres intruding gabbroic rocks likewise can show enriched characteristics in overall abundance and LREE/HREE ratios. Gabbroic rocks that are oxide free typically have REE abundances $<1\times$ to $12\times$ chondrite with strong positive Sr anomalies and weak negative Ti anomalies. Oxide-poor granophyric rocks have higher values from $20\times$ to $85\times$ chondrites, with negative Sr and Ti anomalies and positive or negative Zr anomalies. Oxide gabbros range from $5\times$ to $120\times$ chondrite abundances and typically have strong positive or weak negative Ti anomalies, weaker positive Sr or strong negative Sr anomalies, and positive or negative Zr anomalies. Oxide-bearing gabbroic rocks have intermediate characteristics between oxide-rich and oxide-free gabbroic samples. All three types of gabbroic rocks typically show distinctive positive Eu anomalies, although some oxide gabbros show slight negative anomalies. Granophyric rocks possess slightly negative Eu anomalies as well.

Trace elements that show compatible element trends include Ni, Cr, and Cu. These show rapid depletion with decreasing whole-rock Mg# (Fig. F22A–F22C), although Cu begins to increase at lower Mg#s, probably due to separation of late sulfide liquids and accumulation of chalcopyrite in oxide gabbros. Petrographic evidence shows abundant chalcopyrite within some oxide gabbros, which would explain the elevated abundance of Cu in more fractionated rocks. The association of chalcopyrite with oxides is likely because consumption of oxygen during oxide crystallization may force sulfide precipitation to buffer oxygen fugacities (Mathez, 1976). Rapid nickel and copper depletion in less

F21. REE of rocks classified using modal opaque oxide percentages, p. 77.



F22. Ni, Cr, and Cu during silicate fractionation and late stage-oxide/sulfide fractionation, p. 78.

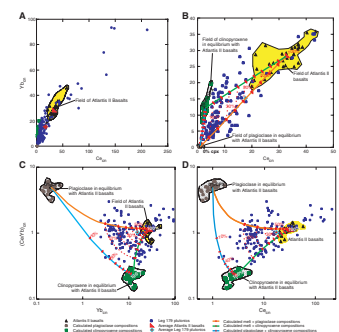


fractionated rocks occurs because both elements are compatible during the crystallization of olivine, with probable small amounts of pentlandite (Miller and Cervantes, 2002) contributing to Ni depletion. Chrome behaves compatibly in clinopyroxene and is likewise rapidly depleted at relatively high Mg#s. Ni and Cu may also partition somewhat into late-stage immiscible sulfide melts. Slightly increasing Cr abundances in oxide gabbros may result from accumulation of oxides in which Cr is more compatible. In primitive rocks, however, Cr depletion trends largely reflect its compatible behavior with clinopyroxene, and Ni is largely controlled by similar compatible behavior during olivine crystallization, both rapidly depleting the melt compositions and resulting in lower abundances in both cumulus minerals with increased fractionation. Of particular note on these diagrams is that only a few samples lie off the depletion trends, whereas the hypothesis of Dick et al. (1991) and Natland et al. (1991) for the origin of Hole 735B oxide gabbro seems to suggest that differentiation products along lateral and vertical channelways invaded a host gabbroic crystal mush that could be much more primitive. This should result in complexes of “mixed” or infiltrated rock whose compatible element compositions resulted from mixtures of primitive cumulus olivine, clinopyroxene, and plagioclase and fractionated melt-derived Fe-Ti oxide cumulate gabbro. Yet the bulk rock plots (Fig. F22) suggest that the rock evolutionary path lacked significant intimate commingling of disparate primitive rock types (more primitive cumulus crystals) with highly evolved melt, although the broadness of the trends observed, may, in part, be explained by mixing with slightly more evolved melts. Thus, if correct, the hypothesis would seem to suggest that the highly evolved oxide-rich channelways did not commingle with a more primitive crystal mush, but perhaps migration was through already solidified more primitive gabbroic rocks. Alternatively, there could be another explanation for the complex juxtaposition of primitive olivine gabbros (and troctolites in Hole 735B) and oxide gabbros. Vanadium and Sc abundances can usually be correlated with modal abundances. Vanadium shows a positive correlation with Ti and generally reflects oxide modal abundances, whereas Sc generally increases with modal clinopyroxene.

Comparison of Atlantis II Basalt and Hole 1105A Plutonic Bulk Average Compositions

Bulk rock incompatible trace elements such as Ce and Yb in most of the more primitive gabbros are likely controlled by the modal percent of clinopyroxene and plagioclase and interstitial trapped melt (e.g., Irvine, 1970; Casey, 1997) or migratory melt cumulate crystallization products (e.g., Coogan et al., 2000). Figure F23A and F23B depicts Ce and Yb concentrations in Atlantis II basalts (Johnson and Dick, 1992), their concentration in equilibrium clinopyroxene and plagioclase calculated from partition coefficients (see Casey, 1997), and the gabbroic rocks analyzed as part of this study. Figure F23C and F23D illustrates Ce/Yb vs. Yb and La, respectively, showing the mixing lines between average basalt and equilibrium clinopyroxene and plagioclase. These three components should exert dominant controls over REE content of the average cumulate (Casey, 1997). Except for highly fractionated (i.e., zircon-apatite bearing) samples, whole-rock concentrations in Hole 1105A plutonic rocks generally plot within or close to the volume defined by the mixing of the three components, average basalt and calculated compositions of average clinopyroxene, and average plagioclase.

F23. Ce_{cn} and Yb_{cn} and $(Ce/Yb)_{cn}$ vs. Yb_{cn} and Ce_{cn} , p. 79.



In particular, the majority of samples analyzed plot parallel to mixing lines depicted between clinopyroxene and plagioclase compositions and indicate 10%–20% or more of the average basalt could be contained within most primitive samples, suggesting a dominantly adcumulate to mesocumulate nature for most of the samples analyzed. The translation of petrographically determined textural types adcumulate, mesocumulate, and orthocumulate to equivalent trapped melt content classification for partial or complete major element reequilibration between trapped melt and cumulus or primary framework crystals is based on the classification and terminology of Irvine (1980, 1982):

Adcumulate = trapped melt contents 0%–7%,

Mesocumulate = trapped melt contents 8%–15%, and

Orthocumulate = trapped melt contents >15%.

We use this classification assuming highly incompatible trace elements can be used as a proxy for estimating minimum trapped melt contents. Alternatively, the trace element enrichment could result from migratory melts and more transient cumulate crystallization from a variety of compositions including ferrobasaltic and silicic melts driven through the cumulate pile; however, the migration rates would likely be very small or entrapment would have to occur to allow extensive reequilibration with plagioclase and clinopyroxene. The nature of cryptic chemical variations tends not to support extensive reequilibration of minerals with migrating melt, as minerals such as olivine and clinopyroxene have very different diffusion rates. If more fractionated liquids or their cumulate crystallization products (e.g., apatite and zircon) were involved as interstitial solidified melt, the calculated “trapped” melt abundance could actually be much lower. Clear subsets of gabbroic rocks are much more enriched in incompatible trace elements and appear to contain higher proportions of more evolved congealed melt components or evolved crystallization products like accessory minor phases (e.g., zircon, apatite, and oxides) that elevate incompatible element abundances. These subsets of rocks are pulled toward the Atlantis II basalt field or beyond to more enriched compositions as depicted in Figure F23. Some of these more enriched rocks are significantly higher in incompatible element concentrations than basalts because of more extensive fractionation (e.g., granophyric melts) and/or accumulation of accessory phases such as zircon and apatite in thin veins (samples with positive Zr anomalies and P₂O₅ enrichment) within oxide gabbros. Zircons tend to have high HREE/LREE ratios (~10,000:1–1500:1), and apatites have high LREE/HREE ratios (~2:1) (e.g., Gillis, 1996). Certain trace element patterns show strongly positive Zr anomalies symptomatic of zircon accumulation on extended REE diagrams (e.g., Figs. F16, F17, F18, F19, F20). Accumulation of either zircon or apatite as an accessory phase can significantly elevate certain incompatible element abundances.

Hart et al. (1999) used the composition of strip samples from nearby Hole 735B to reconstruct major element compositions of the bulk hole. They surmised that the major element composition of the average gabbro from Hole 735B is meltlike. Based on our analysis of the bulk rock data set, we simply averaged all plutonic rock compositions ($N = 196$) and concur that the average of all plutonic rocks including gabbroic, dioritic, and trondhjemitic rocks in Hole 1105A are meltlike in terms of major element abundances (Table T2). In fact, there is an amazing 1:1 correlation between the average major element abundances of the Atlantis II basalt (Johnson and Dick, 1992) and the average for Hole

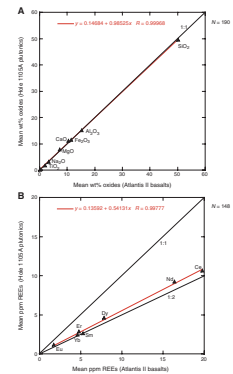
1105A plutonic rocks (Fig. F24A). The average Atlantis II basalt represents a moderately differentiated melt, and therefore an equivalent plutonic average is likely caused by averaging of the more extensive fractionation range from primitive gabbroic samples to granophyric samples represented by the plutonic assemblage (i.e., when compared with the more limited basaltic range). Obviously, the average of all plutonic rocks is likewise much more evolved than any melt composition that could be in equilibrium with oceanic mantle.

We, however, outlined above that most of the plutonic samples have incompatible minor and trace element abundances that are significantly lower than trace element abundances expected within basalt and that they have trace element patterns that demonstrate their cumulate origin (e.g., positive Sr, Eu, and Ti anomalies). REEs, which typically behave as incompatible elements during mantle melting and basaltic fractionation, demonstrate the differences between melt and cumulate gabbroic compositions. A plot of the average REE abundances for Atlantis II basalts vs. the average for all Hole 1105A plutonic rocks shows that REEs constitute approximately one-half the abundances of the basaltic average, even when highly fractionated trace element–enriched dioritic to trondhjemitic rocks are included in the average (Fig. F24B). Without these highly fractionated rocks that are probably close to melt compositions, the average would be significantly lower in the plutonic assemblage. Hart et al. (1999) interpreted the variability in Hole 735B to be caused by local separation of melt and crystals, but that the bulk average indicated no removal of melt. Thus, on average they interpreted the cored Leg 118 section to represent a melt composition, with little large-scale melt removal. We cannot concur with this conclusion or that the cored interval of Hole 1105A is meltlike because incompatible trace elements are so significantly depleted on average when compared with basaltic melts and for reasons summarized above (also see discussions of Hole 735A in Dick et al., 2002; Niu et al., 2002). The mass balance based on trace element bulk average indicated removal of melt from the magma chamber is a necessity. At the same time, it appears that the majority of Hole 1105A cumulates, apart from highly fractionated oxide gabbroic and silicic rocks, would be close to equilibrium assemblages with the moderately evolved Atlantis II basalts analyzed by Johnson and Dick (1992).

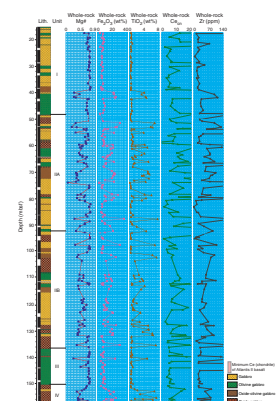
Downhole Bulk Rock Cryptic Chemical Variation

Downhole modal abundance data indicate significant variations in mineral proportions on small scales (<1 m) within Hole 1105A. Bulk rock geochemical data (Fig. F25) likewise show significant downhole variation in both major and trace elements and good correlation with lithologic unit definitions based on detailed shipboard descriptions. Units I and III are typically characterized by low Fe-Ti and high-Mg# gabbroic rocks with short intervals of more Fe-Ti rich gabbroic rocks that typically correspond to oxide-rich intervals noted in the core. Units II and IV are characterized by shorter wavelength variations between Fe-Ti-rich (i.e., oxide rich) and Fe-Ti-poor (oxide poor or oxide free) gabbroic rocks. The scale of sampling downhole for bulk rock measurements varies from <0.5 to 0.8 m; however, the average sampling is ~0.77 m over the 143-m cored interval. In coarsely sampled regions, peaks and troughs in the cryptic chemical variations of Mg#, Fe₂O₃, TiO₂, and incompatible elements Ce_{cn} and Zr show that inflections in trends are often centered on a single sample in both peaks and troughs.

F24. Major and minor element abundances and REEs, p. 80.



F25. Whole-rock cryptic chemical variation of Mg#, Fe₂O₃, TiO₂, Ce_{cn}, and Zr, p. 81.



Where sampling intervals are denser, however (e.g., at the Unit III/IV boundary and within select intervals in Unit II), smoother transitions delineate peaks and troughs. This seems to indicate that, where resolved by a higher sampling rate, boundaries between cryptic units are not abrupt but vary smoothly. In addition, Mg# trends show both “normal” fractionation (Mg# decreasing uphole) and “inverse” fractionation (Mg# increasing uphole) (e.g., base to top of Unit IV and 62–72 mbsf). This is an interesting observation because downhole variations indicate Fe-Ti-rich gabbros are intimately mixed with relatively primitive olivine gabbroic rocks on the scale of a few meters or less, similar to variations observed in Hole 735B. Sampling in Hole 1105A was generally conducted on a finer scale than sampling through the oxide gabbro interval of Hole 735B during Leg 118 (Dick et al., 1991). Natland and Dick (2002) and Dick et al. (2002) described the complex interlayering of oxide and olivine gabbro in Hole 735B, and this is very obvious on the FMS image logs (Miller et al., [Chap. 3](#), this volume; Zarian, 2003) in Hole 1105A. However, these mixtures in Hole 735B have typically been interpreted to indicate that ferrobaltic melts infiltrated through a pre-existing more primitive olivine gabbroic section rather than being cogenetic local derivatives and products of fine-scale crystallization (e.g., thermomechanical boundary layer and in situ crystallization phenomenon). Natland and Dick (2002) interpreted the formation of oxide gabbro to be the result of “buoyant intercumulus melts and their coalescence and ascent in open fractures and shear zones.” They interpreted oxide gabbros to result from numerous intrusions along permeable pathways, often associated with ductile deformation zones. Why presumably massively oxide-precipitating and dense melts (ferrobaltic) rise buoyantly within shear zones with respect to other less dense primitive or highly fractionated iron-depleted granophyric interstitial melts is unclear. The smooth transitions revealed by small-scale sampling in Hole 1105A could indicate that in situ crystallization processes may also be a viable mechanism to produce the fine-scale interlayering observed in both holes. It is clear that an even finer scale of sampling will be necessary to more fully resolve the true nature of cryptic chemical variation and the nature of the contacts between oxide-rich and oxide-poor gabbroic rocks. The transitional nature of these contacts will be further explored below in discussions of mineral chemistry and structural relationships.

The downhole plot in [Figure F25](#) also shows that Mg# trends are typically inverse to Fe_2O_3 and TiO_2 trends, as expected. In addition to major element downhole variations, incompatible elements Ce_{cn} and Zr are displayed downhole. Note that oxide-rich gabbroic rocks (high Fe_2O_3 and TiO_2) appear to correlate with Ce and Zr abundances, but the correlations are far less regular than major element variations. In fact, even in intervals where the major element abundances are nearly constant, trace element abundances of Zr and Ce vary significantly. In addition, values of these trace elements in some oxide-rich gabbroic rocks as well as oxide-poor high-Mg# gabbro can exceed minimum values of the Atlantis II basalts (pink line on Ce_{cn} plot). These rocks typically have positive Zr anomalies, suggesting zircon accumulation is common. Most of the more primitive high-Mg# gabbroic rocks, however, are commonly significantly more depleted in these incompatible trace elements than minimum basaltic values (Johnson and Dick, 1992), again reflecting their cumulate nature. The plot does, however, illustrate that the major element cryptic chemical variation is not perfectly correlated and

is sometimes decoupled from highly incompatible trace element abundances, perhaps consistent with variable percentages of trapped melt components, boundary layer processes, or small late vein systems. In one case within an olivine primitive gabbro that showed a strong positive Zr anomaly, we identified a small silicic vein with a network of zircon crystals that has intruded as a late feature and that obviously significantly altered the bulk rock trace element chemistry. From the abundance of zircon in the vein, it is clear that the zircon accumulates in the vein as a cumulate mineral and imparts a strong positive anomaly to the rock.

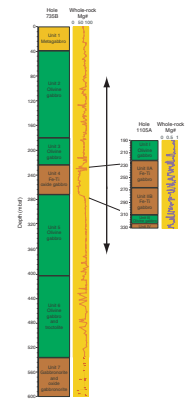
Finally, whole-rock Mg# is plotted downhole over roughly similar intervals and at the same scale (Fig. F26) through the oxide-rich Unit IV of Hole 735B, in which 37 samples were analyzed, and a depth-adjusted downhole Mg# plot of Hole 1105A, in which 109 samples were analyzed within oxide-rich Subunits IIA and IIB. The units in each hole are potentially correlatable. Data for Hole 735B were compiled from all available data reported in the Leg 176 *Scientific Results* volume (Natland, Dick, Miller, and Von Herzen, 2002) and are similar to those depicted in Dick et al. (2002). However, the scale of variability may be deciphered more precisely by the increased sample density in Hole 1105A. The differing sample scales makes direct comparisons between Hole 735B and Hole 1105A more difficult. The more closely spaced sampling intervals in Hole 1105A allow us to more simply identify the scale of cryptic chemical units, although even finer scale sampling may be required to fully document all of the forward and inverse trends between oxide-rich and oxide-poor cryptic chemical units. These units appear cyclic on scales of 5 to 10 m through Subunits IIA and IIB of Hole 1105A. One peculiarity throughout the hole is that the Mg#s of the most primitive gabbroic rocks are similar from top to bottom, perhaps corresponding to the average composition of the chamber interior. Similar scales of variability were suggested by Dick, Natland, Miller, et al. (1999) for Hole 735B, but oxide-rich cryptic units were interpreted to be sill-like intrusions that split preexisting olivine gabbro as they were sequentially injected into the olivine gabbro. It is important to note also that Dick, Natland, Miller, et al. (1999) were able to recognize much larger scale cryptic chemical units, at a scale of hundreds of meters, which they termed rock “series.” These series were defined by clear offsets in the whole-rock Mg#s of the most primitive rocks and apparent upward normal fractionation trends. The normal and inverse cryptic variation described in Hole 1105A on a smaller scale would likely superimpose on this larger scale of variation.

MINERAL CHEMISTRY

Analytical Method

Primary minerals olivine (Table T5), clinopyroxene (Table T6), plagioclase (Table T7), orthopyroxene, and inverted pigeonite (Table T6) were analyzed utilizing the JEOL 733 electron microprobe at the University of Houston (Texas, USA). Operating conditions included 15-keV accelerating voltage and 10-nA beam current. A focused 1- μ m beam was used to analyze olivine and plagioclase. A broad 20- μ m beam was used to analyze clinopyroxene because of exsolution. Both cores and rims were analyzed in each thin section. Zoning was generally absent in all major phases, but a subset of clinopyroxene and plagioclase showed

F26. Mg# in Holes 735B and 1105A, p. 82.



T5. Major element oxides in gabbros, p. 117.

T6. Major element oxides in olivine, p. 120.

T7. Major element oxides in plagioclase, p. 123.

zoning or intrasample heterogeneity within cores. Olivine core and rim analyses differences were negligible in all samples.

Olivine

Of the 137 thin sections used in this study, 100 contain olivine. Olivine grains are typically anhedral to subhedral, occurring either as individual crystals or in clusters. In some thin sections the olivine grains are stringlike in appearance, whereas in others olivine shows a poikilitic relationship with plagioclase or clinopyroxene.

Olivine mineral chemistry (Fig. F27) varies from Fo₇₈ to Fo₃₆, with a gap between 40 and 46 (this gap was also noted by Thy, Chap. 2, this volume). Thy (Chap. 2, this volume) reported an olivine Fo range from 76.4 to 31.6 and suggested that the compositional ranges in Hole 1105A may not be similar to the Hole 735B core. A similar range of Fo₈₄ to Fo₃₀ was observed in nearby Hole 735B (Dick et al., 2002), except that somewhat more primitive troctolites and olivine gabbros were observed in the core analyzed. This is not unexpected when the differences in cored intervals are considered (143 vs. 1500 m). MnO content in olivine shows a systematic nearly linear increase from ~0.3 to 1.1 wt% with decreasing Fo mod%. MnO behaves incompatibly and increases in both olivine and clinopyroxene as the liquid fractionates and becomes enriched. NiO, on the other hand, exponentially decreases from ~0.12 to 0.01 wt% with decreasing forsterite. NiO is highly compatible in olivine and is rapidly depleted with increasing fractionation within the olivine gabbro. Both show systematic relationships: MnO-Fo $R = 0.99$ and NiO-Fo $R = 0.94$. The trend defined by NiO is somewhat broader than that of MnO and may reflect the effect of variable precision of the Ni analysis and postcumulus processes on the nonlinear fractionation trend. Zoning of olivine was not detected in the samples analyzed, a likely consequence of rapid diffusion and reequilibration rates in olivine when compared with clinopyroxene and plagioclase.

Clinopyroxene

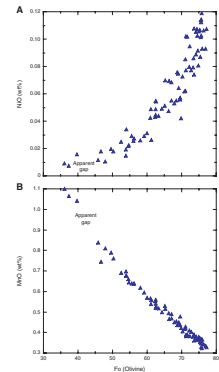
Augite grains were analyzed in all 137 thin sections. The studied grains have a wide range of Mg#s from 50.86 to 86.9 (average = 73.59). Thy (Chap. 2, this volume) reported a similar range of Mg#s from 48.4 to 83.7 for gabbroic rocks from Hole 1105A. Mg# also shows a wide range (42.1–89.3) in the rocks from the nearby Hole 735B (Dick et al., 2002). Cores and rims of each clinopyroxene grain analyzed were examined. The vast majority of high-Ca clinopyroxene grains lack major element zoning, although compositional heterogeneity of cores in a single thin section was observed in a number of samples. Dick et al. (2002) did not report any consistent pattern in clinopyroxene zoning in the rocks of Hole 735B. In this study, clinopyroxenes were defined as Type 1 and Type 2 for graphing purposes:

Type 1 augite: dominant core composition in the thin section.

Type 2 augite: secondary core composition or represented as rims of Type 1 cores.

Type 2 cores are most commonly restricted to a small part of the thin section and may be the cumulate residue of small melt flow channels or localized trapped melt. Similarly, rims of the cores of Type 1 clinopyrox-

F27. NiO in olivine vs. Fo and MnO vs. Fo, p. 83.

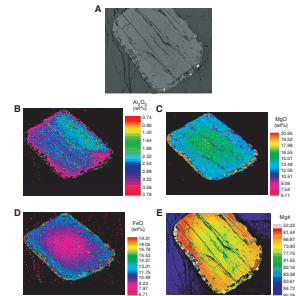


ene can be similar in composition to Type 2 cores in the same rock. In general, Type 2 augites are more fractionated than Type 1, and the zonations are normal, always to more fractionated melt compositions. Figure F28 shows an example of a Type 1 clinopyroxene core rimmed by a normal zonation. It should be emphasized that most of the section examined lacked evidence for this type of zoning, although it was documented locally in certain rocks. Zones of heterogeneous augite cores within single thin sections typically are lower in Mg# than the dominant parts of the thin sections, perhaps indicating narrow porous zones of fractionated melt or inhomogeneous regions of trapped melt. When compared to the structure log for Hole 1105A, the samples that show two types of augite Mg# are commonly close to zones of deformation, possibly suggesting syntectonic melt flow. This may lend some support to the hypothesis of Dick et al. (2002) that melt expulsion is associated with melt-laden shear zones, although it is difficult to say that this is a general condition in the cumulate section.

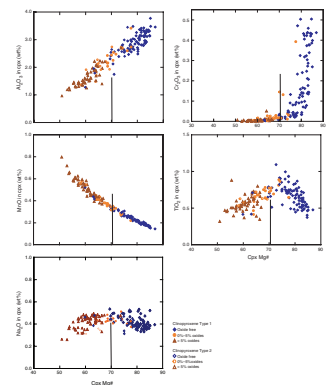
Figure F29A–F29E depicts various elemental variation diagrams for high-Ca clinopyroxene (augite) as a function of Mg# with rock types and Type 1 or 2 cores distinguished by different symbols. Mg#s in clinopyroxene range from 50.86 to 86.9 (average = 73.59). In general, zoning or heterogeneous cores within single thin sections show typically lower Mg#s than dominant parts of the thin section. Thus, Type 2 cores usually plot in the more fractionated portion of each diagram. Al_2O_3 contents of clinopyroxene (Fig. F29A) decrease linearly with decreasing Mg# from olivine gabbros to oxide-rich gabbroic rocks. The variation in Al_2O_3 ranges from 3.77 to 1.24 wt% in the bulk of the samples with a range of 3.44 to 0.95 wt% in heterogeneous regions of single thin sections. Overall, the concentration of Al_2O_3 in pyroxene is relatively low, consistent with low-pressure crustal differentiation of tholeiitic basalts. Al_2O_3 contents in clinopyroxene decrease linearly with decreasing Mg# from olivine gabbros to oxide-rich gabbros. Al_2O_3 contents in Ca-rich pyroxenes are higher than those in the Ca-poor pyroxenes, although very little data are available for Ca-poor pyroxenes. No noticeable overlap of Mg# is seen between Ca-rich pyroxene and Ca-poor pyroxene. This feature is also characteristic of both Bushveld and Skaergaard pyroxenes (Atkins, 1969; Brown, 1957). The trend above of Al_2O_3 is also seen in the octahedral and tetrahedral Al in the pyroxene structure. The amount of Al in both octahedral and tetrahedral positions is greater in the Ca-rich pyroxene than in the coexisting Ca-poor pyroxene; data are very limited for Ca-poor pyroxene. Hole 735B gabbroic rocks show a wider range of Al_2O_3 compared to the tight trend exhibited by the gabbroic rocks from Hole 1105A. The trend of decreasing Al_2O_3 would be consistent with decreasing Al_2O_3 in MORB melts caused by fractionation of plagioclase.

When the clinopyroxenes are plotted in the quadrilateral diagram showing their end-members, the samples plot very close to the Skaergaard and Bushveld trends (Fig. F30A, F30B). The oxide-free samples have higher En%, whereas the oxide gabbro and olivine gabbros have the lowest En%. The low-Ca pyroxenes are below the pyroxene solvus line, indicating that most of the low-Ca pyroxenes are inverted pigeonites or that measurements were of exsolved lamellae of orthopyroxene in clinopyroxene. A comparison of the orthopyroxenes from this study with the available orthopyroxenes from Hole 1105A and those from Hole 735B (Dick et al., 2002) reveals that the last orthopyroxenes from all the holes crystallize at En% = 43. The quadrilateral plot shows that

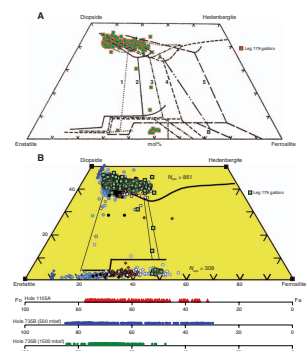
F28. Backscatter and false-color images of a clinopyroxene grain, p. 84.



F29. Mg# vs. Al_2O_3 and Cr_2O_3 and MnO, TiO_2 , and Na_2O in cpx, p. 85.



F30. Pyroxene quadrilateral plot showing pyroxene minima, p. 86.



the trend of pyroxenes from Hole 735B is similar to the trend shown by the samples from this study. Although the trend is close to the Skaergaard trend, they are not parallel (e.g., Thy, [Chap. 2](#), this volume; Dick et al., 2002). The trends from Holes 1105A and 735B have gentler slopes than the Skaergaard trend. When plotted in the diagram of Campbell and Nolan (1974) that shows the pyroxene minima of different intrusions ([Fig. F30A](#)), the overall trend of pyroxenes from Hole 1105A is slightly different from that of the Skaergaard intrusion. The Wo content of the pyroxenes associated with oxide gabbros is higher than the pyroxenes defined by the Skaergaard or Bushveld trends. The pyroxene minimum, defined as the point where Ca-rich pyroxene is in equilibrium with the last or one of the last Ca-poor pyroxenes, is different in the current study from both the Skaergaard and the Bushveld intrusions. The pyroxene minima from Hole 1105A and 735B gabbroic rocks are at higher En% than Skaergaard and Bushveld intrusions. Instead of being prominent as in the Skaergaard and Bushveld trends, these rocks have very gentle and almost no detectable inflection, similar to that of the Palisades sill reported by Walker et al. (1973). Lindsley and Munoz (1969) suggested that the position of the pyroxene minimum depends on the physicochemical condition of the melt. Clinopyroxene En% extends to 34% and has simultaneous olivine crystallization. Olivine continues to crystallize all through the crystallization series except for a noticeable gap around En% = 39%–38%. Olivine continues to crystallize even after low-Ca pyroxene has ceased to crystallize. The apparent gap in crystallization is not seen in Hole 735B olivine, but it was reported by Thy ([Chap. 2](#), this volume) in Hole 1105A. The Fe-rich olivines found in the uppermost 500 m of Hole 735B and those in Hole 1105A are comparable ([Fig. F30B](#)) and strengthen the correlation between the two oxide units previously proposed. Fe-rich olivines are, in turn, absent in the next 1000 m of Hole 735B.

Cr₂O₃ abundances ([Fig. F29B](#)) in clinopyroxene decrease exponentially with decreasing Mg# from 0.50 wt% to below detection limits. The sharpest decreases occur in clinopyroxenes with Mg# between 86.9 and 75. In oxide gabbros and olivine gabbros, Cr₂O₃ is generally <0.1 wt%. Cr is highly compatible in clinopyroxene and rapidly depleted during the early stages of fractionation. One unusual sample (179-1105A-19R-3, 75–80 cm) that was classified as oxide bearing plots with high-chromium oxide-free gabbro and olivine gabbroic rocks, whereas it would be expected to be plot with the oxide-bearing group at lower Cr₂O₃. Closer examination of the sample shows that it is heterogeneous with respect to both clinopyroxene and plagioclase; clinopyroxene Mg# varies between 77.6 and 70.2 and An content of plagioclase varies between 64.5 and 45.1. The oxide grains visible in the sample could be from a late-stage melt that was transported through the sample.

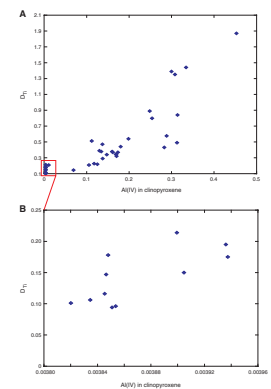
The MnO content of clinopyroxene ([Fig. F29C](#)), like that within olivine, increases systematically with decreasing Mg#. MnO ranges from 0.15 to 0.64 wt% in homogeneous sample suites and from 0.22 to 0.79 wt% in heterogeneous samples. MnO is an incompatible element during silicate fractionation. Oxide gabbroic rocks show the greatest extent of MnO enrichment. TiO₂ also behaves as an incompatible element in basaltic melts until Ti-rich oxides precipitate. TiO₂ contents of clinopyroxene ([Fig. F29D](#)) increase from ~0.37 to 1.10 wt% with decreasing Mg# until Mg# = ~73. At this point, TiO₂ in clinopyroxene reaches a maximum and begins to descend. This inflection point corresponds to the point at which oxide-bearing gabbroic rocks and oxide gabbros are

encountered with decreasing Mg#. This point acts as a lithologic divider between the “oxide-free” and “oxide-bearing” gabbro and olivine gabbro. Anomalous samples, such as 179-1105A-19R-3, 75–80 cm, which plots on the oxide-free domain but contains oxides in its modes, typify rocks with mixed heritage. Generally, inspection of these thin sections and mineral analysis show that the samples are heterogeneous in clinopyroxene and plagioclase compositions and have wide ranges of composition, suggesting possible allochthonous melt infiltration.

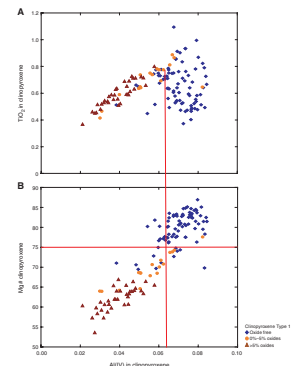
The TiO_2 trend observed in clinopyroxene is very similar to a typical tholeiitic basalt fractionation trend; however, fractionation of basalts (e.g., modeled Atlantis II basalts or Galapagos basalts) lead to peak TiO_2 followed by depletion trends at Mg#s of ~25–30 in the melt before oxides initiate crystallization. The Mg#s of clinopyroxenes in equilibrium with this peak in the melt would be much lower than when the appearance of oxides is observed in Hole 1105A data. The appearance would be in the Mg# range of 52–59 rather than 70–73, as observed. Thus, the peak in clinopyroxene TiO_2 seems to be displaced by ~20 units if Ti melt evolution trends observed in natural basalts caused the inflection. Clearly, the peak Fe-Ti-rich melt would not be in equilibrium with the clinopyroxenes with these higher Mg#s, possibly suggesting an early onset of oxide fractionation that led to the depletion of TiO_2 in clinopyroxene, unrelated to typical PFX trends. This roughly approximated Mg# threshold of ~70–73 in clinopyroxene is essentially the same Fe and Ti enrichment and Si depletion point observed in the bulk rock trends (Fig. F14). Similar trends have also been observed in rocks from Hole 735B (by Ozawa et al., 1991; Dick et al., 2002) and Hole 1105A (by Thy, Chap. 2, this volume). Other authors have interpreted these trends to result from mixtures of primitive olivine gabbros and Fe-Ti-rich interstitial melts.

Another possibility for these trends is that they result from coupled substitution in clinopyroxene and compositional effects on partitioning behavior as the melt evolves. At first glance this seems unlikely in that the dominant controls on distribution coefficients are overall relatively small in terms of variations in major element concentrations (Blundy and Wood, 1994; Wood and Blundy, 1997). Hill et al. (2000) reported the influence of Ca-Tschemmaks (calcium Tschemmaks or CaTs) content of clinopyroxene on the partitioning of trace elements between clinopyroxene and melt. Al exists in pyroxene both in the octahedral and tetrahedral valence states. In a Ca-Tschemmak molecule, Al exists in both the octahedral and the tetrahedral form. Lundstrom et al. (1998) demonstrated positive dependency of clinopyroxene liquid partition coefficients of high-field-strength cations Ti, Zr, Hf, Nb, and Ta on the Al(IV) content of clinopyroxene. Hill et al. (2000), with data from their studies, further confirmed the trend. Figure F31A shows the already established relationship between D_{Ti} and Al(IV), as shown in Lundstrom et al. (1998). This graph precisely suggests that as Al(IV) decreases D_{Ti} also decreases, and so does the ease with which Ti can enter the clinopyroxene structure. Figure F31B is an enlarged view of Figure F31A. The data are from Ray et al. (1983). At lower concentrations of Al(IV) in clinopyroxene the relationship between the two variables holds and D_{Ti} decreases with decreasing Al(IV). The concentrations of Al(IV) in clinopyroxene as shown in Figure F31B are included in the range of the data from Holes 1105A and 735B. Figure F32A shows the relationship between Al(IV) and TiO_2 for clinopyroxenes from the study area. The graph shows a kink, with TiO_2 increasing or variable with decreasing

F31. Al(IV) in cpx and D_{Ti} , p. 87.



F32. Al(IV) vs. TiO_2 and Mg# in cpx, p. 88.



Al(IV) when it is greater than ~ 0.06 and TiO_2 decreasing with decreasing Al(IV) below ~ 0.06 . Figure F32B shows the relationship between Al(IV) and Mg# for clinopyroxene from the study area. Al(IV) decreases systematically with Mg#. Figure F32B shows an Mg# of ~ 73 – 75 separates the oxide-free from oxide-bearing samples, although the range is broad due to some scatter in the data. The correlation between the TiO_2 content and trends in clinopyroxene and the appearance of opaque oxides may suggest that melt was saturated with oxides and evolving in contact with relatively primitive clinopyroxene. Alternatively, the TiO_2 content and trends in clinopyroxene may indicate that variable K_d may play a role in clinopyroxene as a function of evolving melt composition. Walker et al. (1973), in their study on the pyroxenes of the Palisades sill, New Jersey, reported similar behavior of Ti in clinopyroxene with respect to clinopyroxene Mg#, and we observed this behavior in all suites of gabbroic rocks studied. Walker et al. indicated that the decrease in Ti in pyroxene appeared to correspond with the reduction in the Ti content in the liquid at the same time that Ti was being incorporated in ilmenite and titanomagnetite.

Apart from the complexities of coupled substitution in clinopyroxene, the apparent systematic relationships between Mg# of clinopyroxene and the appearance of oxides may imply early crystallization of Fe-Ti opaque oxides and the possible operation of boundary layer fractionation and in situ crystallization and fractionation processes (Casey and Karson, 1981; Langmuir, 1989; Nielson and DeLong, 1992).

Likewise, Na_2O in clinopyroxene shows a similar but somewhat less pronounced trend as TiO_2 . Na_2O abundances are variable but elevated, on average between 0.32 and 0.54 wt%, with decreasing Mg#s in primitive olivine gabbros. Na_2O peaks at Mg# = 70 and then generally decreases as Mg# decreases to <70 . The compositions are most variable in single thin sections of oxide gabbros where zoned rims or heterogeneous clinopyroxene populations tend to be the most depleted in Na_2O , extending to 0.25 wt% in evolved samples (Mg# = 50–65). Ozawa et al. (1991) noted an increase in Na_2O with increasing grain size and interpreted this to indicate both magma composition and subliquidus postcumulus growth and reaction with trapped melt. It, however, is not clear how these processes could lead to reductions in Na_2O content in clinopyroxene, as trapped melt would tend to increase in Na_2O content as crystallization advances. Natland et al. (1991) also pointed out a possibility that immiscible Fe-rich melts will have low Na_2O contents.

Orthopyroxene and Pigeonite

Orthopyroxene is present locally in some samples as an accessory phase (see also Thy, Chap. 2, this volume). It usually occurs as a granular phase in highly evolved rocks. The grains are subrounded to rectangular in habit and are pleochroic. It also occurs as thin reaction rims, generally between olivine and plagioclase. It occurs extensively as an exsolved phase in clinopyroxene. The exsolution lamellae are of different types. Some are very fine, and blebs of orthopyroxene are also visible. In rare instances, inverted pigeonite is observed replacing orthopyroxene or as an intercumulus phase. Typical herringbone twinning is visible in inverted pigeonites. Again, inverted pigeonite is found in oxide-rich rocks. Both orthopyroxene and pigeonite occur in Unit I, Subunits IIA and IIB, and Unit IV, where local oxide abundances are high.

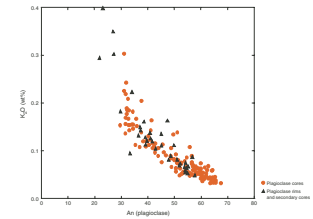
Plagioclase

Plagioclase varies in composition from $An_{67}Ab_{32}$ to $An_{14}Ab_{84}$. Thy (Chap. 2, this volume) showed slightly higher anorthite contents up to An_{70} . Increases in albite content are coupled with systematic increases in K_2O (Fig. F33) with a range of $Or_{0.18-2.85}$. Around An% (30%–35%), the slope suddenly changes (i.e., a small change in An% shows a greater change in K_2O). This trend is also seen in plagioclase from Hole 735B. The slope change takes place as oxides become more prevalent in the mode and the rate of increase in K_2O in plagioclase accelerates. Plagioclase compositions show the widest extent of variability in single thin sections, and zoned rims are generally more abundant, especially in more fractionated oxide gabbros. Overall, however, the extent of major element zoning in most samples is low. The lowest An compositions ($<An_{30}$) occur in felsic veins, which are not part of the cumulate assemblage but probably formed from late-stage melts migrating through the local cumulate pile. Also, the composition of the plagioclase correlates broadly to the lithology of the rock. Anorthite content decreases with progress from “oxide-free” gabbro and olivine gabbro to “oxide-bearing” and “oxide” gabbro and olivine gabbro. Plagioclase compositions are usually very uniform with some local heterogeneity. Some samples show multiple domains of plagioclase, and those samples are the same samples that show multiple domains of clinopyroxene. As previously stated, these samples were probable pathways for melt migration. As pointed out by Ozawa et al. (1991), the plagioclase in oxide-rich gabbroic rocks has a very dirty appearance as a result of the presence of very fine exsolved lamellae of opaque iron oxides. The exsolution lamellae are very thin and mostly detectable in backscatter images, suggesting that the plagioclase in the oxide gabbro and olivine gabbros was Fe rich and they exsolved the Fe as an oxide as cooling proceeded. FeO ranges from 0.1 to 0.4 wt% in Hole 1105A samples. A poorly defined trend of increasing FeO with decreasing An% is visible. This increasing FeO supports the fact that the melt became progressively Fe rich with fractionation. Dick et al. (2002) reported decreasing FeO in plagioclase in the oxide gabbros and also described a second trend of decreasing FeO starting at a higher Fe content and lower An ($<20\%$) content. This trend is not visible in the data from Hole 1105A, and it does not appear to be present in the data from the upper 500 m of Hole 735B.

Fe-Ti Oxides

Thy (Chap. 2, this volume) showed that the Fe-Ti oxide minerals in the oxide gabbros and oxide olivine gabbros of Hole 1105A are granular intergrowths with a composition between magnetite and titanomagnetite. Equilibrium temperatures were calculated and reside between 850° and $675^\circ C$, indicating more extensive subsolidus reequilibration than in silicate phases, which generally show more elevated equilibrium temperatures (700° – $1100^\circ C$). Our ilmenite and magnetite analyses showed equilibrium temperatures of 686° to $872^\circ C$. Magmatic oxides are present in greater than accessory amounts in gabbros with pyroxene Mg# <70 – 73 , the point at which the overall trend of TiO_2 in clinopyroxene begins to decrease with decreasing Mg#, which may suggest oxides first appeared on the liquidus. The presence of oxide gabbros with relatively high Mg# clinopyroxene may argue for early multiple saturation with oxides or a postcumulus melt-rock interaction and partial reequili-

F33. K_2O vs. An in plagioclase, p. 89.



bration between crystals and an evolved trapped melt. The additional precipitation of oxides both from trapped melt and from relatively iron rich melts migrating through the cumulus crystal mass may also help explain their coexistence with high-Mg# pyroxenes. The overall abundance in opaque oxides in some rocks can be >30%, strongly suggesting a cumulus process for origin of the oxides and that oxides were on the liquidus at the time of formation of the cumulus minerals. If the oxides were the result of trapped liquid, oxide modal percentages would be significantly lower.

Other Accessory Phases

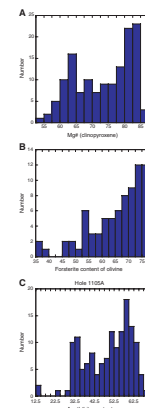
We observed zircon, apatite, and various sulfide accessory phases in the samples, but they were not analyzed. In some of the samples, the accessory phases were along small veinlets a few grains thick that appear to penetrate the gabbroic rocks. In these cases, they usually resulted in trace element spikes in downhole plots. In other cases, they were observed as intergranular phases in silicic granophyres or oxide gabbroic rocks.

Mineral Covariation and Downhole Cryptic Mineral Chemistry Variation

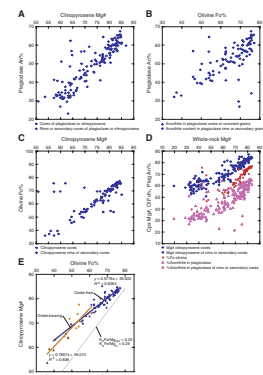
A summary of the major silicate phase compositions is presented in histograms of Fo content of olivine, Mg# of clinopyroxene, and anorthite content of plagioclase (Fig. F34). Both clinopyroxene and plagioclase show a small bimodal distribution of samples, but the general and predictable trend is toward decreasing numbers of more fractionated analyses. A remarkably good correlation exists between the average composition of forsterite-anorthite, Mg# clinopyroxene-anorthite, and Mg# clinopyroxene-forsterite (Fig. F35). The correlation is significant because of the different diffusion timescales for reequilibration for olivine, plagioclase, and clinopyroxene (e.g., Korenaga and Kelemen, 1998). Olivine has very short diffusion times, and plagioclase has long reequilibration times near magmatic temperatures. The first-order correlation between the Mg# of clinopyroxene and anorthite content is especially clear on the downhole plot (Fig. F36). The correlation is aided by the fact that plagioclase and clinopyroxene pairs were sampled in almost all samples and the peaks and troughs in the downhole cryptic chemical variation plots are well correlated. This illustrates that the primary control on rock composition was simple magmatic differentiation along a typical MORB liquid line of descent (LLD) (also see Thy, Chap. 2, this volume; Dick et al., 2002).

Like the whole-rock trends, downhole variations show both normal and inverse variation trends. The forsterite-anorthite or Mg# clinopyroxene vs. forsterite correlation is still strong, although not as robust because of the sparser sampling of olivine. However, general first-order downhole trends are easily correlated where sampling of olivine is adequate. It appears that the original cryptic variation is well preserved in the section and not muted significantly by extensive late-stage permeable melt flow through a crystal matrix. However, there may be considerable hypersolidus reequilibration between evolved trapped melt, olivine, and possibly clinopyroxene and/or subsolidus reequilibration between olivine and clinopyroxene based on the lack of agreement with equilibrium Fe-Mg partition coefficients between clinopyroxene and olivine and melt. Coexisting clinopyroxene and olivine (Fig. F35E)

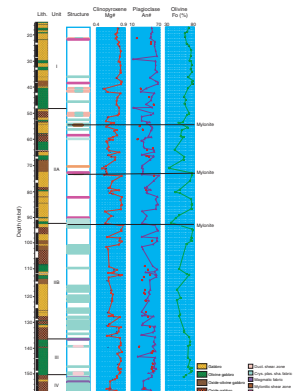
F34. Silicate mineral data, p. 90.



F35. An-plag, Mg#-cpx, Fo-Ol, and An-cpx, p. 91.



F36. Fo, An, and Mg# of cpx, p. 92.

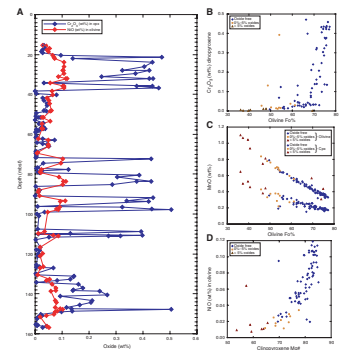


fall well off $K_{d(\text{ol}/\text{liq})} = 0.29$ and $K_{d(\text{cpx}/\text{liq})} = 0.23$ predicted correlation lines (e.g., Grove and Bryan, 1983). However, it is clear that permeable melt flow through the cumulate pile has not significantly altered the fine-scale chemical stratigraphy and covariations between mineral assemblages.

For example, in addition to major elements, the cryptic variations of compatible minor elements such as Cr_2O_3 in clinopyroxene and NiO in olivine also show a strong correlation in terms of the positions of major peaks and troughs, indicating that the original magmatic variation on the scale of a meter or less is well preserved in each of these primary phases (Fig. F37). Cr_2O_3 abundance in clinopyroxene appears to more rapidly deplete to lower levels at higher Mg#s when compared to NiO in olivine. Likewise, plots of Fo in olivine vs. Cr_2O_3 in clinopyroxene and Mg# of clinopyroxene vs. NiO in olivine show strong correlation expected of covariation during fractional crystallization. Incompatible elements such as MnO in clinopyroxene and olivine show very strong correlations with Fo content in olivine. If diffusion rates are so different between olivine and clinopyroxene we would not expect such good correlations if migrating melts were strongly reequilibrating with primary assemblages throughout the section. Such strong correlations between Fo-NiO in olivine (Fig. F37) and Fo- Cr_2O_3 in clinopyroxene (Fig. F37) were interpreted by Korenaga and Kelemen (1998) to indicate the absence of significant late-stage permeable melt flow. Poor correlation of coexisting mineral compositions in rocks with different modal abundances would be expected as the result of reequilibration of the matrix of a crystal mush with melts being transported through it by permeable flow on a large scale. Although each diagram has outliers that appear to represent small channels or melt conduits, as we have previously discussed, and are related to fracturing or concentrated areas of porous flow of unrelated melts, the dominance of highly correlated covariation between the primary phases olivine, clinopyroxene, and plagioclase may support Korenaga and Kelemen's interpretation. Their interpretation follows from the very different solid-state diffusion coefficients for olivine, pyroxene, and plagioclase and differences in reaction rates for different elements (e.g., trivalent vs. divalent cations) within individual phases (e.g., Korenaga and Kelemen, 1998; Kelemen et al., 1997). However, more rapid expulsion of migratory interstitial melts within a narrow boundary layer undergoing in situ heterogeneous nucleation and in communication with a central homogeneous magma chamber, some postcumulus reequilibration with trapped melt, and subsolidus equilibration may explain some of the scatter within each diagram. When the few outliers are eliminated from the covariation diagrams, the covariation correlation coefficients are generally as high as or higher than those depicted by Korenaga and Kelemen (1998) for the Oman ophiolite and tend to be higher than those described by Dick et al. (2002).

In cases where there is widespread melt flow through the cumulates and cryptic peaks in downhole mineral composition profiles are subdued by reequilibration with a migrating melt, the differences in reaction rate cause the peaks in mineral composition to shift relative to one another. Korenaga and Kelemen (1998) showed in a detailed study of a 600-m layered section of the Oman ophiolite excellent covariation of the silicate minerals that precluded large-scale melt migration through the section. They found that the nickel content of olivine correlated well with the forsterite content ($R^2 = 0.89$). By contrast, for Hole 735B gabbros, Dick et al. (2002) suggested no correlation at all between oli-

F37. NiO-Ol, Fo-Ol, Cr_2O_3 -cpx, MnO-cpx, MnO-Ol, and Mg#-cpx, p. 93.



vine nickel and forsterite content other than an increasing upper bound for Ni with increasing Mg#. Similarly, Korenaga and Kelemen (1998) found the correlation coefficient for anorthite and forsterite in their gabbros to be $R^2 = 0.59$, whereas Dick et al. (2002) found a significantly lower correlation coefficient for the Hole 735B olivine gabbros. Dick et al. interpreted their results to indicate extensive late melt-rock reaction and permeable flow. Our results suggest that large-scale melt flow has failed to significantly perturb the chemical stratigraphy in Hole 1105A.

Possible Evidence of In Situ Crystallization (Heterogeneous Nucleation)

Many authors who have described the characteristics of igneous layering in continental layered intrusions have interpreted these characteristics to originate, in part, by in situ crystallization in a boundary layer of graduated solidification (Jackson, 1961; McBurney and Noyes, 1979; Campbell, 1978, 1996). Casey and Karson (1981) proposed in situ crystallization as an important mechanism of layer formation in ophiolite gabbroic sections and, by extension, within the oceanic crust based on the complex and steep (sidewall) layer geometries and observations of clear in situ crystallization features such as harrisitic textures. We noted the occurrence of similar complex, variably inclined (see "[Hole 1105A Deformation Extent and Core Microstructure](#)," p. 34), and laterally discontinuous layering in Hole 1105A. The layering is generally defined by modal abundance and grain size changes. Modal changes relate to the appearance and disappearance of oxide or olivine or by modal proportion changes.

Langmuir (1989) and Nielson and DeLong (1992) explored the geochemical consequences of in situ crystallization utilizing equilibrium and Rayleigh crystallization models, respectively. They showed that having a boundary layer with a graduated temperature gradient between the solidus at the wall of the chamber and convecting primitive melt within the interior of the chamber could result in complex mixing between fractionated, multiply saturated melts formed at the outer wall of the boundary layer and primitive melts in the convecting part of chamber interior. Multiply saturated melts may be expelled and mixed into the more primitive main part of the chamber, a process called compositional convection (e.g., Tait et al., 1984; Sparks et al., 1984). A characteristic of in situ crystallization is that the minerals solidifying in the boundary layer are not necessarily on the liquidus of the convecting crystal-free interior of the chamber. For example, the boundary layers may crystallize clinopyroxene, oxides, or other accessory phases in addition to olivine and plagioclase, but they are not necessarily on the liquidus in the interior of the chamber. Melts in the interior of the chamber would be continually enriched in incompatible elements and also show evidence of clinopyroxene or oxide crystallization. Langmuir (1989) suggested in situ crystallization was a possible explanation for the well-known "clinopyroxene paradox" in MORB (also see Langmuir et al., 1992; Nielson and DeLong, 1992), where melts with olivine and plagioclase on the liquidus show evidence of extensive clinopyroxene fractionation (phantom crystallization). The mineral assemblage in the boundary layer is dependent on the extent of crystallization prior to the point where the liquid escapes (Nielson and DeLong, 1992). We expect this process depends on the temperature/density gradient on the margin of the chamber, which may vary in time and space along the cham-

trend illustrated by clinopyroxene data using constant partition coefficients, we conducted boundary layer fractionation modeling (Nielson and DeLong, 1992) of one of the most primitive Atlantis II basalts in which we assumed a boundary layer represented 5% of the magma chamber volume and the extent of fractionation in the boundary layer was as high as 70%. We were able to match the trend illustrated by calculated melts in equilibrium with clinopyroxene. In boundary layer fractionation, the extent of fractionation determines the extent of multiple saturation. In the case of 60%–70% fractionation, the melt can saturate even in minor phases. Most basaltic magmas would readily saturate with opaque oxides in the solidification zone under the modeling conditions imposed, leading to the TiO₂ depletion trend at the high Mg#s observed. Unlike the saturation achieved in the boundary layer, the central homogeneous magma chamber would not be saturated in these late crystallizing phases (e.g., Atlantis II basalts are not). TiO₂ in this case would show enrichment in the homogeneous convecting part of the magma chamber but a more limited or flattened extent of enrichment in the boundary layer. The basalt trend observed follows the homogeneous magma chamber trend, whereas the cumulates seem to follow a boundary layer trend with respect to the clinopyroxene mineral chemistry and modal relationships. Apatite fractionation evident in some of the oxide gabbros further supports the idea of saturation in minor phases within the boundary layer. The extent of fractionation over small intervals (1 m) suggests strong thermal gradients across the boundary layer, consistent with small or high-level magma chambers.

An important observation in our analysis is that the appearance of magmatic (or abundant) oxides in the mode of the gabbroic and meta-gabbroic rocks analyzed corresponds to calculated liquid compositions of Mg# = ~45 or below. Fifty-two samples below this value contained magmatic oxides; only three did not contain oxides. One sample that contained oxides had an Mg# in the equilibrium liquid > 45; the remainder of the samples with liquid Mg#s > 45 (57 samples) lacked magmatic oxides. This apparent boundary between oxide-bearing and oxide-barren gabbroic samples (Mg# = ~45 in liquid) also corresponds to the point where the liquid and equilibrium clinopyroxene (Mg# = ~70–73) show the initiation of a TiO₂ depletion trend. It is important to note that PFX modeling at or near quartz-fayalite-magnetite (QFM) buffer would predict oxide precipitation at or below liquid Mg# = 30.

This may not, however, be a unique solution because it is possible that the partition coefficient for TiO₂ in clinopyroxene is not constant, as previously discussed. In Figure F38B, we conducted the same type of PFX and boundary layer fractionation (BLF) modeling with varying K_d . As discussed in “Mineral Chemistry,” p. 21, TiO₂ concentrations in the clinopyroxene structure may depend on Al(IV) in the structure. Thus, as shown in Figure F31 (Al[IV] vs. Ti), as Al(IV) decreases, D_{Ti} decreases and so does the ease with which Ti can enter the clinopyroxene structure. So Al(IV) was calculated for all the samples using stoichiometric relationships. The Al(IV)- D_{Ti} correlation equation obtained from Figure F31 was used to calculate D_{Ti} in each individual sample using the previously calculated Al(IV), giving us the D_{Ti} for each individual sample; thus, D_{Ti} was a variable and not a constant value. This variable D_{Ti} was used to calculate the amount of TiO₂ in the liquid in equilibrium with the clinopyroxene in the gabbros. Figure F38B shows a plot between calculated Mg# of melts and calculated TiO₂ in melts (using variable D_{Ti}) in equilibrium with the clinopyroxene grains. The plot is significantly dif-

ferent from Figure F38A. The distinct peak observed in the melt in equilibrium with cumulates is absent, and a more gentle BLF curve almost parallel to the PFX LLD is observed. A very subtle kink is observed in the BLF curve. The boundary separating the oxide free from the oxide bearing and oxide rich is not a well-defined peak, but it is still clearly seen. Although the BLF curve is not very distinct and runs almost parallel to the PFX curve, maximum TiO_2 occurs much earlier compared to PFX under same conditions of fractionation. Like oxygen fugacity modeling that we conducted, BLF modeling was completed to find a suitable model to match the melt compositions. In our modeling the boundary layer was 10% of the total chamber volume, oxygen fugacity was decreased to 2 log units below the QFM buffer, and the amount of fractionation in the boundary layer was taken to be 40%. The plot shows the curve, and it is a reasonable fit, but as suggested by Nielson and DeLong (1992), at lower extents of fractionation in the boundary layer it is difficult to observe the effects of BLF. Rather, the results are similar to homogeneous fractionation. The concentrations of TiO_2 in the equilibrium melts along the LLD are different in the models (PFX and BLF). PFX predicts much more TiO_2 enrichment than does BLF. Also, the BLF estimation seems to be much closer to the melts in equilibrium with the clinopyroxene grains in the gabbroic rocks. Although choosing between variable K_d for TiO_2 or constant K_d creates a degree of ambiguity on which models appropriately describe the process, in both cases BLF remains a viable process for the formation of the gabbroic rocks and, in particular, an early appearance of opaque oxides.

Natland and Dick (2002) and Thy (Chap. 2, this volume) interpreted oxides in gabbroic rocks of Holes 735B and 1105A, respectively, and their association with primitive olivine gabbros to indicate that gabbros were impregnated by evolved intercumulus melts that were saturated in oxides and that the association of oxides with zones of ductile deformation demand that these zones were hypersolidus mush zones impregnated by oxide-saturated melts. Our analysis shows that the most primitive olivine gabbros (with high Fo, An, and Mg# in clinopyroxenes) in Hole 1105A are generally not oxide bearing, with one exception, and that only more evolved gabbroic rocks and mineral chemistries are associated with oxides. The model of Dick et al. (2002) predicts random impregnation of both primitive and more evolved intervals, but clearly oxides in Hole 1105A core do not necessarily appear randomly in primitive gabbros, except locally in those sections noted, and there is a systematic progression of phase chemistry and bulk rock compositions leading to the appearance of oxides. Alternatively, both models may have some commonality and shared consequences.

Our analysis may suggest that in situ crystallization processes may help to explain the proximity and interlayering of more primitive olivine gabbros and oxide gabbros. In part, the models of Dick et al. (2002) and Thy (Chap. 2, this volume) may be compatible because boundary layer fractionation would predict removal or extraction of much of the interstitial fractionated boundary layer melt and delivery to the main body of the magma chamber as the cumulates texturally matured. Certain observations of impregnation zones of oxide-saturated melts and higher incompatible element abundances thus may be consistent with this type of short-distance transport, melt reequilibration with cumulus minerals, in situ fractionation within pore space, and melt extraction to the interior of the chamber. The relative enrichment in incompatible elements over those expected in perfect adcumulate crystal growth in

many of the gabbroic rocks coupled with lack of zoning in most samples may indicate a certain amount of reequilibration in many samples. However, the strong and intricate cryptic chemical covariations among cumulus phases outlined above do not support widespread porous melt transport and reequilibration throughout the cumulate pile significant enough to alter peak and trough covariations between mineral phases with long and short equilibration times. Localized transport along fractures or shear zones may be supported by the fact that some samples show significant differences in core to core and core to rim compositions.

Other mechanisms that have been proposed for the complex juxtaposition of oxide gabbros and more primitive gabbroic rocks such as in the Skaergaard intrusion (e.g., McBirney, 1995; also see Thy and Dilek, 2000) seem to involve boundary layer fractionation along the strongly cooled walls and roof zone of a magma chamber and leakage of dense ferrobaltic liquids back into the magma chamber that en masse sink in the less dense, more primitive magma in the interior of the chamber to the chamber floor. This process would cause complex juxtaposition of primitive and highly fractionated gabbroic rocks. In fact, upper isotropic gabbroic rocks within ophiolites are commonly oxide bearing and contain abundant trapped melt. This suggests that the strongly chilled and hydrothermally cooled upper contacts of magma chambers may be factories for the production for ferrobaltic liquids that could be density driven to escape into the magma chamber, resulting in dense fingers that sink to the chamber floor.

HOLE 1105A DEFORMATION EXTENT AND CORE MICROSTRUCTURE

We have already discussed the possible mode of emplacement of the Atlantis Massif and largely agree with the interpretation of Dick et al. (1991, 2002) that the massif was unroofed as a core complex at the northern RTI between the Atlantis II Transform and the Southwest Indian Ridge. The discussion that follows represents an analysis of the structural features of the core from microstructures to mesoscopic structures. Miller et al. (**Chap. 3**, this volume) described successfully mapping structural features in the core using FMS logging images and correlating features with the structural and lithologic descriptions in the VCDs. We take two approaches that include examination of the microstructure of each sample and identification of structures within the core.

Microstructural analysis of Hole 735B gabbros during ODP Leg 118 (Robinson, Von Herzen, et al., 1989; Dick et al., 1991) is interpreted to indicate that some gabbros were deformed in the crystal mush stage before they completely crystallized. This magmatic deformation is believed to have produced foliation and a strong plagioclase crystallographic fabric. Later, solid-state deformation occurred at progressively lower temperatures and increased availability of hydrothermal water, probably as the gabbros moved away from the ridge axis (Cannat, 1991). Microstructural studies showed a sharp change of deformation processes in the gabbros as the temperature decreased from the stability conditions of granulite-facies metamorphic assemblages to the stability conditions of amphibolite-facies metamorphic assemblages. Temperature-dependent diffusion processes may have controlled the deformation of all minerals in granulite-facies metamorphic

conditions. Disorganized plagioclase and olivine fabric patterns characterize this deformation.

Dick, Natland, Miller, et al. (1999), during Leg 176 on the same gabbroic massif, suggested that deformation was localized from hypersolidus to low-temperature subsolidus conditions and affected the migration of late crystallizing melts. They reported that thick intervals of the core in Hole 735B are either isotropic or contain local domains with weak to moderate magmatic foliations, often overprinted by a weak parallel crystal-plastic fabric. Further, they indicated that magmatic and crystal-plastic foliations have a consistent strike over the entire core but show no systematic distribution or change in dip with depth.

Similar microstructural study in gabbroic shear zones from the MARK area (Agar et al., 1997) revealed that dynamic and static recrystallization in gabbroic rocks occurred at relatively high temperatures, probably $>700^{\circ}\text{C}$. Deformation was accommodated primarily by dislocation creep. It is possible that some recrystallization of plagioclase occurred at lower temperatures ($>450^{\circ}\text{C}$), but more evidence of synkinematic cracking of olivine and pyroxene during bulk deformation at these temperatures would be expected. Therefore, it was suggested that most of the deformation in the samples ceased under upper amphibolite facies conditions during which brown amphibole was precipitated around pyroxene recrystallized grain boundaries. During this high-temperature deformation, crosscutting relations indicate that late-stage magmatic fractionates were mobilized into deformed regions (that may have still been deforming). Possible synkinematic shearing at hypersolidus conditions could have generated the crystallographic preferred orientations observed in leucocratic veins. The introduction of fractionated melts apparently changed the bulk composition of the deformed (or deforming) regions.

Dick, Natland, Miller, et al. (1999), in describing the results of Leg 176, suggested that the most fractionated oxide gabbros are generally systematically associated with shear zones, and deformation-driven differentiation may explain the apparent association of crystal-plastic deformation with oxide-rich gabbroic rocks. In this hypothesis, shear zones propagate through a crystal-rich mush and act as low-stress conduits that assist in the migration of fractionated melts into the upper portions of the crust (Dick et al., 1991, 1992). To test this model they tried to evaluate whether a correlation between crystal-plastic fabric intensities and the degree of fractionation as measured by whole-rock Mg# exists. If deformation drives the differentiation, then the more deformed samples should have lower Mg#,s, reflecting their more fractionated character. They found only a very weak correlation, at best, between deformation and differentiation.

An alternative hypothesis is that late-crystallizing intercumulus oxide-rich melts behaved as deformation localization zones. The presence of melt lowers the effective normal stress by the amount of pore fluid pressure, and a decrease in the normal stress may cause the rock to cross the failure envelope and crack along shear planes. Melts can then migrate along shear fractures.

Strain localization could also be evidenced under subsolidus conditions by the presence of more abundant oxide minerals, which are generally considered the weakest mineral under crystal-plastic conditions. In addition, oxide minerals are likely to behave in a ductile manner to temperatures of $\sim 450^{\circ}\text{C}$ (Agar et al., 1997), significantly lower than the silicate phases would remain ductile. Thus, significant oxide abun-

dances could significantly lower the ductile strength and help to localize deformation without the existence of a melt phase.

A representative suite of deformation textures in gabbroic shear zones can be observed in a wide variety of modal compositions. Shear zones range from isolated structures at the centimeter scale to >1 m thick. The main scope of this study included

1. Rigorously investigating the correlation between modal composition and the location and intensity of deformation and
2. Understanding the juxtaposition of such contrasting assemblages of primitive and highly fractionated gabbroic rocks.

Also, it is emphasized that correlation between qualitative estimates of finite strain and modal composition are of limited value unless the spatial relationships of strain localization to compositional and textural variations are carefully documented. FMS data were used to constrain these spatial relationships. Also, the scale of observation can change the modal composition estimates of some samples (e.g., thin section vs. core); therefore, an integrated observation of a wide range of scales (microscopic, mesoscopic, and macroscopic) is required to understand the influence of modal composition and primary texture on strain localization.

Hole 1105A Textural Classification

Textures of the plutonic rocks were characterized on the basis of grain shape, mutual contacts, and preferred mineral orientation. Rock textures such as equigranular, inequigranular, intergranular, and granular were used to describe the overall texture of each lithologic interval. Poikilitic, ophitic, subophitic, and interstitial textures were distinguished according to the *predominant* grain shapes in each interval. The textural type attributed to each thin section is not absolutely representative of the whole thin section but represents only the predominant texture of that particular thin section (i.e., >60% of the thin section demonstrates a particular texture). There are examples where two or three different textural types can be identified in each thin section, but only the predominant one is selected as the representative texture. For this study, parameters such as the development of microstructures associated with crystal plasticity (e.g., subgrains, neoblasts, porphyroclasts, sutured grain boundaries, deformation twins, kink bands, percentage of recrystallization subgrains formed, recrystallized grain sizes, degree of shape-preferred orientation, and extent of crystallographic preferred orientation) were recorded for each thin section and used to classify textural types. The textural types outlined here represent only those samples used in this study and do not represent the entire spectrum of deformation textures within Hole 1105A. Similar textures in different samples do not necessarily imply that the samples followed the same deformation paths because there are variable starting protolith textures and compositions and there may be different extents of hypersolidus to solid-state deformation that lead to the same textural type. Igneous lamination can be taken as an indicator of possible hypersolidus processes such as laminar flow or in situ crystallization. The presence of inclusions, overgrowths, and zonation was noted, and the apparent order of crystallization was suggested in the comments section for samples with appropriate textural relationships. The presence and relative abundance of accessory minerals such as Fe-Ti oxides were noted, and modal analysis allowed clear differentiation of the rocks based on oxide modal abundances. The percentage of alter-

ation was also recorded. Deformation textures or categories were assigned to each thin section. The eight textural categories assigned generally reflect increasing strain from 1 to 8, 1 indicating no strain and 8 indicating maximum strain, typically within a mylonitic shear zone. The increase in strain from one category to the next is not by any means linear, and we emphasize that the measure of deformation extent is simply tied to textural categories that we outline below. We used the textural type as a qualitative measure of the extent of deformation downhole and to examine the influence of modal mineralogy on the extent of deformation in the sample. We emphasize that the textural categories are designed to provide qualitative information on the extent of strain and recrystallization downhole.

Undeformed Texture: Textural Category 1

No foliation or lineation is apparent in thin sections or core samples. Crystallographic preferred orientation is not evident with the gypsum plate inserted. Evidence of recrystallized grains of plagioclase or olivine, if observable, is <5% and <2%, respectively. No evidence of clinopyroxene recrystallization can be observed. Intact igneous texture with subhedral to euhedral morphologies and straight exsolution lamellae in clinopyroxene grains indicate that they are relatively undeformed. Some plagioclase grains show local tapering deformation twins but many have blunt ends typical of igneous twins. No kink bands in plagioclase are detected. Although the thin section dominantly appears unaltered and undeformed, some small percentage of alteration, especially within the olivine crystals, can be observed in most thin sections. Most of the textures within this category have granular texture with different grain sizes ranging from fine to coarse grains with euhedral to subhedral mineral shapes.

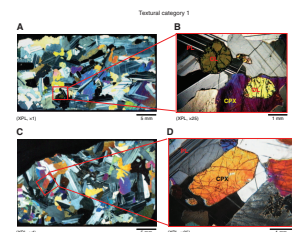
Figure F39A represents a medium- to coarse-grained olivine gabbro with equigranular texture. Plagioclase grains are elongated to equant, clinopyroxene grains are elongated, and olivine grains have an amoeboidal appearance. Figure F39B is a magnified part of Figure F39A. Note the subhedral shape of olivine grains and the straight plagioclase polysynthetic twins. Also, no marginal alteration or bulging is detected around the grain boundaries. Embayment of long plagioclase laths in large clinopyroxene and olivine grains delineates a local subophitic texture in the sample. Little alteration exists in this section, and most of the minerals appear unaltered. Some plagioclase shows strong zoning, but a lack of zoning is typical. Also, undulose extinction can be observed in plagioclase laths, but no significant tapering is observed in plagioclase twins. Very straight exsolution lamellae in clinopyroxene grains at the bottom of the thin section can be clearly identified.

Figure F39C shows a coarse-grained equigranular olivine gabbro with elongated plagioclase laths, equant clinopyroxene grains, and equant olivine grains. Figure F39D is a magnified portion of Figure F39C, where fresh clinopyroxene minerals with no signs of deformation are clearly present. This sample is one of the least deformed thin sections of the whole collection. Even the hexagonal euhedral shapes of the clinopyroxene crystals are preserved.

Weakly Recrystallized Texture: Textural Category 2

In the weakly deformed samples, relict igneous textures are evident. Yet again, no foliation or lineation is apparent in thin sections. Crystal-

F39. Examples of textural Category 1, p. 95.



lographic preferred orientation is generally not evident with the gypsum plate inserted, except for a few small (2–3 mm) domains of weak crystallographic preferred orientation in plagioclase and olivine (but no shaped-preferred orientation). Maximum recrystallization of plagioclase is ~15%, and as much as 5% olivine is recrystallized. Clinopyroxene lacks recrystallization. Relict plagioclase grains commonly display weak undulose extinction and contain thin, tapering deformation twins, primarily on albite but also on pericline. The twins are deformed by gentle bands, kink bands (as wide as 1 mm), and microfaults. A high angle can be measured between most of the kink bands or microfaults and albite twins aligned close to (001), as commonly observed in other studies of plagioclase deformation (e.g., Oleson, 1987; Oleson and Kohlsted, 1985; Agar et al., 1997). Plagioclase neoblasts are generally equant with gently curved boundaries that commonly intersect at 120° triple junctions. There are some lobate protrusions on the boundaries of some neoblasts and relict plagioclase grains, but they are not strongly serrated. Plagioclase neoblast grain size is relatively large (generally >0.1 mm). More than 50% of the neoblasts display twinning, but very few have undulose extinction. Subgrains are rare, but where identified they rotate deformation twins by 2°–15° within the outer margin of relict plagioclase grains. The subgrain size is slightly smaller than those of neoblasts.

A gradual grain size layer contact is observed from one side of the thin section to the other side on Figure F40A. Recrystallization of plagioclase is restricted to the lower left quadrant of the section, where small neoblasts of plagioclase and olivine can be recognized along a narrow shear zone. Strong deformation bands in all olivine crystals are clearly obvious. Figure F40B is a magnified view of deformation bands within an olivine grain. Although the overall texture is granular to subophitic, consertal texture between clinopyroxene-clinopyroxene and clinopyroxene-olivine can be detected. Examples of magmatic twinning of clinopyroxene are also observed.

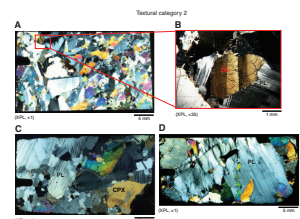
A coarse-grained olivine gabbro with equigranular texture is presented in Figure F40C. Coarse grains of plagioclase, olivine, and clinopyroxene are undeformed, but at the contacts of these coarse grains small neoblasts of pyroxene and plagioclase of different sizes can be observed. In some portions, a gradation in neoblast grain size from coarse to fine grains can be observed. Plagioclase is predominantly fresh and shows clear kink bands, subgrain boundaries, and deformation twins. Olivine is highly fractured, and most oxides are concentrated along olivine fractures. Olivine grains exhibit strong deformation bands. In general, plagioclase neoblasts are relatively large, as are olivine neoblasts.

Another example of weakly recrystallized texture is shown in Figure F40D, where, in fact, the majority of the thin section is covered with a large pegmatitic plagioclase grain that includes olivine and clinopyroxene chadacrysts. At the margins of plagioclase contacts with other grains, very small neoblasts are observed. Tapered deformation twins are present in large plagioclase, along with very strong undulatory extinction in olivine and plagioclase.

Weak to Moderately Recrystallized Texture: Textural Category 3

Oikocrytic relict igneous textures are preserved in clinopyroxene, but some grain boundaries are serrated and surrounded by narrow re-

F40. Examples of textural Category 2, p. 96.



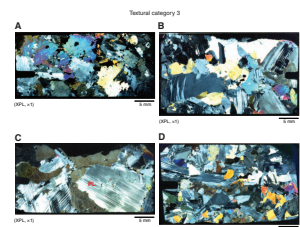
crystallized phases. Subplanar zones of the plagioclase neoblasts define weak foliation. Weak alignment of plagioclase neoblasts, albite twins, and homogeneous interference colors with a gypsum plate indicate domains of moderate crystallographic preferred orientation in plagioclase, but no significant crystal shape-preferred orientation is evident. The percentage of recrystallized plagioclase varies between 15% and 30%, and this extent is distinctive for the category. Olivine can be as much as 20% recrystallized, whereas clinopyroxene is <5% recrystallized and typically is not recrystallized. Undulatory extinction is common in relict plagioclase grains that also contain curved, tapering albite and pericline twins. Microfaults and kink bands at high angles to albite twins are present. Kink bands tend to be narrower and more numerous than those of the weakly recrystallized texture. Plagioclase neoblast grain sizes are still relatively large. Neoblast grain boundaries tend to be more irregular than those in the weakly recrystallized textures. More than 50% of the neoblasts are twinned, but these twins, in contrast to those in weakly recrystallized textures, tend to be more tapered and discontinuous. Subgrains are rare within neoblasts but can be seen in the margins of relict plagioclase grains. Aggregates of recrystallized olivine are generally located toward the margins of olivine porphyroclasts. An igneous morphology is still at least partly evident in most olivine grains. A few domains of recrystallized olivine show crystallographic preferred orientation defined with a gypsum plate. Wherever kink bands are present, subgrains are also identifiable. Clinopyroxene remains largely undeformed except for narrow recrystallized margins in some grains. Clinopyroxene neoblasts, if present, generally have rounded to weakly serrated margins. The recrystallized grain size is noticeably smaller than that of either olivine or plagioclase. Clinopyroxene oikocrysts are generally not recrystallized, but some of them are individually separated into two or more large grains with slightly different extinction angles.

As an example, Figure F41A displays plagioclase laths similar those in subophitic textures that crosscut larger clinopyroxene grains with smaller enclosed euhedral plagioclase chadacrysts. In general, plagioclase chadacrysts remain euhedral, apparently protected by the low internal strain in the clinopyroxene. The presence of the plagioclase neoblasts along the margins creates an incipient porphyroclastic appearance for this thin section. Locally, clinopyroxene is also recrystallized and marginally altered to brown amphibole. In zones where amphibole is not present, clinopyroxene fails to recrystallize, suggesting importance of high-temperature hydration in the deformation response of clinopyroxene. Plagioclase grains show mostly serrated boundaries. A weak crystal-plastic foliation can be detected subvertically parallel to the plagioclase neoblasts.

Another example for this category is shown in Figure F41B. Recrystallization is mostly restricted to the grain contacts, and most of the clinopyroxene is altered to brown and green amphiboles. However, no specific orientation of the foliation defined by shape fabrics can be detected. Most of the oxides and green amphiboles are located along the margins of larger porphyroclasts. Olivine and clinopyroxene are both recrystallized, mostly along the grain contacts. Undulatory extinction is common in relict plagioclase grains. Most of the plagioclase grains are curved and tapered.

Subgrain rotation, serrated boundaries, and narrow zones of kink bands are clearly visible in Figure F41C. Again, most of the neoblasts occur along the grain contacts in narrow zones. Narrow zones of kink

F41. Examples of textural Category 3, p. 97.



bands cut through the relict plagioclase grains. Very coarse plagioclase and clinopyroxene grains dominate the section. On Figure F41D, elongated coarse plagioclase and clinopyroxene grains dominate most of the section, and clinopyroxene is highly altered to pale green amphibole and oxide minerals. Most of the deformation twins in plagioclase laths are curved, and plagioclase grains have sutured boundaries and show strong subgrain rotation. Olivine is recrystallized into aggregates. Crude crystal-plastic foliation can be detected parallel to the curved and elongated plagioclase laths.

Moderately Recrystallized to Porphyroclastic Texture: Textural Category 4

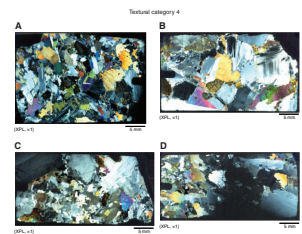
Moderately aligned porphyroclasts of plagioclase (with aspect ratios up to 1:5) surrounded by mantles of dynamically recrystallized plagioclase define this category. Moderate preferred dimensional orientation of porphyroclasts and weak to moderate crystallographic and shape-preferred orientations of recrystallized plagioclase and olivine resemble a more pronounced porphyroclastic texture. A total of 30%–50% of plagioclase is recrystallized; 30%–50% recrystallization occurs in olivine but <20% in clinopyroxene. Plagioclase porphyroclasts contain numerous deformation twins that are strongly curved or kinked. Margins of the porphyroclasts are commonly serrated and irregular and are enveloped by recrystallized plagioclase.

Figure F42A shows an oxide-bearing olivine gabbro with brittle deformation within a plagioclase porphyroclast. Left lateral sense of displacement along the brittle fractures is very common. Brittle deformation was apparently stronger in plagioclase than clinopyroxene. Highly deformed and curved plagioclase porphyroclasts in this section are quite obvious. Deformation twins are common. Brittle deformation appears to be parallel to the crude crystal-plastic foliation, which is defined by the preferred orientation of elongated clinopyroxene and olivine grains. Most of the neoblasts are concentrated along margins of larger grains. Olivine and clinopyroxene show less recrystallization than plagioclase.

Figure F42B represents an oxide-bearing olivine gabbro with very coarse plagioclase and clinopyroxene grains. Neoblasts occur along most of the contact boundaries, producing a porphyroclastic appearance of the rock. Olivine is highly altered in the upper left side of the section but is recrystallized to smaller neoblasts in the lower right portion. It is difficult to define any foliation because of the large size of the porphyroclasts; however, a crude diagonal crystal-plastic foliation may be present. One very coarse clinopyroxene grain includes large plagioclase laths. Clinopyroxene is altered to brown amphibole along margins, and recrystallized portions of the grain edges are also highly altered. Exsolution lamellae and consertal texture are observed in clinopyroxene. Olivine, although altered, still displays strong deformation bands. Plagioclase has curved and tapered deformation twins on the right side of the section, whereas on the opposite side plagioclase displays strong subgrain rotation with serrated boundaries, strong undulose extinction, and a higher percentage of recrystallization due to the higher strain.

Higher aspect ratios of porphyroclasts can be observed on Figure F42C, which shows an olivine porphyroclast with an aspect ratio of 1:4. Elongated pegmatitic plagioclase laths are also observed. Compared to the previous samples, the sample contains a higher percentage of neo-

F42. Examples of textural Category 4, p. 98.



blasts, stronger plagioclase subgrain rotation, and more sutured boundaries. A crude subvertical crystal-plastic fabric can be defined parallel to the elongated olivine and plagioclase porphyroclasts.

An igneous layer contact is presented in Figure F42D, where on the right side of the thin section a pegmatitic gabbro shows minor recrystallization and tapered plagioclase laths. This changes gradually to a finer-grained gabbro in which a moderately recrystallized to porphyroclastic texture occurs toward the left across the grain size contact. Strong undulose extinction, subgrain rotation, and recrystallization of plagioclase are observed. In addition to plagioclase, olivine and clinopyroxene are also recrystallized. Aspect ratios of the porphyroclasts are mostly between 1:2 and 1:3.

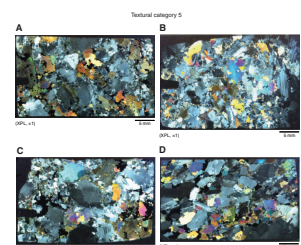
Porphyroclastic Texture: Textural Category 5

Strongly aligned porphyroclasts of plagioclase surrounded by mantles of dynamically recrystallized plagioclase define the porphyroclastic texture. Preferred dimensional orientation of porphyroclasts and the crystallographic and shape-preferred orientations of recrystallized plagioclase and olivine characterize the foliation. As much as 50%–70% of plagioclase can be recrystallized, and as much as 50% recrystallization may also occur in olivine but <30% in clinopyroxene. Plagioclase porphyroclasts contain numerous strongly curved or kinked deformation twins. Margins of the porphyroclasts are commonly serrated and irregular and are enveloped by recrystallized plagioclase (core and mantle structure; White, 1975). Plagioclase neoblasts may have moderate shape-preferred orientation and moderate to strong crystallographic preferred orientation. Also weakly to highly serrated boundaries of plagioclase neoblasts form mantles surrounding porphyroclasts and have undulatory extinction. Plagioclase neoblast grain size is significantly smaller than the weakly or moderately recrystallized textures described above. More than 50% of plagioclase neoblasts are twinned. Subgrain concentrations around the margins of the plagioclase porphyroclasts are common. Olivine porphyroclasts have a weak to moderate shape-preferred orientation. The margins of clinopyroxenes are recrystallized with weakly serrated boundaries. Clinopyroxene porphyroclasts do not appear to have any preferred orientation except as aggregates in pressure shadow regions.

Figure F43A represents an oxide gabbro with porphyroclastic texture. Strong alteration of clinopyroxene to green and brown amphibole and oxide minerals is observed. Corona structure is common. Plagioclase porphyroclasts show strong undulose extinction and strong subgrain rotation. Curved deformation twins are observed within medium-sized plagioclase laths. Some subhedral clinopyroxene porphyroclasts are elongated parallel to the oxide and alteration veins and create a foliation pattern. Different generations of plagioclase neoblasts show size grading.

Figure F43B contains strong kink bands, subgrain rotation, and undulatory extinction in olivine porphyroclasts. Plagioclase porphyroclasts also contain deformation twins, which are bent and have strong undulatory extinction. Olivine is highly altered to secondary minerals and oxides. Plagioclase neoblasts are in a range of grain size belonging to a different generation of recrystallization. Clinopyroxene is marginally altered to brown amphibole. Plagioclase and clinopyroxene porphyroclasts have strong shape-preferred orientations and high aspect

F43. Examples of textural Category 5, p. 99.



ratios, as high as 1:4. Some plagioclase neoblasts even show shape-preferred orientation.

Plagioclase neoblasts in Figure F43C have more equant shapes with 120° triple junctions and strain-free appearance. No undulose extinction is observed in plagioclase neoblasts; however, very strong subgrain rotation and undulose extinction is observed in plagioclase porphyroclasts with serrated boundaries. Olivine and clinopyroxene are both highly recrystallized. Most of the oxide minerals are distributed within the matrix of neoblasts. Some oxide minerals are marginal to the olivine and clinopyroxene porphyroclasts.

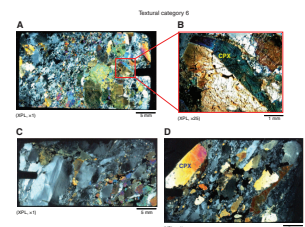
The porphyroclasts in Figure F43D show varying grain size from very coarse to fine grains from right to left diagonally, probably an inherited grain size layer boundary. Different generations of neoblasts can also be identified. Serrated boundaries are very common in most of the plagioclase porphyroclasts. Oxide minerals occur as lenses of recrystallized neoblasts, mostly parallel to the foliation orientation, and are also marginal to the olivine and clinopyroxene porphyroclasts and neoblasts. This unique texture may be a reaction texture because it appears as if oxide lenses were percolating through the rock and replacing olivine and clinopyroxene. Also, plagioclase tends to be highly zoned in places. These oxide lenses could also result from mechanical segregations. A crude modal layering parallel to the crystal-plastic fabric is observed, as clinopyroxene and olivine porphyroclasts tend to segregate between zones of plagioclase and oxide neoblasts. Some zones verge on a protomylonitic texture with highly bimodal grain sizes.

Porphyroclastic to Mylonitic Texture: Textural Category 6

Higher percentages of plagioclase neoblasts (up to 80%) and stronger shape and crystallographic preferred orientation displaying a tendency locally toward mylonitic texture and bands typify this category. Mylonitic textures are commonly spatially gradational with the porphyroclastic textures, and this transition can be observed clearly. The core and mantle structure that characterizes the porphyroclastic texture is only locally present. Exsolution lamellae in clinopyroxene porphyroclasts are commonly bent at subgrain boundaries, and kink bands are oriented at high angles to the foliation. This is the case for the clinopyroxene porphyroclast in Figure F44A, where the exsolution lamellae and magmatic twins of clinopyroxene at high angles to the foliation orientation are bent. Figure F44B is a magnified portion of Figure F44A representing the clinopyroxene porphyroclast. Porphyroclastic to mylonitic texture of the rock is prominent, and strong foliation is observed diagonally across the sample. The long dimensions of clinopyroxene porphyroclasts are oriented parallel to the foliation plane. Aggregates of olivine neoblasts have obviously replaced some former olivine porphyroclasts, perhaps as a consequence of subgrain rotation. In addition to the crystal-plastic foliation, deformation-induced grain size layering is parallel to the foliation orientation. Nearly all the neoblasts show high aspect ratios and strong shape-preferred orientation. More than 80% of plagioclase and most of the olivine grains are recrystallized. Clinopyroxene appears to be the strongest phase in this thin section. Although clinopyroxene porphyroclasts are internally deformed, they are not recrystallized. Magmatic twins in clinopyroxenes, although bent, are still preserved and easily identifiable.

Spatial alternation of porphyroclastic and mylonitic texture can be better observed in Figure F44C, where high-aspect ratio plagioclase, oli-

F44. Examples of textural Category 6, p. 100.



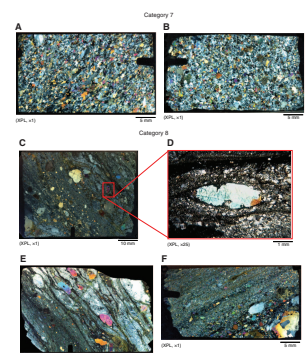
vine, and clinopyroxene porphyroclasts alternate with very fine mylonitic bands of recrystallized plagioclase neoblasts. Recrystallized oxide neoblasts are parallel to these neoblastic plagioclase zones, and they are typically marginal to olivine and clinopyroxene grains. The highest aspect ratio porphyroclasts of the whole collection may be observed in Figure F44D, where olivine and ribbon plagioclase in an oxide olivine gabbro have aspect ratios as high as 1:8. Strong subgrain rotation and undulose extinction in elongated plagioclase porphyroclasts with serrated boundaries are common. Some olivine porphyroclasts are totally altered to brown and green amphibole. Oxide minerals are interstitial parallel to the crystal-plastic foliation and are potential glide surfaces in the matrix. Clinopyroxene porphyroclasts are marginally recrystallized and altered to green and brown amphibole and have strong shape preferred-dimensional orientation.

Mylonitic Texture: Textural Category 7

More extensive recrystallization and more extensive clinopyroxene recrystallization is the most significant difference between mylonites and porphyroclastic mylonites with respect to the preceding porphyroclastic textures (textural Category 6). In addition, the recrystallized matrix is generally >50% of the rock and ranges as high as 90%. Generally, there are few remaining porphyroclasts of clinopyroxene and the rocks appear more equigranular. Plagioclase and olivine relict porphyroclasts are present, but they are scarce. Strong foliation and in some places lineation characterize the mylonitic texture. Fine grain sizes, strong crystallographic preferred orientation, and serrated grain boundary morphology defines this mylonitic to porphyroclastic mylonitic texture. Plagioclase relict porphyroclast aspect ratios range from 1:1 to 1:5. The core and mantle structure that characterizes the porphyroclastic texture is only locally present. Some mylonitic samples preserve neoblasts with strongly serrated margins, whereas others preserve more equant, polygonal neoblasts. Fewer plagioclase neoblasts are twinned when compared to less deformed samples. Subgrains are evident in both plagioclase porphyroclasts and neoblasts, but they do not show distinct rims around the porphyroclasts as in the porphyroclastic texture (above); they are still concentrated in porphyroclast margins. Olivine and clinopyroxene have finer grain sizes than other textures.

Serrated grain boundaries and subgrain rotation on the margins of plagioclase porphyroclasts are clearly visible, which is a unique texture of crystal-plastic foliation in almost equigranular porphyroclastic textures. Most of the plagioclase neoblasts show pentagonal or hexagonal shape, arguing for a grain boundary migration mechanism of deformation. Also, the porphyroclasts are small in relative size, and no strain is observed in most of the grains. Foliation is subvertical in the section. Aggregates of olivine and clinopyroxene are parallel to the foliation direction. Several generations (at least four) of neoblasts in plagioclase, clinopyroxene, and olivine can be identified. Strain patterns and kinking are only observed in porphyroclasts. Neoblasts are mostly strain free except for the sample presented in Figure F45B, where plagioclase neoblasts exhibit undulatory extinction. Undulose extinction is observed in plagioclase neoblasts when different generations of plagioclase neoblasts are present. Horizontal foliation (parallel to the long edge of the thin section) is defined by the orientation of plagioclase neoblasts and elongated clinopyroxene grains. Also, the assemblage of clinopyroxene and olivine grains is common, sometimes overlapping. Yellowish (in

F45. Examples of textural Categories 7 and 8, p. 101.



normal light) oxides are present in some olivine fractures, most probably representing hematite or limonite. Sometimes it is difficult to distinguish between neoblasts and porphyroclasts because of the more uniform grain size distribution (pseudoequigranular texture).

Ultramylonitic Texture: Textural Category 8

Ultramylonitic texture is spatially gradational with mylonitic and porphyroclastic mylonite texture because the mylonitic shear zones can be quite thin. The strain gradient can be remarkably sharp, even on a thin section scale (e.g., see thin section Sample 179-1105A-25R-2, 3–8 cm, in “[Supplementary Material](#)”). Ultramylonitic bands are typically >90% recrystallized matrix; the major difference is the finer grain size of the plagioclase neoblasts (ribbon shape) and the more complete recrystallization of clinopyroxene porphyroclasts. Relict porphyroclasts are dominated by clinopyroxene. The even grain size distribution of olivine and finer grain sizes of neoblasts define the ultramylonitic textures. Oxide bands parallel to foliation are common, giving the mylonite a banded structure. Pressure shadows are common in this category, and the sense of shear can sometimes be determined.

Figure [F45](#) represents an ultramylonitic texture. Bands within the thin section have extremely fine grain sizes and are dominantly neoblasts, often with ribbon-shaped neoblasts. They are described as ultramylonites if the porphyroclast count is low. These fine bands grade rapidly to porphyroclastic mylonite. Figure [F45D](#) represents a magnified portion of Figure [F45A](#), where a small clinopyroxene porphyroclast can be observed within the ribbons of plagioclase neoblasts. Pressure shadow structure defines dextral sense of shear for this porphyroclast. Most of the porphyroclasts are clinopyroxene, which may argue for the stronger rheology of clinopyroxene compared to olivine.

Figure [F45E](#) represents similar texture with a relatively finer grained matrix and progressively larger porphyroclasts left to right across the photo. Most of the oxide mineral bands (dark thin bands) are parallel to the shear zone and shearing direction and appear to help localize shear strain. Some core mantle structures can be observed around plagioclase porphyroclasts (upper left). High alteration of some olivine and plagioclase can be also observed as well as a postkinematic alteration veins cutting normal to the foliation direction (middle of photo). Figure [F45F](#) represents deformation-induced grain-size layering from coarse porphyroclastic grain sizes in the lower right corner of the thin section to very fine grained ultramylonitic texture toward the upper left corner. Oxide minerals also alternate parallel to the ultramylonitic zones.

Downhole Deformation Extent

As described in the previous section, based on the diagnostic microstructures observed in all the available thin sections (137), eight broad microstructural and textural categories were defined:

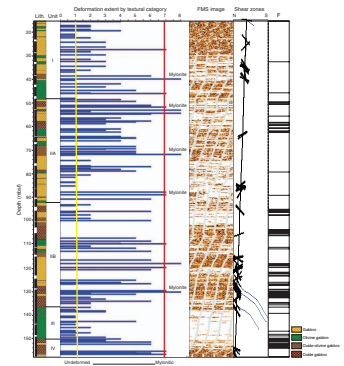
1. Undeformed magmatic,
2. Weakly recrystallized,
3. Moderately recrystallized,
4. Moderately recrystallized to porphyroclastic,
5. Porphyroclastic,
6. Porphyroclastic to protomylonitic,
7. Mylonitic, and
8. Ultramylonitic.

These textural categories represent progressively increasing extents of deformation from 1 to 8, which helps to quantify the downhole deformation. Quantification of deformation extents for thin sections from different depth intervals helps to document the variations in deformation within the borehole and also facilitates several correlations between deformation extent and lithologic and, therefore, rheologic intervals, shipboard structural logging, and FMS image logs. For thin sections that exhibit more than one textural category, a deformation extent representing the predominant textural category is assigned. The downhole deformation extent data described above are presented in Figure F46 for the 137 sections described, along with a static downhole FMS image for the entire core, the lithologic log (see “Appendix” in “Supplementary Data” in Pettigrew, Casey, Miller, et al., 1999), the shipboard downhole foliation log, and an FMS interpretation of ductile shear zones in the core. Most ductile shear zones defined directly correlated with the core descriptions where recovery allowed direct correlation; others were recognized by correlation with shear zone characteristics on the FMS log and definition of crystal-plastic foliation via FMS. Several points are obvious from the diagram. Mylonite zones (deformation categories 7 and 8) are concentrated in oxide-rich units (IIA, IIB, and IV). The FMS static images are generally most conductive in oxide-rich zones (darker colors) and most resistive in nonoxide-bearing zones (lighter colors). There is an overall correlation between conductive zones on the FMS image and deformation. There is a similar correlation between the VCD data (foliated gabbro) and deformation extent. Lastly, the FMS-determined inclinations of the shear zones are represented by apparent dip marks in a north-south plane. Based on FMS data, the shear zones and crystal-plastic foliations dip both toward the ridge axes to the north and away from the ridge axes to the south. Dips away from the ridge axis dominate. The strike of the shear zones forms a strong maximum and is essentially ridge parallel. True dips range from 10° to 60° (average = 45°) (J.F. Casey and P. Zarian, unpubl. data). These apparently conjugate shear zones may result from normal inward-dipping ridge axis faults as well as conjugate faults resulting from bending stresses during footwall rollover and development of the core complex (e.g., Tucholke et al., 1998).

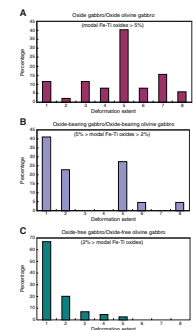
Deformation Extent and Lithologic Correlation

Figure F47 represents a series of three plots indicating the deformation extent vs. frequency percentage of the three main groups of lithologies. We modified the grouping because we noted that some rocks with <2% oxides generally contained only poorly disseminated and interstitial varieties and were typically significantly <2%, approaching zero. Although these oxides may represent important petrogenetic criteria in classifying rocks, the small amounts of oxides are unlikely to influence the rheology of the sample. Thus, we grouped rocks with <2% oxides together with “oxide-free” gabbroic rocks for these plots only. Of note is the group that shows by far the highest extent of deformation and strain in the section, the oxide gabbros and oxide olivine gabbro (>5% oxides) grouping, with the majority of samples plotting in textural category 5 or above. The oxide-bearing group (2%–5% oxides) showed a range of deformation states, the majority of which were category 5 or below. The oxide-free grouping (0%–2% oxides) by far showed the lowest degree of deformation, with a maximum of category 5 and nearly 65% of the samples in textural category 1 (undeformed magmatic texture). The positive correlation between deformation extent

F46. FMS image with lithologic intervals, deformation categories, and extents, p. 102.



F47. Deformation extents, p. 103.

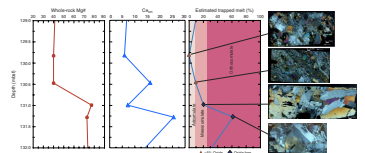


and oxide abundance is therefore striking, suggesting that oxides impart a weak rheology to the rock that lowers its overall strength and tends to localize deformation (e.g., Agar and Lloyd, 1997; Agar et al., 1997). Whether the oxide is symptomatic of initial deformation being hypersolidus as suggested by Dick, Natland, Miller, et al. (1999) is difficult to determine because of the subsolidus deformation overprint that the rocks have now experienced, making it difficult to determine the entire deformation path of each sample.

Evidence of Melt-induced Deformation?

In our estimation of trapped melt within the gabbroic samples utilizing modal estimates, many very highly incompatible whole-rock trace element abundances, and estimates of equilibrium melts for mineral chemistry, we examined a ductile shear zone and the transition between undeformed gabbro and porphyroclastic to porphyroclastic mylonitic gabbro. If shear zones were channelways for late fractionating melts, as suggested for Hole 735B (Dick et al., 2002), we expected that the products of the melt crystallization would be identifiable and that the bulk samples would be very enriched in highly incompatible elements. Estimates of trapped melts, which are made using modal analysis, calculation of equilibrium melt compositions based on BLF liquid lines of descent of primitive Atlantis II basalts (Johnson and Dick, 1992), gabbroic mineral compositions, and bulk rock incompatible element abundances from this study are not compatible with the supposition of melt enrichment in the shear zones (Banerji, 2005). Our results are displayed in Figure F48, which shows a transition from little-deformed oxide-free gabbroic rocks to oxide gabbros that have been partly mylonitized in the core interval from 129 to 132 mbsf. Oxide gabbros are characterized by low bulk Mg#s (~40) and oxide-free gabbroic rocks by higher Mg#s (~73–75). Ironically, estimates of trapped melt indicate the highest abundances are within the lowest undeformed gabbroic rocks (classified geochemically as meso- and orthocumulates with >7% and >25% trapped melt, respectively). The oxide gabbroic rocks had the lowest estimates (classified geochemically as adcumulates; <7% trapped melt). In addition to our estimates of trapped melt, we also display a profile of chondrite-normalized Ce, which is one of the highly incompatible elements used in our estimates. The profile clearly shows that the mylonitized oxide gabbros are depleted in trapped melt constituents, especially considering their evolved mineral chemistry, in comparison to the more primitive oxide-free gabbros outside the shear zone. Based on this evidence we assume that the oxide minerals accumulated in the protolith of the shear zones during crystallization of the original cumulates are perhaps similar, in part, to pyroxene and plagioclase as adcumulus phases. Oxides would not represent the dominant products of an evolved trapped melt, which would be highly enriched in incompatible elements like Ce. Alternatively, perhaps the most intense shearing regions eliminated all late-stage melts as shearing progressed. The major question becomes if higher melt percent induces deformation, why did the oxide-poor gabbroic rocks with estimated higher trapped melt not deform initially or at least along with the adjacent oxide-rich gabbroic rock that underwent shear? The question remains, do high modal percentages of oxide minerals simply present a weak rheology after they have crystallized (Agar and Lloyd, 1997; Agar et al., 1997) that, in turn, tends to localize strain in a subsolidus state, or do they represent a symptom (crystallization product)

F48. Whole-rock Mg# and estimated trapped melt, p. 104.



of a highly allochthonous and late-stage melt phase that localized the deformation in a hypersolidus state as envisioned by Dick, Natland, Miller, et al. (1999) and Dick et al. (2002)? In our example, the melt phase that would be evidenced by an abundance of highly incompatible elements has not remained in the samples that are most highly deformed, and the oxide-rich zone thought to be evidence of hypersolidus deformation appears to lack significant crystallization products of a trapped melt.

CORRELATION OF HOLE 735B AND 1105A OXIDE-RICH ZONES

At first glance it seems reasonable in all respects (similar geochemistry, structure, and magnetostratigraphy) to attempt detailed correlations between the stratigraphies in holes only 1.2 km apart. However, one-to-one matches in geochemical trends and cyclic cryptic chemical and lithologic trends are unlikely between these two holes, given that each section has been affected by crystal-plastic deformation and shear zones and that individual small-scale layer-by-layer lateral continuity in ophiolites is demonstrated to be lacking, although larger lithologic units several hundreds of meters thick can be traced laterally for hundreds of meters (e.g., Casey and Karson, 1981; Casey et al., 1981). This is unlike some layered continental intrusions where single layers can be traced for kilometers or more. Many would also argue that slow-spreading magma chamber dimensions are small, so attempts to correlate are not warranted. Rather, it is probably better to think of the oxide-rich zones in terms of process and as a facies within the magma chamber complex where likely a strong chilled margin along the chamber wall allowed magma characteristics of the interior of the chamber (more primitive magmas) to become intimately intermixed with highly fractionated ferrobasalts formed at the external side of a boundary layer and where boundary layer liquids may be mobile. The boundary layer may be affected by repeated injections, eruption events, and internal small-scale convection and may itself erode and rebuild from time to time. Boundary layer fractionation may help to explain why oxide gabbros seemingly form at elevated Mg#s in the magma chamber complex and may be similar to other intrusions where "apparent" early oxide precipitation has been documented. Thus, we suggest that the processes in both holes may be the same, and, in fact, if the oxide-rich units are regarded as facies within the chamber complex, the broadly defined oxide units may correlate and continue laterally across the 1.2 km between them. This may also provide some constraint on chamber size, but there is no constraint available to suggest that zones crystallized simultaneously, and this seems unlikely. A series of short holes between the two sites may verify continuity, especially considering the many structural complications and shear zones that cut the sections.

SUMMARY AND CONCLUSIONS

Gabbroic to granophyric rocks sampled and analyzed in this study show complex chemical and lithologic stratigraphies with highly fractionated oxide gabbroic rocks intimately interlayered with more primitive gabbro and olivine gabbro. Both normal and inverse cryptic geochemical trends exist downhole through the core. The vertical

chemical stratigraphy does not appear significantly affected (reequilibrated) by porous late melt migration through the cumulate pile except locally along narrow late melt flow zones that upset the mineral chemistry within a single thin section. Chemical variation in all silicate minerals correlates well downhole. Geochemistry appears to document significant melt trapped within the many samples in the cumulate pile, although textural evidence of trapped melt is not abundant in the form of highly zoned minerals. The trapped melt abundance overall is similar to upper isotropic gabbroic rocks in the ophiolite complexes, possibly suggesting the rocks crystallized in the upper plutonic crust or near the roof zone of a magma chamber complex. The most primitive rock silicate minerals are not near equilibrium with mantle, indicating significant fractionation of magmas took place prior to crystallization of the most primitive gabbroic rocks in the section. The bulk average major element chemistry of the core may be close to the regional basaltic average, but bulk rock incompatible element averages of the core are significantly depleted with respect to the basaltic average, helping to demonstrate that the plutonic rocks solidified as cumulates and not as congealed liquids or average of any basaltic liquid.

Oxide-rich and primitive oxide-free gabbroic rocks are intimately interlayered in the Hole 1105A section on a small scale, as demonstrated by FMS images (Miller et al., [Chap. 3](#), this volume). Likewise, cryptic chemical variations show extreme fine-scale variations (scales of tens of meters or less). The mechanism of boundary layer fractionation may help to explain this complex juxtaposition, as simple perfect fractional crystallization fails to explain the rock chemistries observed or their complex juxtaposition, unless the model of Dick et al. (2002) is used, which assumes that highly allocthonous late-stage melts infiltrate primitive gabbro of any composition in the cumulate pile as melts rise from below, predominantly along shear zones. This is a plausible explanation, but we find that, in general, oxides are present where silicate phases are highly fractionated and we also question why late-stage and dense iron-rich melts would rise from below through thick cumulate sections. Silicate mineral evidence shows that their fractionation state is not high enough to have caused precipitation of oxides utilizing a PFX model. A boundary layer fractionation model could produce the complex juxtaposition of rocks if the interior of the chamber was more primitive and the exterior of the boundary layer was strongly fractionated. Local melt migration of dense ferrobaltic melts could explain certain melt flow zones, reaction relationships, and cross-cutting oxide lenses noted in both Holes 1105A and 735B. Reaction between an evolved melt and existing silicate minerals could cause silicate compositions to reequilibrate partially to more evolved compositions and precipitate oxides, but as shown, in some cases the residual melt phase would have to be somehow eliminated from the sample to explain the low incompatible element abundances. The boundary layer model would not have these constraints, as the residual liquid could migrate to the main part of the chamber.

Crystal-plastic deformation textures indicate increasing strain downhole in oxide-rich gabbroic rocks, and this strain appears localized dominantly, although not exclusively, where abundant oxides are present. This may indicate that strain localization in the section is related to the weak rheology of the oxide minerals or a melt phase that precipitated abundant oxides as they penetrated through the cumulate section. The high-temperature subsolidus textural overprint makes it impossible to identify a hypersolidus development phase in shear zone formation

through the section. The nature of the progression of recrystallization and microstructural development during high-temperature crystal-plastic deformation in the gabbroic section suggests that the strongest to weakest minerals are in the progression from clinopyroxene to olivine to plagioclase and opaque Fe-Ti oxides. Plagioclase is a more significantly recrystallized silicate phase, more than olivine or clinopyroxene in moderately strained rocks, and clinopyroxene is the dominant porphyroclastic phase in highly deformed rocks. Synkinematic brown amphibole rimming clinopyroxene porphyroclasts and replacing neoblasts suggests the shear zones undergo high-temperature hydration during deformation and that plagioclase rheology may be affected by these hydrating fluids. Significant clinopyroxene recrystallization is observed only in highly strained rocks. Several mylonite zones have been identified in the section, and some are associated with large excursions in mineral and whole-rock chemistry. One shear zone examined appears to lack evidence of having abundant trapped melt, although the adjacent undeformed olivine gabbro shows abundant trapped melt.

As is typical of studies of plutonic sections, significant questions raised and remaining concern the igneous and structural evolution of the rocks in both Holes 1105A and 735B. Whether extensive oxide-rich zones originated within boundary layers at the edges of magma chambers or, alternatively, deep within a cumulate pile where porous flow allowed evolved intercumulus melts to infiltrate and precipitate oxides is a question that remains. The evidence presented here indicates that either may be a viable explanation but that neither can be excluded. Another related question is a classic chicken-and-egg argument of whether the oxide-rich zones that have undergone deformation are indicators of hypersolidus flow within shear zones where evolved melts accumulated and precipitated oxides or are zones where cumulate crystallization processes led to oxide precipitation within a boundary layer and creation of weak rheologic zones in the solid. In the solid state, the weaker rheology of oxide-rich zones could have acted to localize subsolidus strain as the core complex evolved and was structurally modified, partially hydrated along localized shear zones, cooled, and unroofed.

The ability to examine the short section of gabbro in Hole 1105A in the context of studies of Hole 735B allows extensive comparisons. To date, the bulk of the evidence suggests that the oxide-rich zones in both holes can be correlated laterally, if not necessarily physically, in terms of the processes that produced them. A series of short holes drilled between Hole 1105A and Hole 735B may help to answer further questions about the framework and size of subaxial magma chambers and the magmatic and structural processes operative in plutonic complexes unroofed at slow spreading centers.

ACKNOWLEDGMENTS

The authors would like to thank the officers and crew of the *JOIDES Resolution*, particularly Captain Anthony Ribbens, who made all possible efforts to effect the at-sea transfer of hammer drilling equipment in high seas, quickly adapted to the Hole 1105A contingency drilling plan during Leg 179, and successfully completed leg objectives at the Atlantis Bank and NERO sites. The authors also thank the ODP shipboard staff for their assistance during the cruise. We appreciate the reviewers who provided valuable and challenging input into this paper. In particular, one of the reviewers put considerable effort into detailed sugges-

tions for improving the text of the manuscript. Special thanks to Jay Miller, the ODP shipboard staff scientist, who ably managed the details of Leg 179 and helped devise the plan for contingency drilling of Hole 1105A. The authors also appreciate stimulating discussions on the origins of cumulate rocks and oceanic gabbroic massifs and magma chamber processes over the years with Bill Bryan, John Dewey, Henry Dick, Jeff Karson, Bill Kidd, Peter Meyer, and Leg 179 shipboard scientists Jay Miller, Tsugio Shibata, and Peter Thy.

REFERENCES

- Agar, S.M., Casey, J.F., and Kempton, P.D., 1997. Textural, geochemical, and isotopic variations in gabbroic shear zones from the MARK area. *In* Karson, J.A., Cannat, M., Miller, D.J., and Elthon, D. (Eds.), *Proc. ODP, Sci. Results*, 153: College Station, TX (Ocean Drilling Program), 99–121.
- Agar, S.M., and Lloyd, G.E., 1997. Deformation of Fe-Ti oxides in gabbroic shear zones from the MARK area. *In* Karson, J.A., Cannat, M., Miller, D.J., and Elthon, D. (Eds.), *Proc. ODP, Sci. Results*, 153: College Station, TX (Ocean Drilling Program), 123–141.
- Anders, E., and Grevesse, N., 1989. Abundances of the elements: meteoritic and solar. *Geochim. Cosmochim. Acta*, 53(1):197–214. doi:10.1016/0016-7037(89)90286-X
- Atkins, F.B., 1969. Pyroxenes of the Bushveld intrusion. *J. Petrol.*, 10:222–249.
- Baines, A.G., Cheadle, M.J., Dick, H.J.B., Scheirer, A.H., John, B.E., Kuszniir, N.J., and Matsumoto, T., 2003. Mechanism for generating the anomalous uplift of oceanic core complexes: Atlantis Bank, Southwest Indian Ridge. *Geology*, 31(12):1105–1108. doi:10.1130/G19829.1
- Banerji, D., 2005. Geochemistry of gabbroic rocks, Hole 1105A, Leg 179, Atlantis II Fracture Zone, Southwest Indian Ridge (SWIR): formation of oceanic crust at an ultraslow spreading ridge. [Ph. D. dissert.], Univ. Houston, Texas.
- Blundy, J., and Wood, B., 1994. Prediction of crystal-melt partition coefficients from elastic moduli. *Nature (London, U. K.)*, 372(6505):452–454. doi:10.1038/372452a0
- Brown, G.M., 1957. Pyroxenes from the early and middle stages of fractionation of the Skaergaard intrusion, east Greenland. *Mineral. Mag.*, 31(238):511–543.
- Campbell, I.H., 1978. Some problems with the cumulus theory. *Lithos*, 11(4):311–323. doi:10.1016/0024-4937(78)90038-5
- Campbell, I.H., 1996. Fluid dynamic processes in basaltic magma chambers. *In* Cawthor, R.G. (Ed.), *Layered Intrusions*: New York: (Elsevier), 45–76.
- Campbell, I.H., and Nolan, J., 1974. Factors effecting the stability field of Ca-poor pyroxene and the origin of the Ca-poor minimum in Ca-rich pyroxenes from tholeiitic intrusions. *Contrib. Mineral. Petrol.*, 48(3):205–219. doi:10.1007/BF00383356
- Cannat, M., 1991. Plastic deformation at an oceanic spreading ridge: a microstructural study of Site 735 gabbros (southwest Indian Ocean). *In* Von Herzen, R.P., Robinson, P.T., et al., *Proc. ODP, Sci. Results*, 118: College Station, TX (Ocean Drilling Program), 399–408. doi:10.2973/odp.proc.sr.118.134.1991
- Cannat, M., 1996. How thick is the magmatic crust at slow spreading oceanic ridges? *J. Geophys. Res.*, 101(B2):2847–2858. doi:10.1029/95JB03116
- Cannat, M., and Casey, J.F., 1995. An ultramafic lift at the Mid-Atlantic Ridge: successive stages of magmatism in serpentinized peridotites from the 15°N region. *In* Visers, R.L.M., and Nicolas, A. (Eds.), *Mantle and Lower Crust Exposed in Oceanic Ridges and Ophiolites*: Dordrecht (Kluwer), 5–34.
- Cannat, M., Karson, J.A., Miller, D.J., et al., 1995. *Proc. ODP, Init. Repts.*, 153: College Station, TX (Ocean Drilling Program).
- Cannat, M., Lagabriele, Y., Bougault, H., Casey, J., de Coutures, N., Dmitriev, L., and Fouquet, Y., 1997. Ultramafic and gabbroic exposures at the Mid-Atlantic Ridge: geological mapping in the 15°N region. *Tectonophysics*, 279:193–213. doi:10.1016/S0040-1951(97)00113-3
- Casey, J.F., 1997. Comparison of major- and trace-element geochemistry of abyssal peridotites and mafic plutonic rocks with basalts from the MARK region of the Mid-Atlantic Ridge. *In* Karson, J.A., Cannat, M., Miller, D.J., and Elthon, D. (Eds.), *Proc. ODP, Sci. Results*, 153: College Station, TX (Ocean Drilling Program), 181–241.
- Casey, J.F., Dewey, J.F., Fox, P.J., Karson, J.A., and Rosencrantz, E., 1981. Heterogeneous nature of oceanic crust and upper mantle: a perspective from the Bay of

- Islands ophiolite complex. In Emiliani, C. (Ed.), *The Sea* (Vol. 7) *The Oceanic Lithosphere*: New York (Wiley), 305–338.
- Casey, J.F., and Karson, J.A., 1981. Magma chamber profiles from the Bay of Islands ophiolite complex. *Nature (London, U. K.)*, 292:295–301.
- Coogan, L.A., Kempton, P.D., Saunders, A.D., and Norry, M.J., 2000. Melt aggregation within the crust beneath the Mid-Atlantic Ridge: evidence from plagioclase and clinopyroxene major and trace element compositions. *Earth Planet. Sci. Lett.*, 176(2):245–257. doi:10.1016/S0012-821X(00)00006-6
- Coogan, L.A., MacLeod, C.J., Dick, H.J.B., Edwards, S.J., Kvassnes, A., Natland, J.H., Robinson, P.T., Thompson, G., and O'Hara, M.J., 2001. Whole-rock geochemistry of gabbros from the Southwest Indian Ridge: constraints on geochemical fractionations between the upper and lower oceanic crust and magma chamber processes at (very) slow-spreading ridges. *Chem. Geol.*, 178(1–4): 1–22. doi:10.1016/S0009-2541(00)00424-1
- Dick, H.J.B., MacLeod, C.J., Robinson, P.T., Allerton, S., and Tivey, M.A., 1999. Bathymetry of Atlantis Bank—Atlantis II Fracture Zone: Southwest Indian Ridge. In Dick, H.J.B., Natland, J.H., Miller, D.J., et al., *Proc. ODP, Init. Repts.*, 176: College Station, TX (Ocean Drilling Program), 1–13. doi:10.2973/odp.proc.ir.176.104.1999
- Dick, H.J.B., Meyer, P.S., Bloomer, S., Kirby, S., Stakes, D., and Mawer, C., 1991. Lithostratigraphic evolution of an in-situ section of oceanic Layer 3. In Von Herzen, R.P., Robinson, P.T., et al., *Proc. ODP, Sci. Results*, 118: College Station, TX (Ocean Drilling Program), 439–538. doi:10.2973/odp.proc.sr.118.128.1991
- Dick, H.J.B., Natland, J.H., Alt, J.C., Bach, W., Bideau, D., Gee, J.S., Haggas, S., Hertogen, J.G.H., Hirth, G., Holm, P.M., Ildefonse, B., Iturrino, G.J., John, B.E., Kelley, D.S., Kikawa, E., Kingdon, A., LeRoux, P.J., Maeda, J., Meyer, P.S., Miller, D.J., Naslund, H.R., Niu, Y.-L., Robinson, P.T., Snow, J., Stephen, R.A., Trimby, P.W., Worm, H.-U., and Yoshinobu, A., 2000. A long in situ section of the lower ocean crust: results of ODP Leg 176 drilling at the Southwest Indian Ridge. *Earth Planet. Sci. Lett.*, 179:31–51. doi:10.1016/S0012-821X(00)00102-3
- Dick, H.J.B., Natland, J.H., Miller, D.J., et al., 1999. *Proc. ODP, Init. Repts.*, 176: College Station, TX (Ocean Drilling Program). doi:10.2973/odp.proc.ir.176.1999
- Dick, H.J.B., Ozawa, K., Meyer, P.S., Niu, Y., Robinson, P.T., Constantin, M., Hebert, R., Natland, J.H., Hirth, G., and Mackie, S.M., 2002. Primary silicate mineral chemistry of a 1.5-km section of very slow spreading lower ocean crust: ODP Hole 735B, Southwest Indian Ridge. In Natland, J.H., Dick, H.J.B., Miller, D.J., and Von Herzen, R.P. (Eds.), *Proc. ODP, Sci. Results*, 176: College Station, TX (Ocean Drilling Program), 1–60. doi:10.2973/odp.proc.sr.176.001.2002
- Dick, H.J.B., Robinson, P.T., and Meyer, P.S., 1992. The plutonic foundation of a slow-spreading ridge. In Duncan, R., Rea, D., Kidd, R., von Rad, U., and Weissel, J. (Eds.), *Synthesis of Results from Scientific Drilling in the Indian Ocean*. Geophys. Monogr., 70:1–39.
- Engel, C.G., and Fisher, R.L., 1975. Granitic to ultramafic rock complexes of the Indian Ocean Ridge system, western Indian Ocean. *Geol. Soc. Am. Bull.*, 86(11):1553–1578. doi:10.1130/0016-7606(1975)86<1553:GTURCO>2.0.CO;2
- Fisher, R.L., and Sclater, J.G., 1983. Tectonic evolution of the southwest Indian Ocean since the mid-Cretaceous: plate motions and stability of the pole of Antarctica/Africa for at least 80 Myr. *Geophys. J. R. Astron. Soc.*, 73:553–576.
- Fox, P.J., and Gallo, D.G., 1984. A tectonic model for Ridge-Transform-Ridge plate boundaries: implications for the structure of oceanic lithosphere. *Tectonophysics*, 104(3–3):205–242. doi:10.1016/0040-1951(84)90124-0
- Gillis, K., Mével, C., Allan, J., et al., 1993. *Proc. ODP, Init. Repts.*, 147: College Station, TX (Ocean Drilling Program).
- Gillis, K.M., 1996. Rare earth element constraints on the origin of amphibole in gabbroic rocks from Site 894, Hess Deep. In Mével, C., Gillis, K.M., Allan, J.F., and

- Meyer, P.S. (Eds.), *Proc. ODP, Sci. Results*, 147: College Station, TX (Ocean Drilling Program), 59–75.
- Grove, T.L., and Bryan, W.B., 1983. Fractionation of pyroxene-phyric MORB at low pressure: an experimental study. *Contrib. Mineral. Petrol.*, 84:293–309. doi:10.1007/BF01160283
- Hart, S.R., Blusztajn, J., Dick, H.J.B., Meyer, P.S., and Muehlenbachs, K., 1999. The fingerprint of seawater circulation in a 500-meter section of ocean crust gabbros. *Geochim. Cosmochim. Acta*, 63(23–24):4059–4080. doi:10.1016/S0016-7037(99)00309-9
- Hertogen, J., Emmermann, R., Robinson, P.T., and Erzinger, J., 2002. Lithology, mineralogy, and geochemistry of the lower ocean crust, ODP Hole 735B, Southwest Indian Ridge. In Natland, J.H., Dick, H.J.B., Miller, D.J., and Von Herzen, R.P. (Eds.), *Proc. ODP, Sci. Results*, 176: College Station, TX (Ocean Drilling Program), 1–82. doi:10.2973/odp.proc.sr.176.003.2002
- Hill, E., Wood, B.J., and Blundy, J.D., 2000. The effect of Ca-Tschermaks component on trace element partitioning between clinopyroxene and silicate melt. *Lithos.*, 53(3–4):203–215. doi:10.1016/S0024-4937(00)00025-6
- Holloway, G.L., and Shipboard Scientific Party, 2001. Hammer-drill sites (1180–1182). In Kanazawa, T., Sager, W.W., Escutia, C., et al., *Proc. ODP, Init. Repts.*, 191: College Station, TX (Ocean Drilling Program), 1–47. doi:10.2973/odp.proc.ir.191.105.2001
- Hosford, A., Tivey, M., Matsumoto, T., Dick, H., Schouten, H., and Kinoshita, H., 2003. Crustal magnetization and accretion at the Southwest Indian Ridge near the Atlantis II Fracture Zone, 0–25 Ma. *J. Geophys. Res.*, 108:2169. doi:10.1029/2001JB000604
- Irvine, T.N., 1970. Crystallization sequences in the Muskox intrusion and other layered intrusions. I. Olivine-pyroxene-plagioclase relations. In Visser, D.J.L., and Von Bruenewaldt, G. (Eds.), *Symposium on the Bushveld Igneous Complex and Other Layered Intrusions*. Spec. Publ.—Geol. Soc. S. Africa, 1:441–476.
- Irvine, T.N., 1979. Rocks whose composition is determined by crystal accumulation and sorting. In Yoder, H.S. (Ed.) *The Evolution of the Igneous Rocks*: Princeton, NJ: (Princeton Univ. Press), 245–306.
- Irvine, T.N., 1980. Magmatic infiltration metasomatism, double-diffusive fractional crystallization, and adcumulus growth in the Muskox intrusion and other layered intrusions. In Hargraves, R.B. (Ed.), *Physics of Magmatic Processes*: Princeton, NJ (Princeton Univ. Press), 325–384.
- Irvine, T.N., 1982. Terminology for layered intrusions. *J. Petrol.*, 23:127–162.
- Irvine, T.N., and Baragar, W.R.A., 1971. A guide to the chemical classification of the common volcanic rocks. *Can. J. Earth Sci.*, 8:523–548.
- Iturrino, G.J., Ildefonse, B., and Boitnott, G., 2002. Velocity structure of the lower oceanic crust: results from Hole 735B, Atlantis II Fracture Zone. In Natland, J.H., Dick, H.J.B., Miller, D.J., and Von Herzen, R.P. (Eds.), *Proc. ODP, Sci. Results*, 176: College Station, TX (Ocean Drilling Program), 1–71. doi:10.2973/odp.proc.sr.176.018.2002
- Jackson, E.D., 1961. Primary textures and mineral associations in the ultramafic zone of the Stillwater complex, Montana. *Geol. Surv. Prof. Pap. U.S.*, 358.
- Johnson, K.T.M., and Dick, H.J.B., 1992. Open system melting and temporal and spatial variation of peridotite and basalt at the Atlantis II Fracture Zone. *J. Geophys. Res.*, 97:9219–9241.
- Johnson, K.T.M., and Kinzler, R.J., 1989. Partitioning of REE, Ti, Zr, Hf, and Nb between clinopyroxene and basaltic liquid: an ion microprobe study. *Eos, Trans. Am. Geophys. Union*, 70:1388.
- Karson, J.A., Thompson, G., Humphris, S.E., Edmond, J.M., Bryan, W.B., Brown, J.R., Winters, A.T., Pockalny, R.A., Casey, J.F., Campbell, A.C., Klinkhammer, G., Palmer, M.R., Kinzler, R.J., and Sulanowska, M.M., 1987. Along-axis variations in seafloor spreading in the MARK area. *Nature (London, U. K.)*, 328:681–685.

- Karson, J.A., and Winters, A.T., 1992. Along-axis variations in tectonic extension and accommodation zones in the MARK area, Mid-Atlantic Ridge 23°N latitude: ophiolites and their modern oceanic analogues. *In* Parsons, L.M., Murton, B.J., and Browning, P. (Eds.), *Ophiolites and Their Modern Oceanic Analogues*. Spec. Publ.—Geol. Soc. London, 60:107–116.
- Kelemen, P.B., Koga, K., and Shimizu, N., 1997. Geochemistry of gabbro sills in the crust–mantle transition zone of the Oman ophiolite: implications for the origin of the oceanic lower crust. *Earth Planet. Sci. Lett.*, 146:475–488. doi:10.1016/S0012-821X(96)00235-X
- Korenaga, J., and Kelemen, P.B., 1998. Melt migration through the oceanic lower crust: a constraint from melt percolation modeling with finite solid diffusion. *Earth Planet. Sci. Lett.*, 156(1–2):1–11. doi:10.1016/S0012-821X(98)00004-1
- Langmuir, C.H., 1989. Geochemical consequences of in situ crystallization. *Nature (London, U. K.)*, 340(6230):199–205. doi:10.1038/340199a0
- Langmuir, C.H., Klein, E., and Plank, T., 1992. Petrological systematics of mid-ocean ridge basalts: constraints on melt generation beneath ocean ridges. *In* Morgan, J., Blackman, D., Sinton, J. (Eds.), *Mantle Flow and Melt Generation at Mid-Ocean Ridges*. Geophys. Monogr., 71:183–280.
- Lawver, L.A., and Dick, H.J.B., 1983. The American-Antarctic Ridge. *J. Geophys. Res.*, B, 88:8193–8202.
- Lindsley, D.H., and Munoz, J.L., 1969. Subsolidus relations along the join hedenbergite-ferrosilite. *Am. J. Sci.*, 267A:295–324.
- Lundstrom, C.C., Shaw, H.F., Ryerson, F.J., Williams, Q., and Gill, J., 1998. Crystal chemical control of clinopyroxene-melt partitioning in the Di-Ab-An system: implications for elemental fractionations in the depleted mantle. *Geochim. Cosmochim. Acta.*, 62(16):2849–2862. doi:10.1016/S0016-7037(98)00197-5
- MacLeod, C.J., Dick, H.J.B., Allerton, S., Robinson, P.T., Coogan, L.A., Edwards, S.J., Galley, A., Gillis, K.M., Hirth, G., Hunter, A.G., Hutchinson, D., Kvassnes, A.J., Natland, J.H., Salisbury, M., Schandl, E.S., Stakes, D.S., Thompson, G.M., and Tivey, M.A., 1998. Geological mapping of slow-spread lower ocean crust: a deep-towed video and wireline rock drilling survey of Atlantis Bank (ODP Site 735, SW Indian Ridge). *InterRidge News*, 7(2):39–43.
- Mathez, E.A., 1976. Sulfur solubility and magmatic sulfides in submarine basalt glass. *J. Geophys. Res.*, 81:4269–4276.
- McBirney, A.R., 1995. Mechanisms of differentiation in the Skaergaard intrusion. *J. Geol. Soc. (London, U. K.)*, 152:421–435.
- McBirney, A.R., and Noyes, R.M., 1979. Crystallization and layering of the Skaergaard intrusion. *J. Petrol.*, 20:487–554.
- Meyer, P.S., Dick, H.J.B., and Thompson, G., 1989. Cumulate gabbros from the Southwest Indian Ridge, 54°S–7°16'E: implications for magmatic processes at a slow spreading ridge. *Contrib. Mineral. Petrol.*, 103(1):44–63. doi:10.1007/BF00371364
- Miller, D.J., and Cervantes, P., 2002. Sulfide mineral chemistry and petrography and platinum group element composition in gabbroic rocks from the Southwest Indian Ridge. *In* Natland, J.H., Dick, H.J.B., Miller, D.J., and Von Herzen, R.P. (Eds.), *Proc. ODP, Sci. Results*, 176: College Station, TX (Ocean Drilling Program), 1–29. doi:10.2973/odp.proc.sr.176.009.2002
- Natland, J.H., 2002. Magnetic susceptibility as an index of the lithology and composition of gabbros, ODP Leg 176, Hole 735B, Southwest Indian Ridge. *In* Natland, J.H., Dick, H.J.B., Miller, D.J., and Von Herzen, R.P. (Eds.), *Proc. ODP, Sci. Results*, 176: College Station, TX (Ocean Drilling Program), 1–69. doi:10.2973/odp.proc.sr.176.008.2002
- Natland, J.H., and Dick, H.J.B., 2002. Stratigraphy and composition of gabbros drilled at Ocean Drilling Program Hole 735B, Southwest Indian Ridge: a synthesis of geochemical data. *In* Natland, J.H., Dick, H.J.B., Miller, D.J., and Von Herzen, R.P. (Eds.), *Proc. ODP, Sci. Results*, 176: College Station, TX (Ocean Drilling Program), 1–69. doi:10.2973/odp.proc.sr.176.002.2002

- Natland, J.H., Dick, H.J.B., Miller, D.J., and Von Herzen, R.P. (Eds.), 2002. *Proc. ODP, Sci. Results*, 176: College Station, TX (Ocean Drilling Program). doi:10.2973/odp.proc.sr.176.2002
- Natland, J.H., Meyer, P.S., Dick, H.J.B., and Bloomer, S.H., 1991. Magmatic oxides and sulfides in gabbroic rocks from Hole 735B and the later development of the liquid line of descent. In Von Herzen, R.P., Robinson, P.T., et al., *Proc. ODP, Sci. Results*, 118: College Station, TX (Ocean Drilling Program), 75–111. doi:10.2973/odp.proc.sr.118.163.1991
- Nielsen, R.L., and Delong, S.E., 1992. A numerical approach to boundary layer fractionation: application to differentiation in natural magma systems. *Contrib. Mineral. Petrol.*, 110(2–3):355–369. doi:10.1007/BF00310750
- Niu, Y., Gilmore, T., Mackie, S., Greig, A., and Bach, W., 2002. Mineral chemistry, whole-rock compositions, and petrogenesis of Leg 176 gabbros: data and discussion. In Natland, J.H., Dick, H.J.B., Miller, D.J., and Von Herzen, R.P. (Eds.), *Proc. ODP, Sci. Results*, 176: College Station, TX (Ocean Drilling Program), 1–60. doi:10.2973/odp.proc.sr.176.011.2002
- Norton, I.O., and Sclater, J.G., 1979. A model for the evolution of the Indian Ocean and the breakup of Gondwanaland. *J. Geophys. Res.*, 84:6803–6830.
- O’Hara, M.J., and Fry, N., 1996. The highly compatible trace element paradox; fractional crystallization revisited. *J. Petrol.*, 37(4):859–890.
- Oleson, N.Ø., 1987. Plagioclase fabric development in a high-grade shear zone, Jotunheimen, Norway. *Tectonophysics*, 142(2–4):291–308. doi:10.1016/0040-1951(87)90128-4
- Oleson, N.Ø., and Kohlsted, D.L., 1985. Natural deformation and recrystallization of intermediate feldspars. *Tectonophysics*, 190:31–53.
- Ozawa, K., Meyer, P.S., and Bloomer, S.H., 1991. Mineralogy and textures of iron-titanium oxide gabbros and associated olivine gabbros from Hole 735B. In Von Herzen, R.P., Robinson, P.T., et al., *Proc. ODP, Sci. Results*, 118: College Station, TX (Ocean Drilling Program), 41–73. doi:10.2973/odp.proc.sr.118.125.1991
- Pettigrew, T.L., Casey, J.F., Miller, D.J., et al., 1999. *Proc. ODP, Init. Repts.*, 179: College Station, TX (Ocean Drilling Program). doi:10.2973/odp.proc.ir.179.1999
- Ray, G.L., Shimizu, N., and Hart, S.R., 1983. An ion microprobe study of the partitioning of trace elements between clinopyroxene and liquid in the system diopside-albite-anorthite. *Geochim. Cosmochim. Acta*, 47(12):2131–2140. doi:10.1016/0016-7037(83)90038-8
- Roeder, P.L., and Emslie, R.F., 1970. Olivine-liquid equilibrium. *Contrib. Mineral. Petrol.*, 29(4):275–289. doi:10.1007/BF00371276
- Robinson, P.T., Von Herzen, R., et al., 1989. *Proc. ODP, Init. Repts.*, 118: College Station, TX (Ocean Drilling Program). doi:10.2973/odp.proc.ir.118.1989
- Schwartz, J.J., John, B.E., Cheadle, M.J., Miranda, E.A., Grimes, C.B., Wooden, J.L., and Dick, H.J.B. 2005. Dating the growth of oceanic crust at a slow-spreading ridge. *Science*, 310(5748):654–657. doi:10.1126/science.1116349
- Shipboard Scientific Party, 1999a. Explanatory notes. In Dick, H.J.B., Natland, J.H., Miller, D.J., et al., *Proc. ODP, Init. Repts.*, 176: College Station, TX (Ocean Drilling Program), 1–42. doi:10.2973/odp.proc.ir.176.102.1999
- Shipboard Scientific Party, 1999b. Explanatory notes. In Pettigrew, T.L., Casey, J.F., Miller, D.J., et al., *Proc. ODP, Init. Repts.*, 179: College Station, TX (Ocean Drilling Program), 1–47. doi:10.2973/odp.proc.ir.179.103.1999
- Shipboard Scientific Party, 1999c. Leg 179 summary. In Pettigrew, T.L., Casey, J.F., Miller, D.J., et al., *Proc. ODP, Init. Repts.*, 179: College Station, TX (Ocean Drilling Program), 1–26. doi:10.2973/odp.proc.ir.179.101.1999
- Shipboard Scientific Party, 1999d. Hammer Drill Site (1104 and 1106) and Site 1105. In Pettigrew, T.L., Casey, J.F., Miller, D.J., et al., *Proc. ODP, Init. Repts.*, 179: College Station, TX (Ocean Drilling Program), 1–183. doi:10.2973/odp.proc.ir.179.104.1999

- Smith, S.E., 1994. Geochemistry and petrology of basaltic and plutonic rocks from the Hayes Transform Region, Mid-Atlantic Ridge [Ph.D. dissert.]. Univ. of Houston, Houston, TX.
- Sparks, R.S.J., Huppert, H.E., and Turner, J.S., 1984. The fluid dynamics of evolving magma chambers. *Philos. Trans. R. Soc. London, Ser. A*, 310:511–534.
- Stolper, E., and Walker, D., 1980. Melt density and the average composition of basalt. *Contrib. Mineral. Petrol.*, 74(1):7–12. doi:10.1007/BF00375484
- Sun, S.-S., and McDonough, W.F., 1989. Chemical and isotopic systematics of oceanic basalts: implications for mantle composition and processes. In Saunders, A.D., and Norry, M.J. (Eds.), *Magmatism in the Ocean Basins*. Geol. Soc. Spec. Publ., 42:313–345.
- Tait, S.R., Huppert, H.E., and Sparks, R.S.J., 1984. The role of compositional convection in the formation of adcumulate rocks. *Lithos*, 17:139–146. doi:10.1016/0024-4937(84)90014-8
- Tapscott, C.R., Patriat, P., Fisher, R.L., Sclater, J.G., Hoskins, H., and Parsons, B., 1980. The Indian Ocean triple junction. *J. Geophys. Res.*, 85:4723–4739.
- Thy, P., and Dilek, Y., 2000. Magmatic and tectonic controls on the evolution of oceanic magma chambers at slow-spreading ridges: perspectives from ophiolitic and continental layered intrusions. *Spec. Pap.—Geol. Assoc. Am.*, 349:87–104.
- Tucholke, B.E., Lin, J., and Kleinrock, M.C., 1998. Megamullions and mullion structure defining oceanic metamorphic core complexes on the Mid-Atlantic Ridge. *J. Geophys. Res.*, 103(B5): 9857–9866. doi:10.1029/98JB00167
- Tucholke, B.E., Lin, J., Kleinrock, M.C., Tivey, M.A., Reed, T.B., Goff, J., and Jaroslow, G.E., 1997. Segmentation and crustal structure of the western Mid-Atlantic Ridge flank, 25°25′–27°10′N and 0–29 m.y. *J. Geophys. Res.*, 102(B5):10203–10224. doi:10.1029/96JB03896
- Wager, L.R., and Brown, G.M., 1967. *Layered Igneous Rocks*: San Francisco (W.H. Freeman).
- Walker, K.R., Ware, N.G., and Lovering, J.F., 1973. Compositional variations in the pyroxenes of the differentiated Palisades sill, New Jersey. *Geol. Soc. Am. Bull.*, 84(1):89–110. doi:10.1130/0016-7606(1973)84<89:CVITPO>2.0.CO;2
- White, S.H., 1975. Tectonic deformation and recrystallization of oligoclase. *Contrib. Mineral. Petrol.*, 50(4):287–304. doi:10.1007/BF00394854
- Wood, B.J., and Blundy, J.D., 1997. A predictive model for rare earth element partitioning between clinopyroxene and anhydrous silicate melt. *Contrib. Mineral. Petrol.*, 129(2–3):166–181. doi:10.1007/s004100050330
- Zarian, P., 2003. Integration of borehole imaging and microstructural analyses of plutonic rocks from Hole 1105A, ODP Leg 179, Southwest Indian Ridge. [M.S. thesis], Univ. Houston, Texas.
- Zarian, P., Casey, J.F., and Miller, D.J., 2002. Application of Formation MicroScanner log in structural analysis of an ultra-slow spreading environment, ODP Hole 1105A. *Eos, Trans. Am. Geophys. Union*, 83(47)(Suppl.):T22A-1137. (Abstract)

Figure F1. Modified satellite altimetry free-air gravity map displaying the Southwest Indian Ridge, Atlantis II Fracture Zone (A II Fault zone), and the locations of Holes 735B and 1105A (modified from Shipboard Scientific Party, 1999d). Inset shows Leg 179 drilling locations, the hammer drilling sites near Holes 735B and 1105A and along the Ninetyeast Ridge at Site 1107, where a hole was readied for a seismometer deployment.

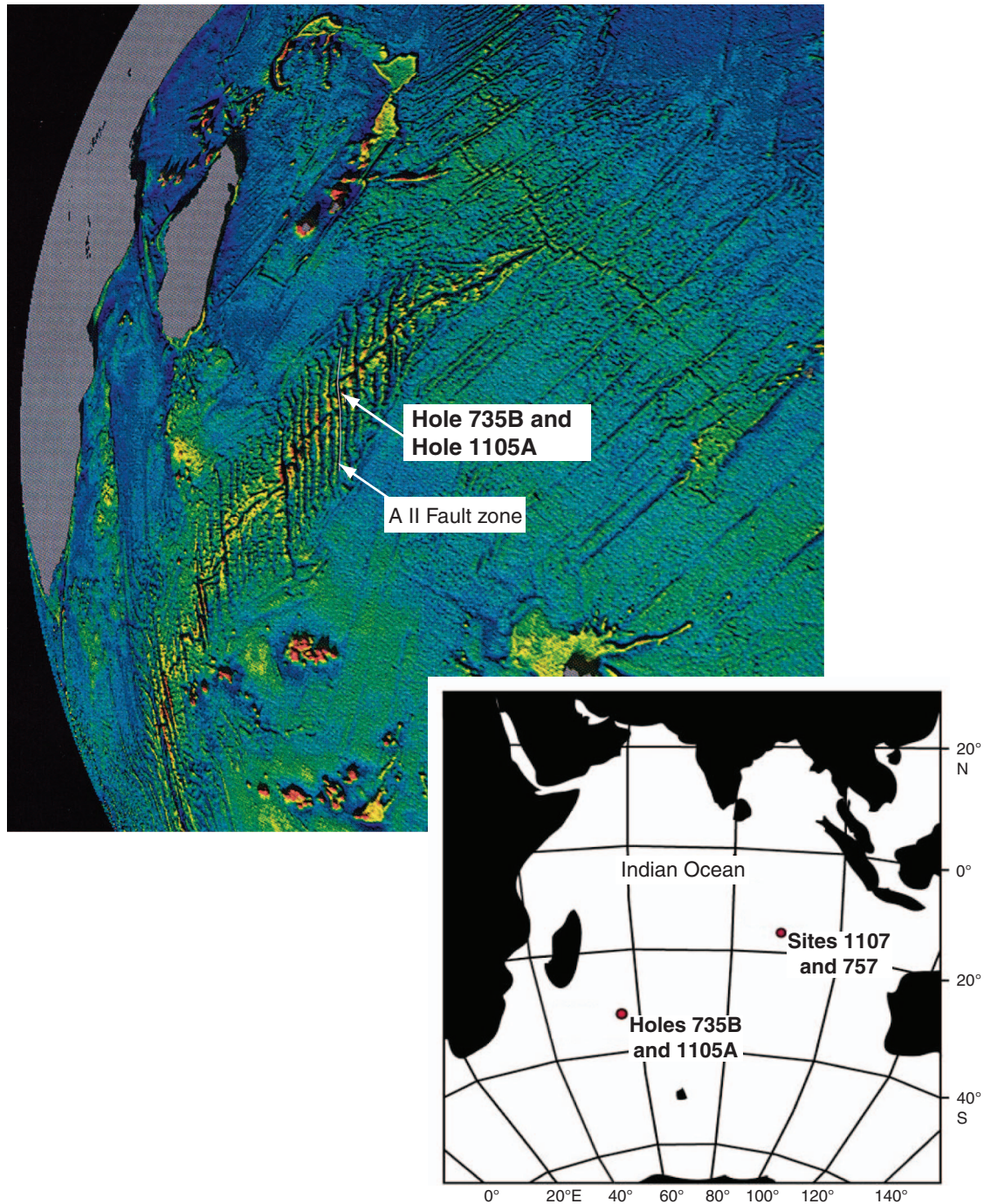


Figure F2. A. Three-dimensional shaded bathymetry of the Atlantis II Transform Fault, showing the northern and southern ridge transform intersection (NRTI and SRTI, respectively), and the median tectonic ridge in the transform. Locations of Hole 1105A and 735B atop the Atlantis Bank represent the highest point along the eastern transverse ridge of the Atlantis II Transform (bathymetric grid provided by H. Dick, pers. comm., 1999). **B.** Three-dimensional shaded-relief image of the Atlantis Bank (looking northeast) along the wall of the Atlantis II Transform Fault (data from Dick et al., 1991). Holes 1105A and 735B and the dimensions of the Atlantis Bank are also shown (modified from Shipboard Scientific Party, 1999c).

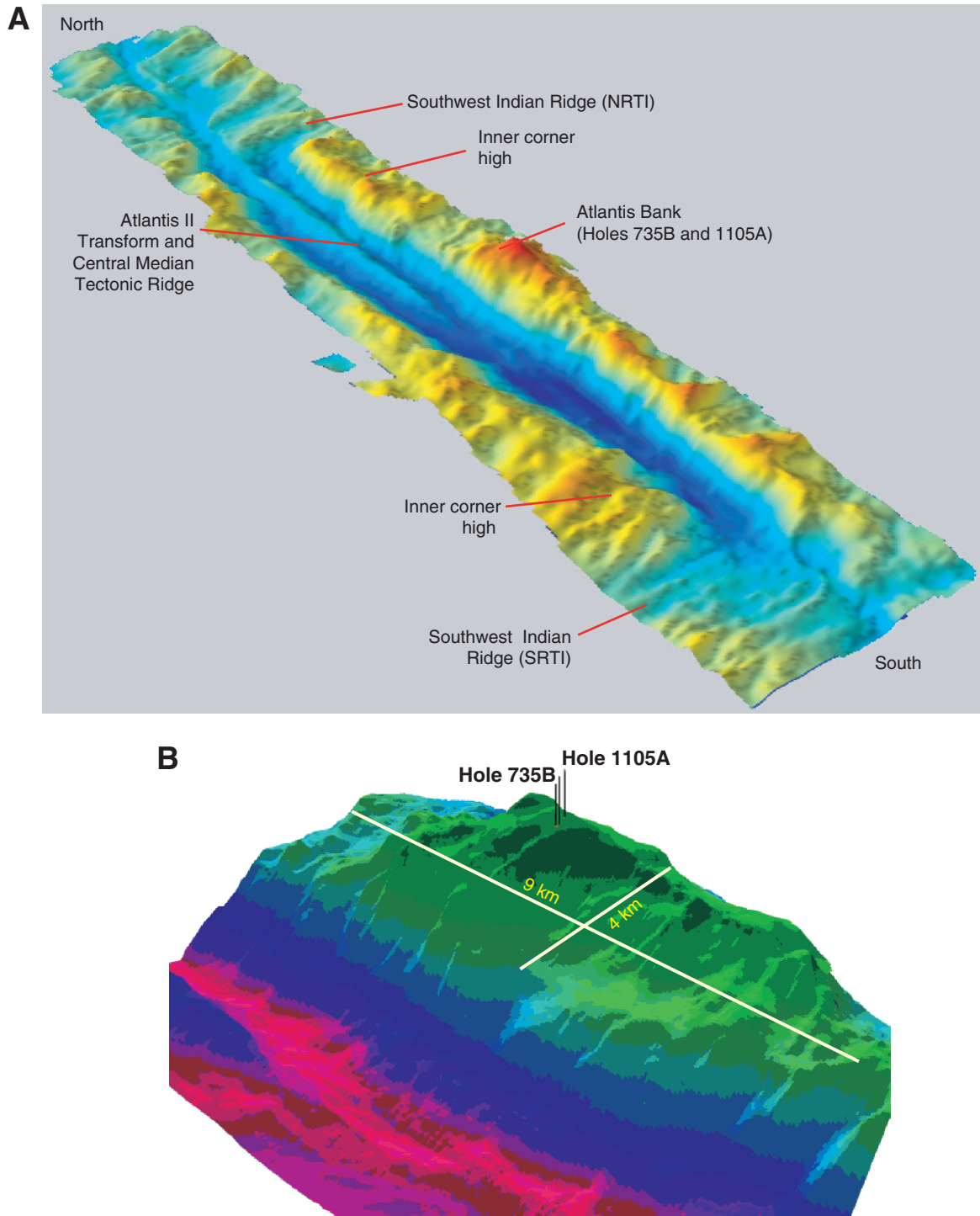


Figure F3. Bathymetric map of part of the Atlantis Bank (modified after Dick et al., 1999). Hole 735B was drilled during Legs 118 and 173, and Hole 1105A was drilled during Leg 179. Distance between holes is ~1.2 km.

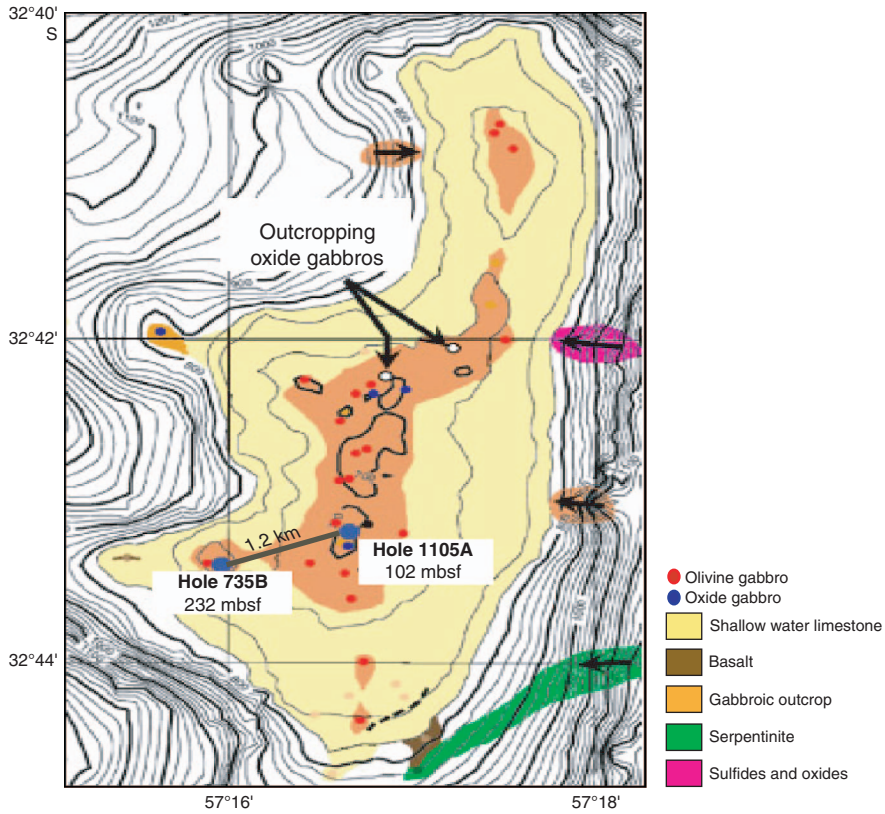


Figure F4. Three-dimensional bathymetric map draped with aspect of slope grid (middle image). Color changes depict changes in slope and slope direction yielding seafloor fabric elements. The map is constructed by first constructing a slope grid of bathymetry and then extracting an aspect map of the slope grid. Color changes mark maximum and minimum in slope and changes in slope direction. Aspect of slope has higher sensitivity in delineating even subtle seafloor fabric when compared to bathymetric contouring. Linearity of the color changes marks the orientation of major and minor bathymetric features or seafloor fabric elements. Red-green color changes indicate morphologic fabric elements that are ridge parallel, whereas blue-yellow color changes indicate morphological elements that are transform (spreading direction) parallel. Note pronounced yellow-blue spreading direction-parallel fabric elements within the transform and along and directly south of the Atlantis Bank on the western part of the transverse ridge. The latter fabric elements may represent corrugations of a core complex along which the lower oceanic crust sampled in Holes 735B and 1105A were exposed. The spreading direction-parallel fabric on the transverse ridge is overprinted by ridge-parallel seafloor fabric elements (multibeam grid provided courtesy of H. Dick and M. Tivey).

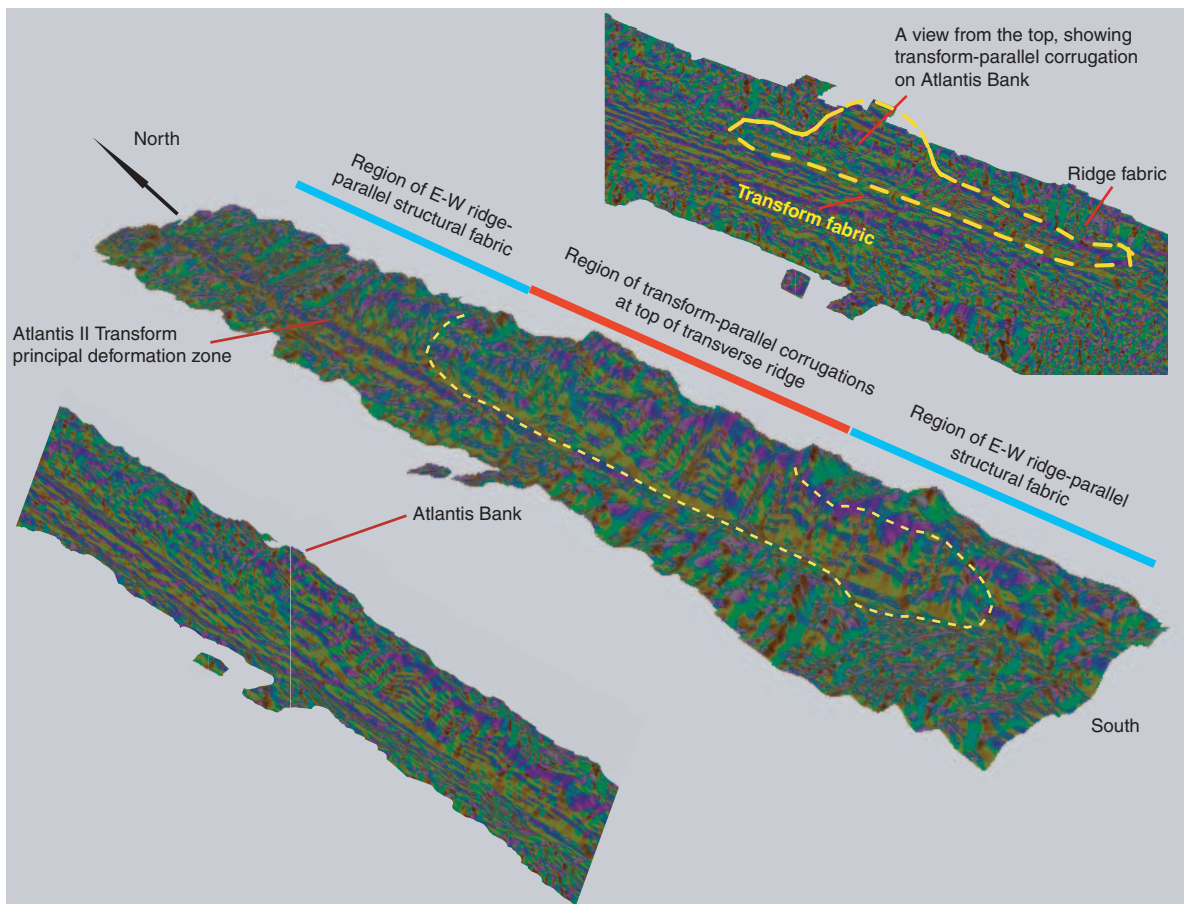


Figure F5. Summary of 142 visually defined lithologic intervals and large-scale units (I–IV) of Hole 1105A. Only the major lithologic rock types are illustrated (modified from Shipboard Scientific Party, 1999c).

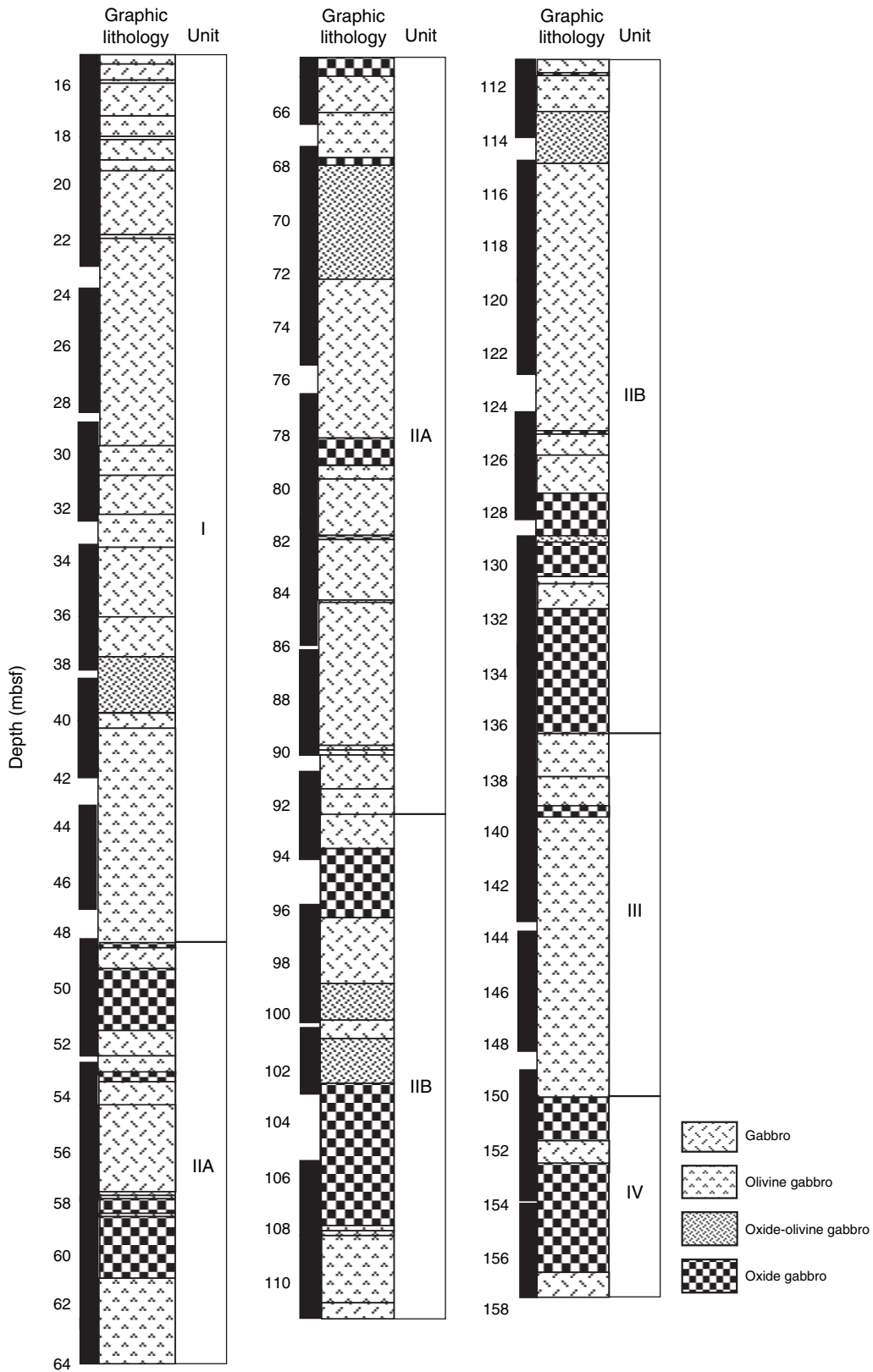


Figure F6. Example of Formation MicroScanner (FMS) image from Hole 1105A; core between 93 and 100 mbsf showing conductive and resistive features of the core and the ability to correlate features identified on the core barrel sheet (image from the Shipboard Scientific Party, 1999c). Also see Miller et al. (**Chap. 2**, this volume).

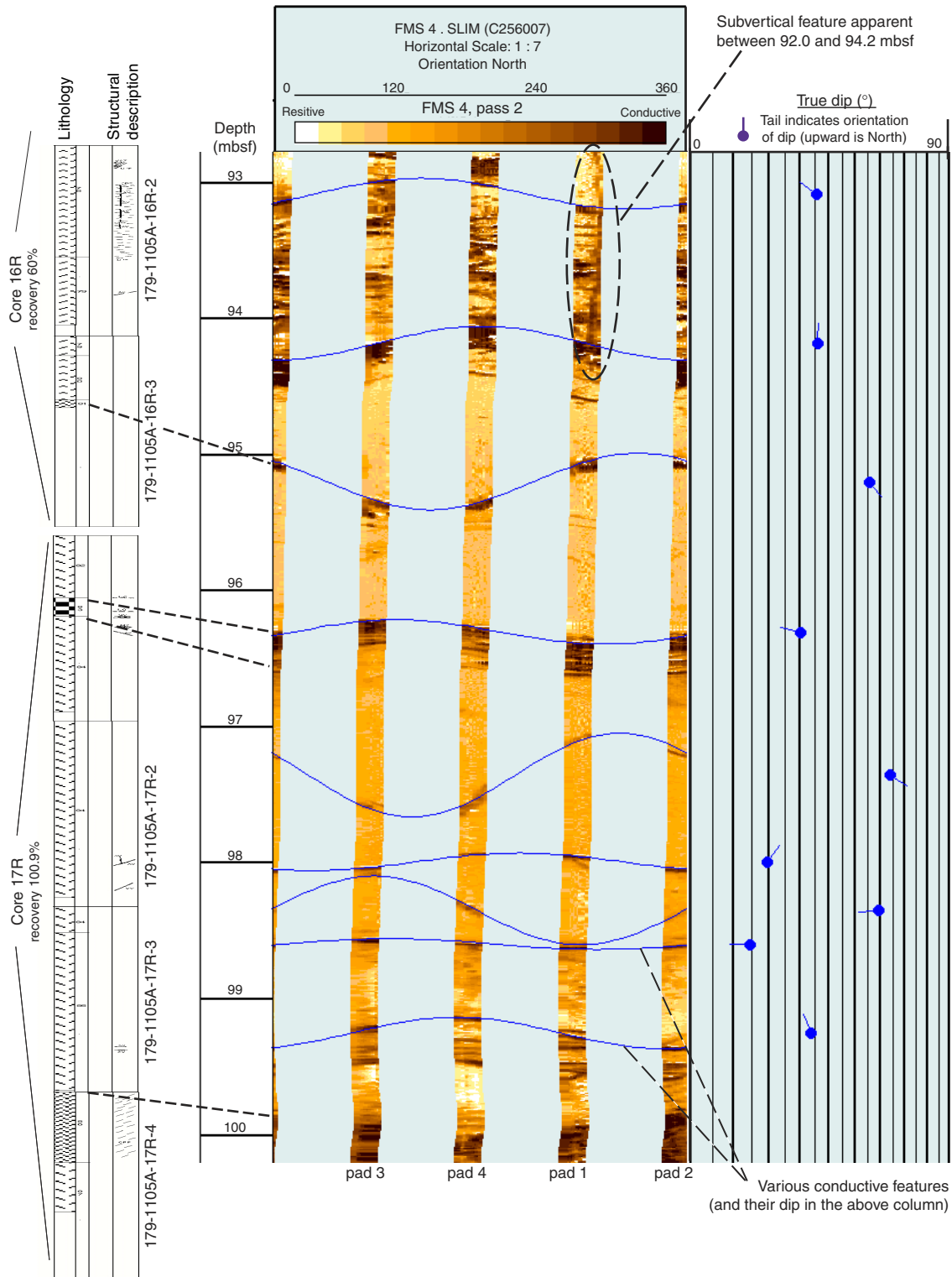


Figure F7. Distribution of igneous laminations, modal and grain-size layering, crystal-plastic foliation fabric, and felsic veins in Hole 1105A (modified from Shipboard Scientific Party, 1999c).

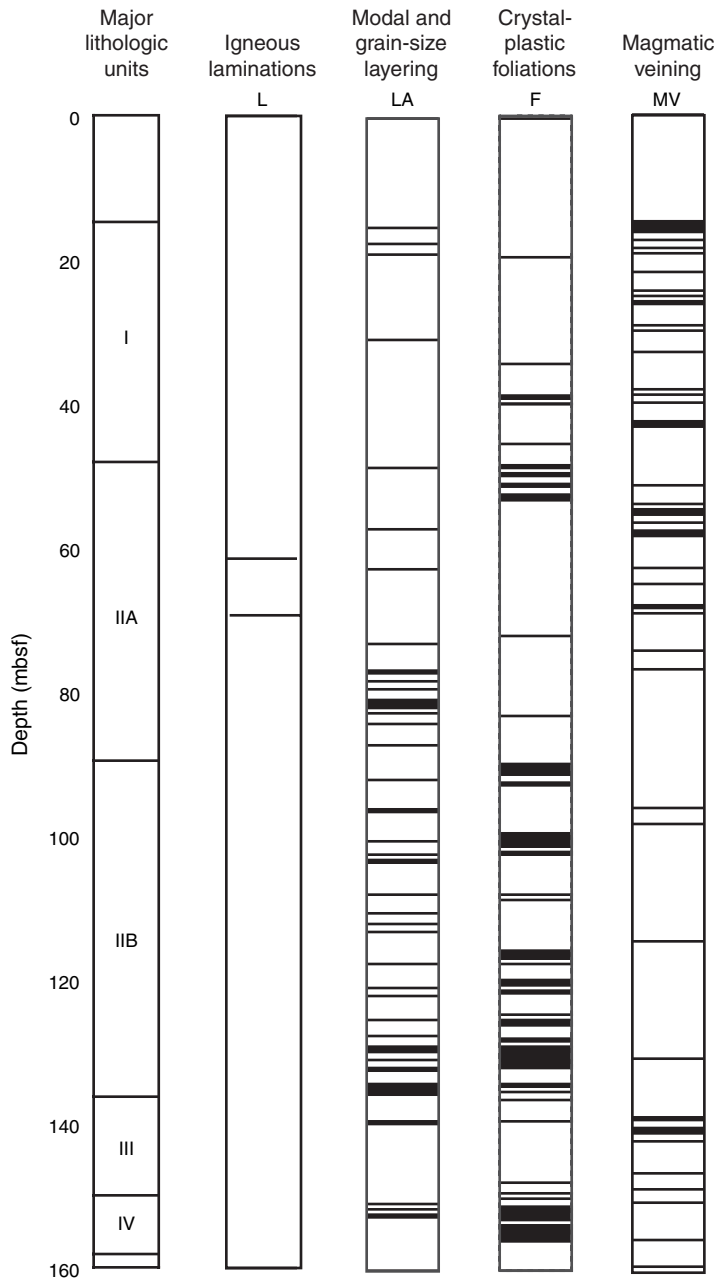


Figure F8. A. Schematic showing potential stratigraphic correlation between Holes 735B and 1105A. Initial correlation was based on similar magnetic susceptibility peak at depth 38.4 mbsf in Hole 1105A data and 212.5 mbsf in Hole 735B data. **B.** Comparison of magnetic susceptibilities between Holes 735B and 1105A. Unit IV of Hole 735B has high magnetic susceptibility, corresponding to oxide gabbros. This layer compares well in susceptibility and lithology to Subunits IIA and IIB of Hole 1105A. Small central diagram of Hole 1105A represents results at the same vertical scale as those of Hole 735B. The regional inclination (or apparent dip) of the oxide-rich zone, if correlatable, is $\sim 10^\circ$ along a line between the two holes.

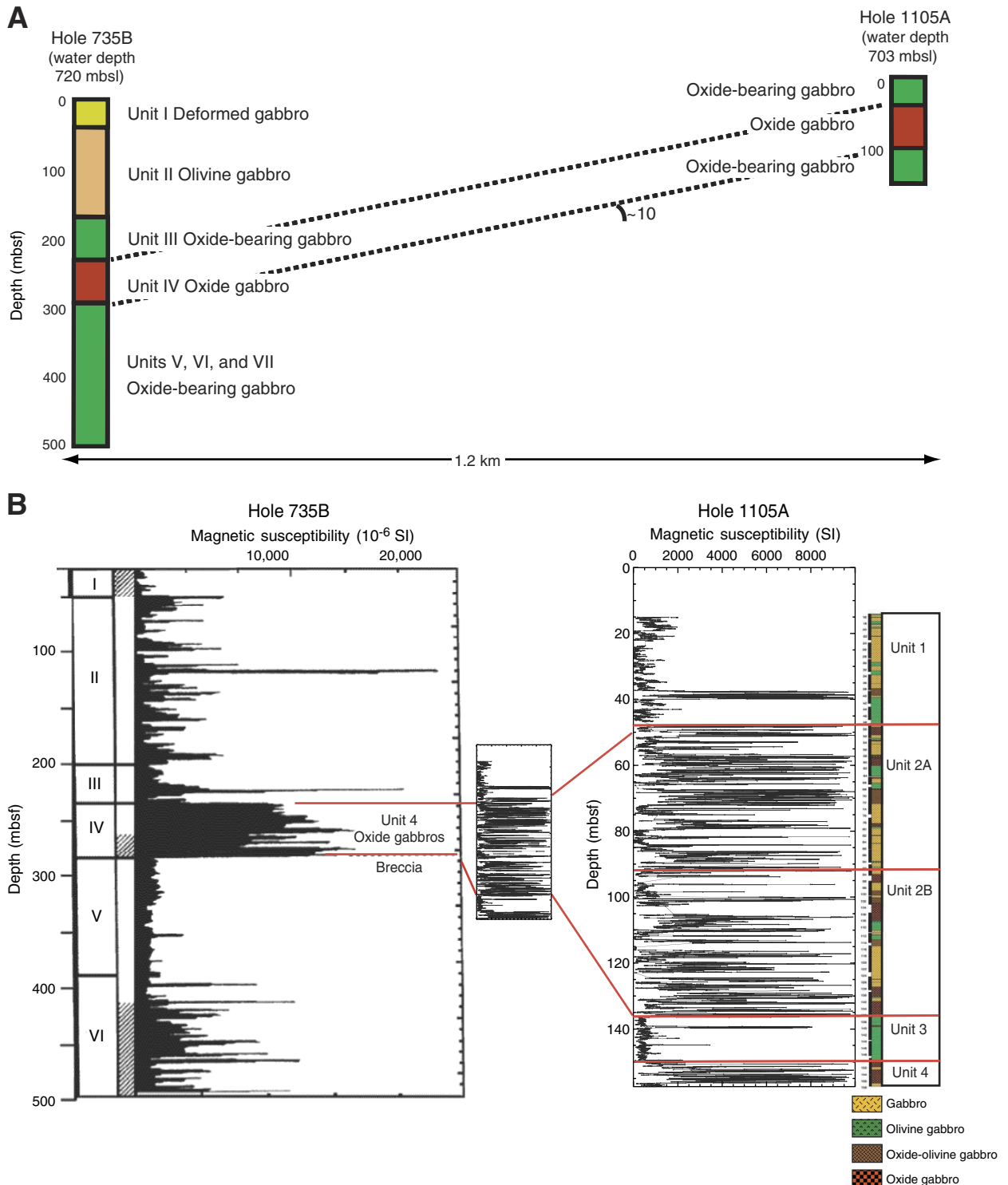
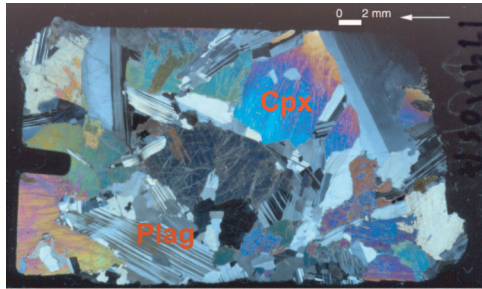


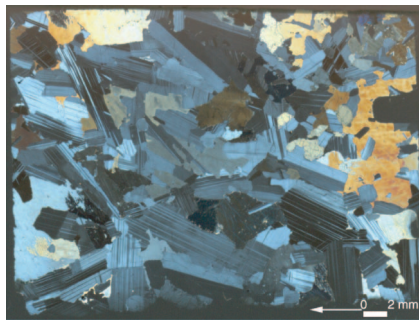
Figure F9. Thin section images from Hole 1105A of igneous cumulate texture. Full-section scans were made under cross-polarized light of all 135 samples and are presented in the volume **“Supplementary Material.”** Scale bars = 2 mm. Up arrows are included in scans; all are pointing in same direction. Modal analysis and microprobe work were conducted on all sections, and each billet was cut from a sample taken for whole-rock analysis. Certain sections utilized for whole-rock geochemical analysis were not available for scanning because of a vendor’s error.



**179-1105A-1R-6 (Piece 3, 33-36 cm)
Depth: 22.15 mbsf**



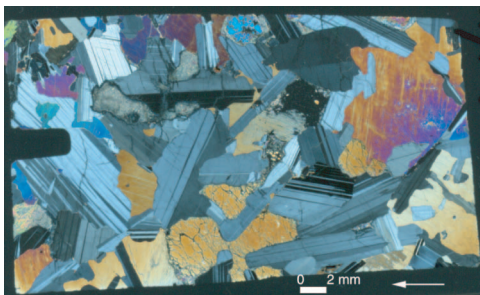
**179-1105A-3R-2 (Piece 11, 109-113 cm)
Depth: 31.29 mbsf**



**179-1105A-4R-3 (Piece 5, 90-93 cm)
Depth: 36.72 mbsf**



**179-1105A-7R-1 (Piece 1A, 19-24 cm)
Depth: 47.99 mbsf**



**179-1105A-14R-2 (Piece 8, 114-119 cm)
Depth: 83.55 mbsf**



**179-1105A-20R-1 (Piece 11, 111-117 cm)
Depth: 110.91 mbsf**

Figure F10. Histogram of the proportion of rock types analyzed from Hole 1105A, based on modal analysis. Olivine gabbros and gabbros are indicated as oxide-free (<0.1 mod% oxide), oxide bearing (0.1–4.9 mod% oxide), or oxide gabbros and oxide olivine gabbros (>5 mod% oxide). The naming of oxide gabbros and oxide olivine gabbros is in accordance to suggestions of the IUGS in using modifiers for plutonic rocks (i.e., accessory phases should be >5% modal abundance). Oxide-bearing was used for all rocks containing some oxides, but <5% oxides, in order to allow some comparison terminology with Leg 176 terminology in distinguishing between rocks with or without magmatic oxides. Note different terminology was used in Hole 1105A (Thy, [Chap. 3](#), this volume) and in Hole 735B (Dick, Natland, Miller, et al., 1999) descriptions (also see the Leg 176 and 179 “Explanatory Notes” chapters, Shipboard Scientific Party, 1999a, 1999b).

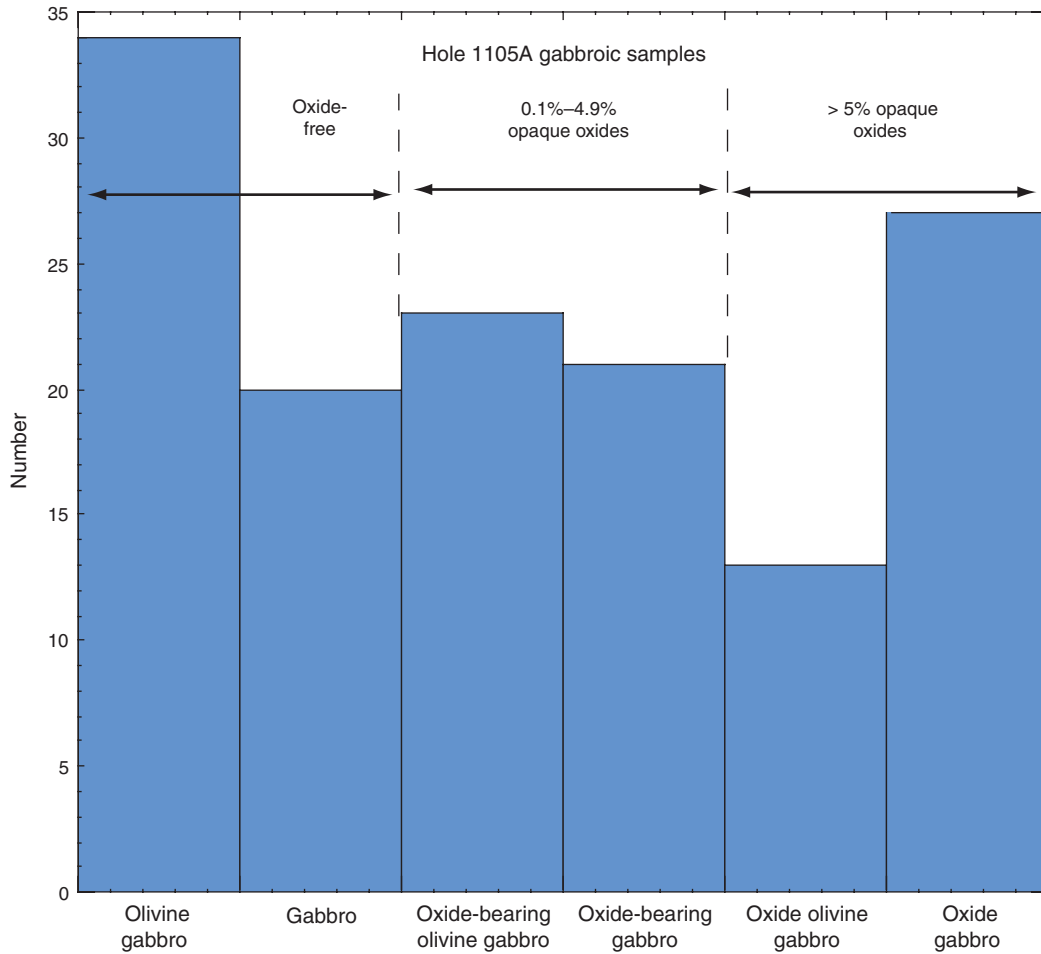


Figure F11. Modal distribution of primary minerals in Hole 1105A. Data collected during this study and that collected during Leg 179 shipboard studies are included. A total of 226 thin sections were used in the plot. Also plotted are the zones where mylonitic texture was observed in the thin section (see Fig. F9, p. 65). Note peaks in oxides (\pm orthopyroxene or inverted pigeonite) occur approximately every 10 m through the section.

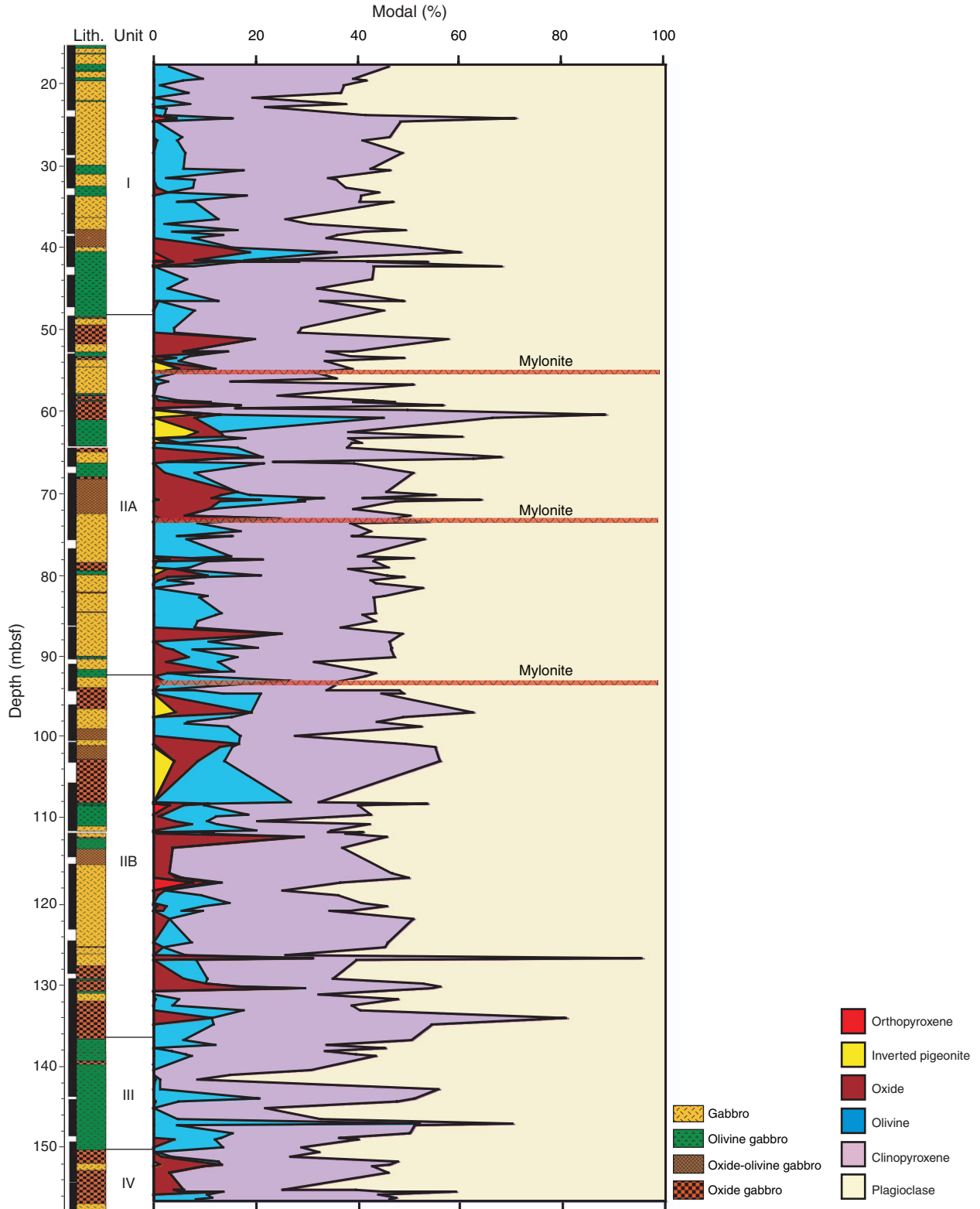


Figure F12. Histogram showing distribution of whole-rock Mg#s. Data also show the Mg# extent of Atlantis II basalts (Johnson and Dick, 1992), range of Fo in olivine, and Mg# clinopyroxene (cpx) in gabbros from Hole 1105A. Note primitive gabbros must be cumulate in origin, rather than solidified melts, because the Fo olivine compositions and whole-rock Mg#s of gabbros are in excess of those that would be represented by melt composition solidification. Mid-ocean-ridge basalt (MORB) from the Atlantis II Transform generally lies within the range of Mg#s representing the window of eruptibility of Stolper and Walker (1980), unlike the majority of cumulate gabbroic rocks.

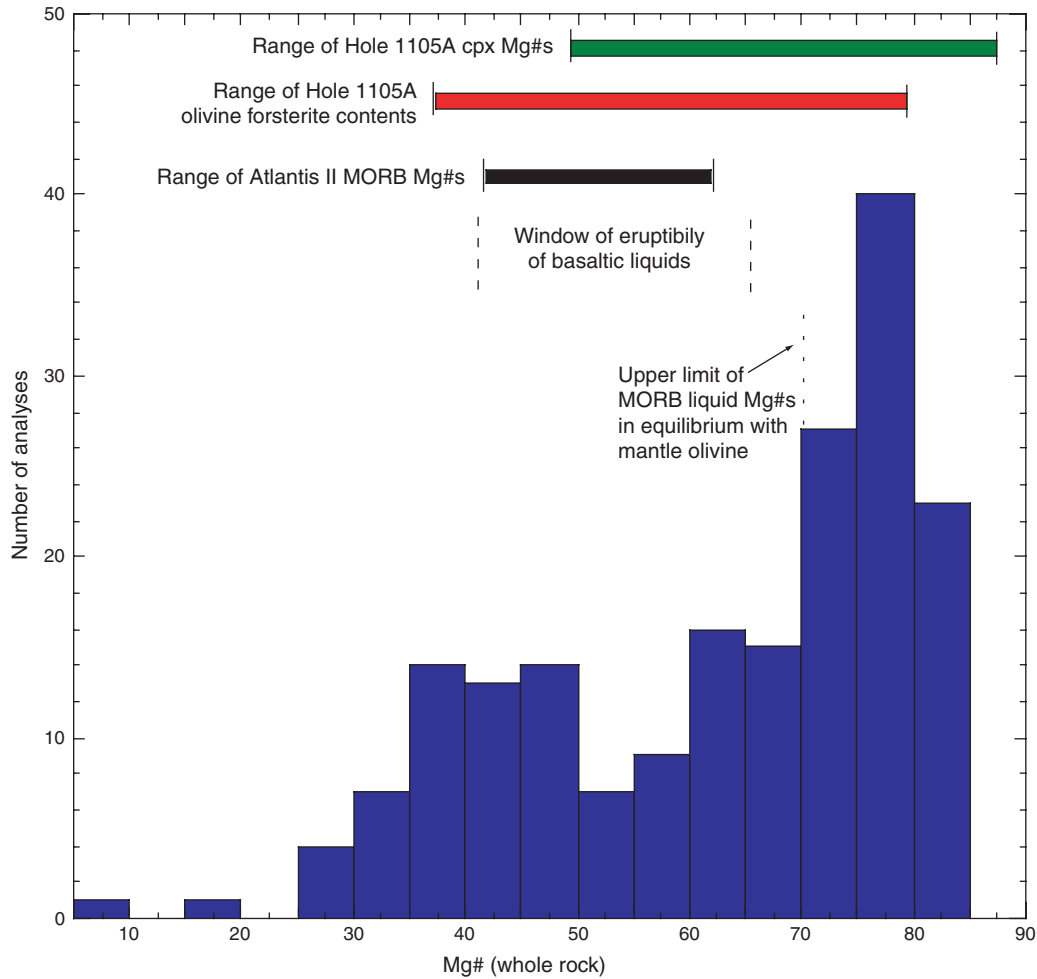


Figure F13. **A.** Histogram of whole-rock Fe_2O_3 (total iron as Fe_2O_3) abundances from 148 Hole 1105A samples analyzed by inductively coupled plasma–atomic emission spectroscopy (ICP–AES) showing extreme enrichment in iron. **B.** Histogram of whole-rock TiO_2 , also showing parallel enrichment with Fe. Range of TiO_2 in Hole 1105A clinopyroxene (cpx) (this study) and Atlantic II basalts (Johnson and Dick, 1992) also shown for reference. **C.** Alkali-iron-magnesium (AFM) plot showing the distribution of FeO, MgO, and $\text{Na}_2\text{O} + \text{K}_2\text{O}$ in the gabbroic rocks from Hole 1105A. Samples are color-coded on the basis of modal abundances of oxides in the gabbroic rocks. Polygons show the data extent of the Kane Fracture Zone area of the Mid-Atlantic Ridge (MARK) (Casey, 1997) and Bay of Islands gabbroic and ultramafic cumulates (BOIC; J.F. Casey, unpubl. data), as well as the Skaergaard (Wager and Brown, 1967) and generalized tholeiitic (Irvine and Baragar, 1971) trends.

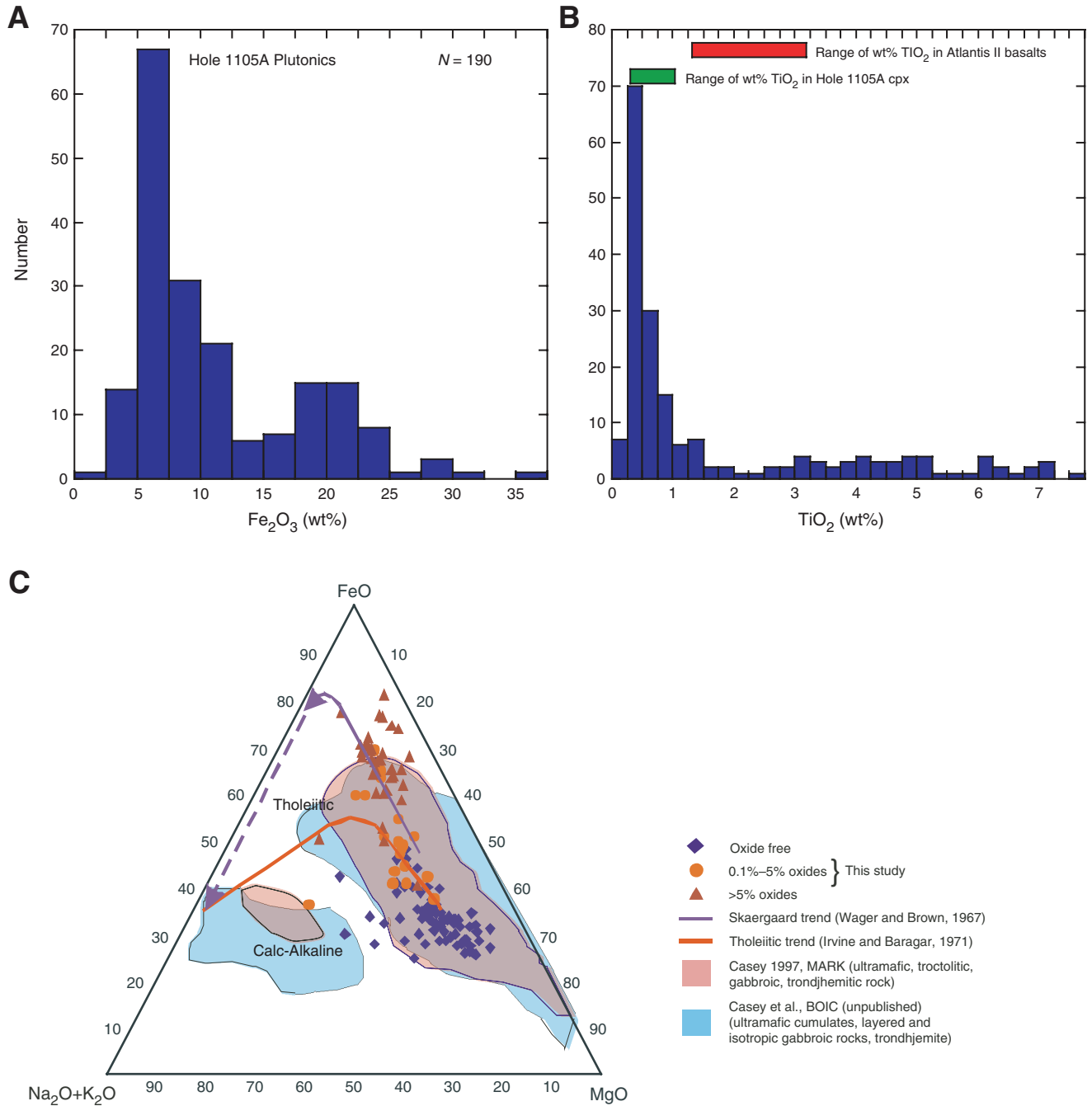


Figure F14. A–F. Whole-rock variation diagrams showing Hole 1105A gabbroic data classified according to rock types and exhibiting the effects on whole-rock chemistry dependent on increasing oxide content (e.g., [A, B] decreasing SiO₂, [C, D] increasing Ti, [E] correlation between Mg# and oxide abundances once oxides crystallize, and [F] between Fe and Ti). Atlantis II basaltic data are also plotted, showing large differences in bulk composition when compared to plutonic samples both at primitive and evolved stages. In D, oxides depress SiO₂ and granophyric veins elevate SiO₂. Note that samples with Mg#s < 71–73 generally contain magmatic oxides, but rocks above this limit lack oxides.

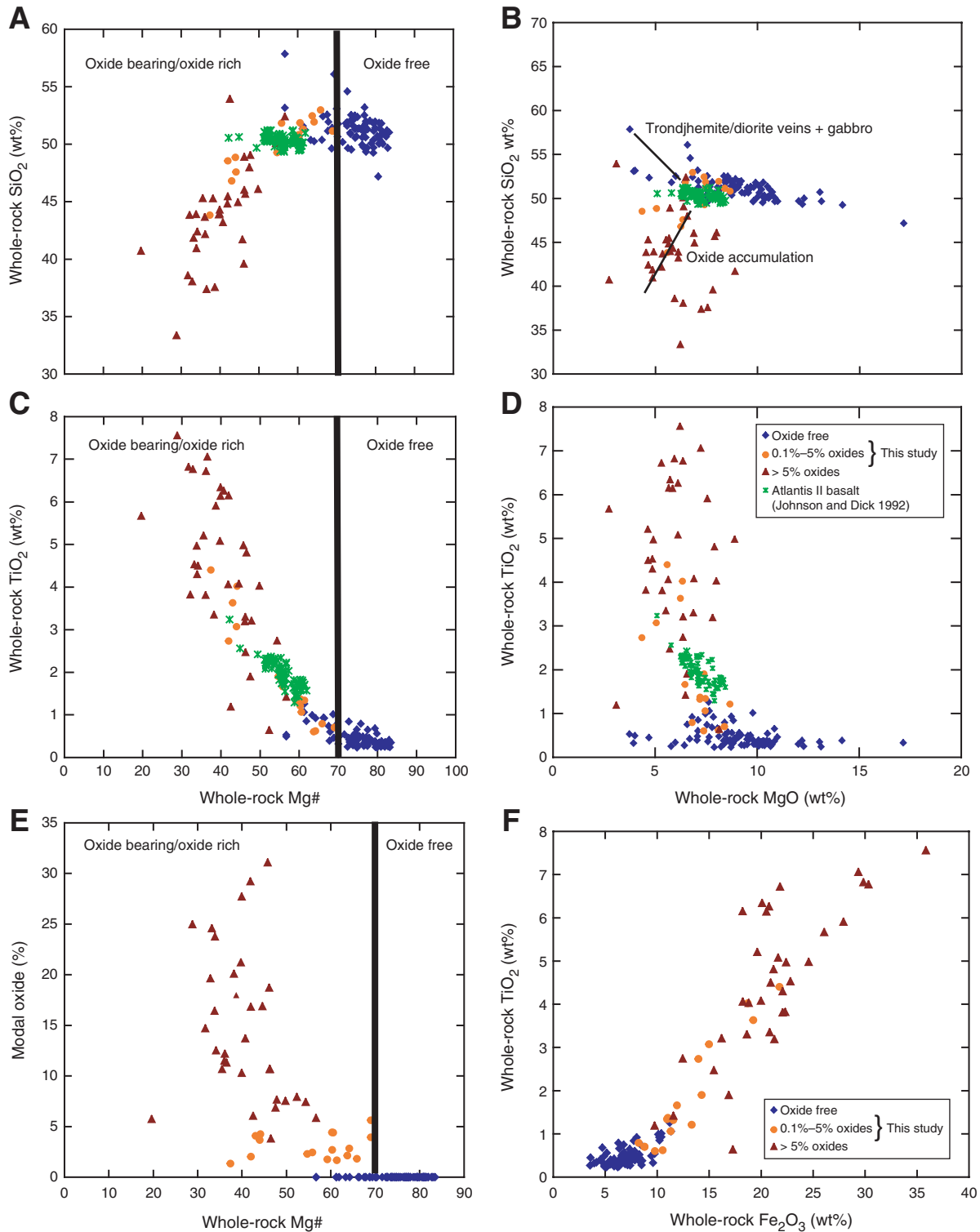


Figure F15. Whole-rock variation diagrams of incompatible minor elements (A) MnO and TiO₂ vs. Mg# and (B) P₂O₅ vs. Mg#. MnO and TiO₂ are negatively correlated with Mg#, and most Hole 1105A nonoxide gabbroic samples are depleted with respect to basaltic compositions. Oxide-rich gabbros become more enriched than the basaltic rocks. P₂O₅ is also incompatible and tends to increase slowly with decreasing Mg# until apatite precipitates in oxide gabbros. P₂O₅ can climb to >2 wt% from low background levels.

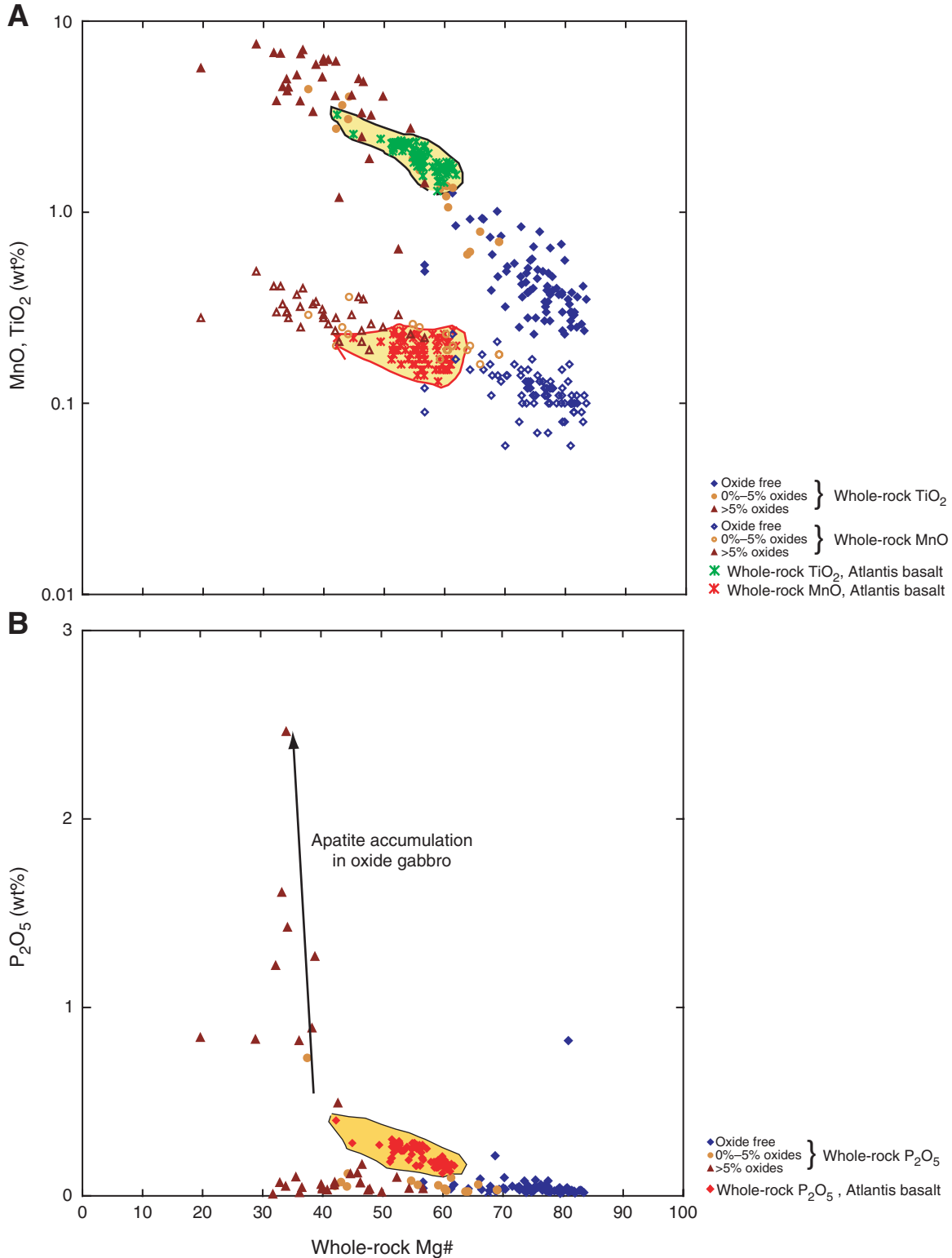


Figure F16. Extended rare earth element (REE) spidergram showing chondrite-normalized trace element abundances of gabbroic rocks from Unit I. Normalization values after Anders and Grevesse (1989).

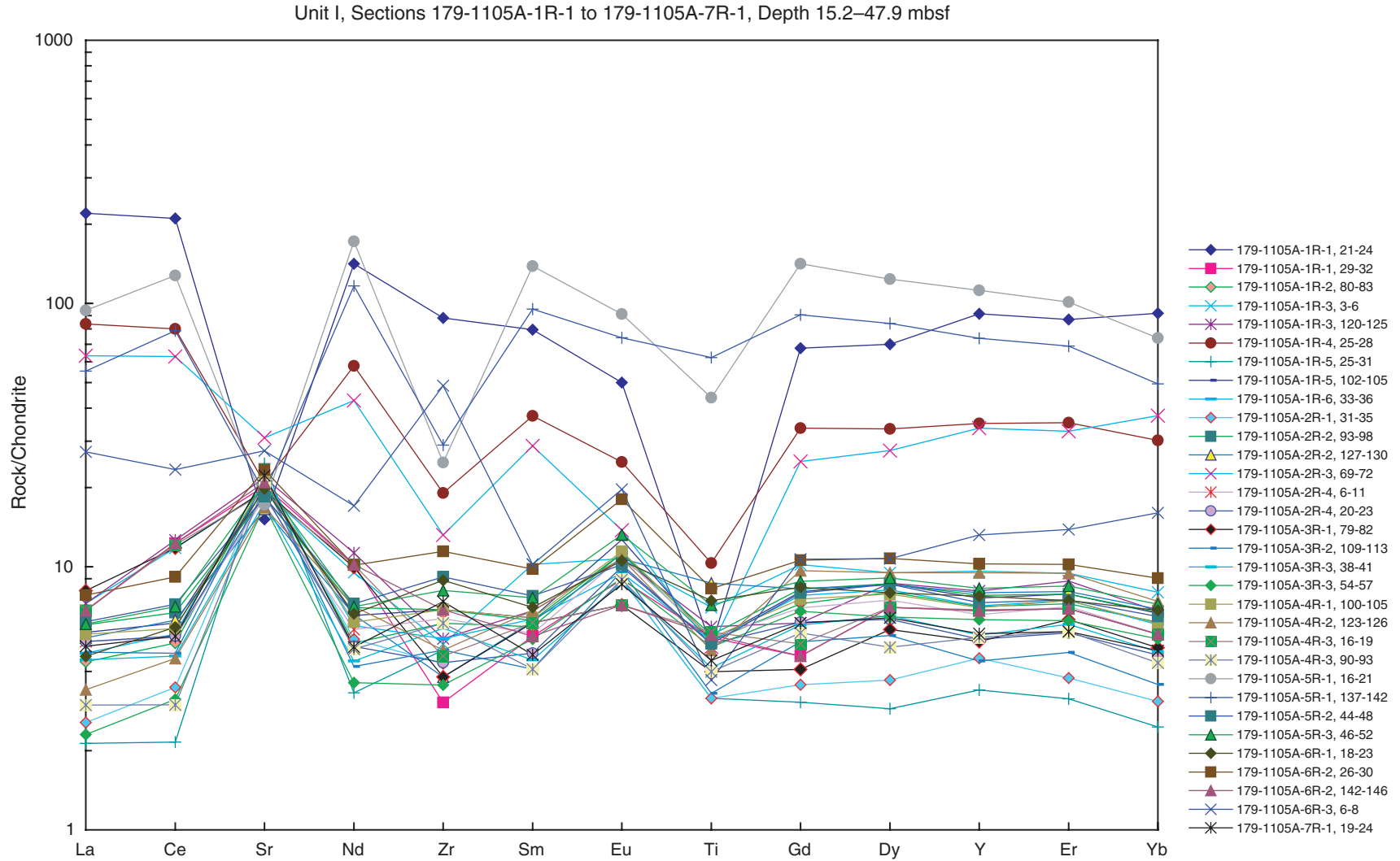


Figure F17. Extended rare earth element (REE) spidergrams showing chondrite-normalized trace element abundances of gabbroic rocks from Sub-unit IIA. Samples in top plot are from the highest level of the unit, and the basal plots show progressively lower levels of the core. Normalization values after Anders and Grevesse (1989).

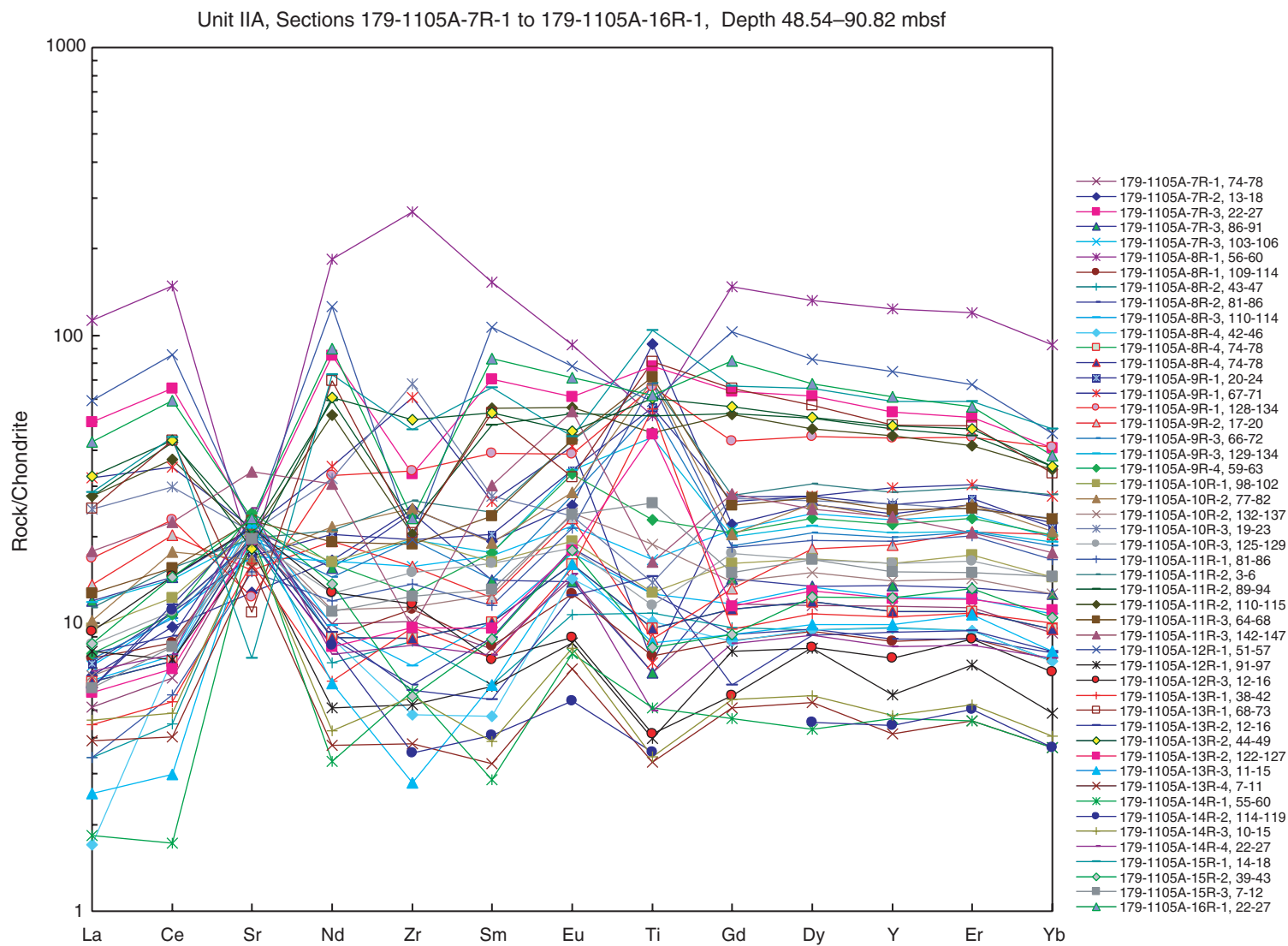


Figure F18. Extended rare earth element (REE) spidergrams showing chondrite-normalized trace element abundances of gabbroic rocks from Sub-unit IIB. Samples in top plot are from the highest level of the unit, and the basal plot shows lower levels of the core. Normalization values after Anders and Grevesse (1989).

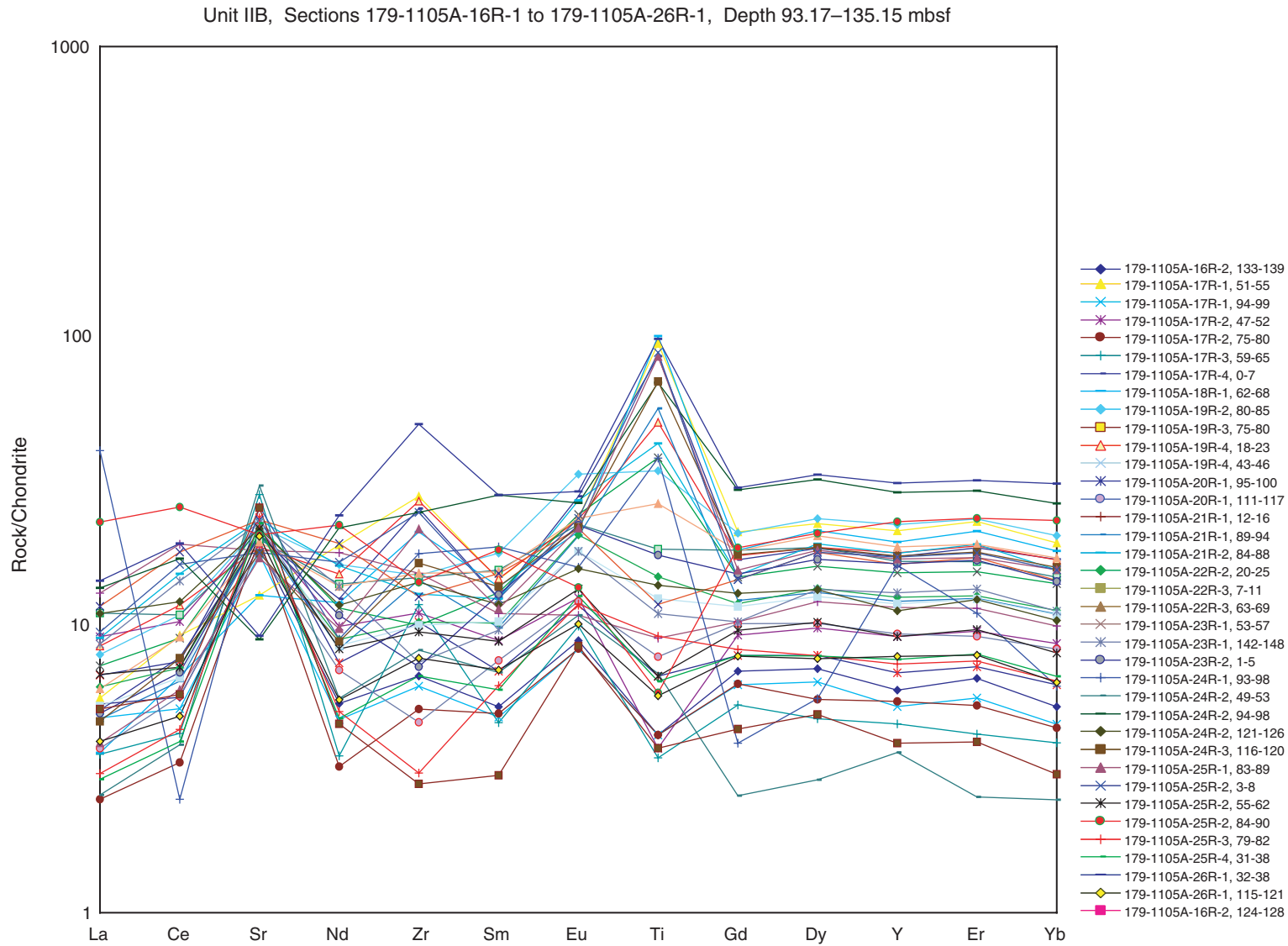


Figure F19. Extended rare earth element (REE) spidergram showing chondrite-normalized trace element abundances of gabbroic rocks from Unit III. Normalization values after Anders and Grevesse (1989).

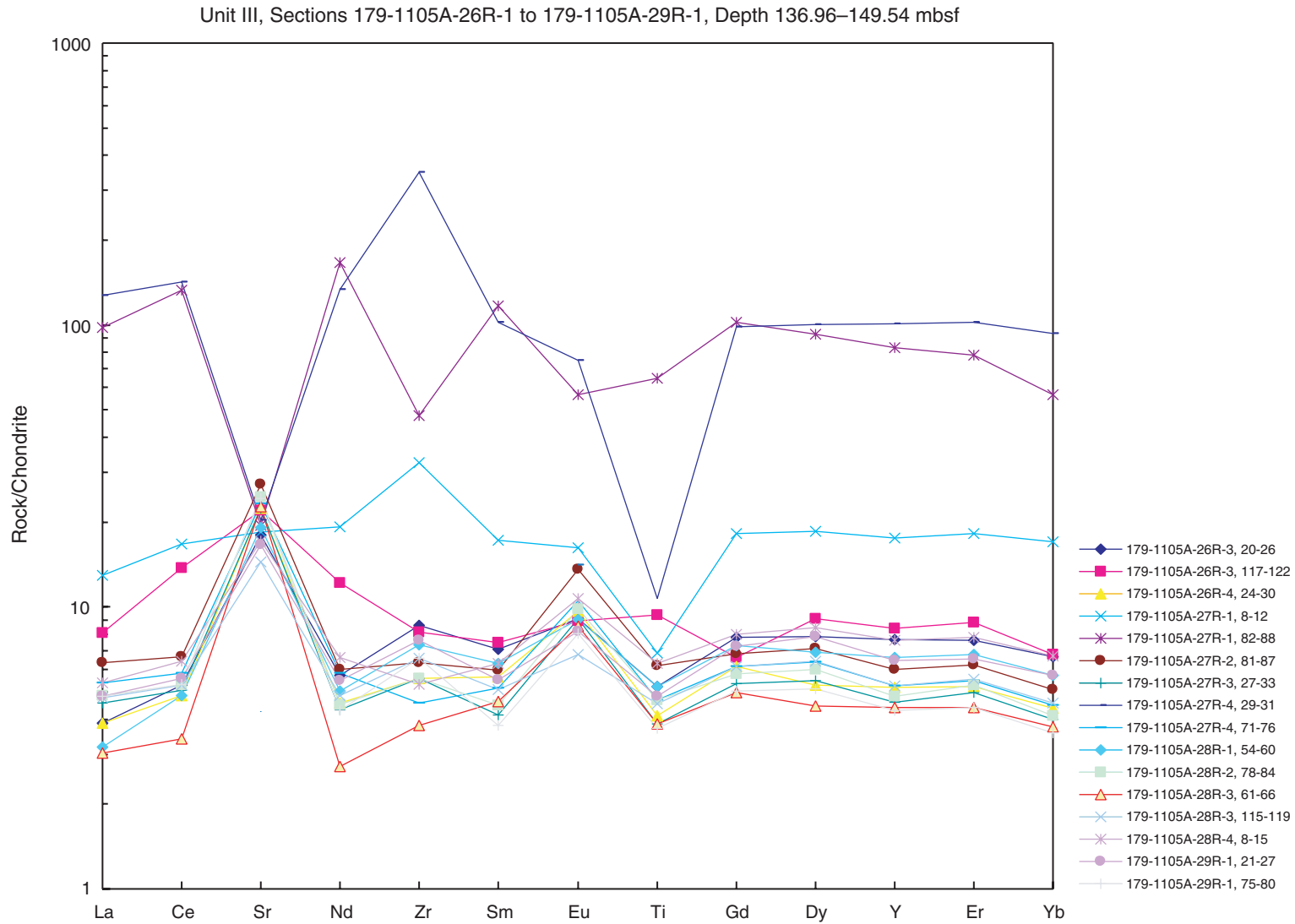


Figure F20. Extended rare earth element (REE) spidergram showing chondrite-normalized trace element abundances of gabbroic rocks from Unit IV. Normalization values after Anders and Grevesse (1989).

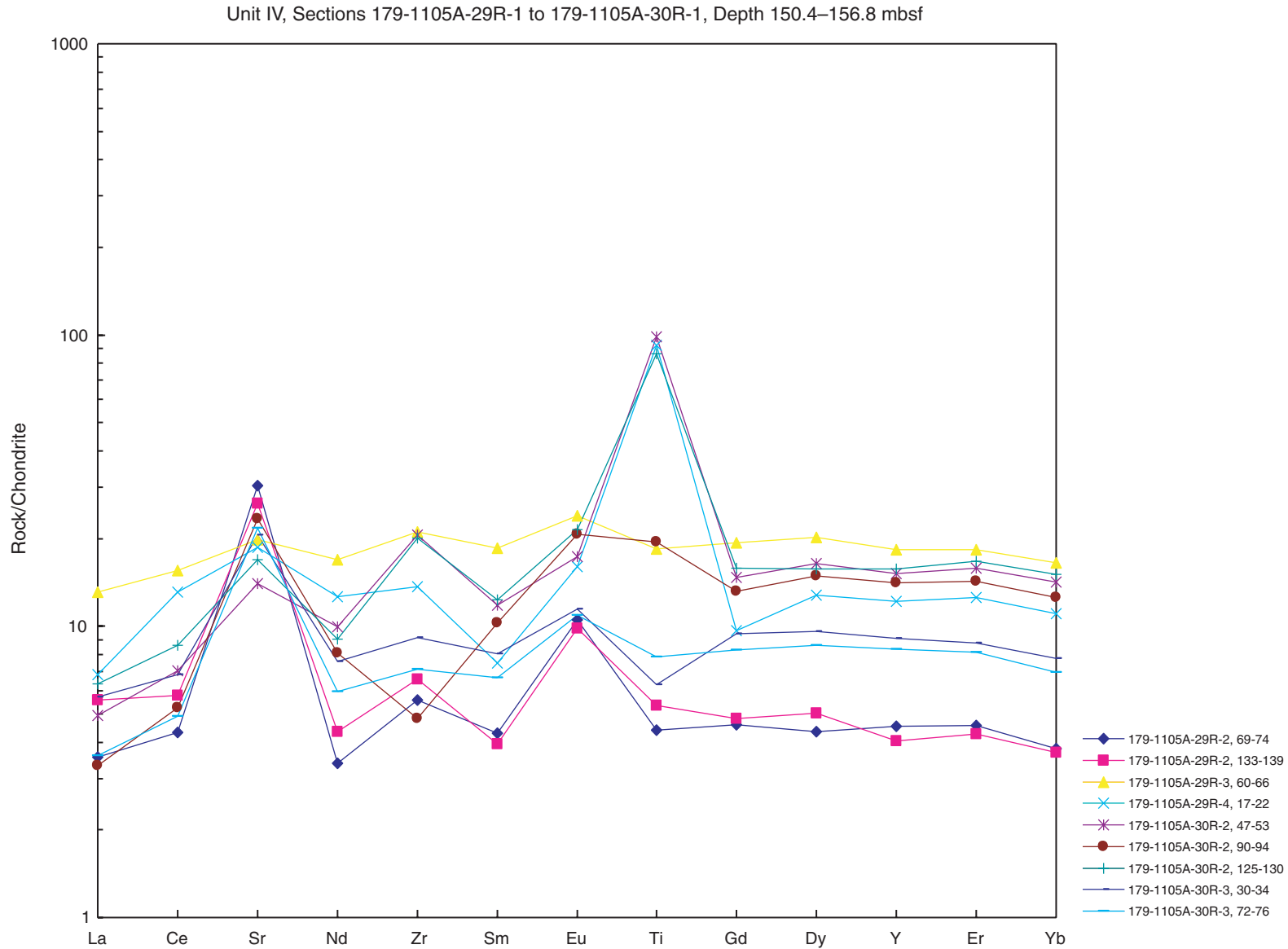


Figure F21. A. Extended rare earth element (REE) spidergram of rocks classified using modal opaque oxide percentage as “oxide-free” gabbro and olivine gabbro. B. Rocks classified using modal opaque oxide percentage as “oxide-bearing” gabbro and olivine gabbro. C. Rocks classified using modal opaque oxide percentage as “oxide” gabbro and olivine gabbro.

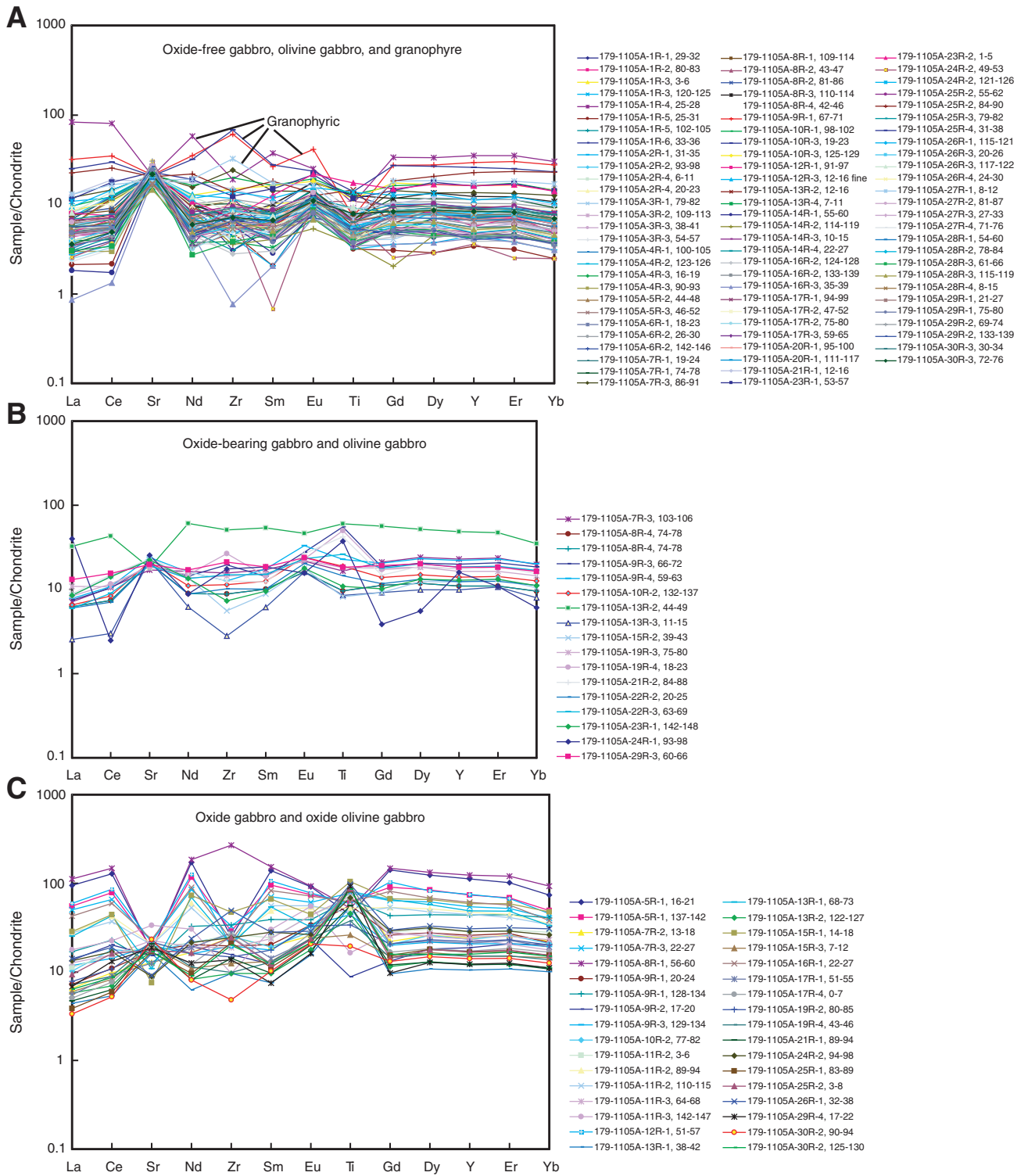


Figure F22. Variation of compatible elements Ni, Cr, and Cu during silicate fractionation and late stage-oxide/sulfide fractionation. **A.** Variation between whole-rock Ni and whole-rock Mg# ($100 \times [\text{Mg}/\text{Mg}+\text{Fe}]$) showing expected decreases in Ni with decreasing Mg#. The depletion trend is from “oxide-free” to “oxide-bearing” to “oxide” gabbros and olivine gabbros. **B.** Variation between whole-rock Cr and whole-rock Mg#. A strong early depletion trend with Cr decreasing with Mg# from “oxide-free” to “oxide-bearing” to “oxide” gabbros and olivine gabbros. A slight increase in Cr in oxide gabbros could be due to the fact that Cr partitions into oxides, and an accumulation of oxides will lead to an increase in whole-rock Cr. **C.** Variation between whole-rock Cu and whole-rock Mg#. “Oxide-free” gabbros and olivine gabbros show a decrease in Cu with decreasing Mg#. A gradual to strong increase in Cu is seen in “oxide-bearing” and “oxide” gabbro and olivine gabbro. This increase in Cu is likely due to late sulfide liquids and accumulation of chalcopyrite.

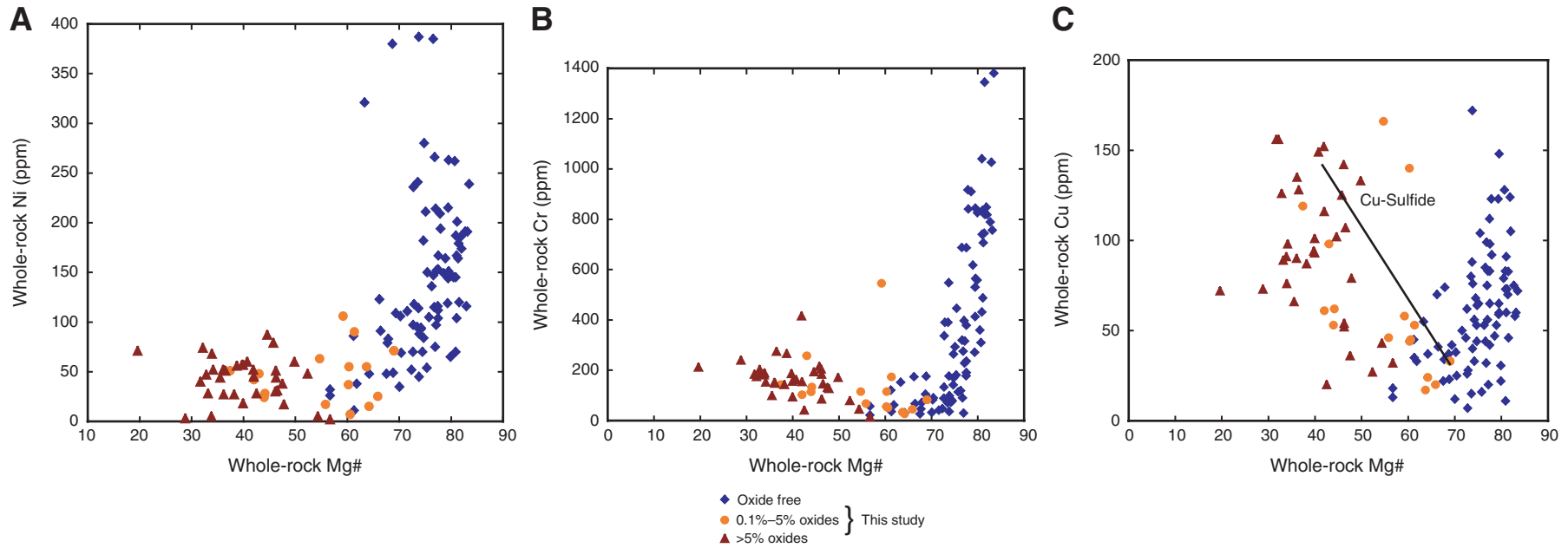


Figure F23. A, B. Cross plots between chondrite-normalized Ce and Yb showing Atlantis II mid-ocean-ridge basalt (MORB) (Johnson and Dick, 1992), the compositions of clinopyroxene and plagioclase calculated to be in equilibrium with the basalts, and Hole 1105A gabbroic rocks. B is an enlarged view of A to show the positions of most of the gabbroic rocks as more depleted than basaltic rocks, yet more enriched than expected of an adcumulate mixture of plagioclase and clinopyroxene. Note that the abundance of these incompatible trace elements lies above the values along a mixing line between the average plagioclase and clinopyroxene cumulate, likely indicating that most samples contain some trapped melt. **C, D.** $(Ce/Yb)_{cn}$ ratio vs. Yb_{cn} and Ce_{cn} . Also plotted are the Atlantis II basalts. Plagioclase and clinopyroxene in equilibrium with Atlantis II basalts tie lines show various mixing proportions of basalt (liquid), cumulate plagioclase, and clinopyroxene. Contours show the percentage of trapped melt that could be contained in the primitive gabbroic rocks. The estimation breaks down during advanced fractionation and if accessory phases such as apatite and zircon accumulate or if granophyric veins impregnate the gabbroic rocks. Then, as shown, the gabbroic rocks may be more enriched than the basalt. More quantitative “trapped” melt estimates for each rock will be presented in J.F. Casey and N.R. Banerjee (unpubl. data).

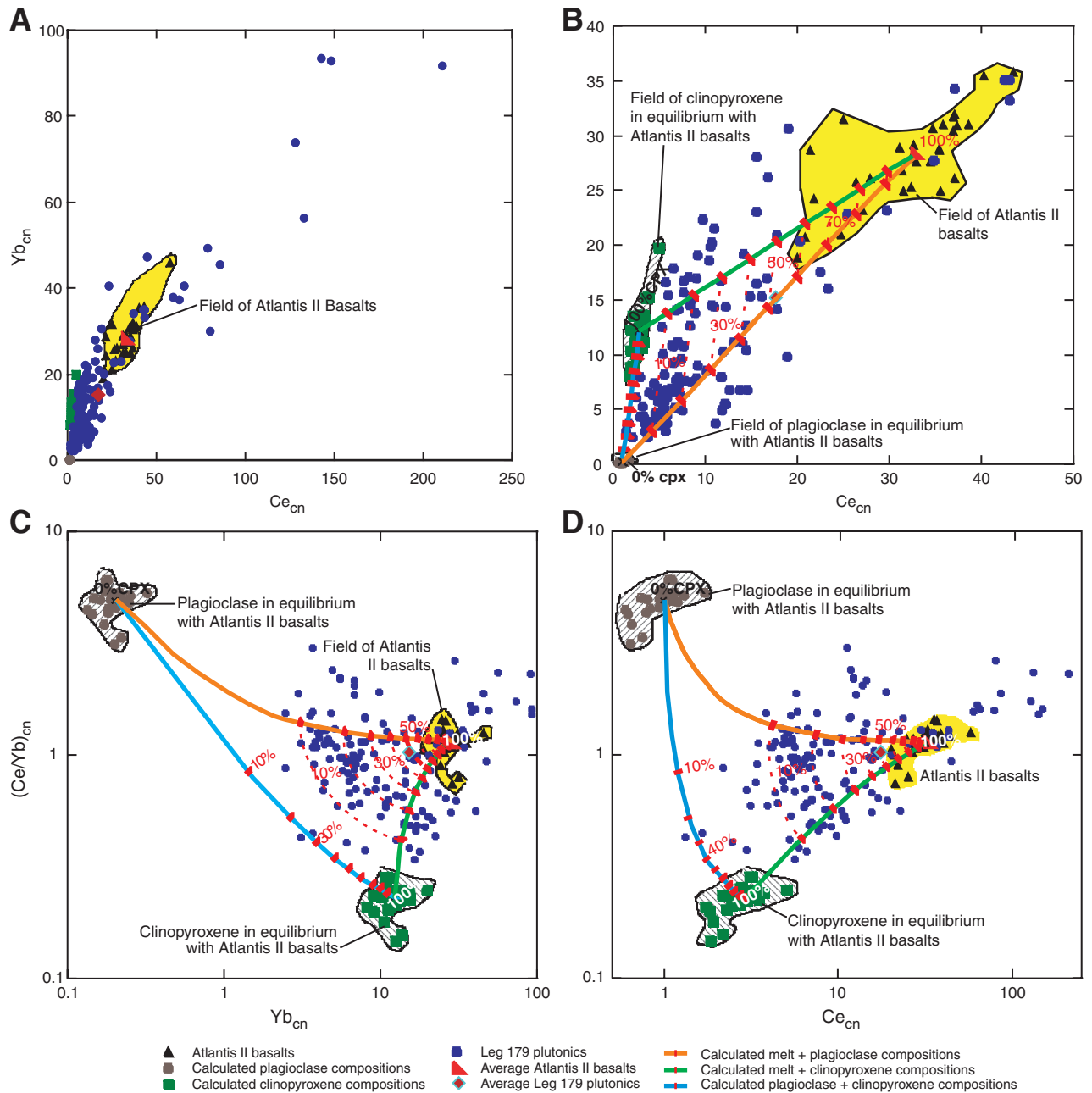


Figure F24. A. Comparison of mean of major and minor element abundances in the suite of Atlantis II basalts analyzed by Johnson and Dick (1992) and the mean major and minor element abundances of Hole 1105A plutonic samples. The best fit line closely follows the 1:1 line, suggesting a one to one relationship between the mean major and minor element compositions of both volcanics and plutonics. **B.** Comparison of the mean abundance of rare earth elements (REEs) in Atlantis II basalts and 148 Hole 1105A plutonic samples. The observed trend is close to the 1:2 line, suggesting that mean REE concentrations in Hole 1105A plutonics is almost half of that present in the mean of volcanics. All samples including granophyres were used in computing means.

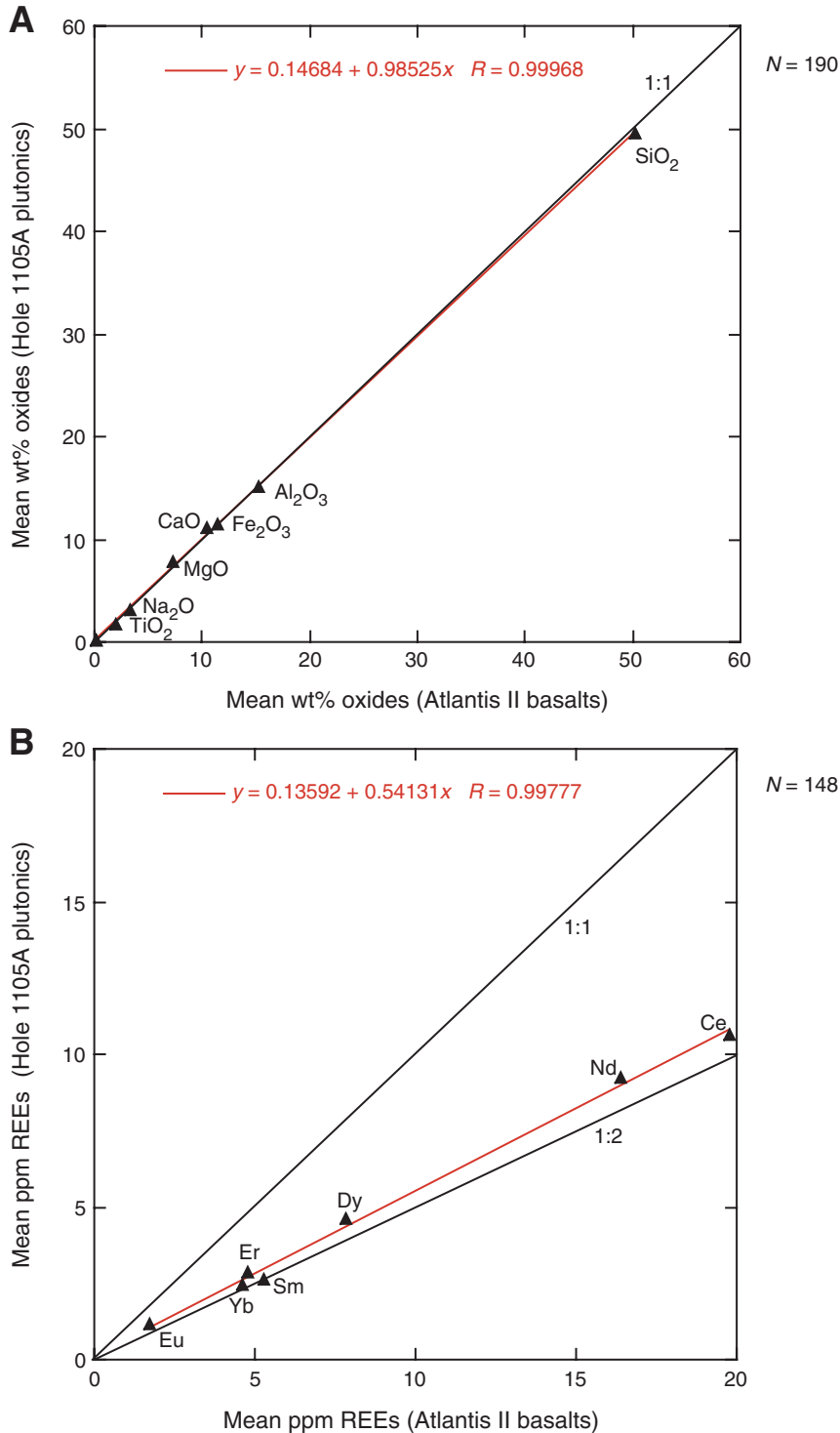


Figure F25. Downhole whole-rock cryptic chemical variation of Mg#, Fe₂O₃, TiO₂, Ce_{cn}, and Zr. Pink line represents the minimum Ce measurement in Atlantis II basalts for reference. Note trace element spikes are not restricted to region of oxide gabbros but can also affect oxide-free gabbroic rocks. This typically indicates the rock has been affected by the addition of more fractionated melt (see text).

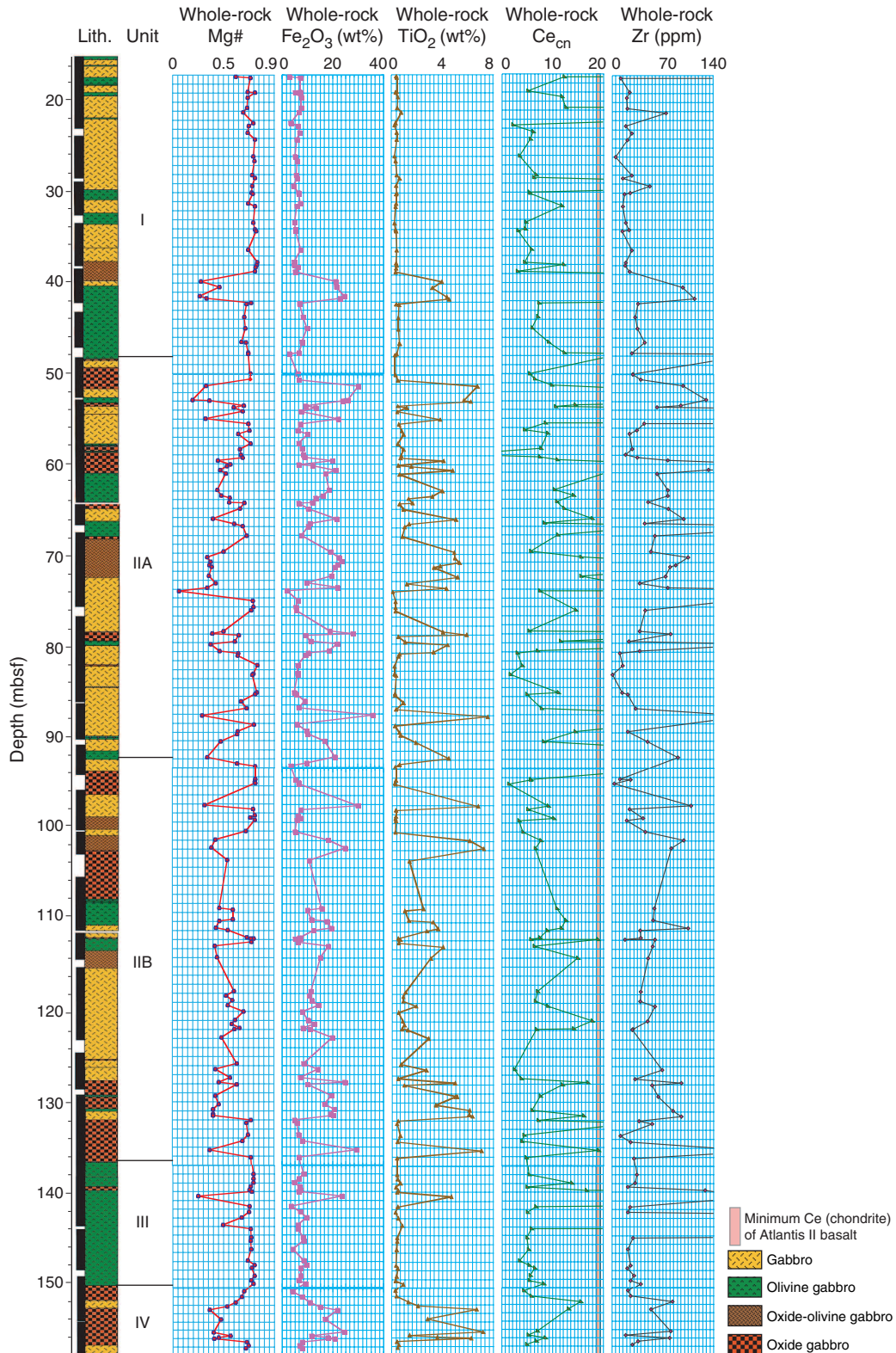


Figure F26. Downhole comparison of Mg# in Holes 735B and 1105A showing the region of the two cores that may correlate based on the high abundance of oxides in each zone (Unit IV of Hole 735B and Subunits IIA and IIB of Hole 1105A). Hole 1105A core has been depth-shifted, and both representations are at the same scale. Direct comparisons are made difficult by the finer scales of variation evident in Hole 1105A data because of the denser sampling. The magnitudes of the variations are, however, similar.

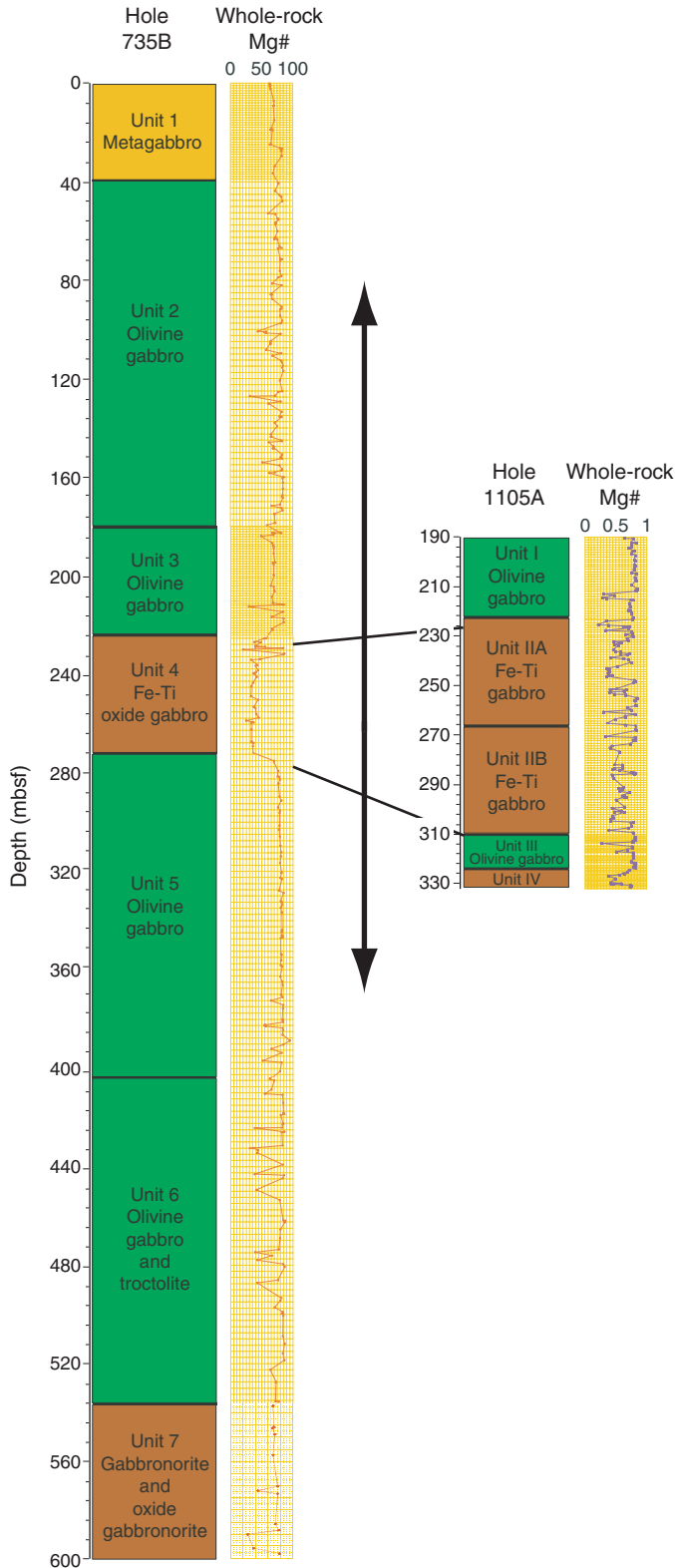


Figure F27. A. Plot of the variation in NiO in olivine vs. Fo showing rapid depletion due to its compatible nature during olivine crystallization. B. Plot of MnO vs. Fo showing a strong enrichment trend because of its incompatible nature during olivine, clinopyroxene, and plagioclase crystallization. Note small gap in compositions also noted by Thy (Chap. 3, this volume). Electron microprobe data collected using the University of Houston JEOL Superprobe.

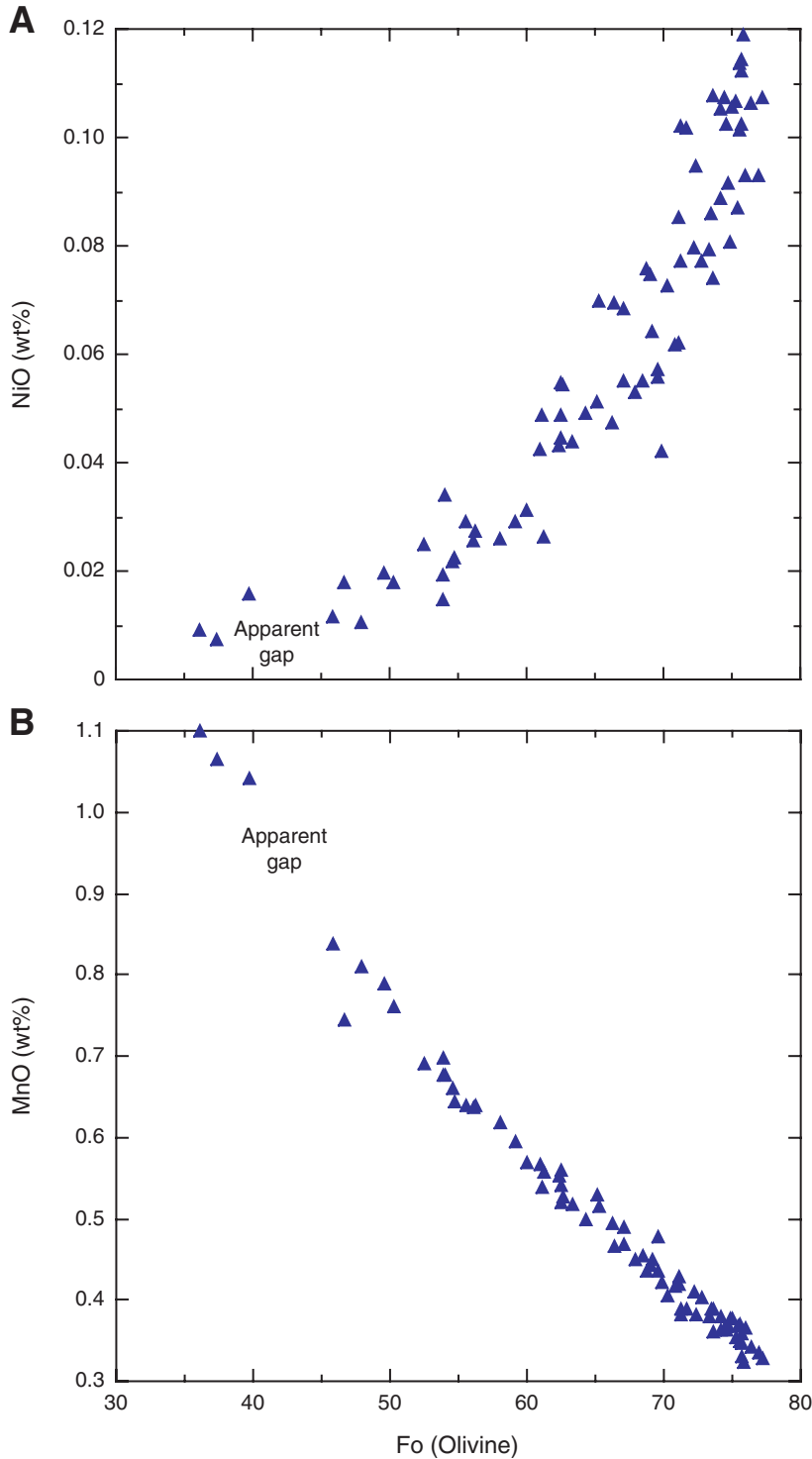


Figure F28. A. Backscatter image of a clinopyroxene grain in Sample 179-1105A-19R-4, 18–23 cm, mapped for elemental abundances. B–E. False-color Al, Mg, Fe, and Mg# maps of the same grain. False-color images are made using National Institute of Health (NIH) image software. Prominent normal zoning is shown in the grain. Values for corresponding colors are shown in the legend. This is an example of fractionated clinopyroxene rim on Type 1 core.

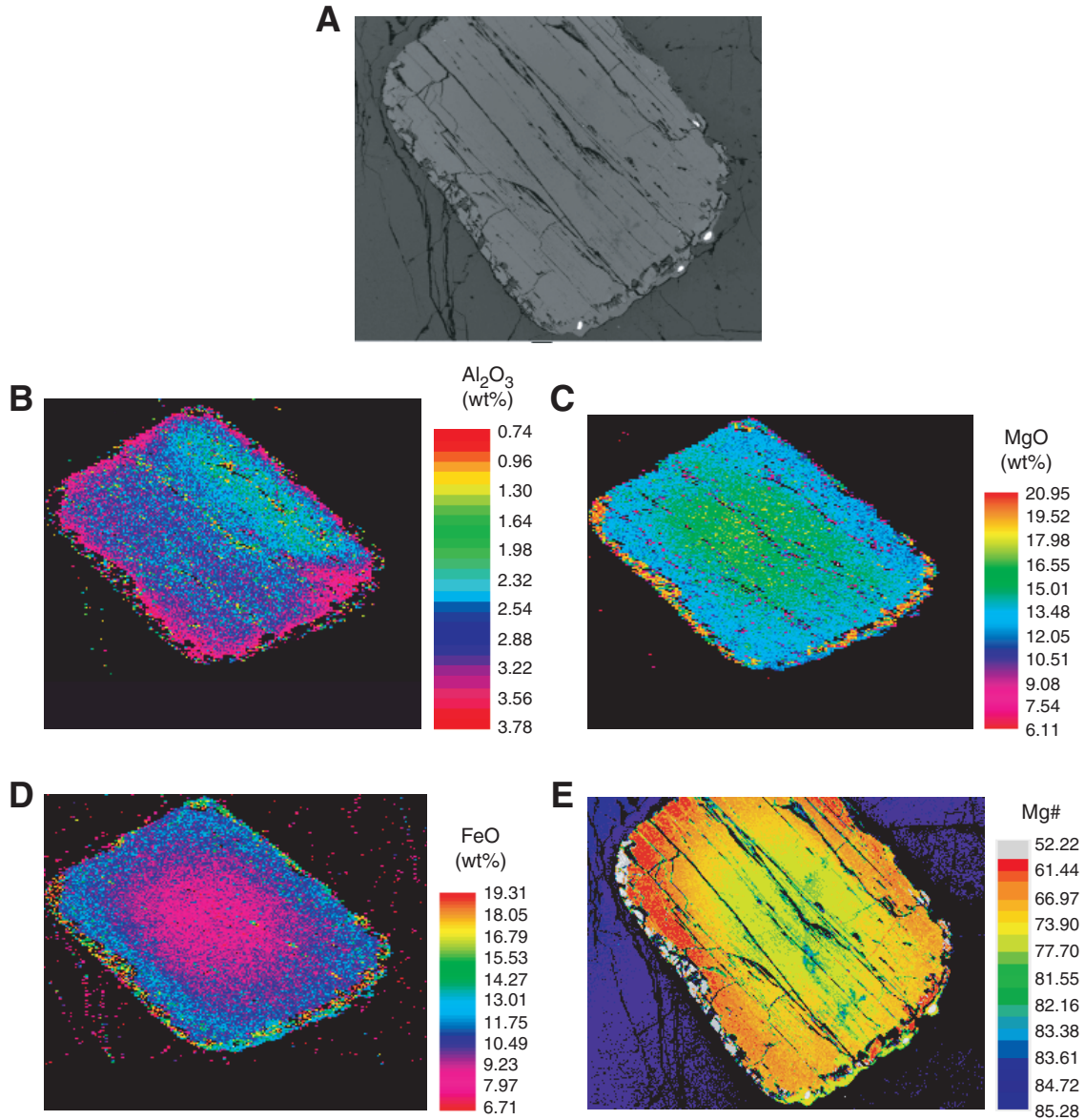


Figure F29. Plots showing relationship between Mg# and compatible elements (A) Al_2O_3 and (B) Cr_2O_3 and incompatible elements (C) MnO , (D) TiO_2 , and (E) Na_2O in clinopyroxene (cpx). Both Type 1 and Type 2 clinopyroxenes are shown, as well as rock type. Oxide precipitation is well correlated with Mg#s < 73–75, and the appearance of oxides does not appear to be random but systematically increasing as Mg# decreases once this threshold has passed. Oxide precipitation is not predicted at such high Mg#s in perfect fractional crystallization models. Black vertical line correlates with the onset of abundant oxide precipitation or occurrence in the samples.

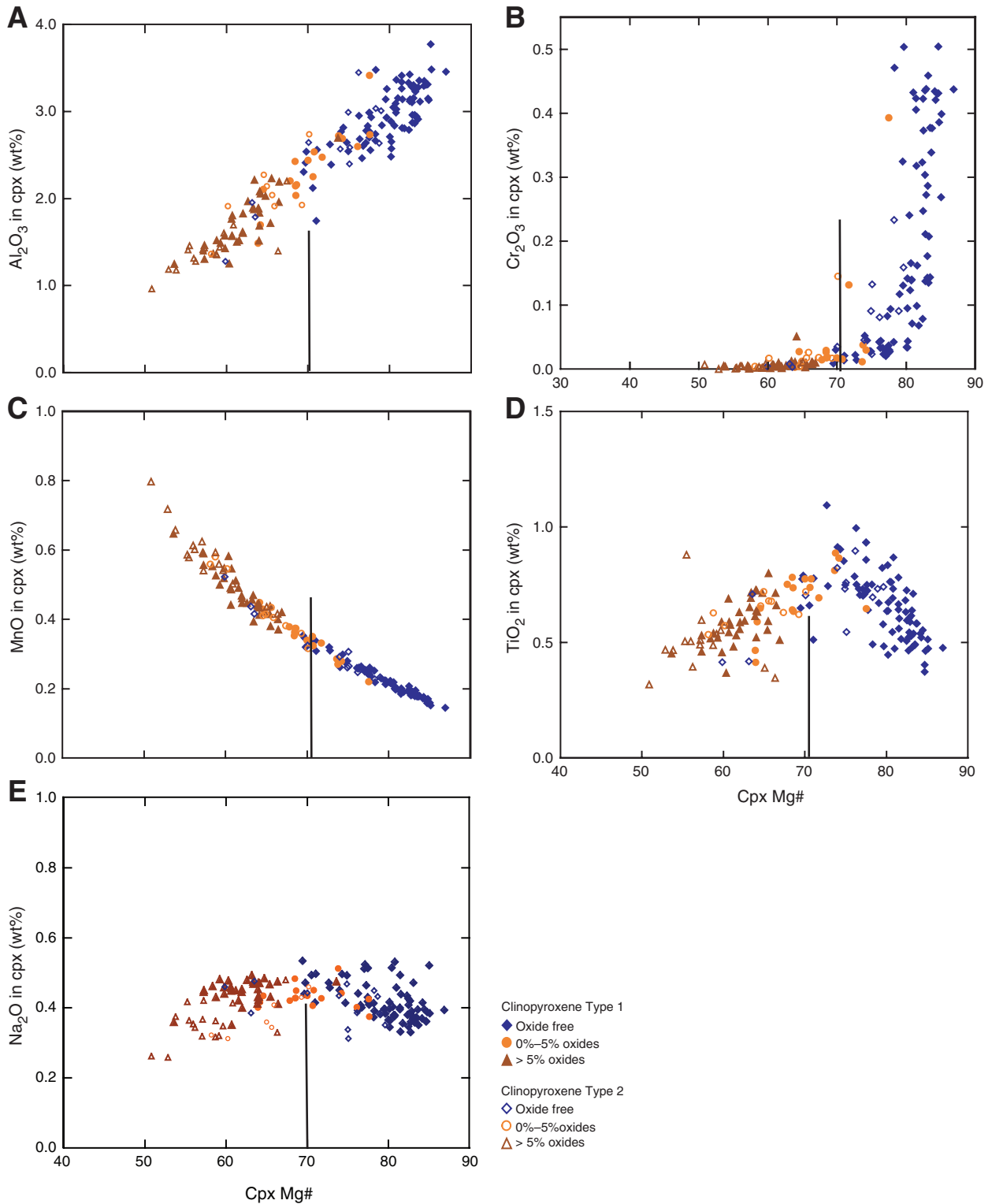


Figure F30. A. Pyroxene quadrilateral plot from Campbell and Nolan (1974) showing pyroxene minima of different layered intrusions: Sudbury = 1, Jemberlana = 2, Skaergaard = 3, Bushveld = 4, Bjerkrem-Songdal = 5. Superimposed green symbols represent pyroxene data from Hole 1105A (this study). **B.** Pyroxene quadrilateral plot showing the Skaergaard trend (black lines). Also plotted is pyroxene data from Hole 1105A (green symbols) on top of data from Hole 735B with the following color scheme: dark blue = troctolites, light blue = olivine gabbro, red = gabbro, white = oxide gabbro on top of data from Hole 735B (Dick et al., 2002). Hole 1105A pyroxene data from this study appear to be broadly similar to Bushveld trend and Skaergaard trend if all of the Hole 735B and 1105A data are considered (e.g., also see Thy, [Chap. 3](#), this volume). Data from both holes show similar trends. Below the quadrilateral line graphs are the corresponding Fo content in olivines for samples from Holes 1105A and 735B. An apparent gap in olivine composition seen in Hole 1105A is not visible in Hole 735B olivine data. Cpx = clinopyroxene, opx = orthopyroxene.

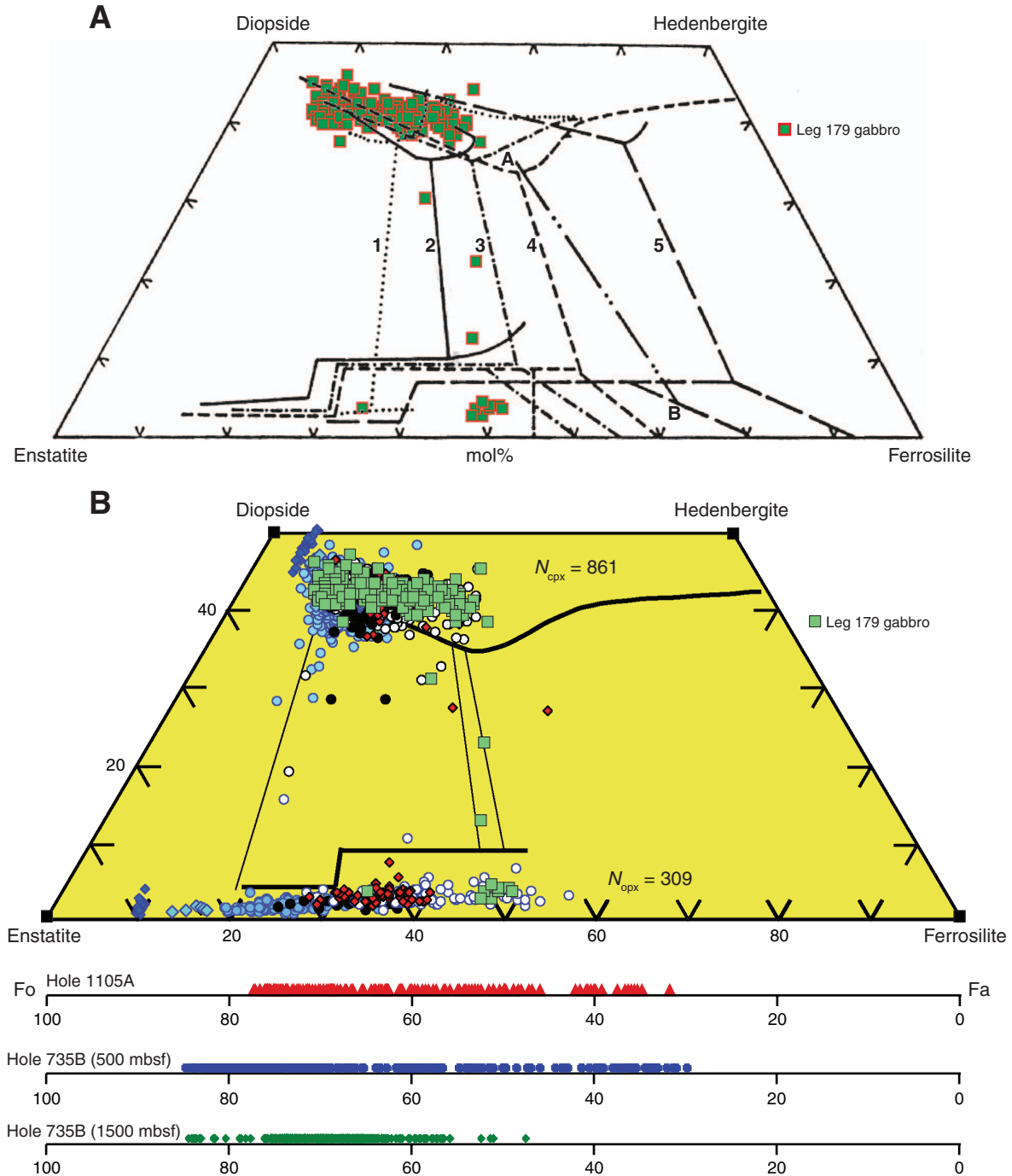


Figure F31. A. Plot showing relationship between tetrahedral Al in clinopyroxene and D_{Ti} (Lundstrom et al., 1998). B. A portion of plot A has been enlarged to show that even at lower tetrahedral Al concentrations in clinopyroxene the Al relationship between D_{Ti} and Al(IV) appears valid. These lower values are in the range of compositions of Hole 1105A gabbroic rocks. The data for B are from Ray et al. (1983), and this apparent compositional effect on partitioning behavior will be used in later modeling.

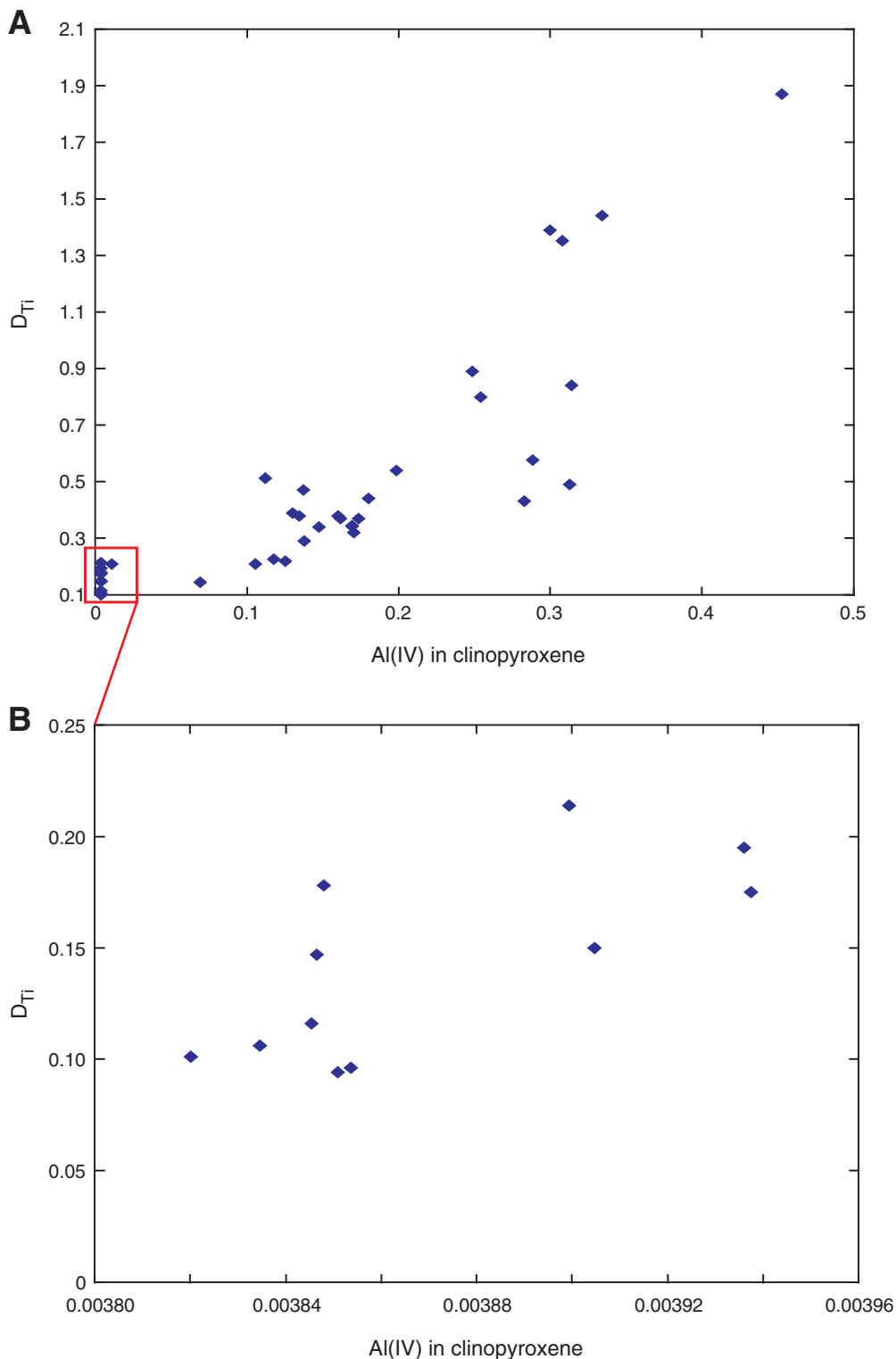


Figure F32. A. Plot showing relationship between tetravalent Al and TiO_2 in clinopyroxene. B. Plot showing relationship between tetravalent Al and Mg# of clinopyroxene. Both the plots have been color-coded according to lithologic groupings used in previous plots. Red lines show the approximate location of oxide mineral introduction in the modes.

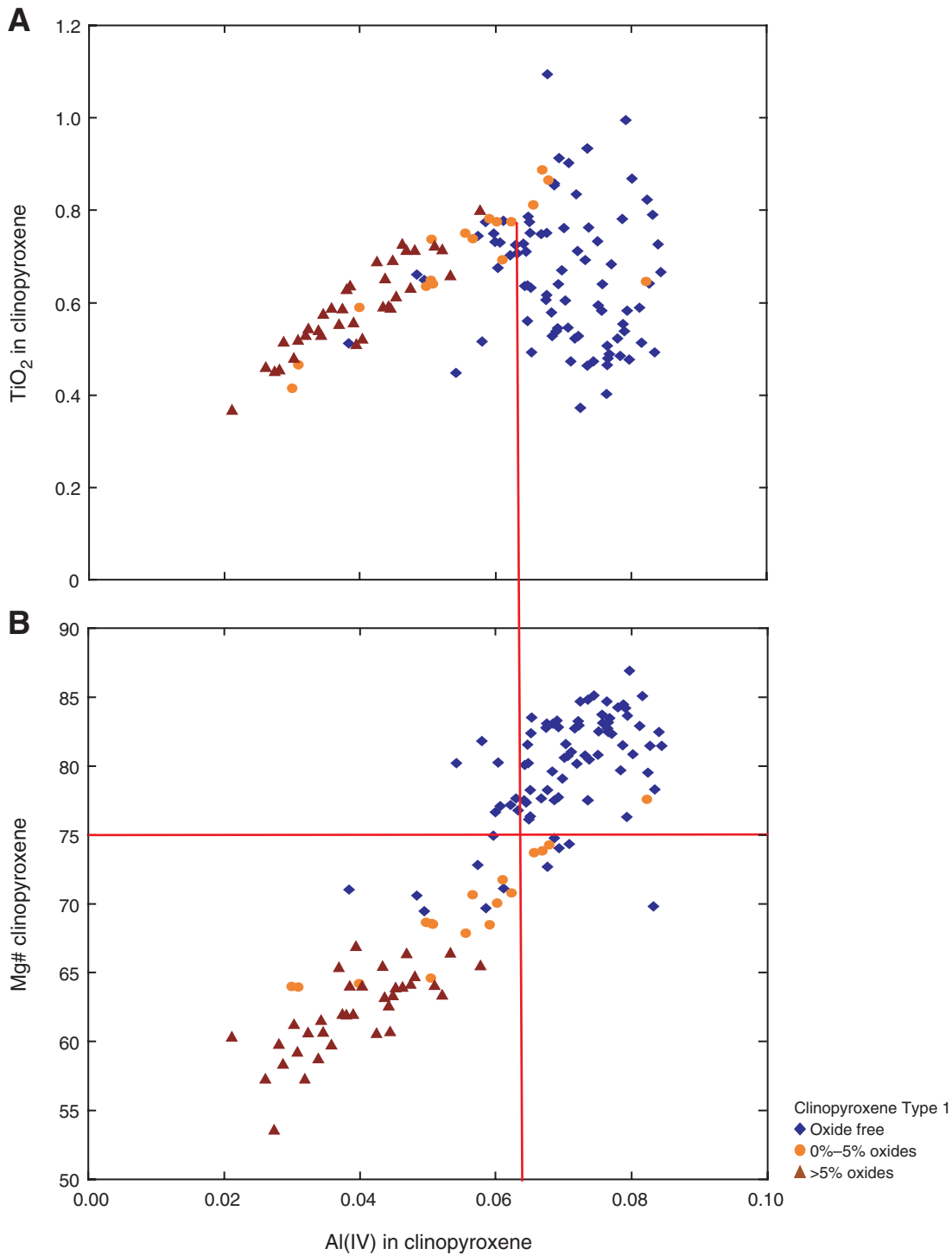


Figure F33. Plot showing the variation of K_2O vs. An in plagioclase. Both secondary core and grain rim are shown when variable in a single thin section. Note change in slope around An_{50} . This correlates with point that oxides appear in the mode (correlates with $Mg\# = 73-75$ in clinopyroxene). This more rapid enrichment is not predicted by perfect fractional crystallization models.

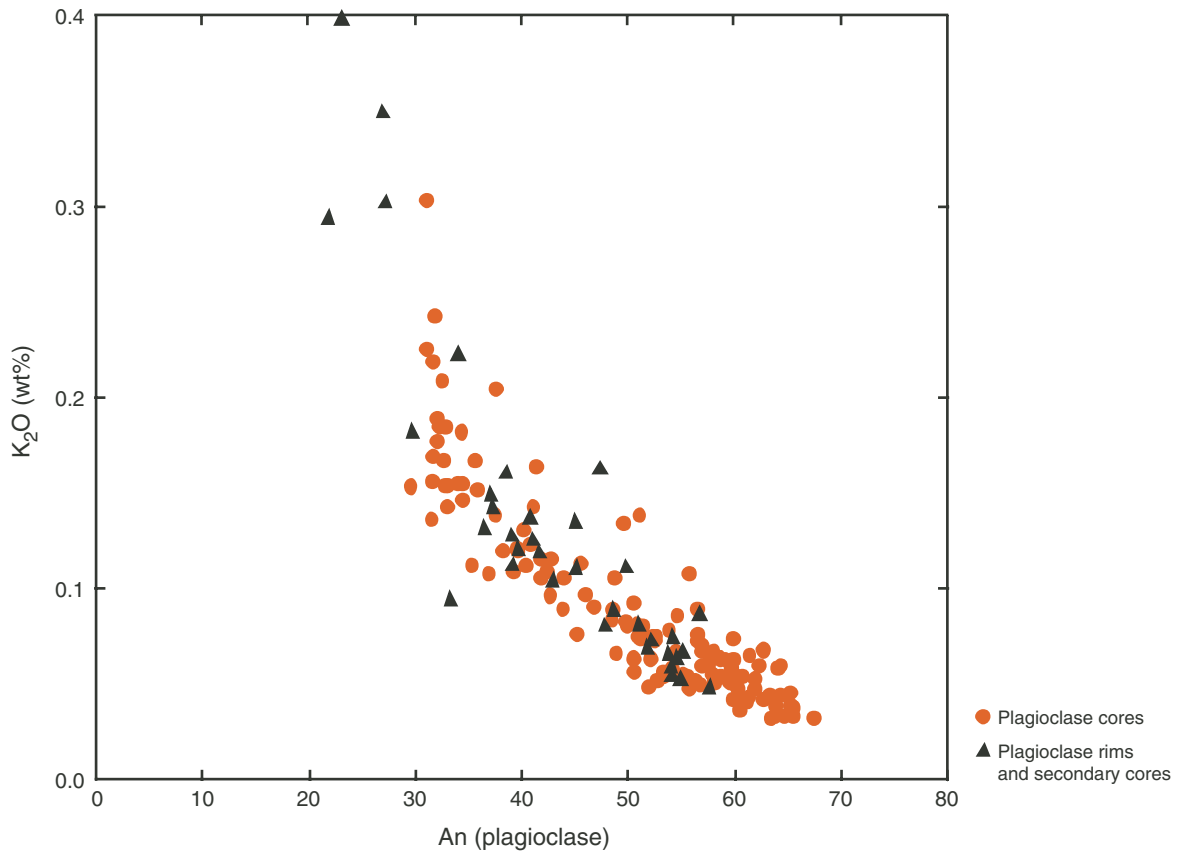


Figure F34. Summary of all silicate mineral data. Histograms of Mg# of (A) clinopyroxene, (B) Fo content of olivine, and (C) An content of plagioclase. Distributions are somewhat bimodal, consistent with whole-rock data.

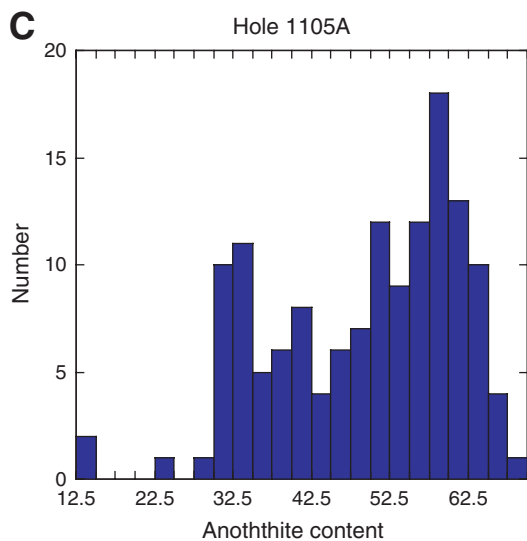
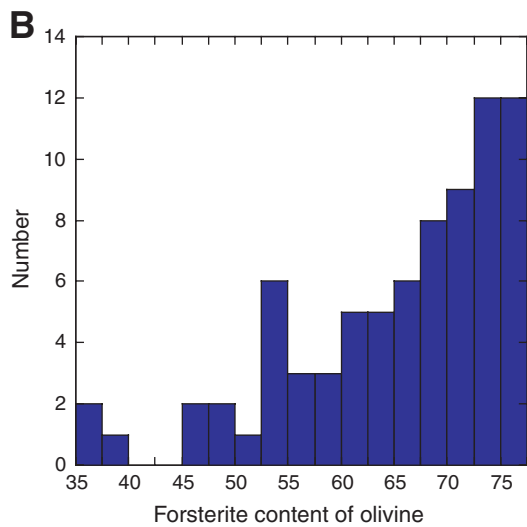
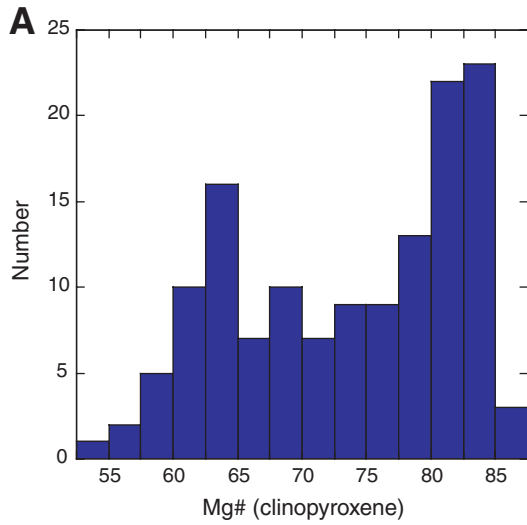


Figure F35. Correlation between (A) An content of plagioclase (plag) and Mg# of clinopyroxene (cpx), (B) An content of plagioclase and Fo content of olivine (Fo-OL), (C) Fo content of olivine and Mg# of clinopyroxene, and (D) An and Mg# of clinopyroxene, Fo content of olivine relative to the whole rock Mg#. (E) Fo vs. Mg# of cpx diagram, which at the primitive end lies close to the calculated FeO/MgO K_d between olivine-melt (0.29) and cpx-melt (0.23) trend of Grove and Bryan (1983), but most of the more fractionated samples lie significantly off the trend. This perhaps is due to reequilibration between trapped melt and olivine, changes in K_d of the melts with increasing fractionation, and/or subsolidus reequilibration. Linear best fit lines are provided for nonoxide and oxide bearing gabbroic rocks.

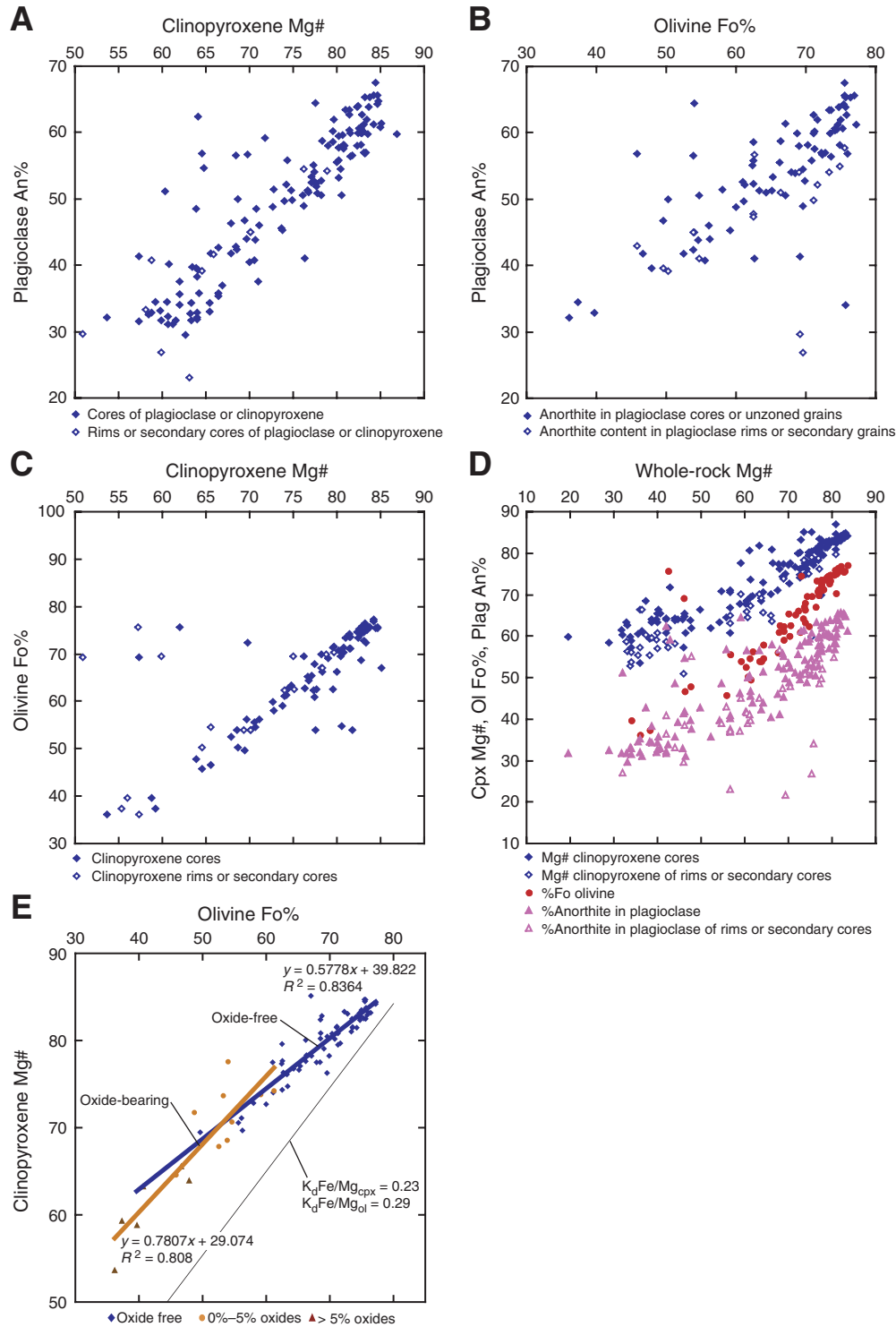


Figure F36. Downhole plot of Fo, An (Ca/[Ca+Mg+K]), and Mg# of clinopyroxene variations placed beside the lithologic and structural log. Note all three fractionation indexes correlate well (although there are fewer olivine analyses). Note positions of three narrow mylonite and many crystal-plastic fabric zones, which could represent significant breaks in the stratigraphy and do show compositional difference as they are crossed. Dots off trend lines indicate analyses of secondary cores or extent of grain rim zonation at various levels in the core.

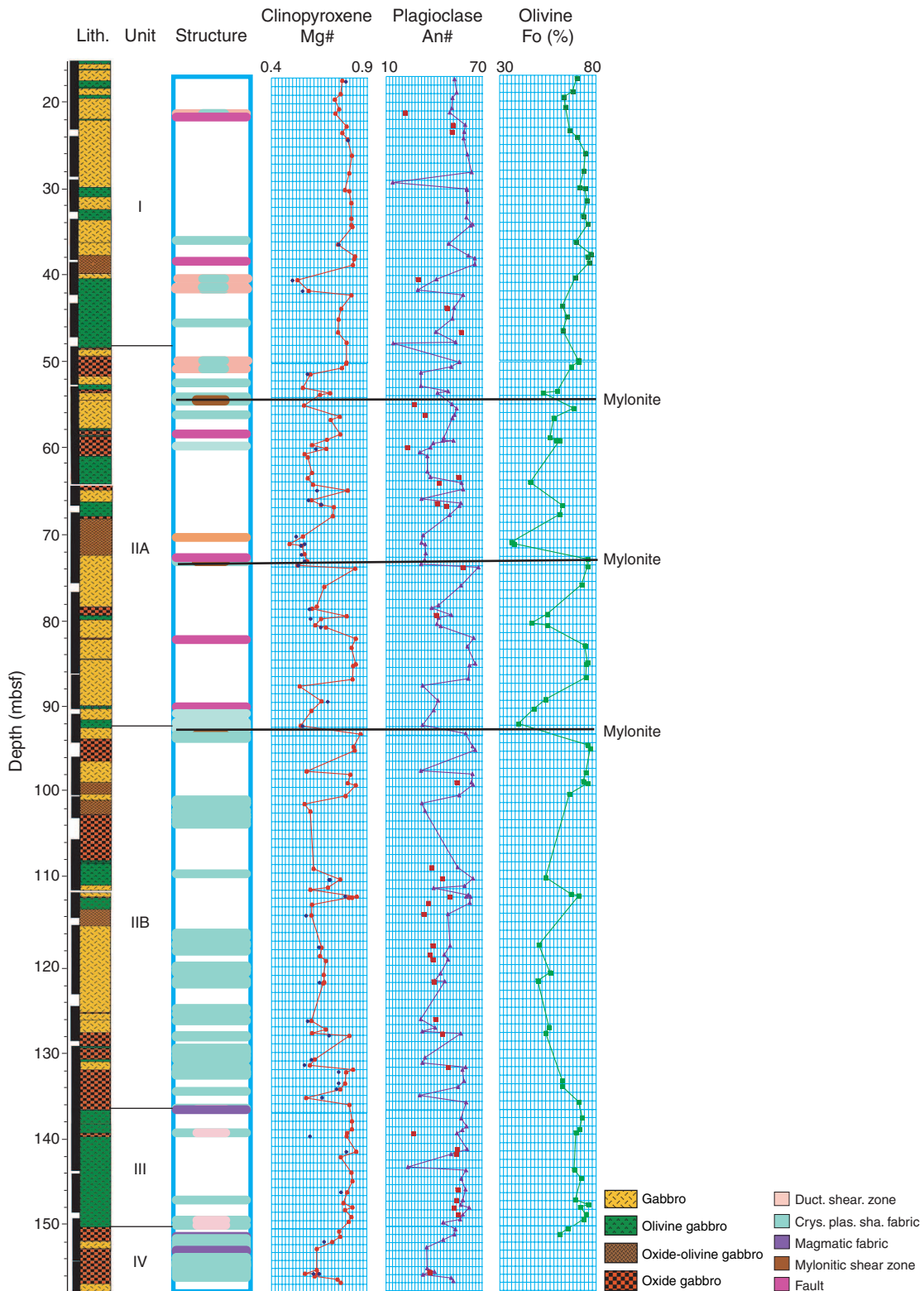


Figure F37. A. Plot showing downhole distribution of NiO in olivine and Cr₂O₃ in clinopyroxene (cpx) in Hole 1105A. The plot shows a good correlation between the two variables. B. Plot showing correlation between Fo in olivine and Cr₂O₃ in clinopyroxene. C. Plot showing relationship between olivine Fo% and MnO in both olivine and clinopyroxene. D. Plot showing the relationship between Mg# in clinopyroxene and NiO in olivine, showing a relatively good correlation. Data from Hole 1105A (this study) have been used for all four the plots. To preserve such good correlations, it is unlikely that the section has been significantly affected by postcumulus and highly allochthonous fractionated late-stage melt impregnation. Aberrant data from the main trend are, however, typically related to secondary cores (open symbols) and possible localized melt flow zones.

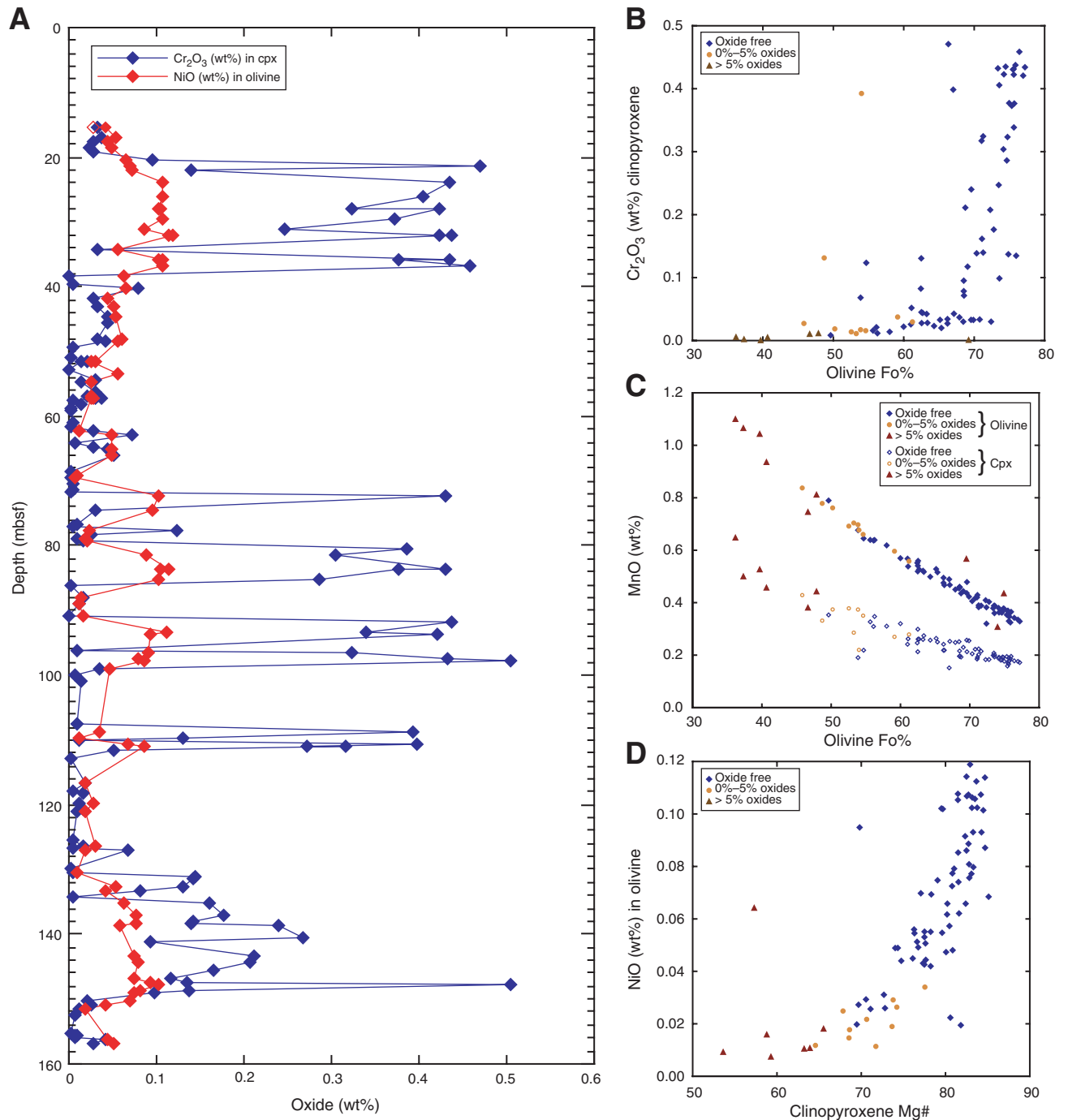


Figure F38. A. Plot showing relationship between Mg# of melt and TiO₂ in melt for a modeled primitive Atlantis II Transform basalt (from Johnson and Dick, 1992). Liquid lines of descent (LLDs) from perfect fractional crystallization (PFX) and boundary layer fractionation (BLF) modeling is plotted. BLF modeling assumes 60% fractionation in the boundary layer. Also plotted is melt in equilibrium with clinopyroxene from Hole 1105A gabbroic samples calculated with constant clinopyroxene (cpx)/melt partition coefficients of 0.23 for FeO/MgO (Roeder and Emslie, 1970) and 0.41 for TiO₂ for (Johnson and Kinzler, 1989). The equilibrium melt is color-coded on the basis of modal oxide abundance in the gabbroic sample. Note when constant Ti K_d is used, BLF modeling fits the liquid trend of the gabbroic rocks. **B.** Plot showing relationship between Mg# of melt and TiO₂ in melt for a modeled primitive Atlantis II Transform basalt (from Johnson and Dick, 1992). LLDs from PFX and BLF model results are plotted. BLF modeling assumes 60% fractionation in the boundary layer. Also plotted is melt in equilibrium with clinopyroxene from Hole 1105A gabbroic samples calculated with constant cpx/melt partition coefficient of 0.23 for FeO/MgO (Roeder and Emslie, 1970) but a variable coefficient for TiO₂. Variable K_d was used to calculate the TiO₂ in equilibrium melt with the clinopyroxene in the gabbroic rocks based on the relationship between D_{Ti} and Al(IV) (see Fig. F30, p. 86, and discussion in text). Note differences in LLDs produced for the plutonic suite and the limited compositional range of Atlantis II MORB in comparison to Hole 1105A plutonics.

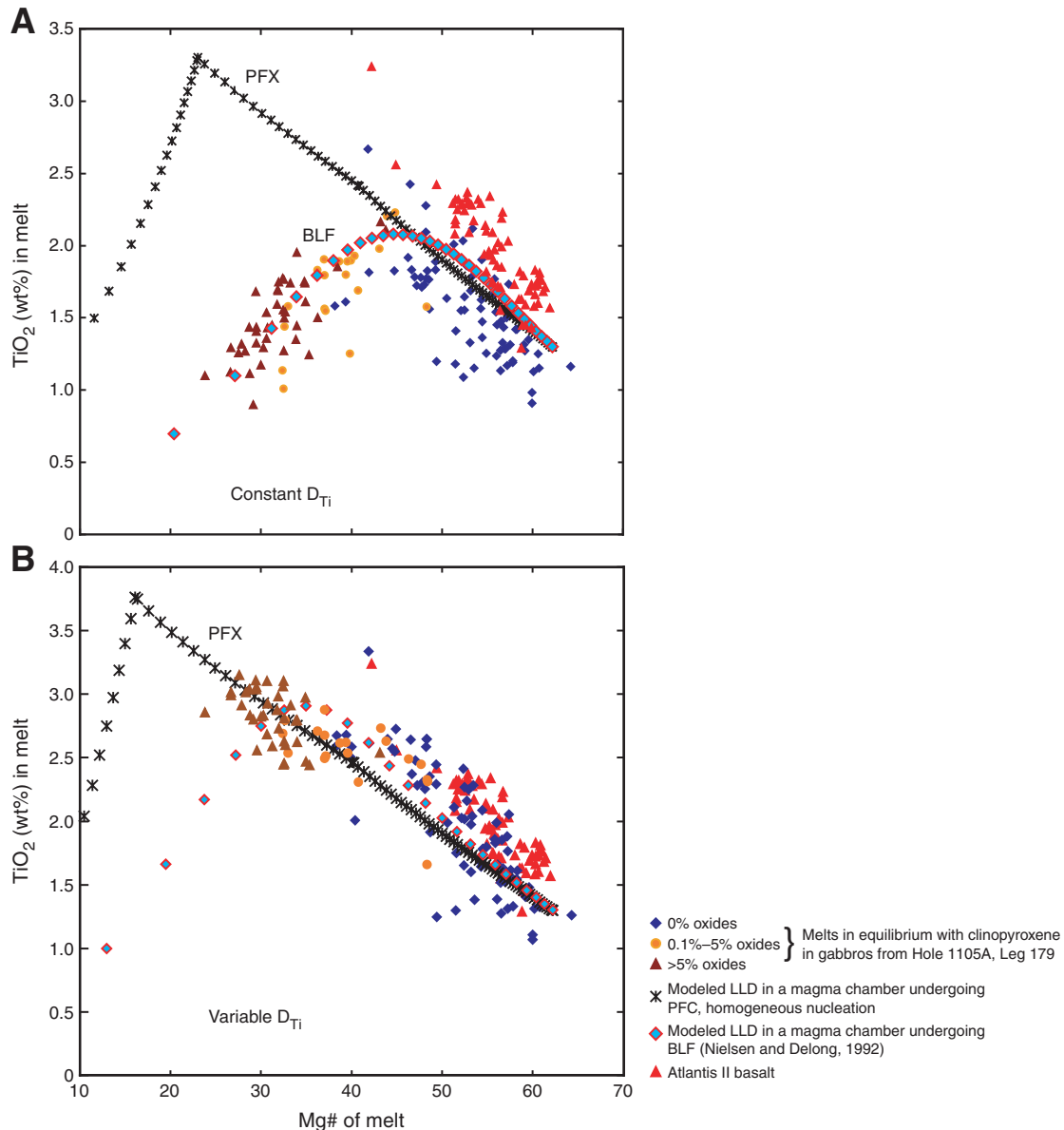


Figure F39. Examples of textural Category 1. Undeformed textures from Hole 1105A (cross-polarized light [XPL]). OL = olivine, PL = plagioclase, CPX = clinopyroxene. A, B. Sample 179-1105A-14R-3, 10–15 cm. C, D. Sample 179-1105A-16R-3, 35–39 cm. Refer to “Undeformed Texture: Textural Category 1,” p. 37, for description of thin sections.

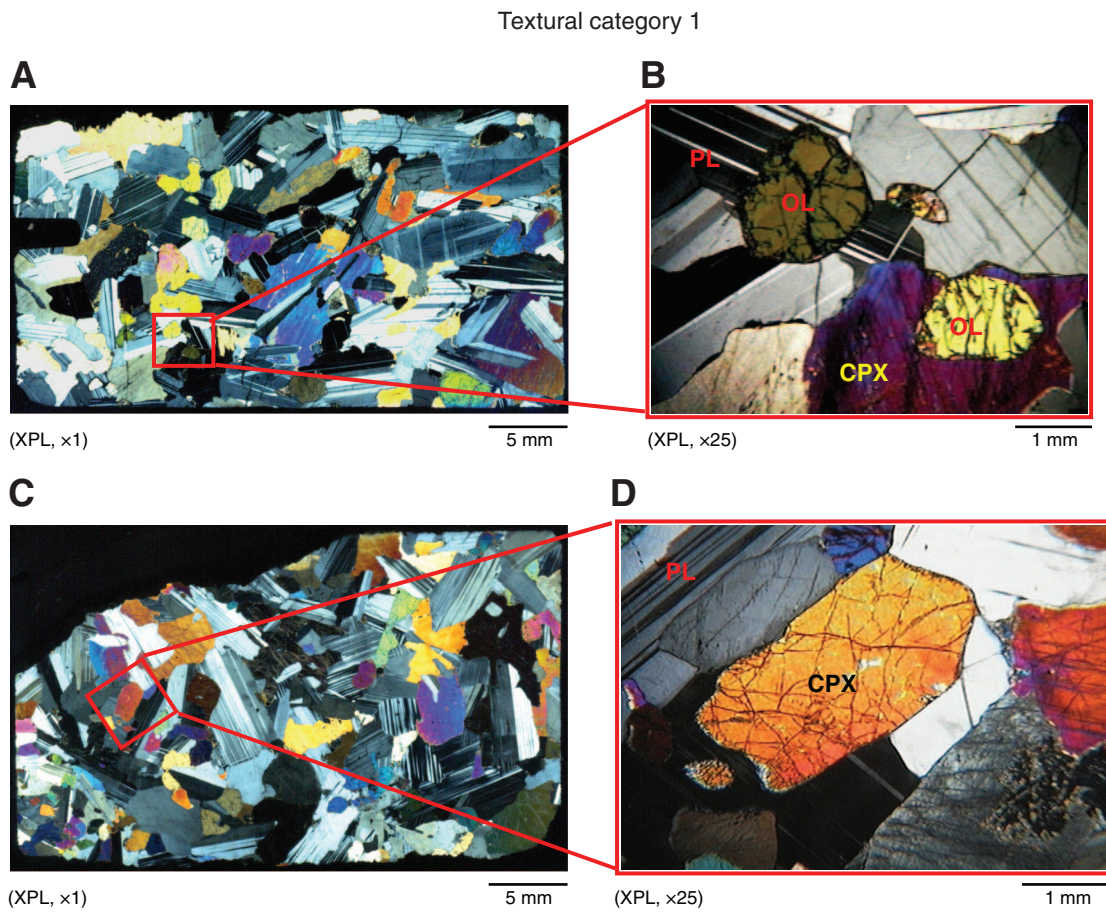


Figure F40. Examples of textural Category 2. Weakly recrystallized textures from Hole 1105A (cross-polarized light [XPL]). OL = olivine, PL = plagioclase, CPX = clinopyroxene. A, B. Sample 179-1105A-17R-2, 47–52 cm. B shows deformation bands in olivine grain. C, D. Sample 179-1105A-4R-1, 100–105 cm. Refer to “Weakly Recrystallized Texture: Textural Category 2,” p. 37, for description of thin sections.

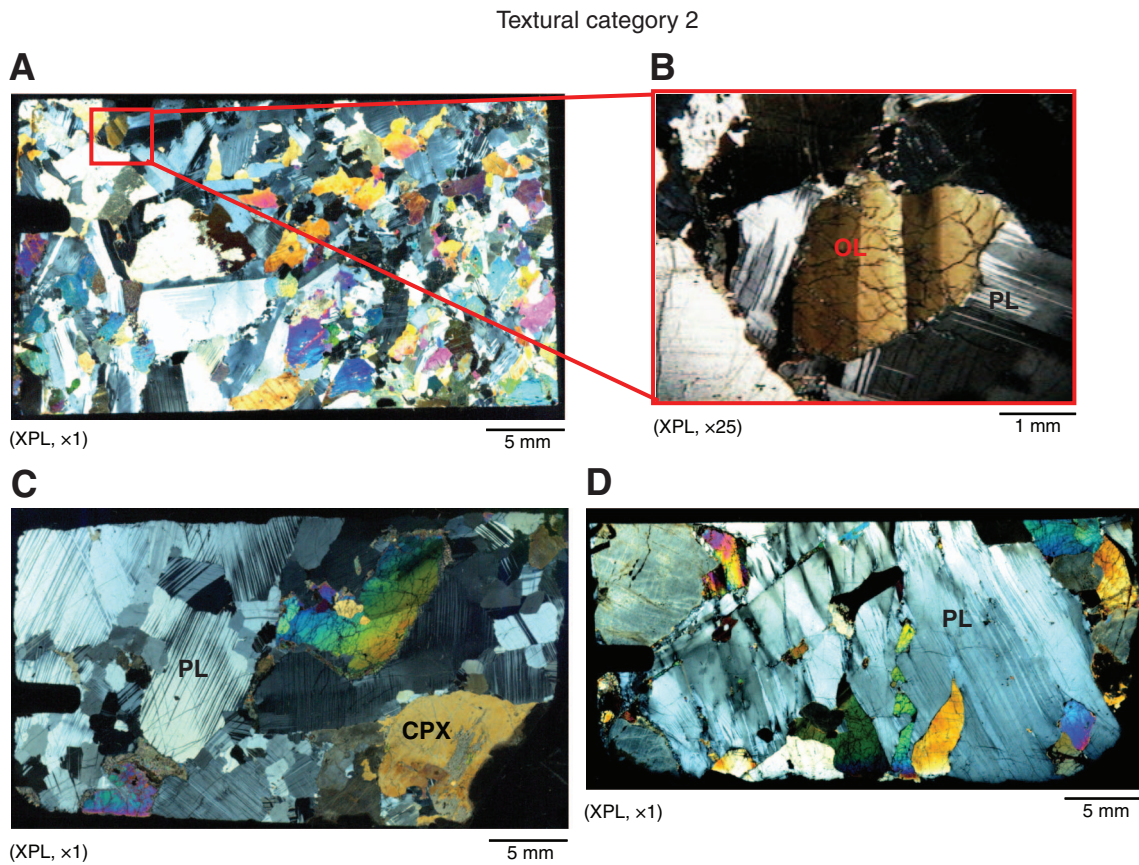
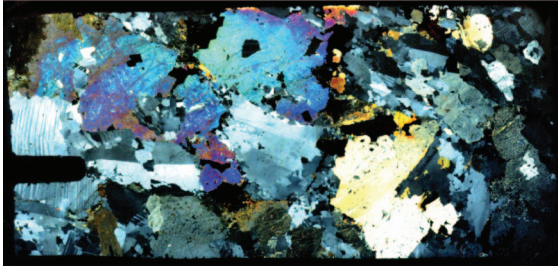


Figure F41. Examples of textural Category 3. Moderately recrystallized textures from Hole 1105A (cross-polarized light [XPL]). PL = plagioclase. A. Sample 179-1105A-9R-3, 129–134 cm. B. Sample 179-1105A-29R-1, 114–116 cm. C. Sample 179-1105A-29R-2, 133–139 cm. D. Sample 179-1105A-3R-1, 79–82 cm. Refer to “Weak to Moderately Recrystallized Texture: Textural Category 3,” p. 38, for description of thin sections.

Textural category 3

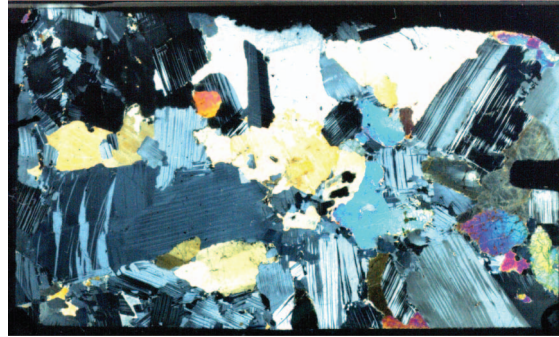
A



(XPL, x1)

5 mm

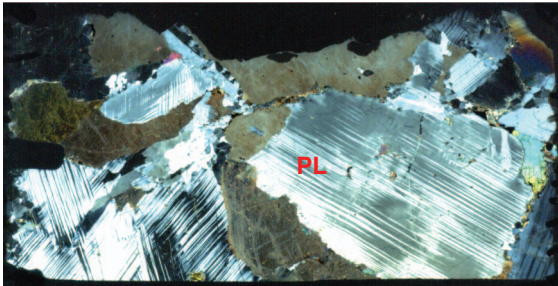
B



(XPL, x1)

5 mm

C



(XPL, x1)

5 mm

D



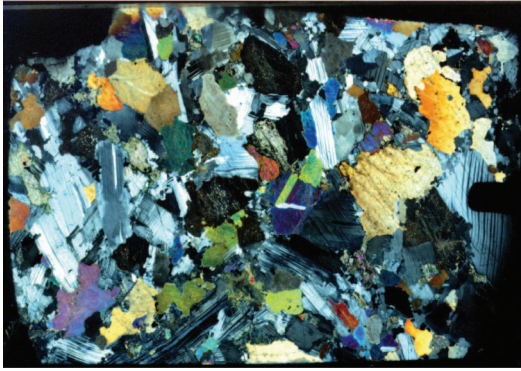
(XPL, x1)

5 mm

Figure F42. Examples of textural Category 4. Moderately recrystallized to porphyroclastic textures (cross-polarized light [XPL]). A. Sample 179-1105A-10R-3, 125–129 cm. B. Sample 179-1105A-29R-2, 69–74 cm. C. Sample 179-1105A-19R-4, 18–23 cm. D. Sample 179-1105A-13R-2, 44–49 cm. Refer to “Moderately Recrystallized to Porphyroclastic Texture: Textural Category 4,” p. 40, for description of thin sections.

Textural category 4

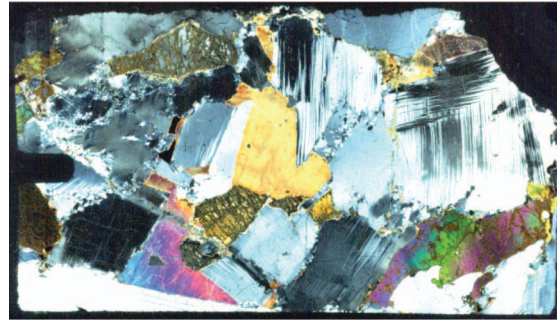
A



(XPL, x1)

5 mm

B



(XPL, x1)

5 mm

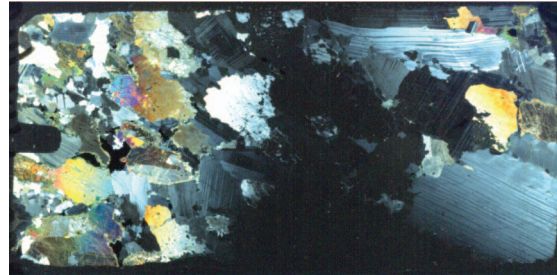
C



(XPL, x1)

5 mm

D



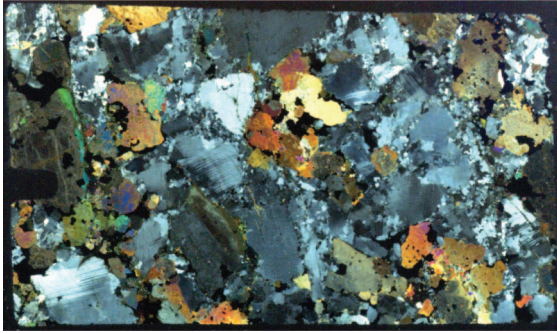
(XPL, x1)

5 mm

Figure F43. Examples of textural Category 5. Porphyroclastic textures from Hole 1105A (cross-polarized light [XPL]). A. Sample 179-1105A-11R-2, 3–6 cm. B. Sample 179-1105A-10R-3, 19–23 cm. C. Sample 179-1105A-11R-3, 64–68 cm. D. Sample 179-1105A-13R-2, 122–127 cm. Refer to “**Porphyroclastic Texture: Textural Category 5,**” p. 41, for description of thin sections.

Textural category 5

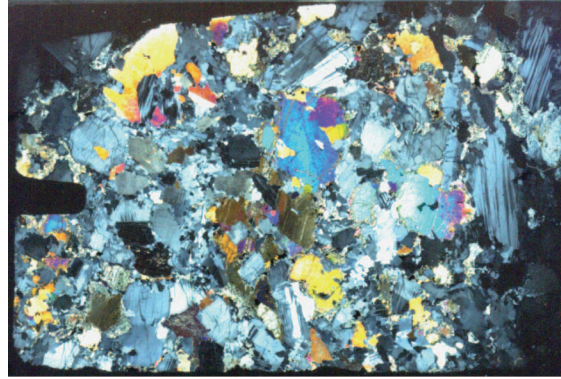
A



(XPL, x1)

5 mm

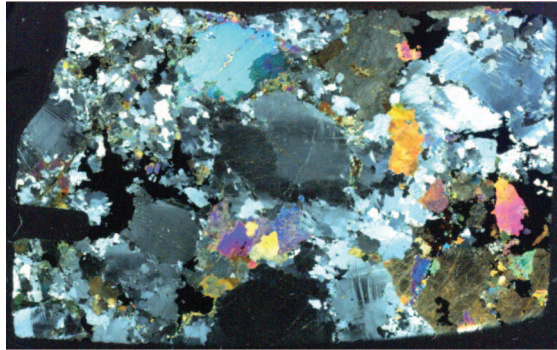
B



(XPL, x1)

5 mm

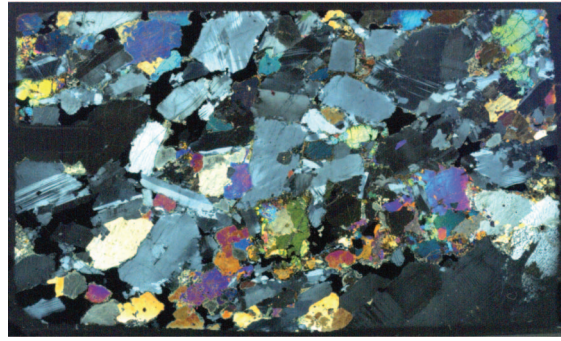
C



(XPL, x1)

5 mm

D



(XPL, x1)

5 mm

Figure F44. Examples of textural Category 6. Porphyroclastic textures from Hole 1105A (cross-polarized light [XPL]). CPX = clinopyroxene. **A, B.** Sample 179-1105A-7R-3, 103–106 cm. **B** shows a bent magmatic twin in a clinopyroxene porphyroclast. **C.** Sample 179-1105A-30R-2, 90–94 cm. **D.** Sample 179-1105A-17R-4, 0–7 cm. Refer to “**Porphyroclastic to Mylonitic Texture: Textural Category 6,**” p. 42, for description of thin sections.

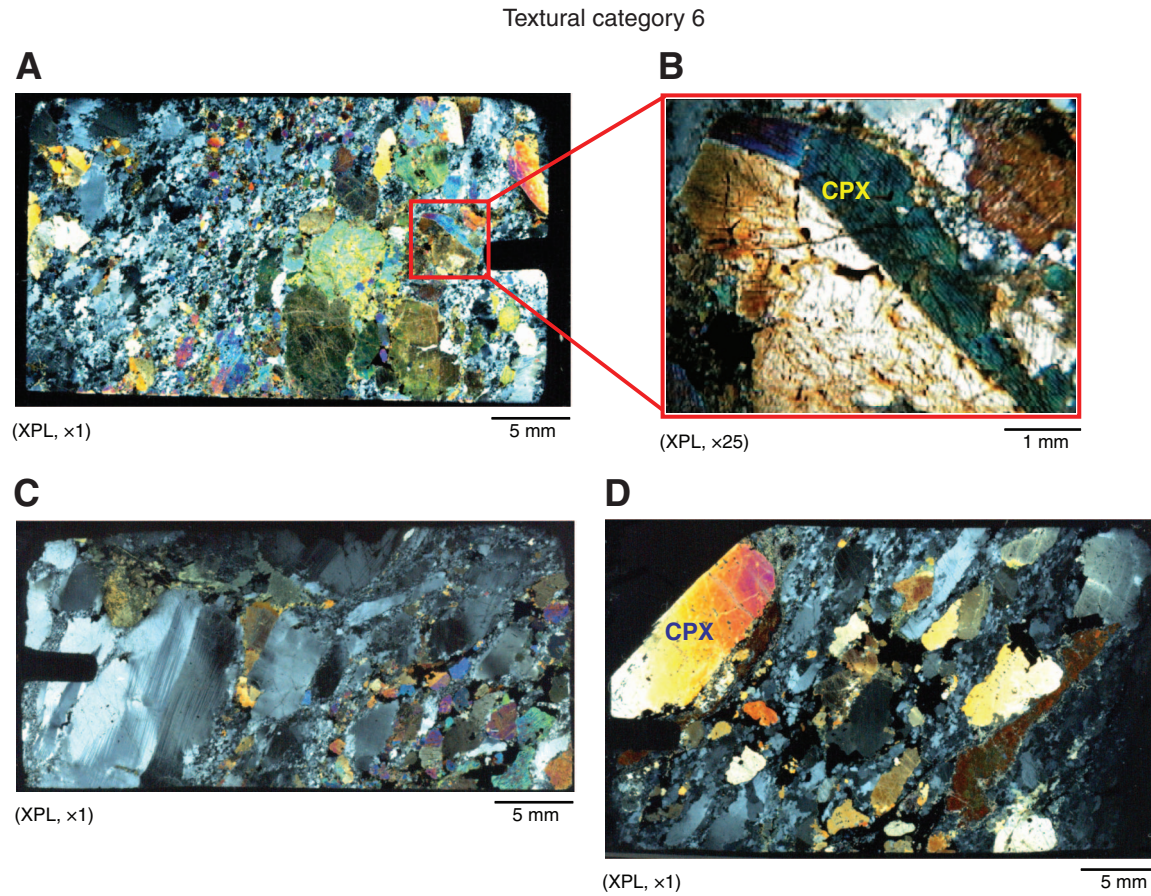


Figure F45. Examples of textural Categories 7 and 8. Porphyroclastic mylonitic textures (Category 7) and ultramylonitic textures (Category 8) from Hole 1105A (cross-polarized light [XPL]). A, B. Porphyritic to equigranular mylonitic textures; (A) Sample 179-1105A-15R-2, 39–43 cm; (B) Sample 179-1105A-23R-1, 53–57 cm. C–F. Ultramylonites grading to porphyroclastic mylonites; (C, D) Sample 179-1105A-5R-1, 137–142 cm; (E) Sample 179-1105A-12R-1, 51–57 cm; (F) Sample 179-1105A-8R-1, 56–60 cm. Refer to “**Mylonitic Texture: Textural Category 7,**” p. 43, and “**Ultramylonitic Texture: Textural Category 8,**” p. 44, for description of thin sections.

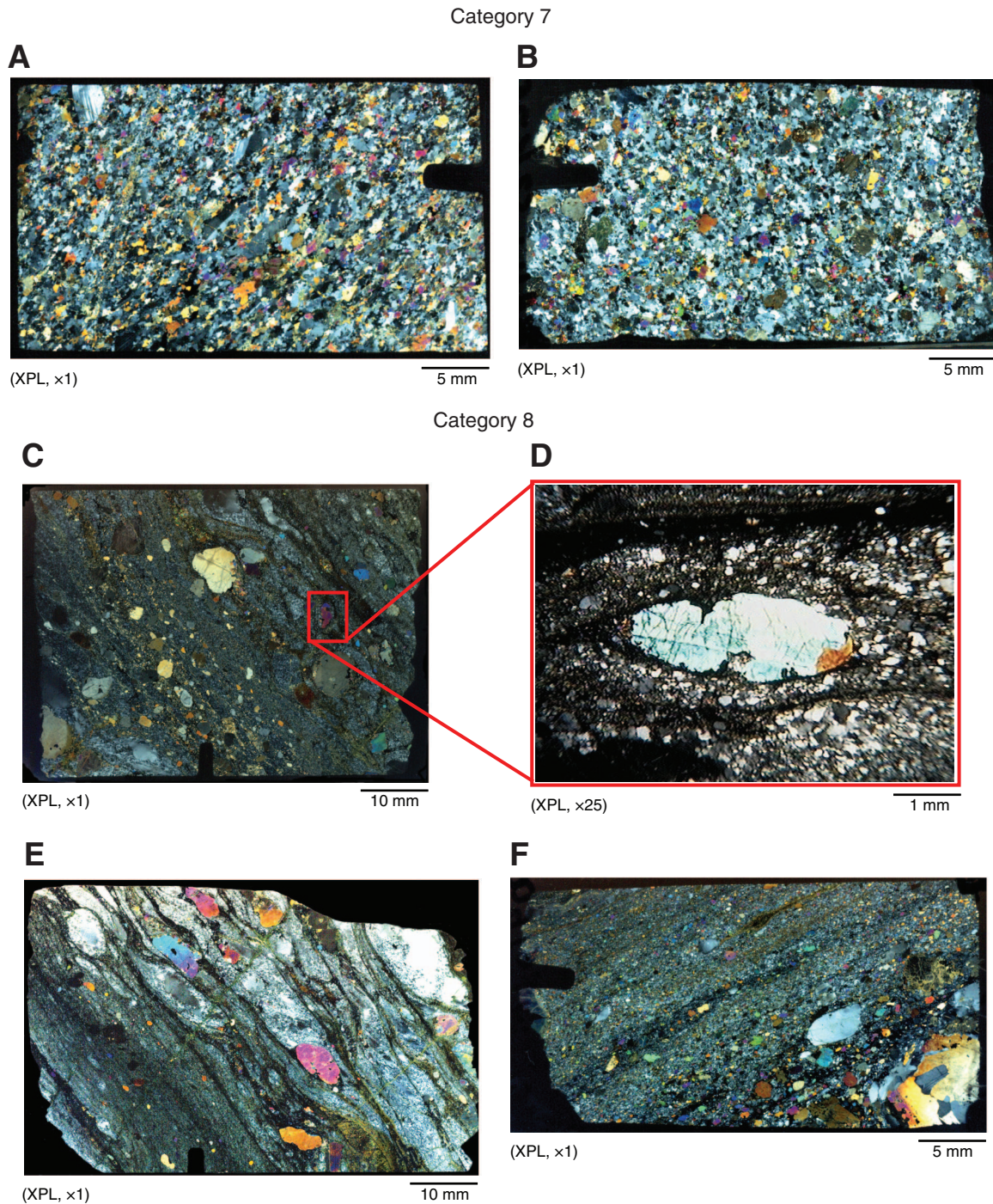


Figure F46. Correlation between the Formation MicroScanner (FMS) image, summary of visually defined lithologic intervals, deformation categories, and extents obtained from microstructural analyses of 147 thin sections from different depth intervals. Also shown are the distribution of shear zones obtained through FMS interpretation and distribution of crystal-plastic foliation fabric in Hole 1105A. FMS image varies between conductive zones (dark) and resistive zones (light). Conductive zones are typically oxide rich. Highest extents of deformation generally, but not always, correlate with conductive zones. Visually defined lithologic intervals and distribution of crystal-plastic foliation fabric are taken from and Shipboard Scientific Party (1999c).

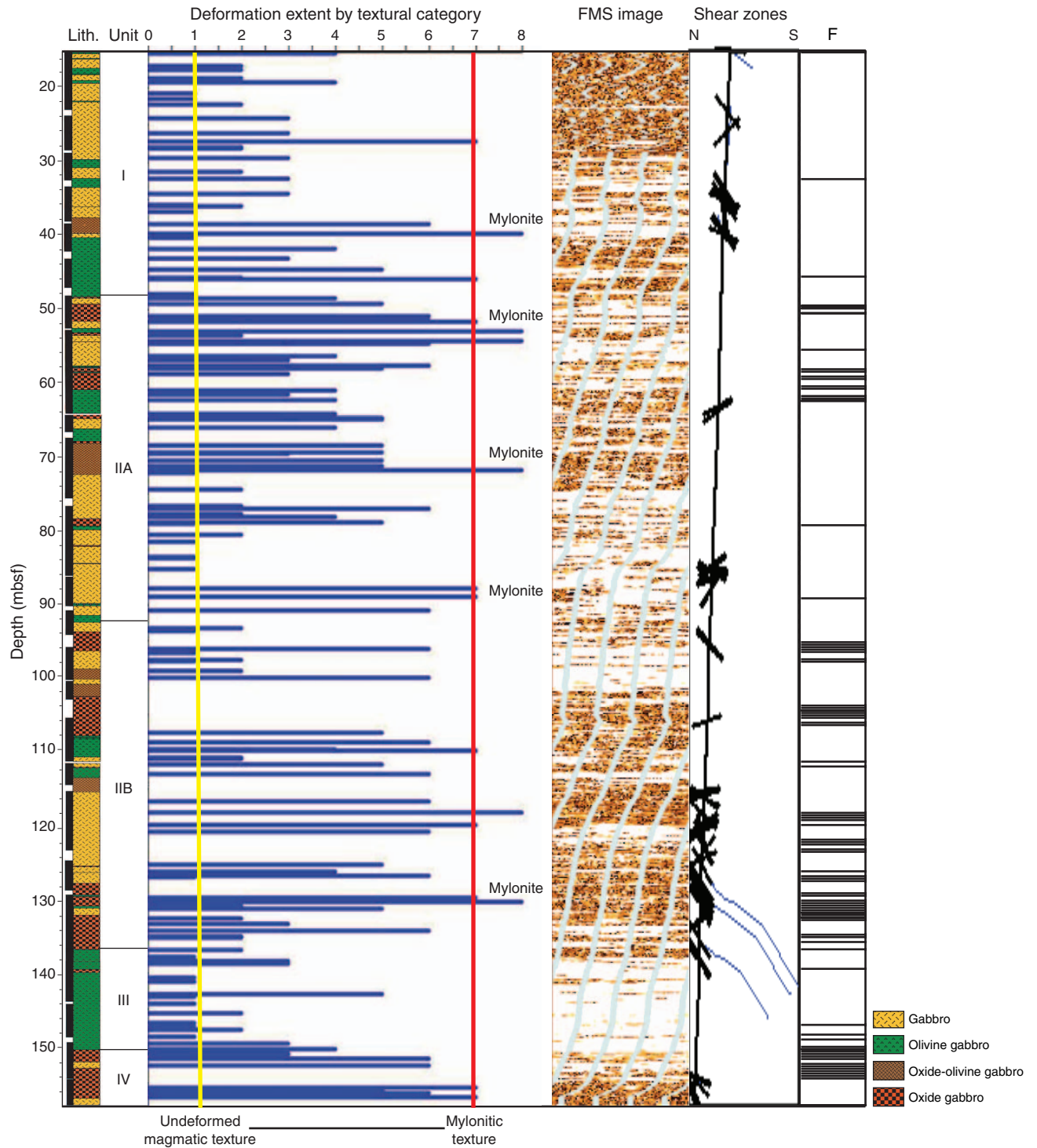


Figure F47. A. Deformation extents (textural category classes) for (A) oxide gabbro and oxide olivine gabbro, oxide > 5%, (B) oxide-bearing gabbro and oxide-bearing olivine gabbro, oxide 2%–5%, and (C) oxide-free (>2% and typical >>>2%–0%) gabbro and olivine gabbro. Based on the results from microstructural analysis of 147 thin sections from different depth intervals of Hole 1105A, the deformation extent is plotted vs. percentage (frequency) of samples in oxide gabbro and oxide olivine gabbro lithologies. In A the majority of the samples show a deformation extent of 5 and above. In B deformation extents for oxide-bearing gabbro and oxide-bearing olivine gabbro show values <3 in some samples, and some samples show deformation extent values >5, with an intermediate average. In general, a bimodal distribution of samples vs. deformation extent is observed for oxide-bearing lithologies. C. Deformation extents for oxide-free gabbro and oxide-free olivine gabbro with no oxides or small amounts of interstitial oxide (<<2%), the majority of the samples show a deformation extent of 4 and below, and the majority of samples are undeformed or only mildly deformed. The diagram suggests that abundant oxide minerals may present a weak rheology that can localize deformation. Whether the oxides indicate melt involvement and hypersolidus flow is difficult to determine from the subsolidus textures that now remain.

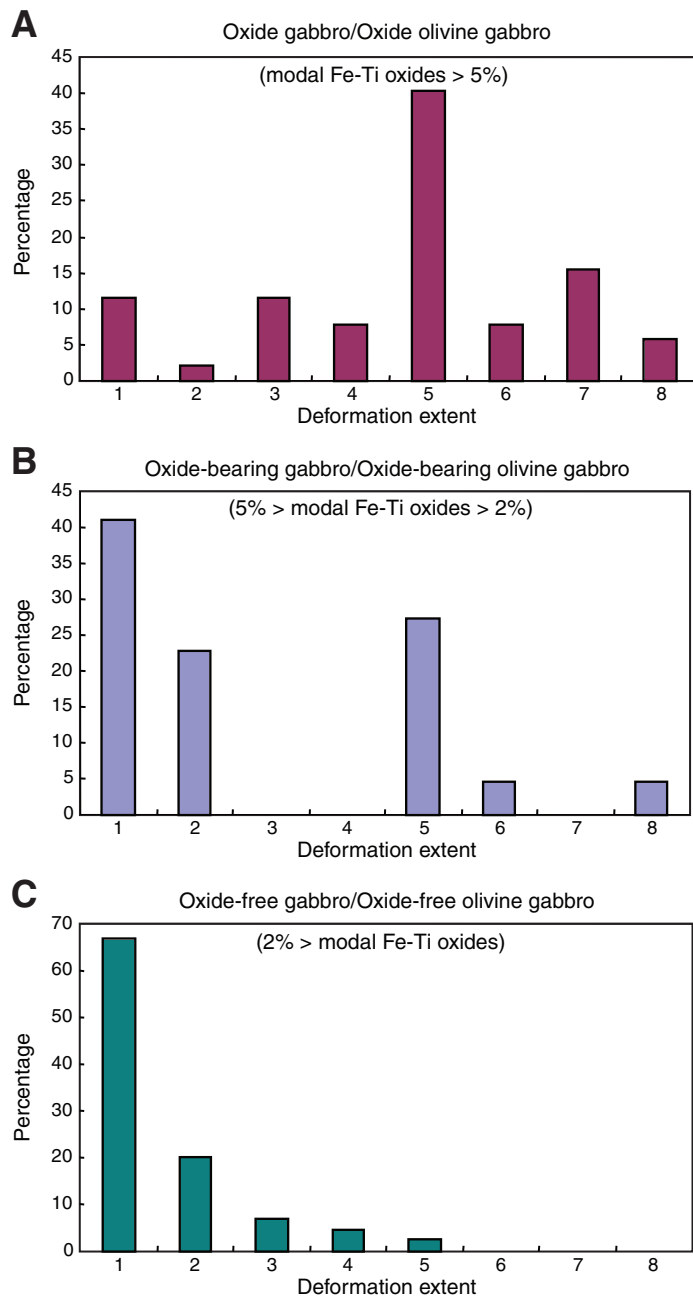


Figure F48. Downhole variation in whole-rock Mg# and estimated trapped melt (Banerji, 2005) over the depth range of 129–132 mbsf. Trapped melt was geochemically, not texturally, estimated using incompatible trace elements, mineral chemistry, modeled BLF liquid lines of descent, trace element K_d for major minerals, and modal analysis. Trapped melt percentages yield traditional textural classification as outlined by Irvine (1979, 1982): accumulates = 0%–7% trapped melt, mesocumulates = 7%–25% trapped melt, and orthocumulates = >25% trapped melt. Also note thin sections of undeformed oxide-free gabbroic Samples 179-1105A-25R-2, 55–62 cm (130.99 mbsf), and 25R-2, 84–90 cm (131.28 mbsf) (lower two thin section images) overlain by deformed oxide gabbroic Samples 25R-1, 83–89 cm (129.83 mbsf), and 25R-2, 3–8 cm (130.47 mbsf). Lowest estimates of trapped melt are associated with the most deformed rocks; oxide-precipitating melts did not necessarily induce deformation starting at hypersolidus temperatures.

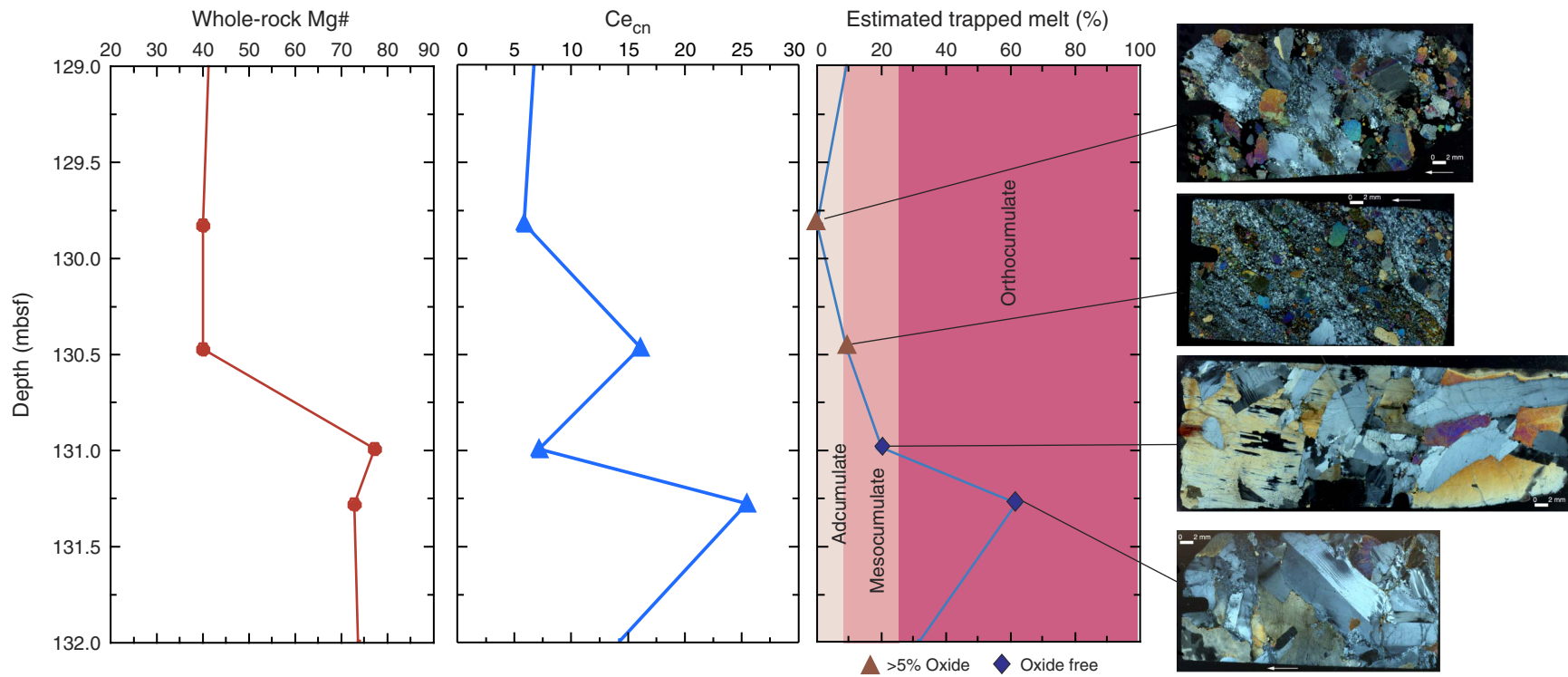


Table T1. Modal analysis of gabbros. (See table note. Continued on next two pages.)

Core, section, interval (cm)	Depth (mbsf)	Phase (mod%)					
		Plagioclase	Clinopyroxene	Olivine	Orthopyroxene	Inverted pigeonite	Opaque oxides
179-1105A-							
1R-1, 21-24	15.21	NA	NA	NA	NA	NA	NA
1R-1, 29-32	15.29	53.56	43.73	2.71	0.00	0.00	0.00
1R-2, 80-83	16.88	60.89	29.44	9.68	0.00	0.00	0.00
1R-3, 3-6	17.48	62.63	36.00	1.37	0.00	0.00	0.00
1R-3, 120-125	18.65	63.37	29.90	6.73	0.00	0.00	0.00
1R-4, 25-28	19.15	80.48	19.52	0.00	0.00	0.00	0.00
1R-5, 25-31	20.61	73.61	23.96	2.43	0.00	0.00	0.00
1R-5, 102-105	21.38	58.64	39.23	2.13	0.00	0.00	0.00
1R-6, 33-36	22.15	51.56	47.83	0.60	0.00	0.00	0.00
2R-1, 31-35	24.01	53.70	40.78	5.52	0.00	0.00	0.00
2R-2, 93-98	26.06	51.37	42.39	6.24	0.00	0.00	0.00
2R-2, 127-130	26.40	NA	NA	NA	NA	NA	NA
2R-3, 69-72	27.25	NA	NA	NA	NA	NA	NA
2R-4, 6-11	28.00	57.53	36.48	5.99	0.00	0.00	0.00
2R-4, 20-23	28.14	53.67	28.65	17.69	0.00	0.00	0.00
3R-1, 79-82	29.49	64.30	27.66	8.04	0.00	0.00	0.00
3R-2, 109-113	31.29	59.18	22.58	18.25	0.00	0.00	0.00
3R-3, 38-41	32.08	59.63	35.76	4.61	0.00	0.00	0.00
3R-3, 54-57	32.24	53.04	38.86	8.10	0.00	0.00	0.00
4R-1, 100-105	34.30	74.18	13.08	12.74	0.00	0.00	0.00
4R-2, 123-126	35.71	50.55	33.15	16.30	0.00	0.00	0.00
4R-3, 16-19	35.98	58.62	37.58	3.81	0.00	0.00	0.00
4R-3, 90-93	36.72	66.00	26.36	7.64	0.00	0.00	0.00
5R-1, 16-21	38.46	39.83	24.28	17.18	0.00	0.00	18.71
5R-1, 137-142	39.67	46.43	25.25	0.00	3.73	0.00	24.59
5R-2, 44-48	40.22	31.89	59.98	8.13	0.00	0.00	0.00
5R-3, 46-52	41.74	57.08	36.30	6.62	0.00	0.00	0.00
6R-1, 18-23	42.98	67.92	29.27	2.81	0.00	0.00	0.00
6R-2, 26-30	44.52	50.76	36.64	12.61	0.00	0.00	0.00
6R-2, 142-146	45.68	55.04	36.93	8.04	0.00	0.00	0.00
6R-3, 6-8	45.82	NA	NA	NA	NA	NA	NA
7R-1, 19-24	47.99	71.02	24.84	4.14	0.00	0.00	0.00
7R-1, 74-78	48.54	71.52	24.35	4.13	0.00	0.00	0.00
7R-2, 13-18	49.26	42.41	37.96	0.00	0.00	0.00	19.63
7R-3, 22-27	50.85	60.75	33.50	0.00	0.00	0.00	5.75
7R-3, 86-91	51.49	61.47	31.57	6.96	0.00	0.00	0.00
7R-3, 103-106	51.66	50.77	43.19	1.64	0.00	0.00	4.40
8R-1, 56-60	52.96	NA	NA	NA	NA	NA	NA
8R-1, 109-114	53.49	68.58	26.52	4.90	0.00	0.00	0.00
8R-2, 43-47	54.25	64.15	35.85	0.00	0.00	0.00	0.00
8R-2, 81-86	54.63	84.95	12.24	2.81	0.00	0.00	0.00
8R-3, 110-114	56.32	75.52	24.48	0.00	0.00	0.00	0.00
8R-4, 42-46	56.95	57.64	38.31	4.05	0.00	0.00	0.00
8R-4, 74-78	57.27	60.78	31.37	3.92	0.00	0.00	3.92
8R-4, 74-78	57.27	52.81	35.96	5.62	0.00	0.00	5.62
9R-1, 20-24	57.60	43.20	39.92	0.00	0.00	0.00	16.88
9R-1, 67-71	58.07	84.04	15.96	0.00	0.00	0.00	0.00
9R-1, 128-134	58.68	11.42	75.55		0.00	9.22	3.81
9R-2, 17-20	59.07	33.33	21.44	37.30	0.00	0.00	7.93
9R-3, 66-72	60.93	61.76	25.21	0.00	0.00	8.79	4.24
9R-3, 129-134	61.56	39.44	46.71	0.00	0.00	6.20	7.66
9R-4, 59-63	62.28	59.17	35.56	0.00	0.00	2.84	2.43
10R-1, 98-102	62.98	62.08	21.68	16.24	0.00	0.00	0.00
10R-2, 77-82	64.12	31.70	47.09	0.00	0.00	0.00	21.20
10R-2, 132-137	64.67	76.39	20.93	0.00	0.00	0.00	2.68
10R-3, 19-23	64.94	60.87	17.40	21.73	0.00	0.00	0.00
10R-3, 125-129	66.00	50.26	43.87	5.87	0.00	0.00	0.00
11R-1, 81-86	67.81	NA	NA	NA	NA	NA	NA
11R-2, 3-6	68.43	54.23	29.33	0.00	0.00	0.00	16.43
11R-2, 89-94	69.29	58.86	7.84	21.79	0.00	0.00	11.51
11R-2, 110-115	69.50	35.79	35.88	7.26	0.00	0.99	20.08
11R-3, 64-68	70.54	60.72	28.62	0.00	0.00	0.00	10.67
11R-3, 142-147	71.32	49.60	44.35	0.00	0.00	0.00	6.05
12R-1, 51-57	71.81	52.44	22.43	0.00	1.35	0.00	23.78
12R-1, 91-97	72.21	45.65	40.94	13.41	0.00	0.00	0.00
12R-3, 12-16	74.37	46.86	46.76	6.39	0.00	0.00	0.00

Table T1 (continued).

Core, section, interval (cm)	Depth (mbsf)	Phase (mod%)					Inverted pigeonite	Opaque oxides
		Plagioclase	Clinopyroxene	Olivine	Orthopyroxene			
13R-1, 38-42	76.68	49.16	43.31	0.00	0.00	0.00	7.53	
13R-1, 68-73	76.98	56.61	22.15	0.00	0.00	3.25	17.99	
13R-2, 12-16	77.82	53.99	38.96	7.06	0.00	0.00	0.00	
13R-2, 44-49	78.14	61.59	34.29	0.00	0.00	2.78	1.34	
13R-2, 122-127	78.92	54.28	24.84	10.23	0.00	0.00	10.65	
13R-3, 11-15	79.15	50.82	38.96	7.40	0.00	0.00	2.83	
13R-4, 7-11	80.51	47.29	52.71	0.00	0.00	0.00	0.00	
14R-1, 55-60	81.55	56.76	34.37	8.88	0.00	0.00	0.00	
14R-2, 114-119	83.55	56.58	30.27	13.15	0.00	0.00	0.00	
14R-3, 10-15	83.74	58.95	28.54	12.51	0.00	0.00	0.00	
14R-4, 22-27	85.31	63.23	28.82	7.96	0.00	0.00	0.00	
15R-1, 14-18	86.14	51.32	23.71	0.00	0.00	0.00	24.97	
15R-2, 39-43	87.89	53.37	26.28	18.23	0.00	0.00	2.11	
15R-3, 7-12	89.04	52.67	30.98	9.49	0.00	0.00	6.86	
16R-1, 22-27	90.82	58.18	26.06	3.23	0.00	0.00	12.53	
16R-2, 124-128	93.17	66.00	34.00	0.00	0.00	0.00	0.00	
16R-2, 133-139	93.26	51.90	40.00	8.10	0.00	0.00	0.00	
16R-3, 35-39	93.69	55.20	23.70	21.10	0.00	0.00	0.00	
17R-1, 51-55	96.11	37.21	43.75	0.00	0.00	4.33	14.71	
17R-1, 94-99	96.54	50.80	33.60	15.60	0.00	0.00	0.00	
17R-2, 47-52	97.49	53.47	40.40	6.13	0.00	0.00	0.00	
17R-2, 75-80	97.77	47.60	37.92	14.48	0.00	0.00	0.00	
17R-3, 59-65	99.04	72.13	10.97	16.90	0.00	0.00	0.00	
17R-4, 0-7	99.95	50.68	32.50	0.00	0.00	0.00	16.82	
18R-1, 62-68	100.82	NA	NA	NA	NA	NA	NA	
19R-2, 80-85	107.50	46.33	42.96	0.00	0.00	0.00	10.71	
19R-3, 75-80	108.80	57.54	23.86	16.84	0.00	0.00	1.76	
19R-4, 18-23	109.69	79.47	9.91	6.54	0.00	0.00	4.09	
19R-4, 43-46	109.94	57.77	29.99	4.81	0.00	0.00	7.42	
20R-1, 95-100	110.75	65.25	14.79	19.96	0.00	0.00	0.00	
20R-1, 111-117	110.91	65.85	34.15	0.00	0.00	0.00	0.00	
21R-1, 12-16	110.92	59.07	29.23	11.69	0.00	0.00	0.00	
21R-1, 89-94	111.69	54.38	16.40	0.00	0.00	0.00	29.23	
21R-2, 84-88	112.98	62.97	33.37	0.00	0.00	0.00	3.66	
22R-2, 20-25	116.70	50.05	44.43	1.12	0.00	0.00	4.39	
22R-3, 7-11	117.75	NA	NA	NA	NA	NA	NA	
22R-3, 63-69	118.31	74.62	23.09	0.00	0.00	0.00	2.30	
23R-1, 53-57	119.93	59.10	26.20	14.70	0.00	0.00	0.00	
23R-1, 142-148	120.82	61.35	33.23	3.61	0.00	0.00	1.81	
23R-2, 1-5	120.91	65.31	25.00	9.69	0.00	0.00	0.00	
24R-1, 93-98	125.33	54.70	43.28	0.00	0.00	0.00	2.02	
24R-2, 49-53	126.32	74.07	19.87	6.06	0.00	0.00	0.00	
24R-2, 94-98	126.77	4.17	64.75	0.00	0.00	0.00	31.08	
24R-2, 121-126	127.04	60.07	31.63	8.30	0.00	0.00	0.00	
24R-3, 116-120	128.32	NA	NA	NA	NA	NA	NA	
25R-1, 83-89	129.83	47.10	42.60	0.00	0.00	0.00	10.30	
25R-2, 3-8	130.47	45.38	24.85	2.05	0.00	0.00	27.72	
25R-2, 55-62	130.99	56.26	43.74	0.00	0.00	0.00	0.00	
25R-2, 84-90	131.28	67.57	32.43	0.00	0.00	0.00	0.00	
25R-3, 79-82	132.62	61.01	35.32	3.67	0.00	0.00	0.00	
25R-4, 31-38	133.33	59.50	22.90	17.60	0.00	0.00	0.00	
26R-1, 32-38	134.32	19.19	69.49	0.00	0.00	0.00	11.31	
26R-1, 115-121	135.15	45.51	42.79	11.71	0.00	0.00	0.00	
26R-3, 20-26	136.96	49.38	44.85	5.77	0.00	0.00	0.00	
26R-3, 117-122	137.93	54.55	45.45	0.00	0.00	0.00	0.00	
26R-4, 24-30	138.41	66.20	30.40	3.40	0.00	0.00	0.00	
27R-1, 8-12	138.78	60.60	33.20	6.20	0.00	0.00	0.00	
27R-1, 82-88	139.52	NA	NA	NA	NA	NA	NA	
27R-2, 81-87	140.69	69.10	30.90	0.00	0.00	0.00	0.00	
27R-3, 27-33	141.29	84.99	15.01	0.00	0.00	0.00	0.00	
27R-4, 29-31	142.81	NA	NA	NA	NA	NA	NA	
27R-4, 71-76	143.23	44.18	54.45	1.36	0.00	0.00	0.00	
28R-1, 54-60	144.24	48.80	30.50	20.70	0.00	0.00	0.00	
28R-2, 78-84	145.58	77.94	22.06	0.00	0.00	0.00	0.00	
28R-3, 61-66	146.87	67.29	28.09	4.62	0.00	0.00	0.00	
28R-3, 115-119	147.41	29.50	18.40	52.10	0.00	0.00	0.00	
28R-4, 8-15	147.76	48.63	46.81	4.56	0.00	0.00	0.00	
29R-1, 21-27	148.61	49.65	35.00	15.34	0.00	0.00	0.00	

Table T1 (continued).

Core, section, interval (cm)	Depth (mbsf)	Phase (mod%)					Inverted pigeonite	Opaque oxides
		Plagioclase	Clinopyroxene	Olivine	Orthopyroxene			
29R-1, 75–80	149.15	63.52	23.32	13.17	0.00	0.00	0.00	
29R-1, 114–116	149.54	NA	NA	NA	NA	NA	NA	
29R-2, 69–74	150.36	70.83	15.43	13.74	0.00	0.00	0.00	
29R-2, 133–139	151.00	67.58	31.90	0.52	0.00	0.00	0.00	
29R-3, 60–66	151.69	73.00	23.59	1.75	0.00	0.00	1.66	
29R-4, 17–22	152.57	53.58	33.03	0.00	0.00	1.21	12.19	
30R-2, 47–53	155.23	NA	NA	NA	NA	NA	NA	
30R-2, 90–94	155.66	74.70	19.46	0.00	0.00	0.00	5.85	
30R-2, 90–94-laminated	155.70	60.44	35.52	0.00	0.00	0.00	4.04	
30R-2, 125–130	156.01	40.70	45.60	0.00	0.00	0.00	13.70	
30R-3, 30–34	156.40	55.96	33.53	10.51	0.00	0.00	0.00	
30R-3, 72–76	156.82	52.48	36.22	11.30	0.00	0.00	0.00	

Note: NA = not analyzed.

Table T2. Major element analysis of gabbros. (Continued on next two pages.)

Core, section, interval (cm)	Depth (mbsf)	Major element oxide (wt%)											
		LOI	SiO ₂	Al ₂ O ₃	TiO ₂	MnO	CaO	MgO	Fe ₂ O ₃ T	Na ₂ O	K ₂ O	P ₂ O ₅	Total
179-1105A-													
1R-1, 21-24	15.21	0.74	64.62	17.82	0.36	0.05	1.88	2.11	2.96	9.39	0.11	0.05	99.33
1R-1, 29-32	15.29	0.91	51.42	16.68	0.39	0.12	12.48	10.07	7.04	3.04	0.00	0.04	101.28
1R-2, 80-83	16.88	0.78	52.13	16.99	0.38	0.13	12.34	8.49	7.01	3.32	0.06	0.02	100.87
1R-3, 3-6	17.48	0.87	51.98	15.77	0.51	0.15	12.18	9.21	7.62	2.97	0.01	0.03	100.45
1R-3, 120-125	18.65	0.64	50.99	16.29	0.43	0.13	12.27	8.89	7.49	3.14	0.04	0.03	99.70
1R-4, 25-28	19.15	0.95	56.09	15.61	0.75	0.13	9.35	6.57	6.77	5.29	0.08	0.03	100.67
1R-5, 25-31	20.61	1.36	50.55	21.09	0.23	0.10	10.75	7.90	6.21	3.15	0.05	0.02	100.05
1R-5, 102-105	21.38	1.08	52.54	17.23	0.38	0.12	12.96	8.36	6.95	2.92	0.07	0.04	101.56
1R-6, 33-36	22.15	0.46	51.36	15.58	0.38	0.11	14.73	10.48	5.71	2.50	0.04	0.03	100.92
2R-1, 31-35	24.01	1.62	51.42	19.81	0.23	0.08	12.99	8.72	5.12	2.72	0.02	0.02	101.13
2R-2, 93-98	26.06	1.13	52.04	17.19	0.40	0.10	14.35	8.67	5.52	2.58	0.08	0.03	100.96
2R-2, 127-130	26.40	1.55	50.90	15.57	0.63	0.11	14.75	10.97	6.00	2.13	0.00	0.05	101.10
2R-3, 69-72	27.25	1.36	57.13	16.43	0.36	0.09	10.00	7.07	4.52	5.03	0.16	0.04	100.83
2R-4, 6-11	28.00	0.89	51.29	17.02	0.39	0.12	13.32	9.82	6.48	2.41	0.06	0.03	100.95
2R-4, 20-23	28.14	1.07	50.08	17.20	0.37	0.11	12.26	10.85	6.76	2.38	0.04	0.03	100.08
3R-1, 79-82	29.49	0.67	50.72	17.08	0.29	0.10	13.48	10.73	5.80	2.43	0.05	0.03	100.71
3R-2, 109-113	31.29	1.30	51.16	19.34	0.24	0.08	13.19	8.23	4.94	2.78	0.06	0.01	100.04
3R-3, 38-41	32.08	1.07	50.10	16.94	0.30	0.10	13.99	9.98	5.44	2.19	0.05	0.03	99.12
3R-3, 54-57	32.24	0.77	51.02	16.60	0.36	0.10	14.34	10.60	5.43	2.23	0.03	0.01	100.72
4R-1, 100-105	34.30	0.67	52.21	17.12	0.39	0.12	11.63	8.92	7.23	3.25	0.06	0.03	100.97
4R-2, 123-126	35.71	0.67	51.02	15.63	0.35	0.10	15.50	10.20	4.71	2.02	0.04	0.02	99.59
4R-3, 16-19	35.98	0.68	51.21	17.29	0.41	0.08	14.74	9.50	4.56	2.31	0.00	0.03	100.13
4R-3, 90-93	36.72	0.69	50.78	18.67	0.29	0.09	13.46	9.51	5.08	2.52	0.03	0.03	100.46
5R-1, 16-21	38.46	0.54	39.59	10.64	3.19	0.34	11.12	7.82	21.28	2.87	0.14	2.33	99.32
5R-1, 137-142	39.67	0.87	41.84	11.65	4.53	0.33	9.35	4.86	22.82	3.08	0.09	1.61	100.16
5R-2, 44-48	40.22	1.05	51.83	15.76	0.37	0.12	13.15	10.28	6.96	2.47	0.04	0.05	101.03
5R-3, 46-52	41.74	0.74	51.77	16.64	0.52	0.14	11.43	8.44	8.28	3.21	0.07	0.04	100.54
6R-1, 18-23	42.98	1.56	50.18	16.25	0.54	0.16	10.59	10.51	9.74	2.81	0.00	0.05	100.84
6R-2, 26-30	44.52	0.71	51.95	18.63	0.60	0.14	10.92	7.10	7.83	3.42	0.10	0.05	100.73
6R-2, 142-146	45.68	1.17	52.50	16.66	0.40	0.11	12.70	8.55	6.76	2.97	0.08	0.03	100.77
6R-3, 6-8	45.82	0.68	60.19	18.33	0.27	0.05	6.84	3.69	2.95	7.11	0.18	0.02	99.62
7R-1, 19-24	47.99	0.38	51.49	17.80	0.32	0.11	12.47	8.83	6.25	3.00	0.05	0.05	100.38
7R-1, 74-78	48.54	0.69	51.29	14.95	0.49	0.13	13.82	9.05	6.56	2.66	0.05	0.06	99.06
7R-2, 13-18	49.26	0.00	38.05	8.42	6.77	0.41	8.51	6.36	30.33	2.11	0.04	0.07	101.07
7R-3, 22-27	50.85	0.00	40.71	12.58	5.67	0.28	6.64	2.73	26.07	3.98	0.17	0.84	99.66
7R-3, 86-91	51.49	0.42	50.65	16.21	0.49	0.14	10.76	9.55	9.44	3.17	0.08	0.10	100.59
7R-3, 103-106	51.66	0.29	50.81	11.65	1.21	0.23	11.97	8.67	13.32	2.87	0.05	0.04	100.81
8R-1, 56-60	52.96	0.02	43.84	10.99	3.82	0.30	9.40	4.54	22.33	3.67	0.18	1.22	100.28
8R-1, 109-114	53.49	0.95	51.62	17.46	0.56	0.13	11.75	9.12	7.39	3.11	0.07	0.05	101.27
8R-2, 43-47	54.25	0.85	51.37	15.15	0.79	0.13	13.93	8.40	6.27	3.03	0.07	0.04	99.19
8R-2, 81-86	54.63	1.07	50.25	17.29	0.92	0.15	10.08	7.86	10.21	3.50	0.05	0.04	100.34
8R-3, 110-114	56.32	0.71	52.42	16.53	0.92	0.15	11.85	6.81	8.02	3.70	0.01	0.03	100.44
8R-4, 42-46	56.95	0.67	52.57	15.41	0.74	0.16	11.79	7.54	8.45	3.52	0.03	0.00	100.22
8R-4, 74-78	57.27	0.37	51.14	15.69	0.70	0.18	12.04	8.40	8.79	3.22	0.07	0.03	100.26
8R-4, 74-78	57.27	0.37	51.14	15.69	0.70	0.18	12.04	8.40	8.79	3.22	0.07	0.03	100.26
9R-1, 20-24	57.60	0.29	44.94	10.35	4.08	0.29	10.29	6.90	19.98	2.56	0.08	0.12	99.59
9R-1, 67-71	58.07	0.57	57.85	17.02	0.53	0.12	6.56	3.74	6.66	6.61	0.15	0.07	99.31
9R-1, 128-134	58.68	0.00	45.67	7.72	4.81	0.35	10.76	7.91	21.20	2.20	0.09	0.17	100.86
9R-2, 17-20	59.07	1.73	50.65	11.71	0.64	0.29	8.76	8.14	17.28	2.86	0.10	0.10	100.53
9R-3, 66-72	60.93	0.00	47.57	11.98	4.02	0.36	8.26	6.35	18.71	3.28	0.11	0.12	100.76
9R-3, 129-134	61.56	0.29	49.06	12.65	3.21	0.26	10.00	6.37	16.21	3.16	0.12	0.04	101.06
9R-4, 59-63	62.28	0.30	51.82	14.29	1.66	0.25	10.62	6.47	11.92	3.81	0.07	0.06	100.97
10R-1, 98-102	62.98	0.39	50.38	15.71	0.93	0.18	11.67	8.74	10.40	3.16	0.06	0.08	101.28
10R-2, 77-82	64.12	0.07	43.87	10.36	5.08	0.31	9.68	6.12	21.64	2.69	0.07	0.06	99.89
10R-2, 132-137	64.67	0.00	50.49	14.68	1.37	0.19	11.75	7.21	11.04	3.11	0.07	0.03	99.95
10R-3, 19-23	64.94	1.20	49.62	16.27	1.01	0.21	10.48	9.79	10.40	3.03	0.07	0.21	101.09
10R-3, 125-129	66.00	1.00	51.59	14.88	0.84	0.15	13.36	8.84	7.75	2.77	0.06	0.05	100.29
11R-1, 81-86	67.81	0.12	45.06	10.04	4.95	0.35	10.76	8.15	19.05	2.51	0.05	0.03	100.95
11R-2, 3-6	68.43	0.00	43.91	11.56	4.97	0.30	8.89	4.91	22.40	3.55	0.11	0.05	100.65
11R-2, 89-94	69.29	0.00	43.66	11.34	3.81	0.32	9.33	5.34	22.07	3.39	0.11	0.82	100.18
11R-2, 110-115	69.50	0.00	45.29	11.48	3.35	0.33	8.99	5.52	20.82	3.36	0.13	0.89	100.15
11R-3, 64-68	70.54	0.00	45.30	12.48	5.21	0.37	8.82	4.64	19.63	3.72	0.09	0.10	100.35
11R-3, 142-147	71.32	0.47	53.94	18.00	1.19	0.21	8.28	3.09	9.74	5.44	0.14	0.49	100.52
12R-1, 51-57	71.81	1.19	40.95	12.14	4.30	0.30	9.17	4.86	22.08	3.17	0.14	2.46	99.57
12R-1, 91-97	72.21	0.72	50.21	16.44	0.29	0.09	14.38	10.27	5.45	2.25	0.05	0.03	99.46
12R-3, 12-16	74.37	0.88	51.99	18.71	0.30	0.10	12.60	8.38	5.67	3.04	0.01	0.02	100.83
13R-1, 38-42	76.68	0.65	46.09	11.77	4.03	0.25	9.43	8.00	18.80	2.45	0.06	0.02	100.92
13R-1, 68-73	76.98	0.00	37.57	6.73	5.91	0.34	11.79	7.56	27.93	1.40	0.04	1.27	100.54

Table T2 (continued).

Core, section, interval (cm)	Depth (mbsf)	Major element oxide (wt%)											Total
		LOI	SiO ₂	Al ₂ O ₃	TiO ₂	MnO	CaO	MgO	Fe ₂ O ₃ T	Na ₂ O	K ₂ O	P ₂ O ₅	
13R-2, 12-16	77.82	0.47	51.32	15.37	1.06	0.18	10.42	7.66	11.32	3.47	0.06	0.02	100.88
13R-2, 44-49	78.14	0.22	43.82	11.33	4.40	0.29	9.03	5.59	21.79	3.08	0.08	0.73	100.13
13R-2, 122-127	78.92	0.06	46.03	12.92	3.30	0.24	9.71	6.88	18.64	2.82	0.08	0.07	100.69
13R-3, 11-15	79.15	0.68	51.93	15.15	0.62	0.20	10.65	8.11	10.54	3.67	0.03	0.02	100.93
13R-4, 7-11	80.51	2.48	49.67	16.33	0.24	0.11	13.33	13.13	6.21	1.80	0.04	0.03	100.87
14R-1, 55-60	81.55	0.97	50.35	17.72	0.37	0.11	12.73	10.34	6.24	2.65	0.01	0.04	100.56
14R-2, 114-119	83.55	0.79	50.65	17.70	0.26	0.09	14.37	10.08	4.92	2.21	0.01	0.03	100.32
14R-3, 10-15	83.74	1.14	50.44	17.27	0.25	0.10	13.11	10.66	5.86	2.26	0.03	0.02	100.00
14R-4, 22-27	85.31	0.90	49.66	19.05	0.36	0.10	12.39	7.59	6.59	3.22	0.03	0.04	99.03
15R-1, 14-18	86.14	0.00	33.37	5.30	7.56	0.49	10.19	6.22	35.86	1.32	0.00	0.83	101.13
15R-2, 39-43	87.89	0.44	52.45	15.46	0.60	0.19	10.59	7.39	9.79	4.04	0.04	0.02	100.56
15R-3, 7-12	89.04	0.13	47.98	13.53	1.90	0.19	9.62	6.56	16.88	3.17	0.05	0.03	99.91
16R-1, 22-27	90.82	0.00	42.40	12.50	4.50	0.28	8.84	4.65	20.92	3.70	0.08	1.42	99.28
16R-2, 124-128	93.17	0.57	51.86	22.39	0.27	0.06	13.41	6.44	3.55	3.25	0.00	0.03	101.26
16R-2, 133-139	93.26	0.55	51.81	16.80	0.30	0.10	14.33	9.91	5.24	2.39	0.05	0.03	100.96
16R-3, 35-39	93.69	0.47	50.02	16.41	0.25	0.11	13.21	12.28	6.34	2.13	0.00	0.02	100.77
17R-1, 51-55	96.11	0.00	38.58	8.16	6.82	0.41	8.48	5.94	29.84	2.21	0.04	0.01	100.50
17R-1, 94-99	96.54	0.75	49.71	16.31	0.30	0.12	12.91	12.02	7.23	2.13	0.06	0.02	100.83
17R-2, 47-52	97.49	0.25	49.95	15.99	0.27	0.12	12.41	10.36	7.40	2.72	0.04	0.03	99.29
17R-2, 75-80	97.77	0.56	50.04	16.61	0.30	0.10	14.11	10.55	5.82	2.31	0.05	0.02	99.91
17R-3, 59-65	99.04	0.40	51.83	21.80	0.25	0.08	11.26	5.78	5.15	3.94	0.06	0.04	100.19
17R-4, 0-7	99.95	0.36	45.46	12.64	6.15	0.28	8.62	5.66	18.23	3.46	0.14	0.07	100.71
18R-1, 62-68	100.82	0.31	40.61	8.65	7.23	0.35	8.89	6.74	24.94	2.28	0.21	0.04	99.94
19R-2, 80-85	107.50	0.53	48.90	14.65	2.47	0.21	10.08	5.71	15.46	3.44	0.19	0.07	101.17
19R-3, 75-80	108.80	0.77	50.37	15.06	1.32	0.17	11.74	7.20	11.55	3.20	0.20	0.06	100.87
19R-4, 18-23	109.69	0.41	46.79	12.13	3.63	0.25	9.13	6.25	19.27	2.96	0.27	0.07	100.75
19R-4, 43-46	109.94	0.33	50.07	14.04	2.74	0.23	11.00	6.36	12.45	3.67	0.11	0.04	100.70
20R-1, 95-100	110.75	0.57	50.89	19.82	0.48	0.10	12.04	8.13	6.81	2.93	0.08	0.08	101.35
20R-1, 111-117	110.91	0.71	51.97	16.06	0.56	0.10	15.03	8.76	5.14	2.51	0.01	0.03	100.16
21R-1, 12-16	110.92	0.38	49.66	15.79	0.65	0.12	12.93	10.85	7.34	2.50	0.04	0.08	99.96
21R-1, 89-94	111.69	0.38	48.83	14.27	4.06	0.24	9.84	5.64	18.24	3.14	0.16	0.06	100.47
21R-2, 84-88	112.98	0.71	48.84	14.08	3.07	0.23	9.36	5.06	15.00	3.91	0.14	0.05	99.73
22R-2, 20-25	116.70	0.61	51.85	14.61	1.06	0.19	11.28	7.46	11.31	3.28	0.15	0.03	101.22
22R-3, 7-11	117.75	1.53	51.15	15.10	0.89	0.19	10.68	7.27	11.87	3.38	0.12	0.05	100.70
22R-3, 63-69	118.31	1.06	49.26	13.21	1.90	0.26	11.13	7.41	14.29	3.16	0.11	0.08	101.24
23R-1, 53-57	119.93	0.43	51.25	15.87	0.85	0.17	10.89	7.11	10.23	3.66	0.06	0.06	100.15
23R-1, 142-148	120.82	0.50	52.96	15.54	0.79	0.16	11.82	6.82	8.23	3.84	0.04	0.06	100.25
23R-2, 1-5	120.91	0.41	51.60	13.80	1.26	0.23	11.80	7.62	11.21	3.19	0.02	0.04	100.76
24R-1, 93-98	125.33	0.28	48.54	15.89	2.73	0.20	9.51	4.35	13.98	4.14	0.09	0.05	99.48
24R-2, 49-53	126.32	0.96	53.16	21.58	0.49	0.09	8.68	4.00	7.12	4.69	0.11	0.04	99.96
24R-2, 94-98	126.77	0.21	41.70	6.48	4.98	0.36	11.82	8.90	24.58	1.53	0.05	0.12	100.52
24R-2, 121-126	127.04	0.96	50.35	16.70	0.99	0.16	11.02	7.47	10.09	3.13	0.13	0.05	100.09
24R-3, 116-120	128.32	0.26	45.02	11.26	5.03	0.25	9.99	6.12	19.36	3.08	0.09	0.02	100.21
25R-1, 83-89	129.83	0.16	44.29	10.80	6.14	0.29	9.17	5.85	20.51	3.03	0.14	0.04	100.26
25R-2, 3-8	130.47	0.21	43.95	11.57	6.34	0.28	8.69	5.73	20.09	3.26	0.12	0.04	100.08
25R-2, 55-62	130.99	0.55	53.20	17.86	0.48	0.10	14.08	7.07	4.87	3.08	0.08	0.03	100.85
25R-2, 84-90	131.28	0.74	54.59	16.50	0.42	0.11	12.56	6.70	5.85	3.67	0.14	0.03	100.57
25R-3, 79-82	132.62	0.56	51.31	17.66	0.66	0.11	13.30	8.05	6.35	2.98	0.05	0.02	100.50
25R-4, 31-38	133.33	0.34	51.42	16.65	0.46	0.14	11.76	7.65	8.08	3.19	0.11	0.02	99.48
26R-1, 32-38	134.32	0.00	37.38	6.29	7.06	0.40	9.76	7.24	29.35	1.74	0.10	0.04	99.37
26R-1, 115-121	135.15	0.77	51.07	16.79	0.41	0.11	13.57	9.62	6.69	2.57	0.11	0.04	100.98
26R-3, 20-26	136.96	0.54	49.24	12.61	0.38	0.15	13.25	14.16	8.55	2.18	0.06	0.04	100.61
26R-4, 24-30	138.41	0.43	49.76	18.62	0.30	0.11	11.77	9.83	6.91	2.95	0.04	0.05	100.33
27R-1, 8-12	138.78	0.66	51.33	15.46	0.50	0.14	12.73	9.67	7.35	2.78	0.15	0.08	100.19
27R-1, 82-88	139.52	0.12	40.51	13.68	4.72	0.24	7.84	3.37	23.55	3.84	0.43	1.12	99.30
27R-2, 81-87	140.69	0.39	52.36	21.71	0.45	0.07	13.36	4.69	3.58	3.63	0.06	0.05	99.96
27R-3, 27-33	141.29	0.47	50.67	18.54	0.28	0.11	11.47	9.23	7.14	2.92	0.08	0.03	100.47
27R-4, 29-31	142.81	0.80	60.30	16.70	0.78	0.11	5.18	2.57	6.18	6.80	0.29	0.17	99.08
27R-4, 71-76	143.23	0.22	50.58	18.29	0.34	0.11	12.39	8.67	6.18	2.96	0.08	0.04	99.59
28R-1, 54-60	144.24	0.28	49.33	15.76	0.38	0.13	11.96	12.20	8.24	1.83	0.03	0.02	99.87
28R-2, 78-84	145.58	0.59	52.52	20.91	0.34	0.07	13.22	5.99	4.14	3.26	0.05	0.03	100.52
28R-3, 61-66	146.87	0.40	49.53	17.99	0.28	0.12	10.97	10.26	8.50	3.18	0.08	0.03	100.91
28R-3, 115-119	147.41	0.39	47.18	12.39	0.33	0.16	10.78	17.16	9.59	1.90	0.04	0.04	99.56
28R-4, 8-15	147.76	1.36	49.68	15.87	0.46	0.12	13.41	10.99	7.29	2.39	0.04	0.02	100.27
29R-1, 21-27	148.61	0.46	50.71	13.96	0.35	0.13	13.32	13.06	7.40	2.14	0.05	0.04	101.16
29R-1, 75-80	149.15	0.52	50.59	18.79	0.27	0.10	11.65	9.37	6.36	2.94	0.04	0.04	100.14
29R-1, 114-116	149.54	0.63	52.12	4.36	0.87	0.21	18.29	15.02	9.12	0.89	0.02	0.03	100.92
29R-2, 69-74	150.36	0.53	53.09	23.34	0.32	0.06	11.45	3.94	3.93	4.23	0.09	0.04	100.49
29R-2, 133-139	151.00	1.00	51.16	20.25	0.39	0.11	10.18	7.06	7.84	3.82	0.12	0.03	100.96

Table T2 (continued).

Core, section, interval (cm)	Depth (mbsf)	Major element oxide (wt%)											
		LOI	SiO ₂	Al ₂ O ₃	TiO ₂	MnO	CaO	MgO	Fe ₂ O ₃ T	Na ₂ O	K ₂ O	P ₂ O ₅	Total
29R-3, 60-66	151.69	0.43	51.29	14.51	1.34	0.20	11.16	7.47	10.96	3.51	0.13	0.10	100.65
29R-4, 17-22	152.57	0.22	42.17	12.20	6.72	0.25	8.57	5.30	21.82	3.14	0.08	0.02	100.24
30R-2, 47-53	155.23	0.00	40.49	9.33	7.19	0.29	8.43	7.07	24.53	2.25	0.09	0.04	99.76
30R-2, 90-94	155.66	0.45	52.40	14.56	1.42	0.22	10.58	6.49	11.56	3.89	0.04	0.00	101.17
30R-2, 125-130	156.01	0.23	43.20	11.26	6.26	0.26	8.73	6.12	20.75	2.91	0.10	0.03	99.62
30R-3, 30-34	156.40	0.54	51.89	15.85	0.46	0.14	12.21	9.10	8.00	2.92	0.06	0.04	100.67
30R-3, 72-76	156.82	0.79	52.19	16.80	0.57	0.17	12.54	8.57	6.84	3.06	0.06	0.03	100.83

Table T3 (continued).

Core, section, interval (cm)	Depth (mbsf)	Trace element (ppm)										
		Zr	V	Ba	Sr	Ni	Cr	Co	Zn	Cu	Sc	Y
13R-2, 12-16	77.82	23	327	33	174	86	121	50	80	45	39.2	14.5
13R-2, 44-49	78.14	201	449	12	141	51	143	95	160	119	43.6	75.9
13R-2, 122-127	78.92	38	911	34	152	51	184	92	132	52	42.2	19.1
13R-3, 11-15	79.15	11	226	11	174	15	26	53	62	24	39.4	15.4
13R-4, 7-11	80.51	15	120	14	122	191	757	43	44	60	32.0	6.4
14R-1, 55-60	81.55	23	116	23	161	215	530	35	65	65	7.3	7.3
14R-2, 114-119	83.55	14	124	14	151	191	789	38	38	75	31.7	6.9
14R-3, 10-15	83.74	22	131	18	149	187	740	31	30	73	31.3	7.5
14R-4, 22-27	85.31	33	88	32	195	118	390	33	44	28	23.9	13.0
15R-1, 14-18	86.14	185	670	2	59	3	240	135	312	73	55.5	91.8
15R-2, 39-43	87.89	22	200	13	180	55	33	46	58	17	39.9	19.1
15R-3, 7-12	89.04	49	372	35	153	38	131	78	109	36	39.8	23.6
16R-1, 22-27	90.82	91	333	24	181	52	152	71	164	98	29.2	95.2
16R-2, 124-128	93.17	11	88	5	197	70	431	27	27	11	20.1	6.0
16R-2, 133-139	93.26	26	155	16	146	120	819	18	26	46	38.6	9.2
16R-3, 35-39	93.69	3	132	3	143	186	848	51	37	124	31.3	6.5
17R-1, 51-55	96.11	109	692	10	98	40	184	140	224	156	47.3	32.8
17R-1, 94-99	96.54	24	134	12	136	263	844	44	44	148	31.3	8.1
17R-2, 47-52	97.49	43	139	35	166	385	688	52	45	85	31.1	14.1
17R-2, 75-80	97.77	20	150	16	153	145	1040	28	30	83	36.8	8.4
17R-3, 59-65	99.04	46	86	16	219	52	47	22	41	46	18.5	7.0
17R-4, 0-7	99.95	99	257	17	156	45	154	143	121	116	43.9	26.7
18R-1, 62-68	100.82	82	712	13	98	262	226	115	174	87	57.8	30.0
19R-2, 80-85	107.50	58	374	4	170	44	85	75	111	54	43.5	34.5
19R-3, 75-80	108.80	57	275	19	153	106	545	42	67	58	41.1	25.7
19R-4, 18-23	109.69	105	373	19	144	48	257	91	119	98	41.4	27.5
19R-4, 43-46	109.94	39	360	10	170	5	45	66	68	43	48.7	23.5
20R-1, 95-100	110.75	40	123	19	182	241	390	46	45	15	22.8	10.6
20R-1, 111-117	110.91	18	188	8	140	65	826	34	32	22	47.9	14.4
21R-1, 12-16	110.92	59	157	31	140	153	687	48	51	83	36.6	17.8
21R-1, 89-94	111.69	56	647	15	161	52	416	95	122	152	39.1	18.7
21R-2, 84-88	112.98	50	325	16	179	24	114	56	104	53	43.3	27.4
22R-2, 20-25	116.70	40	234	17	161	7	51	35	62	45	44.2	19.3
22R-3, 7-11	117.75	39	198	15	173	55	95	58	79	31	36.0	18.3
22R-3, 63-69	118.31	59	316	16	150	63	115	66	95	166	46.0	28.8
23R-1, 53-57	119.93	49	236	36	179	38	62	50	66	33	42.2	25.1
23R-1, 142-148	120.82	29	247	36	175	25	45	27	45	20	48.3	20.0
23R-2, 1-5	120.91	28	289	5	160	11	36	52	71	35	54.5	25.2
24R-1, 93-98	125.33	69	421	19	199	42	102	53	110	61	37.8	25.0
24R-2, 49-53	126.32	32	101	15	235	32	57	43	66	18	8.2	5.6
24R-2, 94-98	126.77	96	929	14	69	79	215	120	180	125	74.1	44.5
24R-2, 121-126	127.04	55	219	15	167	321	152	44	60	55	35.4	17.3
24R-3, 116-120	128.32	64	835	22	137	75	166	84	139	96	55.2	26.8
25R-1, 83-89	129.83	84	646	15	132	57	156	119	137	101	53.2	26.2
25R-2, 3-8	130.47	96	515	9	138	18	94	124	118	93	45.3	26.6
25R-2, 55-62	130.99	37	202	17	167	152	316	11	26	20	44.4	14.1
25R-2, 84-90	131.28	55	165	14	159	236	337	19	46	7	38.9	35.3
25R-3, 79-82	132.62	12	165	5	174	84	264	37	64	44	37.9	11.3
25R-4, 31-38	133.33	26	178	14	174	49	176	37	44	23	37.4	11.8
26R-1, 32-38	134.32	194	1189	16	71	51	275	103	260	128	65.6	48.0
26R-1, 115-121	135.15	30	163	18	157	214	397	37	62	56	37.9	12.1
26R-3, 20-26	136.96	34	166	14	140	144	413	52	54	59	41.7	12.0
26R-3, 117-122	137.93	32	199	31	172	119	271	37	27	123	40.0	13.1
26R-4, 24-30	138.41	22	98	17	175	266	276	32	41	99	23.3	8.1
27R-1, 8-12	138.78	128	150	20	144	150	446	34	60	104	40.0	27.4
27R-1, 82-88	139.52	188	442	27	152	50	297	79	177	112	20.8	129.6
27R-2, 81-87	140.69	25	125	33	212	54	181	16	35	237	24.9	9.4
27R-3, 27-33	141.29	22	105	17	175	211	293	45	44	65	23.3	7.2
27R-4, 29-31	142.81	1369	59	45	159	24	37	24	41	71	17.5	157.8
27R-4, 71-76	143.23	18	116	6	181	147	319	33	40	44	26.7	8.2
28R-1, 54-60	144.24	29	137	14	149	167	379	56	53	98	32.0	10.3
28R-2, 78-84	145.58	22	123	14	191	97	228	32	19	83	27.6	7.5
28R-3, 61-66	146.87	15	90	10	177	387	177	50	50	172	21.8	6.9
28R-3, 115-119	147.41	26	130	12	113	262	310	62	60	128	29.1	8.2
28R-4, 8-15	147.76	21	176	32	134	209	917	47	45	123	37.3	11.9
29R-1, 21-27	148.61	30	175	15	130	145	360	40	34	79	42.1	10.1
29R-1, 75-80	149.15	26	117	14	189	116	178	34	33	112	23.6	6.7
29R-1, 114-116	149.54	40	452	20	33	87	201	39	43	16	107.1	30.5
29R-2, 69-74	150.36	22	81	24	237	35	32	11	33	12	16.4	7.1

Table T3 (continued).

Core, section, interval (cm)	Depth (mbsf)	Trace element (ppm)										
		Zr	V	Ba	Sr	Ni	Cr	Co	Zn	Cu	Sc	Y
29R-2, 133-139	151.00	26	90	21	206	79	46	43	47	34	15.9	6.3
29R-3, 60-66	151.69	83	272	17	155	90	173	63	68	53	46.0	28.6
29R-4, 17-22	152.57	54	979	14	146	27	148	143	129	135	44.6	19.0
30R-2, 47-53	155.23	81	938	12	109	50	192	153	141	176	51.6	23.7
30R-2, 90-94	155.66	19	289	7	182	2	14	54	69	32	45.5	22.0
30R-2, 125-130	156.01	79	777	15	132	60	163	101	136	149	47.5	24.6
30R-3, 30-34	156.40	36	210	17	160	70	88	56	43	62	40.5	14.2
30R-3, 72-76	156.82	28	186	18	170	70	79	31	49	68	39.2	13.0

Table T4. REE analysis of gabbros. (See table note. Continued on next two pages.)

Core, section, interval (cm)	Depth (mbsf)	REE (ppm)								
		La	Ce	Nd	Sm	Eu	Gd	Dy	Er	Yb
179-1105A-										
1R-1, 21-24	15.21	51.70	126.80	64.00	11.70	2.80	13.30	17.00	13.80	14.90
1R-1, 29-32	15.29	1.60	7.40	4.60	0.80	0.50	0.90	1.70	1.10	0.90
1R-2, 80-83	16.88	1.02	3.09	2.32	0.87	0.63	1.42	1.94	1.15	1.00
1R-3, 3-6	17.48	1.70	7.10	4.30	1.50	0.60	2.00	2.30	1.50	1.30
1R-3, 120-125	18.65	1.70	7.60	5.10	1.00	0.60	1.20	2.10	1.40	1.10
1R-4, 25-28	19.15	19.60	48.30	26.20	5.50	1.40	6.60	8.10	5.60	4.90
1R-5, 25-31	20.61	0.50	1.30	1.50	0.30	0.50	0.60	0.70	0.50	0.40
1R-5, 102-105	21.38	1.32	3.68	2.95	0.94	0.71	1.58	2.09	1.25	1.08
1R-6, 33-36	22.15	1.10	3.35	2.70	0.93	0.53	1.53	1.98	1.18	0.98
2R-1, 31-35	24.01	0.60	2.10	2.40	0.30	0.50	0.70	0.90	0.60	0.50
2R-2, 93-98	26.06	1.41	4.04	3.16	0.92	0.63	1.62	2.09	1.25	1.09
2R-2, 127-130	26.40	1.26	3.78	2.97	0.91	0.60	1.62	2.07	1.28	1.12
2R-3, 69-72	27.25	14.87	37.91	19.35	4.23	0.77	4.93	6.70	5.19	6.09
2R-4, 6-11	28.00	1.22	3.24	2.61	0.82	0.61	1.37	1.81	1.12	0.90
2R-4, 20-23	28.14	1.22	3.29	2.25	0.69	0.56	1.21	1.53	0.89	0.75
3R-1, 79-82	29.49	1.90	7.10	4.50	0.90	0.40	0.80	1.40	1.00	0.80
3R-2, 109-113	31.29	1.11	2.83	1.89	0.60	0.54	1.02	1.33	0.75	0.58
3R-3, 38-41	32.08	1.04	2.76	1.98	0.65	0.49	1.18	1.58	0.96	0.77
3R-3, 54-57	32.24	0.54	1.89	1.64	0.78	0.51	1.33	1.56	0.99	0.86
4R-1, 100-105	34.30	1.30	3.51	2.78	0.94	0.64	1.48	1.91	1.18	0.99
4R-2, 123-126	35.71	0.80	2.70	3.20	1.00	0.60	1.90	2.30	1.50	1.20
4R-3, 16-19	35.98	1.60	7.30	4.60	0.90	0.40	1.00	1.70	1.10	0.90
4R-3, 90-93	36.72	0.70	1.80	2.20	0.60	0.50	1.10	1.20	0.90	0.70
5R-1, 16-21	38.46	22.10	77.00	77.90	20.40	5.10	27.80	30.00	16.10	12.00
5R-1, 137-142	39.67	12.99	47.47	52.79	14.01	4.15	17.81	20.39	10.94	8.04
5R-2, 44-48	40.22	1.45	4.34	3.27	1.14	0.57	1.56	2.08	1.19	1.05
5R-3, 46-52	41.74	1.42	4.25	3.19	1.12	0.74	1.73	2.20	1.34	1.17
6R-1, 18-23	42.98	1.07	3.55	3.00	1.03	0.59	1.64	1.93	1.18	1.11
6R-2, 26-30	44.52	1.83	5.52	4.58	1.44	1.01	2.08	2.61	1.62	1.47
6R-2, 142-146	45.68	1.60	7.40	4.60	0.80	0.40	0.90	1.70	1.10	0.90
6R-3, 6-8	45.82	6.40	14.10	7.70	1.50	1.10	2.10	2.60	2.20	2.60
7R-1, 19-24	47.99	1.17	3.28	2.24	0.68	0.48	1.20	1.55	0.90	0.78
7R-1, 74-78	48.54	1.20	3.90	4.50	1.20	0.80	2.30	2.80	1.80	1.50
7R-2, 13-18	49.26	1.54	5.88	7.47	2.83	1.44	4.33	6.27	4.11	3.63
7R-3, 22-27	50.85	11.77	39.43	38.40	10.36	3.42	12.53	14.94	8.24	6.60
7R-3, 86-91	51.49	2.80	8.73	7.06	2.08	0.78	2.81	3.27	2.11	2.05
7R-3, 103-106	51.66	1.67	6.37	7.43	2.53	1.22	4.16	5.83	3.77	3.23
8R-1, 56-60	52.96	26.40	89.40	83.40	22.50	5.20	29.10	32.10	19.10	15.10
8R-1, 109-114	53.49	1.78	5.15	4.07	1.23	0.71	1.71	2.28	1.41	1.21
8R-2, 43-47	54.25	0.80	2.70	3.30	0.90	0.60	1.90	2.30	1.50	1.20
8R-2, 81-86	54.63	1.85	5.46	3.98	1.31	1.02	1.80	2.31	1.40	1.28
8R-3, 110-114	56.32	1.49	4.65	4.45	1.49	0.98	2.29	3.25	1.94	1.75
8R-4, 42-46	56.95	0.40	ND	4.00	0.70	0.80	1.70	2.30	1.50	1.20
8R-4, 74-78	57.27	1.47	4.46	4.03	1.48	0.90	2.20	2.88	1.75	1.55
8R-4, 74-78	57.27	1.47	4.46	4.03	1.48	0.90	2.20	2.88	1.75	1.55
9R-1, 20-24	57.60	1.70	6.60	9.20	3.00	1.90	5.20	6.70	4.30	3.50
9R-1, 67-71	58.07	7.50	21.00	15.90	3.90	2.30	5.40	6.70	4.80	4.50
9R-1, 128-134	58.68	3.96	13.81	14.77	5.72	2.17	8.46	10.78	7.02	6.63
9R-2, 17-20	59.07	3.20	12.20	8.70	1.80	1.30	2.60	4.40	3.30	3.30
9R-3, 66-72	60.93	1.76	6.26	6.53	2.09	1.56	3.66	5.00	3.29	3.02
9R-3, 129-134	61.56	2.78	8.55	7.22	2.59	1.90	3.92	5.27	3.32	3.12
9R-4, 59-63	62.28	1.84	6.48	7.27	2.59	1.85	4.06	5.62	3.67	3.29
10R-1, 98-102	62.98	2.25	7.39	7.41	2.41	1.08	3.17	4.07	2.74	2.35
10R-2, 77-82	64.12	2.40	10.70	9.80	2.80	1.60	4.00	6.30	4.10	3.40
10R-2, 132-137	64.67	1.54	5.03	5.02	1.85	1.35	2.74	3.63	2.27	2.05
10R-3, 19-23	64.94	5.85	17.95	14.43	4.07	1.32	5.34	6.46	3.96	3.76
10R-3, 125-129	66.00	1.98	6.62	5.74	2.37	1.02	3.43	4.04	2.62	2.34
11R-1, 81-86	67.81	0.80	3.40	5.40	1.70	1.20	3.60	4.70	3.20	2.70
11R-2, 3-6	68.43	2.65	9.39	9.49	3.58	2.42	5.47	7.42	4.71	4.56
11R-2, 89-94	69.29	6.50	25.60	26.90	7.20	3.00	10.50	12.50	7.10	5.70
11R-2, 110-115	69.50	6.48	22.37	23.84	8.23	3.14	10.46	11.50	6.57	5.57
11R-3, 64-68	70.54	2.98	9.41	8.67	3.47	2.43	5.06	6.64	3.99	3.75
11R-3, 142-147	71.32	4.19	13.57	13.78	4.43	3.06	5.53	6.05	3.27	2.86
12R-1, 51-57	71.81	13.93	51.56	57.01	15.67	4.37	20.25	19.98	10.74	7.40
12R-1, 91-97	72.21	1.88	4.51	2.30	0.89	0.48	1.57	1.99	1.14	0.79
12R-3, 12-16	74.37	2.20	8.80	5.80	1.10	0.50	1.10	2.00	1.40	1.10

Table T4 (continued).

Core, section, interval (cm)	Depth (mbsf)	REE (ppm)								
		La	Ce	Nd	Sm	Eu	Gd	Dy	Er	Yb
13R-1, 38-42	76.68	1.04	3.23	2.84	1.11	0.87	1.88	2.61	1.72	1.63
13R-1, 68-73	76.98	5.90	26.00	31.40	7.90	1.80	12.90	13.90	7.70	5.40
13R-2, 12-16	77.82	1.40	7.00	4.20	0.80	0.70	1.20	2.20	1.50	1.30
13R-2, 44-49	78.14	7.60	26.00	27.50	7.9	2.60	11.10	12.60	7.50	5.70
13R-2, 122-127	78.92	1.35	4.20	3.74	1.41	1.00	2.26	3.15	1.93	1.81
13R-3, 11-15	79.15	0.60	1.80	2.80	0.90	0.90	1.80	2.40	1.70	1.30
13R-4, 7-11	80.51	0.92	2.43	1.70	0.48	0.39	1.00	1.29	0.73	0.60
14R-1, 55-60	81.55	0.40	1.00	1.50	0.40	0.40	0.90	1.00	0.70	0.60
14R-2, 114-119	83.55	1.40	6.70	3.80	0.60	0.30	0.40	1.10	0.80	0.60
14R-3, 10-15	83.74	1.08	2.93	1.91	0.57	0.46	1.07	1.36	0.83	0.66
14R-4, 22-27	85.31	1.60	4.71	3.52	1.14	0.83	1.67	2.20	1.33	1.23
15R-1, 14-18	86.14	6.70	26.70	33.00	9.70	2.50	13.10	15.90	9.40	7.70
15R-2, 39-43	87.89	2.00	8.70	6.20	1.30	1.00	1.80	3.00	2.10	1.70
15R-3, 7-12	89.04	1.40	5.00	4.98	1.93	1.34	2.95	4.03	2.39	2.36
16R-1, 22-27	90.82	10.00	35.80	40.70	12.20	4.00	16.00	16.50	9.00	6.20
16R-2, 124-128	93.17	1.19	3.44	2.04	0.44	0.47	0.85	1.18	0.62	0.49
16R-2, 133-139	93.26	1.24	3.36	2.40	0.76	0.49	1.35	1.70	1.03	0.84
16R-3, 35-39	93.69	0.20	0.80	2.10	0.30	0.40	0.70	0.90	0.60	0.50
17R-1, 51-55	96.11	1.30	5.50	8.50	2.10	1.30	4.10	5.40	3.60	3.10
17R-1, 94-99	96.54	1.11	3.07	2.11	0.70	0.46	1.21	1.53	0.88	0.73
17R-2, 47-52	97.49	2.12	6.15	4.44	1.29	0.69	1.80	2.35	1.50	1.39
17R-2, 75-80	97.77	0.58	2.00	1.45	0.72	0.46	1.22	1.33	0.83	0.71
17R-3, 59-65	99.04	0.83	2.52	1.58	0.67	0.55	1.03	1.14	0.66	0.63
17R-4, 0-7	99.95	1.18	4.62	5.53	1.81	1.55	3.28	4.43	2.92	2.72
18R-1, 62-68	100.82	0.84	3.98	5.36	1.98	1.17	3.54	5.11	3.33	2.91
19R-2, 80-85	107.50	1.84	6.48	7.27	2.59	1.85	4.06	5.62	3.67	3.29
19R-3, 75-80	108.80	2.56	6.48	6.22	2.26	1.24	3.54	4.47	2.61	2.36
19R-4, 18-23	109.69	1.97	7.01	6.74	2.11	1.29	3.39	4.47	2.96	2.71
19R-4, 43-46	109.94	1.68	5.39	5.14	1.89	1.34	2.86	3.85	2.41	2.24
20R-1, 95-100	110.75	1.56	4.47	3.32	1.01	0.65	1.53	1.89	1.13	1.00
20R-1, 111-117	110.91	0.87	3.39	3.13	1.10	0.67	1.97	2.44	1.44	1.33
21R-1, 12-16	110.92	3.00	11.40	8.00	1.60	0.60	2.00	2.90	1.80	1.60
21R-1, 89-94	111.69	1.10	3.82	3.71	1.43	1.13	2.37	3.12	1.95	1.76
21R-2, 84-88	112.98	2.10	9.00	7.20	1.80	1.50	2.90	4.60	3.00	2.50
22R-2, 20-25	116.70	1.42	4.25	4.00	1.48	1.14	2.31	3.22	1.99	1.81
22R-3, 7-11	117.75	1.22	3.93	3.81	1.50	1.00	2.26	3.02	1.94	1.75
22R-3, 63-69	118.31	1.40	5.43	6.11	2.23	1.30	3.52	4.90	3.00	2.75
23R-1, 53-57	119.93	2.70	10.70	8.60	2.20	1.20	2.80	4.30	2.70	2.30
23R-1, 142-148	120.82	2.00	8.50	6.10	1.40	1.00	2.00	3.20	2.10	1.80
23R-2, 1-5	120.91	1.15	4.10	4.85	1.86	1.23	2.93	4.06	2.64	2.28
24R-1, 93-98	125.33	9.35	1.49	4.01	2.72	0.88	0.76	1.34	1.73	0.99
24R-2, 49-53	126.32	0.60	2.30	2.50	0.10	0.60	0.50	0.70	0.40	0.40
24R-2, 94-98	126.77	3.13	10.16	9.75	4.11	1.47	5.73	7.68	4.60	4.25
24R-2, 121-126	127.04	2.55	7.20	5.26	1.72	0.87	2.51	3.19	1.93	1.67
24R-3, 116-120	128.32	1.08	4.59	3.93	1.98	1.21	3.42	4.46	2.82	2.55
25R-1, 83-89	129.83	0.91	3.57	4.36	1.66	1.20	3.02	4.37	2.70	2.50
25R-2, 3-8	130.47	2.20	9.70	7.40	1.80	1.30	2.80	4.30	2.80	2.50
25R-2, 55-62	130.99	1.57	4.27	3.71	1.28	0.74	1.87	2.46	1.52	1.29
25R-2, 84-90	131.28	5.29	15.33	9.95	2.66	0.75	3.61	5.00	3.69	3.71
25R-3, 79-82	132.62	0.71	2.60	2.25	0.90	0.66	1.60	1.89	1.18	1.03
25R-4, 31-38	133.33	0.68	2.36	2.13	0.87	0.70	1.53	1.88	1.25	1.07
26R-1, 32-38	134.32	3.31	11.47	10.75	4.11	1.61	5.83	7.98	4.99	4.98
26R-1, 115-121	135.15	0.92	2.89	2.47	1.02	0.56	1.52	1.84	1.24	1.02
26R-3, 20-26	136.96	0.91	3.19	2.59	1.04	0.51	1.53	1.90	1.21	1.08
26R-3, 117-122	137.93	1.90	8.30	5.50	1.10	0.50	1.30	2.20	1.40	1.10
26R-4, 24-30	138.41	0.91	2.92	2.07	0.83	0.54	1.21	1.28	0.83	0.71
27R-1, 8-12	138.78	3.04	10.06	8.68	2.54	0.91	3.58	4.50	2.89	2.76
27R-1, 82-88	139.52	23.03	80.10	75.18	17.25	3.18	20.06	22.52	12.39	9.17
27R-2, 81-87	140.69	1.49	4.01	2.72	0.88	0.76	1.34	1.73	0.99	0.83
27R-3, 27-33	141.29	1.07	3.05	1.95	0.61	0.51	1.05	1.33	0.79	0.65
27R-4, 29-31	142.81	29.90	85.70	60.50	15.00	4.20	19.40	24.30	16.20	15.20
27R-4, 71-76	143.23	1.26	3.51	2.63	0.76	0.59	1.21	1.55	0.87	0.73
28R-1, 54-60	144.24	0.75	2.93	2.28	0.93	0.51	1.43	1.68	1.08	0.93
28R-2, 78-84	145.58	1.14	3.18	2.04	0.66	0.55	1.14	1.46	0.84	0.67
28R-3, 61-66	146.87	0.71	2.06	1.23	0.68	0.48	0.98	1.08	0.70	0.61
28R-3, 115-119	147.41	1.12	3.19	2.19	0.75	0.38	1.21	1.56	0.88	0.74
28R-4, 8-15	147.76	1.26	3.88	3.00	0.93	0.60	1.57	2.05	1.24	1.09
29R-1, 21-27	148.61	1.13	3.36	2.48	0.81	0.46	1.43	1.91	1.04	0.93
29R-1, 75-80	149.15	1.13	3.21	1.94	0.56	0.45	0.99	1.24	0.70	0.58

Table T4 (continued).

Core, section, interval (cm)	Depth (mbsf)	REE (ppm)								
		La	Ce	Nd	Sm	Eu	Gd	Dy	Er	Yb
29R-1, 114–116	149.54	1.20	4.97	5.93	2.02	0.79	3.51	4.78	3.27	2.78
29R-2, 69–74	150.36	0.83	2.61	1.53	0.63	0.59	0.90	1.05	0.73	0.62
29R-2, 133–139	151.00	1.31	3.49	1.97	0.58	0.55	0.95	1.22	0.68	0.60
29R-3, 60–66	151.69	3.07	9.40	7.68	2.73	1.34	3.80	4.90	2.92	2.68
29R-4, 17–22	152.57	1.60	7.90	5.70	1.10	0.90	1.90	3.10	2.00	1.80
30R-2, 47–53	155.23	1.16	4.24	4.50	1.74	0.97	2.89	3.99	2.51	2.30
30R-2, 90–94	155.66	0.78	3.16	3.66	1.51	1.16	2.59	3.61	2.27	2.04
30R-2, 125–130	156.01	1.49	5.19	4.09	1.81	1.20	3.12	3.83	2.65	2.45
30R-3, 30–34	156.40	1.34	4.11	3.43	1.18	0.64	1.85	2.33	1.39	1.26
30R-3, 72–76	156.82	0.84	2.96	2.70	0.98	0.61	1.63	2.09	1.30	1.13

Note: ND = not determined.

Table T5. Major element oxides in clinopyroxene. (See table note. Continued on next two pages.)

Core, section, interval (cm)	Depth (mbsf)	Modifier	Major element oxide (wt%)									
			SiO ₂	Al ₂ O ₃	FeO	MgO	MnO	TiO ₂	Cr ₂ O ₃	CaO	Na ₂ O	Total
179-1105A-												
1R-1, 21-24	15.21		NA	NA	NA	NA	NA	NA	NA	NA	NA	
1R-1, 29-32	15.29	Core	51.71	2.67	7.85	15.83	0.26	0.77	0.03	19.17	0.41	98.70
1R-1, 29-32	15.29	Rim	51.69	2.64	7.17	14.91	0.24	0.85	0.03	21.11	0.43	99.08
1R-2, 80-83	16.88		52.01	2.70	8.05	15.53	0.25	0.86	0.04	19.96	0.42	99.80
1R-3, 3-6	17.48		50.97	2.64	8.89	14.76	0.27	0.85	0.03	19.97	0.41	98.80
1R-3, 120-125	18.65		51.67	2.60	8.28	15.36	0.26	0.71	0.02	19.75	0.40	99.04
1R-4, 25-28	19.15		51.86	2.54	9.08	15.23	0.28	0.75	0.03	19.43	0.49	99.68
1R-5, 25-31	20.61		52.24	2.65	7.03	16.08	0.22	0.64	0.10	20.54	0.34	99.83
1R-5, 102-105	21.38		51.16	3.48	7.73	15.63	0.22	0.49	0.47	19.76	0.39	99.33
1R-6, 33-36	22.15	Core	51.74	2.99	6.75	15.89	0.21	0.69	0.14	20.21	0.37	98.97
1R-6, 33-36	22.15	Rim	51.48	2.93	7.19	15.81	0.22	0.74	0.16	19.98	0.35	98.87
2R-1, 31-35	24.01		52.21	3.29	6.21	16.71	0.18	0.46	0.44	19.53	0.38	99.42
2R-2, 93-98	26.06		51.67	3.34	6.54	16.08	0.19	0.64	0.41	20.55	0.39	99.81
2R-2, 127-130	26.40		NA	NA	NA	NA	NA	NA	NA	NA	NA	
2R-3, 69-72	27.25		NA	NA	NA	NA	NA	NA	NA	NA	NA	
2R-4, 6-11	28.00		51.61	3.14	7.38	16.11	0.22	0.82	0.32	19.71	0.40	99.72
2R-4, 20-23	28.14		52.03	3.41	6.59	16.25	0.19	0.67	0.42	20.25	0.40	100.21
3R-1, 79-82	29.49		52.48	3.14	6.24	16.52	0.19	0.59	0.37	20.33	0.41	100.28
3R-2, 109-113	31.29		51.44	3.43	6.35	16.64	0.21	0.73	0.25	19.48	0.42	98.94
3R-3, 38-41	32.08		51.54	3.12	6.26	16.56	0.19	0.51	0.42	20.09	0.35	99.03
3R-3, 54-57	32.24		51.67	3.30	5.90	16.08	0.19	0.59	0.44	20.74	0.39	99.30
4R-1, 100-105	34.30	Type 1	51.32	2.95	8.37	15.06	0.26	0.99	0.03	19.82	0.39	99.20
4R-1, 100-105	34.30	Type 2	52.56	2.40	10.63	17.94	0.31	0.76	0.02	14.91	0.34	99.85
4R-2, 123-126	35.71		52.50	3.29	5.58	16.67	0.17	0.54	0.43	20.68	0.37	100.24
4R-3, 16-19	35.98		52.40	3.11	5.79	16.76	0.18	0.58	0.38	20.45	0.35	100.00
4R-3, 90-93	36.72		52.55	3.23	6.07	16.84	0.18	0.48	0.46	19.91	0.36	100.07
5R-1, 16-21	38.46	Type 1	51.03	1.31	14.74	11.10	0.59	0.46	0.00	19.13	0.44	98.80
5R-1, 16-21	38.46	Type 2	50.94	0.96	21.83	12.64	0.80	0.32	0.01	11.53	0.26	99.29
5R-1, 137-142	39.67	Type 1	50.53	1.97	12.92	12.14	0.45	0.59	0.01	19.68	0.48	98.76
5R-1, 137-142	39.67	Type 2	50.60	1.28	17.44	12.60	0.60	0.39	0.00	15.53	0.34	98.79
5R-2, 44-48	40.22		52.73	2.79	6.30	16.62	0.20	0.63	0.08	20.31	0.38	100.04
5R-3, 46-52	41.74		51.31	2.56	7.94	15.54	0.26	0.72	0.03	20.26	0.41	99.02
6R-1, 18-23	42.98		52.39	2.46	8.14	14.97	0.26	0.73	0.03	20.74	0.41	100.15
6R-2, 26-30	44.52		51.66	2.68	8.45	15.32	0.26	0.75	0.04	19.71	0.44	99.92
6R-2, 142-146	45.68		52.09	2.57	6.97	15.95	0.22	0.67	0.04	20.04	0.36	98.92
6R-3, 6-8	45.82		NA	NA	NA	NA	NA	NA	NA	NA	NA	
7R-1, 19-24	47.99		52.04	2.89	6.89	15.67	0.22	0.83	0.03	20.60	0.41	99.60
7R-1, 74-78	48.54		52.51	2.74	8.05	16.23	0.25	0.75	0.04	19.45	0.37	100.40
7R-2, 13-18	49.26	Type 1	50.94	1.88	12.81	12.43	0.47	0.69	0.00	19.41	0.47	99.11
7R-2, 13-18	49.26	Type 2	51.14	1.36	18.06	14.44	0.59	0.49	0.00	12.55	0.32	98.94
7R-3, 22-27	50.85		51.66	1.43	14.04	11.73	0.55	0.46	0.00	19.62	0.44	99.92
7R-3, 86-91	51.49		51.73	2.62	9.64	14.38	0.32	1.09	0.02	19.37	0.47	99.65
7R-3, 103-106	51.66		51.00	2.20	11.61	13.68	0.38	0.75	0.01	18.97	0.42	99.02
8R-1, 56-60	52.96		51.94	1.25	13.98	11.93	0.58	0.37	0.00	19.75	0.48	100.27
8R-1, 109-114	53.49		51.84	2.99	7.86	15.18	0.25	0.93	0.03	20.42	0.51	100.10
8R-2, 43-47	54.25		52.08	2.78	8.02	15.20	0.25	0.70	0.03	20.49	0.52	100.08
8R-2, 81-86	54.63		51.82	2.39	9.67	14.48	0.31	0.74	0.01	19.99	0.46	99.87
8R-3, 110-114	56.32		51.84	2.99	7.86	15.18	0.25	0.93	0.03	20.42	0.51	100.01
8R-4, 42-46	56.95		51.00	2.56	9.97	13.75	0.31	0.78	0.02	19.66	0.50	98.54
8R-4, 74-78	57.27		51.78	2.69	9.33	15.08	0.28	0.86	0.03	19.73	0.44	100.22
8R-4, 74-78	57.27		51.65	2.72	9.20	14.52	0.27	0.89	0.04	20.49	0.51	100.28
9R-1, 20-24	57.6		50.88	2.08	12.79	12.79	0.44	0.72	0.01	18.68	0.43	98.82
9R-1, 67-71	58.07	Type 1	52.11	1.74	10.08	13.85	0.34	0.51	0.01	20.83	0.41	99.89
9R-1, 67-71	58.07	Type 2	51.84	1.95	15.21	14.69	0.44	0.42	0.01	14.38	0.38	99.33
9R-1, 128-134	58.68		51.54	1.57	13.50	11.70	0.49	0.58	0.00	19.82	0.46	99.64
9R-2, 17-20	59.07		51.12	1.83	13.38	12.23	0.46	0.56	0.00	19.29	0.45	99.32
9R-3, 66-72	60.93		50.98	1.69	12.57	12.62	0.45	0.59	0.00	19.51	0.42	98.84
9R-3, 129-134	61.56		51.53	1.60	13.54	12.42	0.45	0.59	0.00	19.45	0.40	99.99
9R-4, 59-63	62.28		50.83	2.10	12.45	12.72	0.43	0.65	0.03	19.31	0.43	98.96
10R-1, 98-102	62.98	Type 1	51.52	3.36	6.54	15.54	0.20	0.87	0.07	20.54	0.53	99.16
10R-1, 98-102	62.98	Type 2	51.00	1.79	12.74	12.46	0.42	0.71	0.00	19.28	0.47	98.88
10R-2, 77-82	64.12	Type 1	51.07	1.89	12.79	12.71	0.44	0.73	0.01	18.66	0.45	98.75
10R-2, 77-82	64.12	Type 2	51.32	1.44	17.41	14.15	0.56	0.54	0.00	13.28	0.32	99.02
10R-2, 132-137	64.67	Type 1	51.51	2.14	10.92	13.33	0.36	0.64	0.03	20.30	0.43	99.66
10R-2, 132-137	64.67	Type 2	51.91	1.91	13.03	14.14	0.41	0.68	0.03	17.43	0.41	99.93
10R-3, 19-23	64.94		51.16	2.82	9.11	14.81	0.30	0.90	0.05	19.59	0.50	99.22

Table T5 (continued).

Core, section, interval (cm)	Depth (mbsf)	Modifier	Major element oxide (wt%)									
			SiO ₂	Al ₂ O ₃	FeO	MgO	MnO	TiO ₂	Cr ₂ O ₃	CaO	Na ₂ O	Total
10R-3, 125-129	66.00		51.54	2.77	8.75	14.73	0.26	0.91	0.05	19.88	0.45	99.35
11R-1, 81-86	67.81		NA	NA	NA	NA	NA	NA	NA	NA	NA	
11R-2, 3-6	68.43	Type 1	50.85	1.57	14.01	11.67	0.52	0.59	0.00	19.28	0.46	98.95
11R-2, 3-6	68.43	Type 2	50.73	1.18	21.22	13.35	0.72	0.47	0.00	11.17	0.26	99.08
11R-2, 89-94	69.29	Type 1	51.32	1.25	18.64	12.07	0.65	0.45	0.01	15.42	0.36	100.16
11R-2, 89-94	69.29	Type 2	51.22	1.43	15.18	11.43	0.54	0.60	0.00	18.94	0.42	99.77
11R-2, 110-115	69.50	Type 1	51.41	1.49	14.25	11.63	0.50	0.52	0.00	19.37	0.48	99.64
11R-2, 110-115	69.50	Type 2	51.21	1.41	17.05	11.83	0.59	0.51	0.00	16.61	0.42	99.62
11R-3, 64-68	70.54	Type 1	51.33	1.76	13.94	12.03	0.49	0.69	0.00	19.27	0.46	99.98
11R-3, 64-68	70.54	Type 2	50.73	1.46	18.26	12.77	0.58	0.88	0.00	14.86	0.36	99.89
11R-3, 142-147	71.32	Type 1	51.45	1.62	13.16	12.03	0.47	0.63	0.00	19.94	0.44	99.74
11R-3, 142-147	71.32	Type 2	51.49	1.40	18.19	13.64	0.59	0.51	0.00	13.35	0.37	99.52
12R-1, 51-57	71.81	Type 1	50.91	1.46	15.44	11.63	0.56	0.53	0.00	18.50	0.45	99.48
12R-1, 51-57	71.81	Type 2	50.95	1.18	18.90	12.34	0.66	0.47	0.00	14.81	0.37	99.69
12R-1, 91-97	72.21		52.39	3.30	5.54	16.93	0.17	0.55	0.43	20.18	0.39	99.89
12R-3, 12-16 fine	74.37	Fine	50.74	2.54	9.85	13.82	0.32	0.79	0.03	20.10	0.47	98.67
12R-3, 12-16 coarse	74.37	Coarse	50.92	2.51	10.79	13.99	0.32	0.76	0.03	19.09	0.45	98.88
13R-1, 38-42	76.68		50.84	2.19	11.72	13.04	0.37	0.66	0.01	19.43	0.41	98.67
13R-1, 68-73	76.98	Type 1	51.84	1.84	12.84	12.83	0.45	0.52	0.00	19.45	0.42	100.19
13R-1, 68-73	76.98	Type 2	51.66	1.60	17.12	14.21	0.54	0.55	0.01	14.32	0.35	100.35
13R-2, 12-16	77.82		52.33	2.84	6.93	16.12	0.22	0.76	0.12	20.19	0.40	99.91
13R-2, 44-49	78.14	Type 1	51.15	2.42	10.98	13.37	0.35	0.78	0.03	19.83	0.48	99.40
13R-2, 44-49	78.14	Type 2	50.88	1.91	17.57	14.93	0.55	0.57	0.02	13.47	0.31	100.20
13R-2, 122-127	78.92		50.41	2.23	12.25	13.05	0.38	0.80	0.01	19.21	0.43	98.77
13R-3, 11-15	79.15	Type 1	51.20	2.25	10.38	13.98	0.35	0.74	0.02	19.64	0.41	98.96
13R-3, 11-15	79.15	Type 2	51.14	2.04	14.85	15.84	0.43	0.68	0.02	13.71	0.34	99.04
13R-4, 7-11	80.51		51.63	3.13	5.29	16.53	0.17	0.46	0.39	20.82	0.39	98.80
14R-1, 55-60	81.55		52.11	3.10	6.08	16.33	0.19	0.52	0.30	20.40	0.42	99.46
14R-2, 114-119	83.55		52.32	3.31	5.42	16.81	0.17	0.40	0.43	20.42	0.36	99.64
14R-3, 10-15	83.74		52.25	3.27	5.96	16.92	0.18	0.49	0.38	19.80	0.37	99.62
14R-4, 22-27	85.31		52.04	3.24	5.83	16.17	0.18	0.64	0.29	20.61	0.47	99.47
15R-1, 14-18	86.14		50.94	1.37	14.61	11.51	0.55	0.52	0.00	18.69	0.46	98.65
15R-2, 39-43	87.89	Core	51.75	2.03	11.42	13.93	0.37	0.74	0.02	19.16	0.43	99.85
15R-2, 39-43	87.89	Rim	51.76	1.92	10.70	13.53	0.36	0.62	0.02	20.24	0.43	99.57
15R-3, 7-12	89.04		51.70	1.89	12.88	12.88	0.44	0.61	0.01	19.40	0.41	100.21
16R-1, 22-27	90.82	Core	51.39	1.52	14.71	11.77	0.53	0.54	0.00	18.67	0.43	99.55
16R-1, 22-27	90.82	Rim	51.37	1.31	17.37	12.40	0.61	0.50	0.00	15.91	0.35	99.84
16R-2, 124-128	93.17		52.75	3.46	4.44	16.54	0.15	0.48	0.44	22.03	0.39	100.66
16R-2, 133-139	93.26		52.30	3.36	5.55	15.99	0.18	0.58	0.34	21.20	0.39	99.89
16R-3, 35-39	93.69		52.38	3.35	5.63	16.91	0.18	0.52	0.42	19.95	0.41	99.74
17R-1, 51-55	96.11		50.77	1.52	13.18	11.86	0.49	0.53	0.01	19.85	0.42	98.63
17R-1, 94-99	96.54		52.12	3.33	6.22	16.27	0.19	0.68	0.32	19.88	0.43	99.46
17R-2, 47-52	97.49		52.47	3.15	6.72	16.06	0.20	0.47	0.43	20.09	0.46	100.05
17R-2, 75-80	97.77		52.85	3.15	5.60	17.37	0.16	0.37	0.50	20.07	0.36	100.44
17R-3, 59-65	99.04		52.25	2.71	7.17	16.15	0.22	0.64	0.03	20.32	0.36	99.85
17R-4, 0-7	99.95		51.47	1.57	14.12	12.22	0.44	0.54	0.01	18.93	0.45	99.76
18R-1, 62-68	100.82		50.98	1.79	12.96	12.54	0.44	0.70	0.01	19.90	0.48	99.79
19R-2, 80-85	107.50		51.49	2.03	12.33	12.72	0.42	0.71	0.01	19.91	0.48	100.11
19R-3, 75-80	108.80	Type 1	51.67	3.41	7.95	15.41	0.22	0.65	0.39	19.64	0.42	99.77
19R-3, 75-80	108.80	Type 2	51.15	2.74	10.44	13.78	0.32	0.72	0.14	20.00	0.46	99.74
19R-4, 18-23	109.69		51.11	2.47	10.07	14.38	0.33	0.69	0.13	19.11	0.43	98.73
19R-4, 43-46	109.94	Variation	51.38	2.21	13.04	12.67	0.39	0.72	0.01	18.81	0.47	99.70
20R-1, 95-100	110.75	Type 1	52.70	3.48	5.11	16.39	0.15	0.47	0.40	20.79	0.38	99.88
20R-1, 95-100	110.75	Type 2	52.18	3.04	7.58	15.34	0.23	0.70	0.23	19.88	0.45	99.63
20R-1, 111-117	110.91		52.42	3.15	5.98	16.37	0.18	0.53	0.27	20.56	0.38	99.84
21R-1, 12-16	110.92		52.21	3.26	6.45	15.95	0.18	0.78	0.32	20.30	0.49	99.95
21R-1, 89-94	111.69		51.47	2.06	12.49	12.57	0.41	0.63	0.05	19.54	0.47	99.70
21R-2, 84-88	112.98	Type 1	51.79	1.49	12.68	12.59	0.44	0.47	0.00	19.82	0.40	99.68
21R-2, 84-88	112.98	Type 2	51.58	1.36	17.48	13.63	0.56	0.53	0.00	14.73	0.32	100.20
22R-2, 20-25	116.70	Type 1	51.66	2.16	11.05	13.56	0.37	0.63	0.02	20.00	0.45	99.90
22R-2, 20-25	116.70	Type 2	51.19	2.27	12.75	13.06	0.41	0.66	0.00	18.89	0.43	99.66
22R-3, 7-11	117.75		51.25	2.09	11.25	13.27	0.38	0.62	0.01	19.57	0.59	99.02
22R-3, 63-69	118.31		50.83	2.53	10.33	14.04	0.32	0.77	0.02	19.03	0.45	98.32
23R-1, 53-57	119.93		51.79	2.41	10.82	13.95	0.35	0.77	0.01	19.33	0.44	99.87
23R-1, 142-148	120.82	Type 1	51.72	2.44	10.65	13.94	0.34	0.77	0.02	19.80	0.43	100.11
23R-1, 142-148	120.82	Type 2	51.63	2.14	14.30	14.90	0.41	0.72	0.01	15.55	0.36	100.02
23R-2, 1-5	120.91		51.61	2.30	10.68	13.66	0.35	0.65	0.01	19.68	0.53	99.48
24R-1, 93-98	125.33	Type 1	51.97	1.52	12.59	12.56	0.44	0.41	0.01	20.04	0.43	99.95
24R-1, 93-98	125.33	Type 2	51.55	1.35	17.38	13.90	0.58	0.63	0.00	14.14	0.36	99.89

Table T5 (continued).

Core, section, interval (cm)	Depth (mbsf)	Modifier	Major element oxide (wt%)										Total
			SiO ₂	Al ₂ O ₃	FeO	MgO	MnO	TiO ₂	Cr ₂ O ₃	CaO	Na ₂ O		
24R-2, 49-53	126.32		51.51	2.12	10.17	13.68	0.33	0.66	0.02	19.98	0.49	98.96	
24R-2, 94-98	126.77		51.03	1.69	12.55	12.49	0.43	0.64	0.01	19.02	0.47	98.33	
24R-2, 121-126	127.04	Type 1	53.02	2.81	6.55	16.52	0.19	0.52	0.07	20.00	0.35	100.02	
24R-2, 121-126	127.04	Type 2	51.33	2.64	10.62	13.94	0.32	0.70	0.03	19.41	0.44	99.45	
24R-3, 116-120	128.32		NA	NA	NA	NA	NA	NA	NA	NA	NA		
25R-1, 83-89	129.83	Type 1	51.92	1.72	12.19	12.93	0.41	0.55	0.00	19.99	0.47	100.19	
25R-1, 83-89	129.83	Type 2	51.66	1.69	15.68	13.68	0.50	0.58	0.01	15.98	0.41	100.19	
25R-2, 3-8	130.47	Type 1	50.63	1.89	12.73	12.27	0.46	0.65	0.00	19.64	0.49	98.76	
25R-2, 3-8	130.47	Type 2	50.99	1.41	19.25	14.35	0.62	0.49	0.00	11.65	0.32	99.14	
25R-2, 55-62	130.99		52.79	2.91	6.01	17.07	0.18	0.49	0.14	20.01	0.37	99.99	
25R-2, 84-90	131.28	Type 1	52.78	2.48	7.12	16.23	0.22	0.45	0.14	20.36	0.40	100.18	
25R-2, 84-90	131.28	Type 2	51.78	2.99	9.02	15.11	0.26	0.73	0.09	19.40	0.47	99.85	
25R-3, 79-82	132.62	Type 1	51.73	2.93	7.22	15.92	0.21	0.58	0.13	20.02	0.40	98.94	
25R-3, 79-82	132.62	Type 2	51.39	2.59	9.93	16.93	0.27	0.55	0.13	16.84	0.31	98.94	
25R-4, 31-38	133.33	Type 1	52.23	2.83	7.96	15.28	0.25	0.71	0.08	19.95	0.46	99.75	
25R-4, 31-38	133.33	Type 2	52.21	2.57	9.79	15.57	0.29	0.82	0.05	18.31	0.43	100.03	
26R-1, 32-38	134.32	Type 1	51.84	1.50	13.72	12.18	0.51	0.48	0.00	19.13	0.45	99.80	
26R-1, 32-38	134.32	Type 2	52.17	1.40	11.78	13.03	0.42	0.35	0.01	20.40	0.33	99.87	
26R-1, 115-121	135.15		52.50	3.14	6.54	16.20	0.19	0.60	0.16	20.11	0.44	99.88	
26R-3, 20-26	136.96		52.44	2.96	6.10	16.79	0.18	0.53	0.18	20.19	0.37	99.73	
26R-3, 117-122	137.93		52.77	2.86	6.10	16.88	0.19	0.62	0.14	20.17	0.37	100.10	
26R-4, 24-30	138.41		51.87	3.02	6.87	16.25	0.20	0.73	0.14	20.09	0.38	99.56	
27R-1, 8-12	138.78	Type 1	51.43	3.05	6.93	16.01	0.21	0.76	0.24	20.10	0.51	99.24	
27R-1, 8-12	138.78	Type 2	50.61	1.28	14.20	11.86	0.52	0.41	0.00	19.14	0.46	98.48	
27R-1, 82-88	139.52		NA	NA	NA	NA	NA	NA	NA	NA	NA		
27R-2, 81-87	140.69	Core	52.01	3.77	5.24	16.75	0.16	0.51	0.27	19.93	0.52	99.17	
27R-2, 81-87	140.69	Rim	51.91	3.01	7.29	15.33	0.23	0.73	0.09	20.20	0.38	99.16	
27R-3, 27-33	141.29		51.59	2.93	7.52	14.76	0.24	0.64	0.09	21.20	0.41	99.39	
27R-4, 29-31	142.81		NA	NA	NA	NA	NA	NA	NA	NA	NA		
27R-4, 71-76	143.23		52.81	2.96	6.23	16.92	0.19	0.54	0.21	20.19	0.36	100.41	
28R-1, 54-60	144.24		52.16	2.94	6.07	17.03	0.18	0.54	0.21	19.80	0.36	99.29	
28R-2, 78-84	145.58	Core	52.41	3.09	7.07	16.61	0.20	0.55	0.17	19.50	0.38	99.98	
28R-2, 78-84	145.58	Rim	51.19	3.45	8.59	15.46	0.25	0.90	0.08	19.26	0.38	99.55	
28R-3, 61-66	146.87		51.33	2.84	7.58	16.04	0.23	0.67	0.12	19.33	0.38	98.51	
28R-3, 115-119	147.41		52.60	2.93	6.18	17.22	0.20	0.71	0.13	19.58	0.36	99.90	
28R-4, 8-15	147.76		51.80	3.26	7.41	16.30	0.21	0.48	0.50	18.98	0.38	99.34	
29R-1, 21-27	148.61		52.62	2.87	6.28	16.93	0.19	0.61	0.14	19.63	0.33	99.59	
29R-1, 75-80	149.15		52.64	2.81	6.81	16.87	0.20	0.56	0.10	19.37	0.33	99.70	
29R-1, 114-116	149.54		NA	NA	NA	NA	NA	NA	NA	NA	NA		
29R-2, 69-74	150.36		51.79	2.64	8.26	15.60	0.25	0.73	0.02	19.77	0.51	99.57	
29R-2, 133-139	151.00		52.25	2.77	8.19	15.86	0.24	0.73	0.03	19.06	0.43	99.56	
29R-3, 60-66	151.69	Type 1	51.39	2.70	9.51	14.95	0.29	0.81	0.01	19.13	0.47	99.26	
29R-3, 60-66	151.69	Type 2	50.85	2.20	11.34	13.14	0.38	0.63	0.02	19.45	0.48	98.48	
29R-4, 17-22	152.57		51.54	1.96	11.78	13.06	0.40	0.71	0.01	19.79	0.47	99.73	
30R-2, 47-53	155.23		51.47	2.06	12.03	13.31	0.42	0.72	0.00	18.96	0.47	99.44	
30R-2, 90-94	155.66	Core	51.46	1.81	16.46	14.28	0.55	0.59	0.01	14.49	0.35	99.98	
30R-2, 90-94	155.66	Rim	51.73	1.68	12.36	12.89	0.44	0.39	0.01	19.83	0.36	99.67	
30R-2, 90-94	155.70	Laminated	52.07	1.79	11.89	13.47	0.42	0.51	0.01	19.48	0.41	100.04	
30R-2, 125-130	156.01		51.75	1.90	12.34	13.15	0.44	0.59	0.01	19.32	0.43	99.92	
30R-3, 30-34	156.40		52.08	2.59	8.44	15.06	0.26	0.79	0.04	20.45	0.40	100.11	
30R-3, 72-76	156.82		52.27	2.73	8.04	15.64	0.24	0.75	0.03	19.92	0.37	99.99	

Note: NA = not analyzed.

Table T6. Major element oxides in olivine. (Continued on next two pages.)

Core, section, interval (cm)	Depth (mbsf)	Major element oxide (wt%)						Total
		SiO ₂	FeO	MgO	MnO	CaO	NiO	
179-1105A-								
1R-1, 21-24	15.21							
1R-1, 29-32	15.29	36.81	26.46	34.46	0.42	0.07	0.04	98.27
1R-2, 80-83	16.88	36.61	28.03	33.28	0.45	0.04	0.05	98.47
1R-3, 3-6	17.48	36.11	31.65	30.71	0.52	0.06	0.04	99.09
1R-3, 120-125	18.65	36.10	30.90	31.23	0.50	0.06	0.05	98.85
1R-4, 25-28	19.15							
1R-5, 25-31	20.61	36.82	27.85	34.02	0.46	0.07	0.07	99.29
1R-5, 102-105	21.38	36.36	29.35	32.43	0.47	0.05	0.07	98.73
1R-6, 33-36	22.15	37.18	26.33	35.05	0.41	0.06	0.07	99.11
2R-1, 31-35	24.01	37.83	23.07	37.74	0.36	0.07	0.11	99.18
2R-2, 93-98	26.06	37.64	23.87	37.26	0.36	0.05	0.11	99.28
2R-2, 127-130	26.40							
2R-3, 69-72	27.25							
2R-4, 6-11	28.00	37.35	25.70	35.78	0.38	0.04	0.10	99.35
2R-4, 20-23	28.14	37.70	23.25	37.56	0.36	0.07	0.11	99.05
3R-1, 79-82	29.49	37.94	22.28	38.18	0.35	0.06	0.11	98.91
3R-2, 109-113	31.29	37.53	23.78	36.97	0.39	0.08	0.09	98.83
3R-3, 38-41	32.08	37.61	22.04	38.38	0.33	0.04	0.11	98.52
3R-3, 54-57	32.24	37.90	21.90	38.60	0.32	0.05	0.12	98.89
4R-1, 100-105	34.30	36.94	26.90	34.48	0.44	0.09	0.06	98.91
4R-2, 123-126	35.71	38.23	20.84	39.63	0.33	0.07	0.11	99.20
4R-3, 16-19	35.98	37.95	22.04	38.52	0.35	0.07	0.10	99.03
4R-3, 90-93	36.72	38.10	21.45	38.99	0.34	0.07	0.11	99.07
5R-1, 16-21	38.46	36.97	27.25	34.37	0.45	0.08	0.06	99.19
5R-1, 137-142	39.67							
5R-2, 44-48	40.22	36.82	27.85	34.02	0.46	0.07	0.07	99.29
5R-3, 46-52	41.74	36.01	32.30	30.26	0.56	0.09	0.04	99.26
6R-1, 18-23	42.98	36.40	30.02	31.49	0.53	0.19	0.05	98.68
6R-2, 26-30	44.52	35.85	32.15	30.35	0.53	0.05	0.05	98.99
6R-2, 142-146	45.68							
6R-3, 6-8	45.82							
7R-1, 19-24	47.99	36.92	25.82	35.09	0.42	0.07	0.06	98.39
7R-1, 74-78	48.54	36.58	28.96	33.19	0.47	0.04	0.06	99.29
7R-2, 13-18	49.26							
7R-3, 22-27	50.85							
7R-3, 86-91	51.49	35.32	34.07	28.66	0.57	0.04	0.03	98.69
7R-3, 103-106	51.66	34.44	39.33	24.47	0.69	0.04	0.02	98.99
8R-1, 56-60	52.96							
8R-1, 109-114	53.49	36.56	27.84	33.90	0.45	0.05	0.06	98.86
8R-2, 43-47	54.25							
8R-2, 81-86	54.63	35.32	35.52	27.53	0.62	0.04	0.03	99.06
8R-3, 110-114	56.32							
8R-4, 42-46	56.95	34.71	36.82	26.42	0.64	0.05	0.03	98.66
8R-4, 74-78	57.27	35.71	33.58	29.76	0.56	0.05	0.03	99.68
8R-4, 74-78	57.27	35.41	34.86	28.30	0.60	0.04	0.03	99.24
9R-1, 20-24	57.60							
9R-1, 67-71	58.07							
9R-1, 128-134	58.68							
9R-2, 17-20	59.07							
9R-3, 66-72	60.93							
9R-3, 129-134	61.56							
9R-4, 59-63	62.28	33.48	43.30	20.55	0.84	0.05	0.01	98.24
10R-1, 98-102	62.98	37.19	27.83	34.06	0.46	0.06	0.05	99.65
10R-2, 77-82	64.12							
10R-2, 132-137	64.67							
10R-3, 19-23	64.94	35.85	32.33	30.24	0.54	0.07	0.05	99.08
10R-3, 125-129	66.00	35.72	33.60	29.61	0.54	0.06	0.05	99.58
11R-1, 81-86	67.81							
11R-2, 3-6	68.43							
11R-2, 89-94	69.29	32.21	49.38	15.71	1.10	0.15	0.01	98.57
11R-2, 110-115	69.50	32.62	48.79	16.30	1.06	0.09	0.01	98.86
11R-3, 64-68	70.54							
11R-3, 142-147	71.32							
12R-1, 51-57	71.81							
12R-1, 91-97	72.21	37.63	22.06	38.17	0.37	0.09	0.10	98.42
12R-3, 12-16 fine	74.37	37.33	24.60	36.20	0.38	0.03	0.09	98.65

Table T6 (continued).

Core, section, interval (cm)	Depth (mbsf)	Major element oxide (wt%)						Total
		SiO ₂	FeO	MgO	MnO	CaO	NiO	
12R-3, 12–16 coarse	74.37							
13R-1, 38–42	76.68							
13R-1, 68–73	76.98							
13R-2, 12–16	77.82	34.77	37.81	25.59	0.64	0.09	0.02	98.92
13R-2, 44–49	78.14							
13R-2, 122–127	78.92	33.63	42.89	21.04	0.74	0.09	0.02	98.41
13R-3, 11–15	79.15	34.64	37.64	25.41	0.66	0.06	0.02	98.44
13R-4, 7–11	80.51							
14R-1, 55–60	81.55	37.47	23.30	37.51	0.38	0.05	0.09	98.79
14R-2, 114–119	83.55	37.57	22.10	38.43	0.35	0.09	0.11	98.66
14R-3, 10–15	83.74	37.66	22.52	37.85	0.38	0.07	0.11	98.59
14R-4, 22–27	85.31	37.56	22.75	37.55	0.36	0.05	0.10	98.38
15R-1, 14–18	86.14							
15R-2, 39–43	87.89	34.65	38.11	24.97	0.70	0.05	0.01	98.50
15R-3, 7–12	89.04	33.79	42.11	21.73	0.81	0.05	0.01	98.49
16R-1, 22–27	90.82	32.82	46.67	17.22	1.04	0.09	0.02	97.87
16R-2, 124–128	93.17							
16R-2, 133–139	93.26	38.06	21.86	38.08	0.36	0.07	0.11	98.55
16R-3, 35–39	93.69	38.18	21.08	39.50	0.34	0.05	0.09	99.24
17R-1, 51–55	96.11							
17R-1, 94–99	96.54	37.78	22.89	37.99	0.37	0.04	0.09	99.16
17R-2, 47–52	97.49	37.66	24.01	37.12	0.38	0.04	0.08	99.29
17R-2, 75–80	97.77	37.88	22.29	38.41	0.37	0.05	0.09	99.09
17R-3, 59–65	99.04	36.48	29.52	32.47	0.49	0.06	0.05	99.07
17R-4, 0–7	99.95							
18R-1, 62–68	100.82							
19R-2, 80–85	107.50							
19R-3, 75–80	108.80	34.69	38.08	25.09	0.68	0.07	0.03	98.64
19R-4, 18–23	109.69	34.18	41.38	22.05	0.78	0.09	0.01	98.49
19R-4, 43–46	109.94							
20R-1, 95–100	110.75	36.56	28.78	32.83	0.49	0.07	0.07	98.79
20R-1, 111–117	110.91							
21R-1, 12–16	110.92	37.22	25.66	35.37	0.42	0.06	0.09	98.81
21R-1, 89–94	111.69							
21R-2, 84–88	112.98							
22R-2, 20–25	116.70	34.30	40.57	22.96	0.76	0.07	0.02	98.68
22R-3, 7–11	117.75							
22R-3, 63–69	118.31							
23R-1, 53–57	119.93	35.01	36.41	26.27	0.64	0.04	0.03	98.40
23R-1, 142–148	120.82							
23R-2, 1–5	120.91	34.12	41.04	22.68	0.79	0.06	0.02	98.72
24R-1, 93–98	125.33							
24R-2, 49–53	126.32	35.00	36.93	25.98	0.64	0.09	0.03	98.65
24R-2, 94–98	126.77							
24R-2, 121–126	127.04	34.70	38.05	24.93	0.68	0.09	0.02	98.47
24R-3, 116–120	128.32							
25R-1, 83–89	129.83							
25R-2, 3–8	130.47	33.34	47.03	18.08	0.94	0.08	0.01	99.47
25R-2, 55–62	130.99							
25R-2, 84–90	131.28							
25R-3, 79–82	132.62	35.81	32.04	29.95	0.52	0.06	0.05	98.44
25R-4, 31–38	133.33	35.89	32.15	29.97	0.55	0.07	0.04	98.67
26R-1, 32–38	134.32							
26R-1, 115–121	135.15	37.11	25.56	35.30	0.43	0.10	0.06	98.57
26R-3, 20–26	136.96	37.43	24.41	36.61	0.40	0.07	0.08	98.99
26R-3, 117–122	137.93							
26R-4, 24–30	138.41	37.21	25.61	35.65	0.39	0.05	0.08	98.99
27R-1, 8–12	138.78	37.06	27.02	34.69	0.48	0.06	0.06	99.36
27R-1, 82–88	139.52							
27R-2, 81–87	140.69							
27R-3, 27–33	141.29							
27R-4, 29–31	142.81							
27R-4, 71–76	143.23	36.76	27.66	34.13	0.44	0.05	0.08	99.10
28R-1, 54–60	144.24	37.38	24.87	36.40	0.41	0.07	0.08	99.21
28R-2, 78–84	145.58							
28R-3, 61–66	146.87	36.79	27.29	34.20	0.44	0.06	0.07	98.85
28R-3, 115–119	147.41	37.96	21.92	38.87	0.37	0.05	0.09	99.26
28R-4, 8–15	147.76	37.31	25.39	36.00	0.39	0.05	0.10	99.24
29R-1, 21–27	148.61	37.86	22.72	37.94	0.38	0.07	0.08	99.04

Table T6 (continued).

Core, section, interval (cm)	Depth (mbsf)	Major element oxide (wt%)						Total
		SiO ₂	FeO	MgO	MnO	CaO	NiO	
29R-1, 75-80	149.15	37.48	23.77	37.15	0.39	0.06	0.07	98.91
29R-1, 114-116	149.54							
29R-2, 69-74	150.36	36.24	30.25	32.00	0.52	0.06	0.07	99.14
29R-2, 133-139	151.00	35.66	33.38	29.32	0.57	0.06	0.04	99.03
29R-3, 60-66	151.69	34.64	38.88	24.86	0.70	0.07	0.02	99.17
29R-4, 17-22	152.57							
30R-2, 47-53	155.23							
30R-2, 90-94	155.66							
30R-2, 90-94-	155.70							
30R-2, 125-130	156.01							
30R-3, 30-34	156.40	36.10	31.91	30.82	0.52	0.02	0.04	99.43
30R-3, 72-76	156.82	36.40	29.53	32.47	0.48	0.05	0.05	98.98

Table T7. Major element oxides in plagioclase. (Continued on next two pages.)

Core, section, interval (cm)	Depth (mbsf)	Modifier	Major element oxide (wt%)							Total
			SiO ₂	Al ₂ O ₃	FeO	MgO	CaO	Na ₂ O	K ₂ O	
179-1105A-										
1R-1, 21-24	15.21		NA	NA	NA	NA	NA	NA	NA	
1R-1, 29-32	15.29		55.18	29.25	0.16	0.02	10.75	5.29	0.05	100.70
1R-2, 80-83	16.88		54.92	29.53	0.16	0.02	11.05	5.14	0.06	100.88
1R-3, 3-6	17.48		55.32	29.04	0.36	0.02	10.48	5.45	0.08	100.75
1R-3, 120-125	18.65		55.86	29.01	0.17	0.03	10.40	5.47	0.07	101.03
1R-4, 25-28	19.15	Type 1	55.94	29.07	0.16	0.02	10.23	5.65	0.08	101.15
1R-4, 25-28	19.15	Type 2	66.40	24.26	0.13	0.00	3.11	5.99	0.29	100.20
1R-5, 25-31	20.61	Type 1	52.92	30.14	0.29	0.08	12.20	4.57	0.05	100.24
1R-5, 25-31	20.61	Type 2	55.88	28.96	0.17	0.03	10.54	5.38	0.07	101.02
1R-5, 102-105	21.38	Type 1	53.00	30.20	0.20	0.02	11.96	4.60	0.05	100.05
1R-5, 102-105	21.38	Type 2	55.49	29.09	0.20	0.04	10.42	5.47	0.08	100.79
1R-6, 33-36	22.15		53.07	30.08	0.26	0.09	11.97	4.72	0.05	100.23
2R-1, 31-35	24.01		52.28	30.58	0.17	0.02	12.43	4.45	0.04	99.96
2R-2, 93-98	26.06		51.81	31.03	0.20	0.02	13.01	4.13	0.04	100.24
2R-2, 127-130	26.40		NA	NA	NA	NA	NA	NA	NA	
2R-3, 69-72	27.25		68.14	22.84	0.07	0.00	1.89	6.30	0.11	99.35
2R-4, 6-11	28.00		51.54	30.70	0.22	0.03	12.64	4.58	0.05	99.75
2R-4, 20-23	28.14		51.69	30.80	0.20	0.03	12.72	4.58	0.05	100.06
3R-1, 79-82	29.49		51.00	30.69	0.17	0.03	12.50	4.47	0.04	98.90
3R-2, 109-113	31.29		51.82	30.54	0.19	0.03	12.56	4.61	0.04	99.80
3R-3, 38-41	32.08		51.36	30.75	0.19	0.08	12.99	3.99	0.06	99.42
3R-3, 54-57	32.24		51.05	31.03	0.14	0.03	13.11	4.27	0.04	99.68
4R-1, 100-105	34.30		54.63	28.77	0.21	0.04	10.41	5.97	0.07	100.08
4R-2, 123-126	35.71		51.71	30.57	0.14	0.04	12.68	4.40	0.04	99.60
4R-3, 16-19	35.98		52.11	31.22	0.16	0.03	13.10	3.82	0.05	100.49
4R-3, 90-93	36.72		52.40	31.53	0.14	0.05	13.22	3.85	0.04	101.23
5R-1, 16-21	38.46	Type 1	62.42	27.39	0.17	0.00	6.03	4.61	0.16	100.79
5R-1, 16-21	38.46	Type 2	60.17	25.15	0.21	0.01	6.10	7.88	0.18	99.71
5R-1, 137-142	39.67		60.79	25.52	0.35	0.06	6.23	8.10	0.15	101.21
5R-2, 44-48	40.22		53.98	30.28	0.16	0.03	11.24	4.46	0.05	100.19
5R-3, 46-52	41.74	Type 1	53.13	28.96	0.15	0.04	10.61	5.28	0.08	98.25
5R-3, 46-52	41.74	Type 2	55.00	28.43	0.15	0.02	9.86	5.89	0.08	99.43
6R-1, 18-23	42.98		54.09	29.20	0.18	0.04	10.88	5.67	0.07	100.14
6R-2, 26-30	44.52	Type 1	56.73	27.58	0.13	0.02	8.84	6.92	0.14	100.36
6R-2, 26-30	44.52	Type 2	53.12	30.34	0.15	0.02	11.65	4.86	0.09	100.22
6R-2, 142-146	45.68		53.35	29.61	0.14	0.02	11.31	5.45	0.06	99.93
6R-3, 6-8	45.82		64.47	23.12	0.12	0.01	2.94	9.49	0.49	100.63
7R-1, 19-24	47.99		53.44	29.86	0.15	0.03	11.34	4.92	0.05	99.80
7R-1, 74-78	48.54		54.10	29.25	0.12	0.02	10.77	5.77	0.06	100.09
7R-2, 13-18	49.26		59.50	25.99	0.25	0.04	6.85	8.07	0.16	100.87
7R-3, 22-27	50.85		60.12	25.53	0.24	0.08	6.30	7.38	0.17	99.81
7R-3, 86-91	51.49		55.96	28.58	0.11	0.01	9.93	5.69	0.11	100.39
7R-3, 103-106	51.66		57.29	27.22	0.16	0.04	8.43	6.40	0.11	99.65
8R-1, 56-60	52.96	Core	55.57	29.16	0.13	0.01	10.34	5.38	0.14	100.73
8R-1, 56-60	52.96	Rim	61.84	24.88	0.13	0.01	5.52	7.97	0.30	100.64
8R-1, 109-114	53.49		54.61	29.38	0.18	0.04	10.93	5.12	0.08	100.33
8R-2, 43-47	54.25	Type 1	54.27	29.24	0.16	0.01	10.77	5.34	0.07	99.85
8R-2, 43-47	54.25	Type 2	59.44	26.07	0.17	0.01	6.98	7.34	0.22	100.23
8R-2, 81-86	54.63		55.03	28.83	0.14	0.02	10.41	5.39	0.08	99.90
8R-3, 110-114	56.32		NA	NA	NA	NA	NA	NA	NA	
8R-4, 42-46	56.95		56.05	27.56	0.21	0.02	9.29	5.95	0.10	99.17
8R-4, 74-78	57.27		54.02	29.64	0.16	0.02	11.09	5.59	0.06	100.58
8R-4, 74-78	57.27		55.94	28.61	0.15	0.03	9.69	6.43	0.08	100.92
9R-1, 20-24	57.60		58.69	27.10	0.15	0.02	7.82	6.61	0.11	100.49
9R-1, 67-71	58.07	Type 1	58.68	26.63	0.14	0.01	7.74	6.97	0.20	100.38
9R-1, 67-71	58.07	Type 2	62.56	24.71	0.20	0.00	4.72	8.44	0.40	101.02
9R-1, 128-134	58.68		60.81	25.63	0.27	0.01	6.39	7.68	0.23	101.01
9R-2, 17-20	59.07		59.32	26.18	0.17	0.02	7.30	7.18	0.17	100.32
9R-3, 66-72	60.93		59.14	26.15	0.18	0.02	7.23	7.05	0.15	99.91
9R-3, 129-134	61.56	Type 1	58.89	26.50	0.20	0.02	7.72	7.00	0.14	100.47
9R-3, 129-134	61.56	Type 2	53.98	29.46	0.18	0.01	11.30	5.05	0.07	100.08
9R-4, 59-63	62.28	Type 1	53.05	29.29	0.32	0.08	11.55	4.79	0.07	99.16
9R-4, 59-63	62.28	Type 2	57.32	27.43	0.16	0.01	8.77	6.39	0.10	100.18
10R-1, 98-102	62.98		53.31	29.98	0.15	0.02	11.95	4.72	0.07	100.20
10R-2, 77-82	64.12		60.29	25.80	0.20	0.02	6.53	7.51	0.19	100.54
10R-2, 132-137	64.67	Type 1	53.69	29.63	0.22	0.02	11.57	4.85	0.07	100.04
10R-2, 132-137	64.67	Type 2	57.65	27.31	0.18	0.02	8.54	6.54	0.12	100.36
10R-3, 19-23	64.94	Type 1	53.99	29.62	0.16	0.03	11.44	4.94	0.11	100.29

Table T7 (continued).

Core, section, interval (cm)	Depth (mbsf)	Modifier	Major element oxide (wt%)							Total
			SiO ₂	Al ₂ O ₃	FeO	MgO	CaO	Na ₂ O	K ₂ O	
10R-3, 19-23	64.94	Type 2	56.05	28.00	0.29	0.07	9.69	5.84	0.16	100.09
10R-3, 125-129	66.00		55.36	28.64	0.14	0.02	10.20	5.63	0.13	100.13
11R-1, 81-86	67.81		NA	NA	NA	NA	NA	NA	NA	NA
11R-2, 3-6	68.43		59.61	26.48	0.55	0.01	6.74	7.41	0.15	100.97
11R-2, 89-94	69.29		59.92	25.74	0.25	0.02	6.64	7.65	0.18	100.39
11R-2, 110-115	69.50		59.56	26.68	0.23	0.02	7.08	7.33	0.15	101.04
11R-3, 64-68	70.54		59.55	26.35	0.25	0.02	7.06	7.30	0.15	100.66
11R-3, 142-147	71.32		59.59	26.03	0.19	0.01	6.91	7.32	0.16	100.21
12R-1, 51-57	71.81		60.81	25.52	0.37	0.08	6.30	7.46	0.14	100.68
12R-1, 91-97	72.21	Type 1	50.31	31.67	0.22	0.04	13.75	3.63	0.03	99.66
12R-1, 91-97	72.21	Type 2	52.63	30.11	0.25	0.06	11.79	4.75	0.05	99.64
12R-3, 12-16	74.37	Fine	53.30	29.53	0.13	0.03	11.54	4.83	0.08	99.42
12R-3, 12-16	74.37	Coarse	NA	NA	NA	NA	NA	NA	NA	NA
13R-1, 38-42	76.68		56.68	27.22	0.16	0.01	8.66	6.37	0.10	99.20
13R-1, 68-73	76.98		58.03	26.38	0.29	0.02	7.81	6.88	0.12	99.54
13R-2, 12-16	77.82	Type 1	54.91	28.47	0.18	0.03	10.32	5.51	0.09	99.51
13R-2, 12-16	77.82	Type 2	57.56	26.90	0.18	0.03	8.38	6.57	0.13	99.74
13R-2, 44-49	78.14		57.16	27.46	0.18	0.03	8.74	6.40	0.12	100.07
13R-2, 122-127	78.92		57.16	27.03	0.19	0.02	8.55	6.49	0.12	99.55
13R-3, 11-15	79.15		56.29	27.44	0.24	0.07	8.91	6.23	0.09	99.25
13R-4, 7-11	80.51		51.15	30.83	0.11	0.03	13.12	3.94	0.03	99.22
14R-1, 55-60	81.55		52.69	30.64	0.12	0.03	12.47	4.46	0.04	100.44
14R-2, 114-119	83.55		50.87	31.05	0.15	0.04	13.26	3.83	0.03	99.22
14R-3, 10-15	83.74		52.01	30.28	0.16	0.04	12.56	4.22	0.05	99.32
14R-4, 22-27	85.31		52.24	30.27	0.14	0.02	12.43	4.33	0.04	99.48
15R-1, 14-18	86.14		59.60	25.45	0.21	0.01	6.59	7.40	0.21	99.47
15R-2, 39-43	87.89		57.19	27.11	0.15	0.01	8.64	6.41	0.11	99.63
15R-3, 7-12	89.04		58.03	26.68	0.16	0.01	8.12	6.76	0.12	99.88
16R-1, 22-27	90.82		60.46	25.92	0.22	0.01	6.68	7.45	0.15	100.88
16R-2, 124-128	93.17		52.62	30.15	0.22	0.03	12.20	4.50	0.05	99.78
16R-2, 133-139	93.26		51.81	30.88	0.17	0.05	13.14	4.08	0.04	100.17
16R-3, 35-39	93.69		51.33	31.13	0.16	0.05	13.48	3.88	0.04	100.07
17R-1, 51-55	96.11		59.84	25.16	0.20	0.01	6.52	7.61	0.22	99.55
17R-1, 94-99	96.54		51.87	30.96	0.12	0.02	13.16	4.09	0.03	100.26
17R-2, 47-52	97.49	Type 1	51.86	30.85	0.11	0.02	13.06	4.14	0.03	100.08
17R-2, 47-52	97.49	Type 2	54.46	29.40	0.12	0.02	11.23	5.23	0.05	100.50
17R-2, 75-80	97.77		51.60	31.14	0.15	0.04	13.23	4.03	0.04	100.23
17R-3, 59-65	99.04		53.91	29.76	0.15	0.03	11.54	5.06	0.05	100.50
17R-4, 0-7	99.95		60.10	25.85	0.19	0.03	6.71	7.65	0.19	100.72
18R-1, 62-68	100.82		58.59	25.95	0.32	0.04	7.10	7.41	0.15	99.56
19R-2, 80-85	107.50	Type 1	54.05	29.41	0.24	0.02	11.24	5.10	0.09	100.13
19R-2, 80-85	107.50	Type 2	58.41	26.85	0.17	0.01	7.96	6.93	0.16	100.49
19R-3, 75-80	108.80	Type 1	51.67	31.24	0.19	0.02	13.26	4.01	0.06	100.44
19R-3, 75-80	108.80	Type 2	56.63	27.81	0.15	0.02	9.31	6.20	0.11	100.24
19R-4, 18-23	109.69		52.72	30.14	0.20	0.02	12.07	4.57	0.06	99.77
19R-4, 43-46	109.94		58.17	27.01	0.15	0.01	8.25	6.85	0.12	100.57
20R-1, 95-100	110.75		52.50	30.66	0.16	0.03	12.64	4.35	0.07	100.40
20R-1, 111-117	110.91		52.85	30.39	0.20	0.03	12.35	4.52	0.07	100.42
21R-1, 12-16	110.92	Type 1	52.18	30.88	0.19	0.03	12.93	4.20	0.07	100.47
21R-1, 12-16	110.92	Type 2	55.47	28.69	0.17	0.02	10.32	5.67	0.11	100.46
21R-1, 89-94	111.69	Type 1	52.23	30.78	0.25	0.03	12.83	4.24	0.06	100.40
21R-1, 89-94	111.69	Type 2	59.10	26.51	0.22	0.02	7.59	7.21	0.13	100.78
21R-2, 84-88	112.98	Type 1	55.70	28.45	0.17	0.03	10.04	5.83	0.08	100.29
21R-2, 84-88	112.98	Type 2	59.59	26.00	0.17	0.03	6.90	7.59	0.09	100.37
22R-2, 20-25	116.70	Type 1	54.51	28.60	0.16	0.03	10.31	5.66	0.08	99.34
22R-2, 20-25	116.70	Type 2	57.78	26.99	0.13	0.01	8.09	6.89	0.11	100.02
22R-3, 7-11	117.75	Type 1	55.93	28.06	0.24	0.02	9.54	6.03	0.09	99.91
22R-3, 7-11	117.75	Type 2	58.53	26.80	0.15	0.04	7.63	7.01	0.14	100.30
22R-3, 63-69	118.31	Type 1	55.26	28.04	0.15	0.01	9.93	5.75	0.09	99.24
22R-3, 63-69	118.31	Type 2	58.09	26.55	0.16	0.02	7.98	6.81	0.13	99.74
23R-1, 53-57	119.93		56.78	27.49	0.15	0.01	9.11	6.34	0.11	99.99
23R-1, 142-148	120.82		57.99	27.02	0.16	0.02	8.39	6.77	0.11	100.45
23R-2, 1-5	120.91	Type 1	56.15	28.20	0.16	0.02	9.69	6.02	0.09	100.33
23R-2, 1-5	120.91	Type 2	58.17	26.90	0.20	0.03	8.22	6.83	0.12	100.47
24R-1, 93-98	125.33	Type 1	60.05	25.73	0.21	0.02	6.63	7.68	0.24	100.56
24R-1, 93-98	125.33	Type 2	58.01	27.36	0.16	0.02	8.50	6.73	0.14	100.91
24R-2, 49-53	126.32		57.54	26.98	0.26	0.21	8.36	6.62	0.12	100.10
24R-2, 94-98	126.77		60.18	26.04	0.20	0.02	6.74	7.51	0.18	100.87
24R-2, 121-126	127.04	Type 1	53.81	29.74	0.18	0.04	11.66	4.89	0.09	100.40

Table T7 (continued).

Core, section, interval (cm)	Depth (mbsf)	Modifier	Major element oxide (wt%)							Total
			SiO ₂	Al ₂ O ₃	FeO	MgO	CaO	Na ₂ O	K ₂ O	
24R-2, 121–126	127.04	Type 2	56.63	27.78	0.32	0.03	9.30	6.19	0.14	100.37
24R-3, 116–120	128.32		NA	NA	NA	NA	NA	NA	NA	
25R-1, 83–89	129.83		59.64	26.07	0.58	0.10	7.04	7.31	0.18	100.93
25R-2, 3–8	130.47		59.35	25.96	0.39	0.10	6.95	7.81	0.17	100.72
25R-2, 55–62	130.99	Type 1	52.42	30.13	0.18	0.03	12.29	4.53	0.06	99.62
25R-2, 55–62	130.99	Type 2	55.77	28.06	0.17	0.02	9.97	5.77	0.09	99.86
25R-2, 84–90	131.28		52.05	29.90	0.18	0.02	12.15	4.88	0.06	99.25
25R-3, 79–82	132.62		52.47	30.12	0.18	0.03	12.32	4.76	0.06	99.94
25R-4, 31–38	133.33		53.21	29.57	0.16	0.02	11.62	5.19	0.05	99.82
26R-1, 32–38	134.32		60.13	25.77	0.17	0.01	6.72	8.04	0.30	101.15
26R-1, 115–121	135.15		51.99	30.34	0.18	0.04	12.62	4.62	0.06	99.84
26R-3, 20–26	136.96		52.57	29.80	0.15	0.03	11.99	4.96	0.06	99.55
26R-3, 117–122	137.93		52.07	30.31	0.22	0.04	12.58	4.55	0.05	99.83
26R-4, 24–30	138.41		52.67	30.00	0.17	0.03	12.09	4.87	0.06	99.89
27R-1, 8–12	138.78	Type 1	53.43	29.53	0.16	0.04	11.49	5.27	0.07	99.98
27R-1, 8–12	138.78	Type 2	60.13	25.58	0.24	0.01	5.83	8.52	0.35	100.66
27R-1, 82–88	139.52		NA	NA	NA	NA	NA	NA	NA	
27R-2, 81–87	140.69	Type 1	51.79	30.50	0.22	0.03	12.79	4.52	0.05	99.90
27R-2, 81–87	140.69	Type 2	53.40	29.42	0.21	0.03	11.44	5.30	0.08	99.88
27R-3, 27–33	141.29	Core	55.21	28.71	0.22	0.03	10.50	5.56	0.08	100.30
27R-3, 27–33	141.29	Rim	53.68	29.06	0.23	0.02	11.12	5.24	0.07	99.40
27R-4, 29–31	142.81		61.69	24.70	0.22	0.01	5.21	9.03	0.36	101.22
27R-4, 71–76	143.23		52.05	30.36	0.20	0.04	12.58	4.63	0.05	99.92
28R-1, 54–60	144.24		52.92	29.84	0.20	0.05	11.98	4.95	0.07	100.00
28R-2, 78–84	145.58	Type 1	52.37	30.15	0.28	0.04	12.51	4.66	0.05	100.06
28R-2, 78–84	145.58	Type 2	54.20	29.48	0.33	0.04	11.35	5.18	0.06	100.63
28R-3, 61–66	146.87	Type 1	52.52	29.98	0.28	0.09	12.18	4.84	0.05	99.95
28R-3, 61–66	146.87	Type 2	53.70	29.35	0.18	0.03	11.41	5.33	0.06	100.05
28R-3, 115–119	147.41		52.47	29.74	0.20	0.05	11.97	5.00	0.05	99.47
28R-4, 8–15	147.76	Type 1	51.13	30.58	0.21	0.03	12.97	4.36	0.05	99.33
28R-4, 8–15	147.76	Type 2	54.08	28.93	0.21	0.04	11.06	5.55	0.07	99.93
29R-1, 21–27	148.61	Type 1	52.45	29.95	0.21	0.05	12.23	4.83	0.05	99.76
29R-1, 21–27	148.61	Type 2	53.33	29.42	0.22	0.04	11.59	5.21	0.05	99.86
29R-1, 75–80	149.15		52.45	29.56	0.24	0.08	11.84	5.04	0.05	99.26
29R-1, 114–116	149.54		55.39	28.50	0.19	0.02	9.84	6.38	0.09	100.41
29R-2, 69–74	150.36		53.55	29.21	0.19	0.03	11.28	5.40	0.05	99.71
29R-2, 133–139	151.00		53.90	29.07	0.21	0.02	11.13	5.48	0.08	99.89
29R-3, 60–66	151.69		57.06	27.77	0.19	0.02	9.30	6.08	0.11	100.53
29R-4, 17–22	152.57		58.39	26.28	0.15	0.01	7.59	7.60	0.11	100.14
30R-2, 47–53	155.23		58.18	26.09	0.22	0.03	7.63	7.45	0.15	99.74
30R-2, 90–94	155.66	Type 1	56.70	27.08	0.18	0.01	8.57	6.96	0.13	99.61
30R-2, 90–94	155.66	Type 2	57.65	26.62	0.16	0.01	7.95	7.35	0.15	99.89
30R-2, 90–94	155.70	Laminated	58.28	26.68	0.15	0.01	7.95	7.44	0.11	100.62
30R-2, 125–130	156.01		58.73	26.12	0.18	0.02	7.17	7.95	0.14	100.31
30R-3, 30–34	156.40		53.81	29.20	0.17	0.02	10.81	5.79	0.06	99.86
30R-3, 72–76	156.82		54.04	29.43	0.14	0.02	11.07	5.63	0.05	100.36